Development of Cold Spray Cr Coatings on Zr-alloy for Advanced Nuclear Fuel Cladding

By

Tyler Alexander Dabney

A dissertation submitted in partial fulfillment of

the requirements for the degree of

Doctor of Philosophy

(Materials Science & Engineering)

at the

UNIVERSITY OF WISCONSIN-MADISON

2024

Date of final oral examination: 08/27/2024

This dissertation is approved by the following members of the Final Oral Committee:

Kumar Sridharan, Professor, Materials Science & Engineering and Nuclear Engineering & Engineering Physics

Frank Pfefferkorn, Professor, Mechanical Engineering

Shiva Rudraraju, Associate Professor, Mechanical Engineering

Lianyi Chen, Associate Professor, Mechanical Engineering

Hwasung Yeom, Assistant Professor, Division of Advanced Nuclear Engineering, Pohang University of Science and Technology

Yinbin Miao, Principal Materials Scientist, Argonne National Laboratory

Abstract

Zirconium alloys (Zr-alloys) have been used as materials for fuel cladding (tubes that contain the uranium-bearing fuel) on account of their high neutron transparency, strength, and corrosion resistance. Several generations of Zr-alloys have been developed with minor adjustments in already low concentration of alloying elements (e.g., Fe, Sn, Nb, Cr) with the goal of imparting improvements to high temperature strength and corrosion resistance. In recent years, there has been a drive to enhance the oxidation resistance and accident tolerance of Zr-alloy fuel cladding in loss-of-coolant accident (LOCA) scenarios, where the temperature can significantly exceed the normal reactor operating temperature. A potential solution is to apply a thin coating of an oxidation-resistant material to the outer surface of the Zr-alloy cladding. This research focuses on the development of chromium (Cr) coatings using cold spray deposition technology. Although not the focus of this study, such a coating can potentially enhance the ballooning and bursting resistance of the cladding, a requirement for the use of economically attractive higher enrichment, higher burnup fuel. In cold spray, powder particles of the coating material are propelled at supersonic velocities towards the surface of a substrate, where upon impact they plastically deform at high strain rates to form a coating. The particle temperature is low, and deposition occurs in solid state. The research was conducted using the commercial 4000-34 CGT cold spray facility at the University of Wisconsin, Madison.

This research focused on four areas crucial to the development of Cr cold spray coatings on Zr-alloy for advanced nuclear fuel cladding, namely: (i) coating formation mechanisms, (ii) irradiation effects, (iii) mechanical behavior of the coating and coating-substrate system, and (iv) hydrothermal corrosion and high temperature oxidation of the coatings. The research was conducted using powders referred to in this thesis as electrolytic soft Cr powders, that were produced commercially by a combination of an electrolytic method and a gentle impact milling process. Zr-alloys used in reactors for cladding, namely Zircaloy-4, ZIRLO^{TM}, and Optimized ZIRLO^{TM} (OPZ) in either flat or tubular cladding geometry were used as substrates for various phases of this research. Deposition was conducted using either nitrogen or helium or a mixture of these carrier gases to propel the particles though the converging-diverging de Laval nozzle and to then accelerate them at supersonic velocities towards the substrate.

Given the importance of the powder microstructure in solid state processes such as cold spray, extensive characterization of the feedstock Cr powder particles was conducted using techniques such as scanning electron microscopy (SEM), transmission electron microscopy (TEM), electron backscattered diffraction (EBSD), transmission Kikuchi diffraction (TKD), and X-ray diffraction (XRD). The powders were phase-pure and consisted of large grains in the central regions and fine elongated nanocrystalline grains near the edges, a result of the manufacturing route. Nanoindentation tests of the powders showed low hardness – a beneficial feature for cold spray – as it is indicative of the ability of the particles to plastically deform upon impact. Coating depositions were performed by varying select parameters that are known to profoundly influence the microstructure and other characteristics of the coating, including carrier gas composition, gas preheat temperature, and gun traverse speed. Dense thick coatings (25 to over 150 μm) with strong adhesion to the substrate were achieved. Typical of cold spray, the coatings exhibited a heterogeneous structure over multiple length scales, consisting of elongated and dynamically recrystallized grains (ultrafine to nanocrystalline), high dislocation density and strained structures, gradation in grain size, and interparticle boundaries.

A fundamental understanding of the coating formation mechanisms both in the interfacial bonding and buildup phases was achieved by single particle impact studies of Cr-on-Zr-alloy and Cr-on Cr, respectively. Cold spray parameters were adjusted to deposit individual Cr particles on these substrates, leading to the identification of two regimes of impact and two distinct sets of critical velocities for bonding. Deposition efficiency was measured by taking the ratio of the number of adhered particles to the total number of particles impacted as a function of particle velocity, and the critical velocity was determined as the velocity where deposition efficiency became non-zero. The particle velocity was predicted using computation fluid dynamics (CFD) codes. For the Cr-on-Zr system, characterization of impacted particle cross-sections using SEM and EBSD revealed that changes due to impact were confined to the outer regions of the Cr particle,

while the near-interface regions of the Zr-alloy consisted of a dynamically recrystallized nanograined structure. High resolution TEM (HR-TEM) imaging and Fast Fourier Transform (FFT) analysis showed the evolution of crystallographic coherency between the Cr and Zr-alloy which, in combination with microscopic mechanical interlocking, resulted in strong particle-substrate adhesion. For the Cr-on-Cr system, the deformation and high dislocation densities extended into the particle interior and regions of dynamically recrystallized grains were observed at the interparticle boundaries. A particularly notable finding was that interparticle bonding in this system could be achieved even at particle velocities where severe plastic deformation and jetting was not observed. In other words, the critical factor governing Cr interparticle cohesion was the localized plastic strain necessary to initiate dynamic recrystallization across interparticle boundaries, rather than that necessary for jetting as has been widely established for more deformable material systems. The microstructural developments in single particle impact studies correlated well with the microstructure of the Cr coatings on Zr-alloy characterized using TKD. A more insightful understanding of coating deposition based on microstructure and quality was achieved in terms of the parameter, η, the ratio of the particle velocity to the critical velocity. The experimental results on deposition were benchmarked by simulations of single particle and multiparticle impact using finite element modeling (FEM) code.

To reduce the interface roughness, experiments were conducted via low particle velocity deposition to first maintain low interface roughness followed by a high particle velocity deposition for coating buildup. This seed layer approach was not successful in reducing interface roughness but provided insights into deformation processes at play during multiple particle impacts. Depositing Cr particles at higher traverse speeds to decrease the number of particles impacting the substrate per unit time showed more promising results. Shot peening using stainless steel shot media was very effective in reducing the inherent coating surface roughness resulting from cold spray deposition. Based on this study, a novel cold spray shot peening (CSSP) process was developed, where the cold spray gun was used for shot peening in conjunction with larger Cr particles (as the shot media) and low spray velocity conditions. This approach also showed notable

reductions in surface roughness and inherently presents no concerns of cross-contamination of materials. CSSP promises to be a more economic and sustainable approach for reducing surface roughness of as-deposited Cr coatings as an alternative to conventional mechanical grinding.

Cr-coated Zr-alloy samples were irradiated using 80 MeV Xe^{26+} ions to assess the effects of irradiation damage on the Cr-Zr interface and within the cold spray Cr coating. STEM characterization of the as-deposited Cr-Zr interface revealed coherent bonding and cold spray induced co-segregation of Cr and Fe starting at the near-interface and extending up to 200 nm into the Zr-alloy substrate. Irradiation led to homogenization of Fe in the Zr-alloy matrix and the formation of a ~20 nm thick amorphous layer of the Cr/Zr interface, a result supported in part by thermodynamic calculations. Irradiation within the Cr coating saw elimination of elongated grains, and both partial recrystallization and slight grain growth were observed at the interparticle boundaries. In essence, irradiation promoted densification of the coating by effectively obliterating interparticle boundaries. Nanoindentation testing revealed slight softening of the coating, which was attributed to irradiation-induced recrystallization and deformation recovery. Overall, the results show that cold spray Cr coatings on Zr-alloys exhibit good radiation resistance for advanced nuclear fuel applications.

In addition to microhardness and nanoindentation methods used routinely for measuring the mechanical behavior of the coating and substrate, high energy synchrotron X-ray diffraction in the transmission mode was performed *in situ* during uniaxial tensile testing to understand the deformation and cracking behavior of cold spray Cr-coated Zr-alloy samples in both the as-deposited and annealed conditions. Both elastic and plastic deformation mechanisms during tensile deformation were quantified using detailed X-ray line profile analysis. High dislocation density with a unique distribution of edge and screw fractions and non-zero lattice strain was determined to be present in the Cr coating due to high strain-rate deformation during cold spray deposition. The annealing treatment reduced both residual lattice strain and dislocation density (with preferentially higher reduction in edge dislocation fractions) in the Cr coating. This led to a heterogeneous distribution of dislocation density and character among different grains that enhanced

resistance to crack propagation in the annealed Cr coating. The mechanical properties of the Zr-alloy were not significantly altered by the presence of the cold sprayed Cr coating.

To gain more fundamental understanding of the deformation behavior of the coating-substrate system, microcantilever beams were prepared for cold spray Cr coated Zr-alloy using focused ion beam (FIB) to create samples such that the cantilever was perpendicular to and incorporated the coating-substrate interface at its base. In addition to as-deposited samples, samples annealed at 600 °C to simulate initial loss of coolant, and 1000 °C to simulate inter-diffusion during LOCA, as well as irradiated samples were also tested. The bend tests, intended to force failure by cracking, and performed with *in situ* SEM imaging in concert with acquisition of load-displacement profiles provided holistic information about the failure mechanisms. As-deposited coatings displayed high adhesion strength at the interface and brittle fracture at the interface, while samples annealed at 600 °C showed very ductile behavior with peeling of the Cr-Zr interface. The 1000 °C annealed sample showed fracture behavior due to the existence of a thin, $ZrCr_2$ intermetallic layer formed at the interface during high temperature inter-diffusion, however crack propagation was readily restricted by the now-ductile Cr coating and Zr-alloy substrate. For example, cracking occurred in short spurts followed by immediate recovery. The ion-irradiated Cr coatings showed mixed brittle-ductile behavior, which was attributed to various effects stemming from differences in displacement damage to ion beam mixing to thermal recovery of dislocations. Overall, all mechanical tests were reflective of potential improvements to the mechanical performance of Zr-alloy by the addition of cold spray Cr coating.

Hydrothermal corrosion tests were conducted in autoclave pressure vessels set to 360 °C and 18.6 MPa for 30 days in two different environments: static pure water and Li-enhanced water to simulate pressurized water reactor (PWR) conditions. For the coatings tested in pure water, weight change measurements showed a significant reduction in corrosion rate due to Cr coatings compared to uncoated Zr-alloy cladding, and additionally corrosion rates were similar for Cr coatings sprayed with helium and nitrogen carrier gases. For the coatings tested in elevated Li water chemistry, STEM imaging revealed a thin (<50 nm) continuous oxide scale on the surface of the Cr coatings confirmed to be Cr_2O_3 using STEM-EDS. Electron probe micro-analysis (EPMA) in conjunction with wavelength dispersive X-ray spectroscopy (WDS) revealed similar distribution of oxygen at the inter-particle boundaries before and after corrosion testing and no evidence of corrosion at the interface of the Cr coating and the Zr-alloy substrate, suggesting that the particle boundaries are bonded thoroughly enough to prevent undercoating corrosion. High temperature oxidation tests in air and steam environments showed formation of a thin protective Cr_2O_3 layer (<10 µm) representing a significantly slower oxidation kinetics than Zr-alloy, which formed a thick ZrO_2 oxide layer (>100 µm) under the same test conditions.

Acknowledgments

I would like to express my sincere thanks and gratitude to my advisor, Dr. Kumar Sridharan. First, for granting me an interview to join his research group even though the application window was closed. Second, for providing me countless opportunities to travel to conferences, present my work, and meet with industry partners all while being an undergraduate student! Third, for connecting me to various researchers at national laboratories which resulted in several internships during my time in graduate school. The list goes on, but your patience and overwhelming support throughout my graduate education is the reason I am here today.

I am also very grateful to have had the opportunity to work with three amazing scientists and engineers. Dr. Ben Maier's expertise was the reason I fell in love with cold spray, and his guidance in helping me craft my Ph.D. research was extremely helpful. Dr. Sung Yeom's hard work, tenacity, and careful planning of research taught me that all things were possible if you set your mind to it. I am grateful for our long talks (both work and non-work related) and am happy to have him as a friend. Finally, Dr. K. N. Sasidhar filled the mentorship gap when Dr. Yeom left the group, and he was an invaluable support during my final push to the finish line. From day-to-day help with characterization to providing the needed pizazz in journal articles, I can't thank you enough. The work of these staff members is critical to the success of the research performed by the NAMRG group.

I would also like to thank the many researchers I got to know through my internships at the national laboratories. Thank you to Dr. Laura Jamison at Argonne, for suggesting using the *in situ* synchrotron beams at the APS and continuously providing me time at the ATLAS beamline for irradiation studies. Thank you to Dr. Kun Mo and Dr. Yinbin Miao for performing the experiments during the COVID lockdowns and providing weekly support during the data analysis phase, and to Dr. Peter Mouche for helping me assist with the irradiations in person and teaching me along the way. Also, thank you to Dr. Stu Maloy for finding interest in my work during my presentation at the IMAT conference, which led to an internship at Los Alamos National Laboratory. Thank you to Dr. Nan Li and Dr. Ben Eftink for sponsoring my time at LANL and showing me what it's like to be a successful materials scientist. Also, thank you to Dr. Dongyue Xie and Dr. Tongjun Niu for helping me fabricate the micro-cantilever beams and in performing the bending tests, and to Dr. Peter Beck for integrating my cold spray coatings into your Ph.D. research on ring-pull testing.

Financially, this work has been supported by a Graduate Fellowship through the University Nuclear Leadership Program, though which I was able to live out my dream of working at a National Laboratory and pursue research topics that I was interested in. I was also supported by several grants from the

Department of Energy, Office of Nuclear Energy regarding Accident Tolerant Fuel Claddings. Additionally, the support from everyone at Westinghouse – Dr. Ben Maier, Ms. Jorie Walters, Mr. Nick Pocquette, Ms. Katerina Frederick, Mr. Ernesto Pittruzzella, and Ms. Henrietta Jenkins – was invaluable during my graduate studies. Thank you for your hard work in bringing this technology to industry.

I was also assisted by multiple undergraduate students over the years. Alex Budke and Rogelio Ramirez, who helped me develop techniques for measuring residual stresses and cold spray shot peening, which were tremendous successes. Nicole Fessler, Lane Meddaugh, and Alfredo Navarete-Nunez, who were champions of using ANSYS to model the cold spray process. JP Lacy and Carson Lukas, who were the best office mates anyone could ask for. Greg Johnson and Evan Willing, my fellow cold spray experts who performed countless spray runs with me, and Bennett LaSalle for your tenacious sample preparation and characterization of cold spray coatings. I would also like to acknowledge the staff at the NIAC, particularly Dr. Julie Morasch, Dr. Alex Kvit, and Dr. Don Savage, for all support with the characterization instruments. Last but not least Dr. Kyle Quillin, my friend who walked the same path with me from undergraduate research to Ph.D. completion. I am lucky to have someone there by my side through the highs and lows of graduate research – congratulations to us!

Finally, I would like to end by recognizing my friends and family who supported me all along the way. Many thanks to my friends Steven, John, Dan, and Nicole for tolerating me as I spent nearly a decade as a college student. My extended family Lori, Courtney, Christine, and Ryan for staying interested as I rambled on about research at family gatherings. And to my family, Sue, CJ, Josh, and Kaity, for their unconditional love, encouragement, and support along the way. Your past and continued support means the world to me.

Table of Contents

List of Figures

List of Tables

Abbreviations

APS – advanced photon source

ATF – accident tolerant fuel

ATLAS – Argonne Tandem Linac Accelerator System

BC – band contrast

BDBA – beyond design basis accident

BDTT – brittle-to-ductile transition temperature

BF – bright field

cDRX – continuous dynamic recrystallization

CFD – computational fluid dynamics

CSSP – cold spray shot peening

Cr-He – Cr coatings deposited using 95%He/5%-N_2 gas preheated to 500 °C and 3.8 MPa pressure

Cr-N2 – Cr coating deposited using 100%-N_2 gas preheated to 750 °C and 4.0 MPa pressure

CSSP – cold spray shot peening

DE – deposition efficiency

DF – dark field

dpa – displacements per atom

EBSD – electron backscatter diffraction

EDS – energy dispersive X-ray spectroscopy

EPMA – electron probe micro-analysis

FEM – finite element modeling

FFT – fast Fourier transform

gDRX – geometrical dynamic recrystallization

GOS – grain orientation spread

GROD – grain reference orientation deviation

HAADF – high angle annular dark field

HR-TEM – high-resolution transmission electron microscopy

IPF – inverse pole figure

JC – Johnson-Cook

KAM – kernel average misorientation

LOCA – loss-of-coolant accident

LWR – light water reactor

NIAC – nanoscale imaging and analysis center

PWR – pressurized water reactor

SAED – selected area electron diffraction

SEM – scanning electron microscopy

SP – shot peening

SPH – smooth particle hydrodynamics

STEM – scanning transmission electron microscopy

TEM – transmission electron microscopy

WDS – wavelength dispersive X-ray spectroscopy

WEC – Westinghouse Electric Company

XRD – X-ray diffraction

Zr-alloy – zirconium-alloy

1. Background and Motivation

1.1. Materials for nuclear energy

1.1.1. Overview of nuclear power in the United States

Nuclear power plays an important role in clean energy production in the United States and world-wide. Nuclear plants provide about 13% of the total electric power generated worldwide and have steadily constituted about 20% of total annual U.S. electricity generation since the 1990s [1]. Nearly all commercial nuclear reactors in the U.S. are light water reactors (LWR) which use water as a coolant. LWRs are classified as either pressurized water reactors (PWR) or boiling water reactors (BWR), with the main difference being the water circuit designed for boiling resulting in associated differences in water chemistry, phase, and temperature [2]. Schematic illustrations of PWR and BWR are shown in Fig. 1.1.

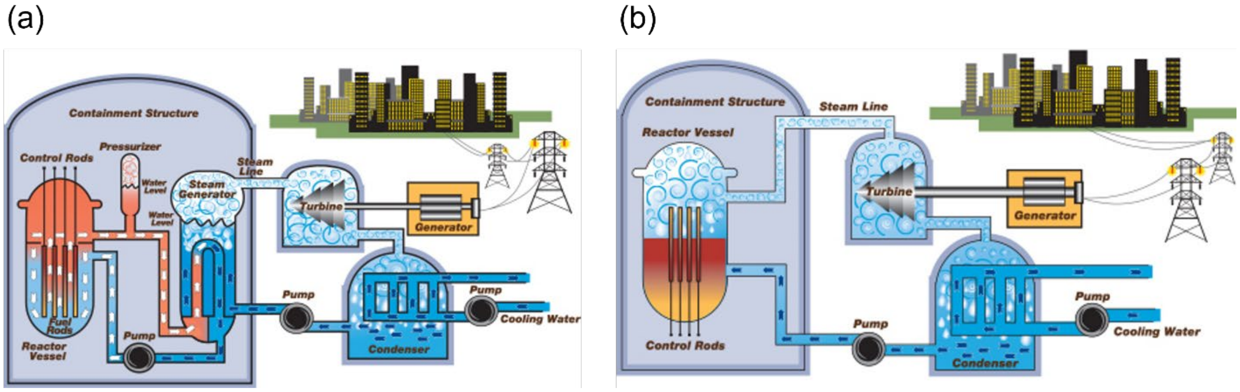

Fig. 1.1. Simplified schematic of light water (LWR) nuclear reactors: (a) pressurized water reactor (PWR); (b) boiling water reactor (BWR), reproduced from [3].

The reactor pressure vessel (RPV) shown in Fig. 1.1 house fuel cladding assemblies that contain the primary fuel that undergoes continuous atomic fission within the *reactor core*. Water coolant flows around the cladding tubes. The fuel comprises enriched uranium in the form of 1 cm long cylindrical uranium dioxide *fuel pellets*, shown in Fig. 1.2 (a). The pellets are encased in metal tubes called *fuel cladding*, which are 9-10 mm in diameter and about 4 m in length (Fig. 1.2 b). The cladding is typically made of a zirconium alloy (Zr-alloy) due to their good strength, excellent corrosion resistance in LWR water coolant at operating temperatures, and low absorption cross-section of Zr for thermal neutrons [4]. The fuel and cladding in combination are referred to as *fuel rod* (Fig. 1.2 c), and these rods are bundled together to create *fuel assemblies* (Fig. 1.2 d). A fuel assembly contains about 300 fuel rods and a typical reactor core contains about 200 fuel assemblies, which generate an immense amount of carbon-free electric power.

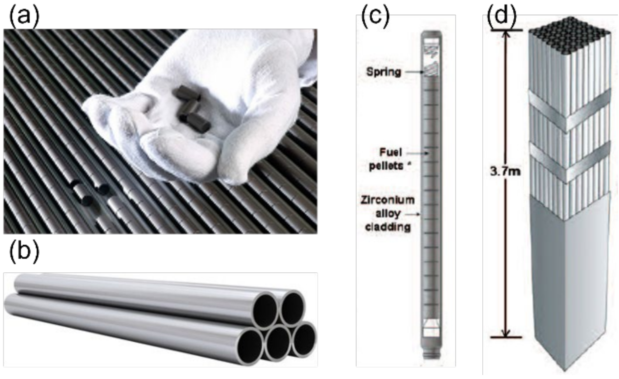

Fig. 1.2. Photographs of (a) UO_2 pellets and (b) Zr-alloy fuel cladding that make up the fuel rod shown schematically in (c). These fuel rods are bundled together in fuel assemblies, shown in (d). Reproduced from the NRC website.

1.1.2. Reactor environmental effects on materials

The environment in reactor core is harsh, with a combination of elevated temperatures, corrosion, neutron irradiation, and mechanical stresses acting synergistically on the structural components and contributing to the degradation of core materials, particularly the cladding [4]. Temperatures in PWRs range from 290 to 320 °C and the water chemistry consists of elevated levels of hydrogen, boron, and lithium for radiolysis, reactivity, and pH control [4]. The high temperature water environment causes uniform corrosion of Zr-alloy cladding leading to a normally protective oxide. Particulates of corrosion products from various materials in the reactor core, referred to as CRUD (Chalk River Unidentified Deposits), may deposit on the fuel cladding leading to changes in thermal conductivity and axial offsets from uneven mechanical stresses. Decades of research has produced an extensive amount of corrosion data for Zr-alloy in LWRs, allowing for safe and reliable operation of nuclear plants under normal operating conditions.

Materials degradation processes (e.g., corrosion, creep, embrittlement) in the reactor core are exacerbated by irradiation produced by fission in the reactor core. Fission products consist of high energy neutrons and gamma rays that are slowed down via collisions with the coolant and structural components [4]. Irradiation damage consists of elastic interactions between fast neutrons and atoms and structural materials, such as the Zr-alloy cladding. These neutrons transfer kinetic energy to the target atom which displaces the atom from its lattice site. The *primary knocked-on atom* (PKA) can interact with other atoms in the alloy along its path, producing *point defects* such as vacancies or interstitials [5]. The collided atoms can then interact with other atoms creating a *displacement cascade* within the crystal lattice. The primary measure of irradiation damage is in units of *displacements per atom* (dpa), which is the number of times an atom is displaced from its lattice site. Due to its relatively low thermal neutron absorption cross-section (~0.18 barn), Zr-alloys are relatively neutron transparent and experience an average of 3.9 dpa per year, for about 15-16 dpa per fuel cycle (~5 years) [4,5].

Point defects caused by radiation damage can accumulate into *defect clusters,* such as voids and dislocation loops. Some consequences of irradiation damage on material microstructure include hardening and associated embrittlement, radiation-induced segregation (RIS), and void swelling, all of which adversely affect cladding performance [6]. As mentioned earlier, alloying elements in Zr-alloys such as Nb, Sn, Cr, and Fe that have shown to improve the corrosion resistance and/or creep strength, but they may also beneficially affect the irradiation damage resistance under PWR conditions [5].

1.1.3. Accident tolerant fuels

The Fukushima Daiichi nuclear accident in 2011 highlighted the need for increased oxidation resistance and accident tolerance of fuel cladding during severe accident scenarios. In the event of a *design basis accident* (DBA), *beyond design basis accident* (BDBA), or *loss-of-coolant accident* (LOCA), coolant water in the reactor is diminished and the continued decay heat production boils off the remaining coolant in the core, causing the fuel rods to rapidly rise to temperatures in excess of 700 °C [7,8]. At these temperatures, various degradation phenomena including cladding ballooning and burst, high temperature oxidation, and low temperature eutectic melting between contacting materials may occur. As temperatures continue to rise to above 1200 °C, zirconium rapidly oxidizes via an exothermic reaction with steam, producing even more heat and hydrogen byproduct as shown in Eqn. 1.1. The transition of ductile α-Zr to brittle ZrO_2 degrades the mechanical integrity of the cladding, leading to the possibility of fuel fragmentation, dispersal, and fission gas release to the reactor core and the environment.

$$Zr_{(s)} + 2H_2O_{(g)} \rightarrow ZrO_{2(s)} + 2H_{2(g)} \qquad \textit{Eqn. 1.1}$$

The aforementioned limitation of Zr-alloy triggered active research and development programs world-wide for the development of accident tolerant fuels (ATFs) that can provide superior oxidation resistance at temperatures in excess of 1200 °C [7,8]. Two approaches are being considered, namely, a long-term option and a relatively near-term option. The long-term option is to entirely replace the Zr-alloy as fuel cladding material with more oxidation materials such as FeCrAl and SiC-SiC_f (f stands for fiber) [9]. These materials exhibit oxidation rates several orders of magnitude lower than Zr-alloys at elevated temperatures, allowing for improved safety margins during BDBAs as shown in Fig. 1.3 [9]. The low oxidation rates stem from the formation of protective thermodynamically stable Al_2O_3 or SiO_2 layers on the surface of the material in reaction with the environment. Additionally, ATF materials must maintain or improve corrosion kinetics at normal operating conditions (~300 °C, hydrothermal corrosion) with low susceptibility to hydriding, which can lead to brittleness. Of course, the entire replacement of Zr-alloy with a different material will entail significant and expensive changes in reactor design.

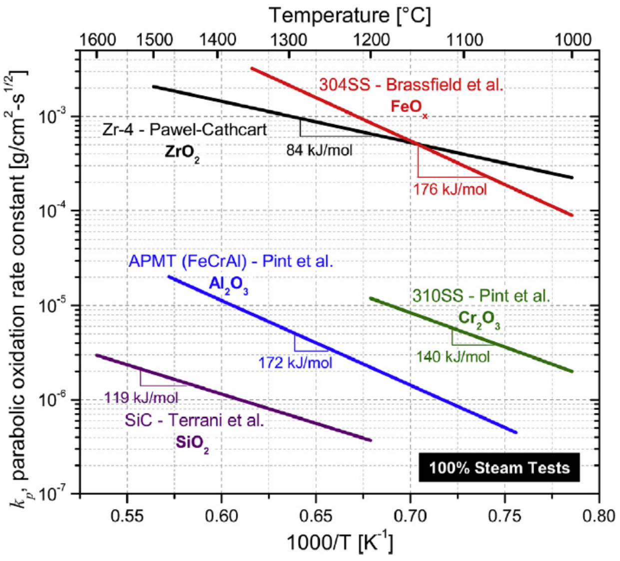

Fig. 1.3. The thermodynamic stability of various oxides in oxidative steam environments, in terms of the parabolic oxidation rate constant. Reproduced from [9].

The near-term option involves deposition of a thin, oxidation-resistant coating on the surface of existing Zr-alloy cladding. Chromia, alumina, and silica-forming materials are the most promising due to their stability in steam and parabolic oxidation kinetics that are roughly two orders of magnitude lower than zirconia [9]. It should be noted that the coated cladding ATF concepts may also provide improved strength to current Zr-alloy cladding, allowing for improved economics by, for example. increasing burnup limits from 62 gigawatt-days per metric ton of uranium (GWd/MTU) to 75-80 GWd/MTU [10]. This would allow for improved fuel cycle efficiency via longer reactor cycles. Many coating materials have been investigated, such as MAX-phase coatings [11–13], nitride coatings [14–17], alloy coatings [18–23], and pure metal coatings [24–27]. In particular, FeCrAl coatings have the potential to provide dual protection at operating conditions through formation of a Cr-rich surface oxide layer during normal operation hydrothermal corrosion conditions, and through formation of protective Al_2O_3 at the surface under accident conditions [28]. An important limitation of using FeCrAl as a coating material on Zr-alloy is the formation of a low temperature eutectic phase at 928 °C due to diffusion of Fe into the underlying Zr cladding, resulting in melting [29,30]. A dual-layer FeCrAl/Mo (Mo as a diffusion barrier interlayer) coating was successful in preventing interdiffusion between Fe and Zr up to 1200 °C as shown in studies performed by the present author [31].

More recently, pure Cr has emerged as the coating material of choice due to its high melting point (1907 °C), relatively low thermal neutron absorption cross-section (~3.0 barn), high eutectic temperature with Zr (~1332 °C), and superior resistance to oxidation in PWR operating conditions [32,33]. Several methods for deposition of Cr have been investigated including cold spray [34–37], plasma spray [38,39], physical vapor deposition (PVD) [40–42], and vacuum arc plating [43–45]. The next section provides an overview of the advantages and limitations of using Cr-coated Zr-alloy as an ATF cladding material. Some of the work cited in these sections refer to cold spray coatings – the focus of this thesis work – and therefore will be covered separately in greater detail in subsequent sections of this chapter of the thesis.

1.2. Chromium coatings for accident tolerant fuel

1.2.1. Corrosion and high temperature oxidation of Cr coatings

The hydrothermal corrosion behavior of Cr coatings on Zr-alloy cladding has been studied extensively [26]. Corrosion tests are typically performed in pressurized water at 360 °C and 18.6 MPa, which corresponds to the typical normal operating environment in PWRs. The Pourbaix diagram for Cr is shown in Fig. 1.4, and it reveals a large window of electrode potential and pH combinations in which a protective Cr_2O_3 is expected to form [46]. The results of corrosion testing of Cr-coated Zr-alloy cladding (summarized by Yang et al. [26]) reveal that the weight gain of the coated samples was considerably lower than that of the uncoated Zr-alloy.

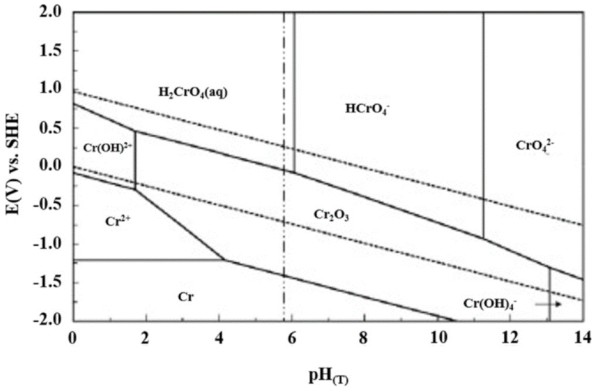

Fig. 1.4. Pourbaix diagram for Cr at 350 °C, 25 MPa, and an oxygen concentration of 10^{-6} mol/kg, showing the favorable Cr species as a function of electrode potential and pH. Reproduced from [46].

High temperature oxidation testing of Cr-coated Zr-alloy is not as standardized as hydrothermal corrosion testing. Testing is typically performed between 1000 to 1300 °C for exposure times ranging from 5-300 minutes in either flowing steam or ambient air environments [26]. The oxidation behavior of chromium in high temperature steam environments is different than in pure oxygen or ambient air environments; for example, formation of volatile chromium oxides (CrO_3) and chromium oxy-hydroxides ($CrO_2(OH)_2$) are possible in wet oxygen or steam environments [47,48]. However, the formation of stable chromia (Cr_2O_3) at LOCA temperatures makes Cr very effective in imparting high temperature oxidation resistance. The high temperature oxidation kinetics of Cr in the temperature range of 900 to 1400 °C have been studied extensively and are usually found to obey a parabolic growth kinetics [26]. In general, Cr coatings provides several orders of magnitude higher resistance to high temperature oxidation compared to Zr-alloys. The oxidation performance can be improved by maximizing the density, thickness, and mechanical integrity of the coatings.

1.2.2. Mechanical properties and testing of Cr coatings

In recent years, there have been efforts to study mechanical behavior of Cr coated Zr-alloy [49]. In reactor environment, for example, cladding tubes are subjected to biaxial mechanical loading (axial and circumferential) due to *pellet-cladding mechanical interaction* (PCMI) [50]. Under LOCA conditions, the cladding may experience pressure from the coolant water outside the cladding, as well as pressure from the inside of the cladding due to fuel pellet swelling and fission gas release, especially during a reactivity initiated accident (RIA) condition [51]. The coating deposition process used will influence the stress state of the Cr coating and may determine how the coating will resist these pressures under both normal and accident conditions.

Chromium has historically been used as an alloying element and, as a result, the deformation behavior of pure Cr has not been investigated extensively. BCC metals present a challenge for modeling deformation due to their sensitivity to strain rate and temperature. Previous mechanical behavior studies of Cr on Zr-alloy have included ring and C-ring compression testing, expanding plug testing, and uniaxial and biaxial tensile testing [52–58]. The deformation and fracture behavior of PVD and cold spray Cr coated Zr-alloy has been investigated using both *in situ* and *ex situ* SEM characterization, digital image correlation, acoustic emission detection, X-ray micro-computed tomography imaging, and finite element analysis [52–58]. Results from these tests have generated many similar conclusions: (i) Cr coatings undergo brittle failure at room temperature, but experience a *brittle-to-ductile transition temperature* (BDTT) between 25 °C and 500 °C; (ii) cracks typically propagate linearly and perpendicular to the loading direction, though cracks become more circuitous as the testing temperature increases; (iii) crack number density decreases as coating thickness increases; (iv) cracks propagate through the coating and are arrested at the interface, with no delamination of the coatings observed, indicating high adhesion of Cr to Zr-alloy; and (v) cracking typically initiates and then saturates between 0.1-3% strain.

Due to the relatively low thickness of these coatings (<30 μm) as required for ATF cladding, standard mechanical testing methods may not provide the most useful data. Instead, the use of small-scale mechanical testing provides the means of obtaining qualitative and semi-quantitative assessments of Cr-coated Zr-alloy cladding integrity. For example, multi-length scale mechanical tests (e.g., nano-indentation, micro-pillar compression, and cantilever beam bending tests) were previously performed on single-crystal and ultrafine grained Cr to gain insights on the influence of microstructure, temperature, and strain rate on the plasticity and strengthening behavior of BCC metals [59–62], and this technique has now been extended to Cr coatings on Zr-alloy cladding . In recent years, micro-tensile testing with *in situ* synchrotron diffraction has been used to characterize the evolution of lattice strain, dislocation density and character distribution, and load partitioning phenomena in a wide variety of materials during uniaxial tensile tests [63–66], and this approach has been investigated in this research. These techniques are promising developments and may be extended to assess hydrogen embrittlement, delamination and cracking mechanisms following irradiation, and high strain cladding ballooning and burst behavior during accident scenarios [49,67].

1.2.3. Irradiation damage of Cr coatings

Neutron irradiation of Cr coatings is restricted to test reactors, and therefore is a time-consuming process taking years to implement, perform, and analyze [49]. Ion irradiation has demonstrated success in reproducing microstructural and property effects from neutron irradiation with orders of magnitude reduction in time and cost [68]. While ion irradiation data of bulk chromium, Cr coatings, and Cr alloys at various temperatures and conditions are quite sparse compared to more common reactor structural materials, a summary of the literature is presented herewith.

BCC metals tend to show good resistance to radiation, consistently showing lower void swelling than FCC metals [2,69–71]. Kuprin et al. irradiated cathodic arc evaporated Cr coatings on Zr-alloy cladding using 1.4 MeV argon ions at 400 °C from 5 dpa to 25 dpa [72], and between 300-550 °C to 25 dpa [73], where they measured swelling ranging between 0.16 % to 1.6 %. Using 5 MeV Fe ions, Ryabikovskaya et al. [74] found that pure Cr swelled at a rate of ~0.03-0.04%/dpa, with void swelling reaching ~2% after 50 peak dpa irradiation. Heavy ion irradiation experiments produced a maximum of 9% swelling at a dose of 180 dpa around 750 °C [75]. With a maximum damage dose accumulation of 25 dpa after 5 years in reactor, it is reasonable to assume that Cr coatings on Zr-alloy cladding will not exhibit significant void swelling that would cause detriment to adhesion or mechanical properties [72].

The microstructure of cold sprayed Cr coatings consists of a heterogeneous microstructure containing grain boundaries, inter-particle boundaries, ultrafine grains (<1 μm) and high dislocation density, which act as sinks for irradiation-induced defects [76,77]. Maier et al. [36] showed that the plastically deformed cold spray Cr microstructure delayed both the onset and growth of irradiation-induced defects compared to an annealed bulk Cr microstructure. The relative stability of dislocations and dislocation loops in Cr under irradiation [75,78,79], as well as its inherently low vacancy accumulation [80], makes it innately resistant to irradiation damage. In addition, radiation-induced recrystallization has been shown to occur in heavily cold worked microstructures, which may impart some ductility to the cold spray Cr coating [81].

BCC metals are susceptible to irradiation hardening and embrittlement at low temperatures (<0.3-0.4 T_M) due to formation of a high density of defect clusters [69]. The hardness of vacuum and magnetron sputtered Cr films has been shown to increase during irradiations [82,83], and the DBTT can increase with irradiation, promoting embrittlement [84]. However, Chen et al. [85] observed irradiation softening of arc-ion plated Cr coatings on Zr-alloy at low (< 1) dpa, which they attributed to recombination of coating defect sinks and irradiation defects, and to irradiation-induced deformation recovery. Gong et al. [86] irradiated arc-ion Cr coatings up to 20 dpa and correlated hardening to the crystallinity of the coating. Hardening was found in coatings with large voids and low (110)-oriented crystallinity while softening occurred with many small voids in increasing (110)-crystallinity coatings [86]. The variation in results among various studies shows that the process used to deposit the coatings influences the texture, grain size, and inherent defects within the coatings, all of which contribute to their irradiation damage response [85].

Finally, irradiation may change the nature of the Cr/Zr interface. HR-TEM characterization of a PVD Cr coating on Zr-alloy showed crystallinity across the near-interface regions of Cr/Zr interface, containing a mixture of $Zr(Fe,Cr)_2$ Laves phases [87,88]. After Kr^{8+} irradiation at 400 °C up to 10 dpa, crystallinity and atomic row matching were maintained, though some differences in phases at the interface were observed. Fazi et al. [89] observed a crystalline, intermixed boundary region near the unirradiated cold spray Cr/Zr interface, with increased concentrations of Cr, Fe, and Nb within the Zr-side of the interface.

Cold spray results in high velocity impact, shear, and mixing of constitutive elements at the interface, and irradiation may enhance diffusion that could accelerate the nucleation and growth of Laves phases or other nonequilibrium phases in this mixed region [37,89]. For example, Kennas et al. [20] irradiated thermally annealed cold spray FeCrAl on Zry-4 using Zr^{2+} ions at 400 °C from 50-150 dpa. Thermal annealing promoted $(Fe,Cr)_2Zr$ phase formation at the interface, and irradiation resulted in complete amorphization of this phase.

1.3. Cold spray coating deposition process

1.3.1. Overview of gas flow, temperature, and pressure

Historically, it was commonly accepted that particles must be heated to high temperatures to ensure melting in the gas flow to deposit a coating [90]. In these *thermal spray* processes, feedstock materials in the form of powder, wire, or rods are melted into molten droplets using electrical or chemical energy and heated anywhere from 1000-15,000 °C [91]. The droplets are propelled onto a substrate surface via subsonic or supersonic gas streams at high velocities, where upon impact they spread out and solidify at extremely high cooling rates ranging from 10^4-10^8 K/s [91]. An enormous selection of feedstock materials in various forms can be deposited on a variety of substrates using thermal spray due to its expanded range of particle temperatures and velocities.

Cold spray is similar in that micron-sized feedstock powder particles are accelerated to supersonic velocities with a preheated, pressurized gas towards a substrate to form a coating. Unlike thermal spray, the *particle temperature is low, and deposition occurs in solid state*. The primary reason for heating the gas is not to melt (or even heat) the material but rather to increase the sonic velocity of the gas in the throat of the converging-diverging (or *de Laval*) nozzle, which is similar to the design of a rocket nozzle [91,92]. A schematic cross-section of a de Laval nozzle is shown in Fig. 1.5. A compressed gas (typically air, nitrogen, helium, or a mixture thereof) is pressurized up to 60 bar (6.0 MPa) and preheated up to temperatures in the range of 100 to 900 °C [91–93]. Because expansion of the gas in the diverging section of the nozzle rapidly cools the gas, it exits the spray gun nozzle at a much lower temperature. Additionally, since the dwell time of the particles in contact with the gas is brief, the particles remain well below the initial gas preheat temperature and arrive at the substrate in their original solid form [93]. Hence, the name "cold spray" gets its name from the solid-state nature of the deposition process relative to the low temperature of the particles during coating formation.

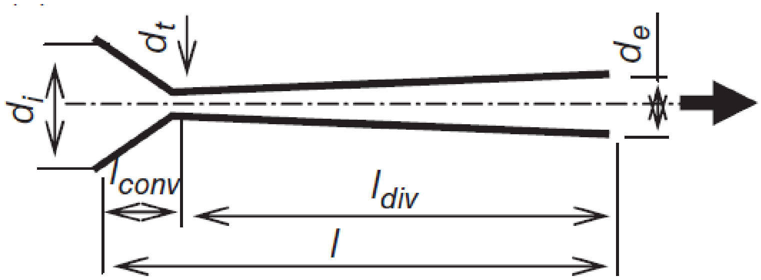

Fig. 1.5. Schematic cross-section of a converging-diverging de Laval nozzle, repurposed from Sakaki [92].

The gas flow through the nozzle can be modeled using a quasi-one-dimensional isentropic flow [92]. The pressure P, temperature T_g, and velocity U_g of the gas flow through the nozzle can be calculated from the ratio of the cross-sectional area A at any given point up to the nozzle throat area A_t using the following equations [92,93]:

$$\frac{P_t}{P_i} = \left(\frac{2}{\kappa + 1}\right)^{\frac{\kappa}{\kappa+1}} \qquad \textit{Eqn. 1.2}$$

$$\frac{A}{A_t} = \sqrt{\frac{\left(\frac{\kappa - 1}{2}\right)\left(\frac{2}{\kappa + 1}\right)^{(\kappa+1)(\kappa-1)}}{\left[\left(\frac{P}{P_i}\right)^{\frac{2}{\kappa}} - \left(\frac{P}{P_i}\right)^{\frac{\kappa+1}{\kappa}}\right]}} \qquad \textit{Eqn. 1.3}$$

$$T_g = T_{gi}\left(\frac{P}{P_i}\right)^{\frac{\kappa-1}{\kappa}} \qquad \textit{Eqn. 1.4}$$

$$U_g = \sqrt{2\frac{\kappa}{\kappa - 1}RT_i\left[1 - \left(\frac{P}{P_i}\right)^{\frac{\kappa-1}{\kappa}}\right] + U_{gi}^2} \qquad \textit{Eqn. 1.5}$$

where κ is the gas specific heat ratio (1.4 for N_2, 1.66 for He), R is the gas constant (8.314 J/mol·K), and the subscripts g, i, t represent the gas, inlet, and throat of the nozzle, respectively. Preheating the gas increases the sonic velocity of the gas at the throat up to Mach 1, after which the gas thermal energy is converted to kinetic energy (i.e., velocity) by way of energy conservation. The gas must increase its velocity to maintain the same mass flow rate as it expands through the diverging section of the nozzle, where it reaches velocities up to Mach 2-3 at the nozzle exit [94]. Furthermore, since the particles flow with the gas, higher gas velocities generally result in higher particle velocities. Eqn. 1.5 can be further simplified in terms of the molecular weight (M_w) of the gas species:

$$v = (\gamma RT/M_w)^{\frac{1}{2}} \qquad \textit{Eqn. 1.6}$$

Eqn. 1.6 shows that a useful way to increase the carrier gas velocity (and therefore, particle velocity) is to increase the preheat temperature of gas or to reduce its molecular weight, i.e., including helium in the gas stream. Increasing the inlet gas pressure does not result in an increase in gas velocity since the flow through the nozzle becomes sonic and is “choked” at the throat (at typical processing conditions). Cold spray systems typically come in two configurations: (i) low pressure cold spray (LPCS), in which powder is injected into the diverging section of the nozzle at low pressures; (ii) high pressure cold spray (HPCS), in which powder is injected upstream of the converging section of the nozzle [95,96].

1.3.2. Critical velocity for particle bonding in cold spray

Initial cold spray experiments involved spraying particles towards a substrate at different particle velocities. The deposition efficiency, k_d, of the powder that bonded to the substrate was measured via Eqn. 1.7:

$$k_d = \Delta m_s/M_p \qquad \textit{Eqn. 1.7}$$

where Δm_s is the change in weight of the substrate and M_p is the weight of all particles that interacted with the substrate [90,97]. These measurements helped discover that a critical velocity, v_{cr}, was needed for particles to bond to the substrate. At low particles velocities ($v_p < v_{cr}$), k_d~0 meaning particles rebounded upon impact with the substrate. At $v_p \geq v_{cr}$, k_d>1 and the deposition process begins. If the particle velocity becomes too high ($v_p \gg 2v_{cr}$), erosion of the substrate can be a concern. Thus, the particle velocity is generally seen as the most important process parameter for controlling bonding.

Researchers have found that the critical velocity is material dependent and relies on factors such particle density, temperature, specific heat capacity, size, and dynamic yield strength [96,98–100]. Schmidt et al. [98] were among the first to estimate the critical velocity for Cu using materials parameters:

$$v_{crit}^{Cu-Cu} = \sqrt{\frac{C_1 \sigma_{TS}}{\rho_p}\left(1 - \frac{T_{pi} - T_r}{T_m - T_r}\right) + C_2 c_p (T_m - T_i)} \qquad \textit{Eqn. 1.8}$$

where σ_{TS} is the tensile strength of the particle, ρ_p is the density of the particle, c_p is the specific heat of the particle, T_{pi} is the temperature of the particle upon impact, T_m is the melting temperature, and T_r is a reference temperature (usually set to 298 K). C_1 and C_2 are calibration factors set to 0.25 and 1.0, respectively. The ratio of v_p/v_{cr} was found to correlate well with deposition efficiency, particle flattening ratio, and coating cohesive strength [98]. Though, it is important to note that Eqn. 1.8 is only valid for similar materials systems, specifically Cu impacts on a Cu substrate, a widely investigated materials system for cold spray. Generating empirical equations for critical velocity is possible through the use of single-particle impact experiments, in which cold spray parameters are tuned to only allow deposition of individual particles on a substrate surface [101–107]. Particle velocities are estimated numerically through the use of computational fluid dynamics (CFD) simulations, or can be measured experimentally using high speed cameras with infrared or laser light sources [108].

In recent years, researchers have begun to expand critical velocity measurements to dissimilar materials systems using the laser-induced projectile impact test, or LIPIT [104,109,110]. In this test, a particle is accelerated by rapidly expanded gases from laser ablation of a thin film of gold or a polymer material. Ultrafast monochromatic laser pulses are used to image the particle at all stages before and after collision with the substrate, enabling precise quantification of particle velocity and coefficient of restitution, which is the ratio of the particle's rebound velocity to its impact velocity. When the coefficient reaches zero, the particle is considered bonded and thus represents its critical velocity. Hassani et al. [101] investigated a number of similar and dissimilar metallic systems using the LIPIT system to identify the critical velocities of many unique particle/substrate combinations. With advances in technology, future single-particle impact studies will be able to incorporate other conditions, such as particle size, temperature, density, oxide thickness, and impact angle, all of which affect the mechanisms for particle-substrate bonding.

1.3.3. Bonding mechanisms in cold spray

Bonding in cold spray consists of two distinct stages: (i) particle-to-substrate bonding, which forms the first layer of particles and is responsible for coating adhesion, and (ii) particle-to-particle (a.k.a., interparticle) bonding, which is responsible for coating build-up and coating cohesion. Solid-state metallic bonding takes place when the clean surfaces of two metals are brought into intimate contact [100,111]. In practice, however, the surfaces of most metallic materials are covered by a thin native oxide layer or contamination film. One way to achieve metal-to-metal contact is to compress and stretch the interfacial region via plastic deformation, causing fracture of the oxide layer leading to intimate contact of the metal surfaces at the atomic level, thereby initiating *metallurgical* bonding. This phenomenon is shown schematically in Fig. 1.6. This relationship between bond strength and surface exposure is seen in all solid-state bonding processes, including cold welding, explosive welding, and cold spray.

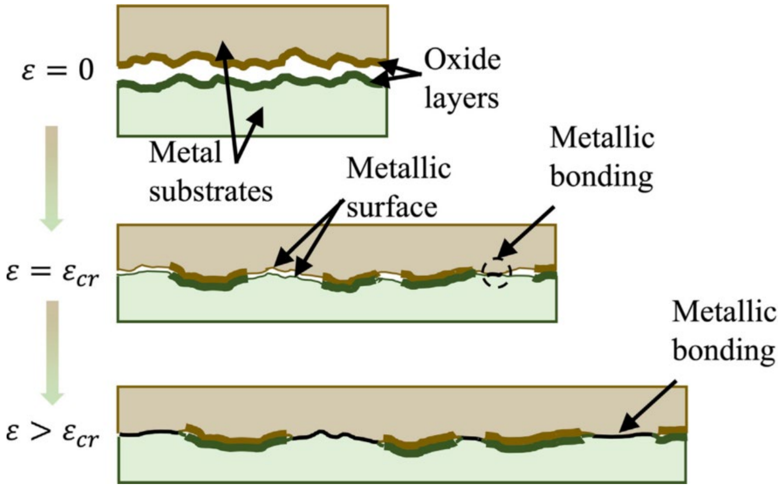

Fig. 1.6. Schematic of solid-state bonding resulting from plastic deformation. At some threshold strain $\varepsilon=\varepsilon_{cr}$, *exposed fresh metallic surfaces come into contact resulting in bonding. Reproduced from Hassani et al. [111].*

During cold spray deposition, high velocity particle impact leads to plastic deformation at extremely high strain rates (10^6-10^9 s^{-1}). Upon impact at $v_p \geq v_{cr}$, a jet composed of both particle and substrate material is formed at the particle/substrate contact surface. This causes an intense outward flow of material that effectively breaks up the native oxide present on the metallic surfaces [111,112]. When the jet reaches the free surface, it forms a lip that fractures material ahead of the jet front, effectively ejecting material away from the bonding interfaces. Thus, this jetting phenomenon has been presumed to be a necessary criterion for providing the clean metallic surfaces and hydrostatic pressures required for metallurgical bonding in cold spray [113]. The extremely short contact times (~40 ns), relatively low impact kinetic energy of deposited particles, and inter-diffusion coefficients near the melting temperature (10^{-15}-10^{-13} m^2/s) tend to exclude interfacial melting and long-scale atomic inter-diffusion as bonding mechanisms in cold spray [112].

For many years, *adiabatic shear instabilities* (ASI) produced at the particle/substrate interface has been considered the primary cause of jetting. To explain on a physical level, Fig. 1.7 shows a standard stress-strain curve for a typical work-hardening material under isothermal conditions, in which the flow stress increases monotonically with plastic strain [112]. Under adiabatic conditions, however, plastic strain energy dissipates as heat increases the temperature, causing thermal softening. This causes the flow stress to reach a maximum, whereafter it continues to decrease with increasing plastic strain. In real materials, fluctuations in stress, strain, temperature, and microstructure give rise to shear localization, [112]. This stops the straining and heating in the surrounding material, causing the flow stress to rapidly drop to zero. To summarize, adiabatic shear instabilities lead to concentration of plastic deformation at the particle-substrate interface, forming a narrow jet composed of highly deformed material. The high contact pressure and localized plastic deformation causes a spike in temperature contained within this region on a very short time scale, which may further aid in metallurgical bonding.

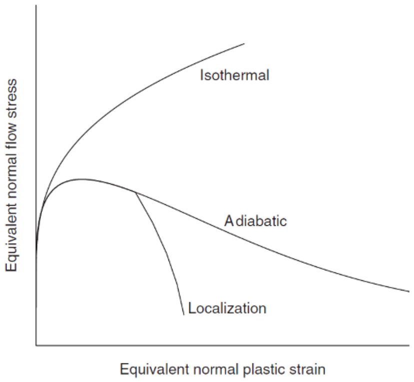

Fig. 1.7. Schematic stress-strain curves in a normal strain-hardening material ('isothermal'), an adiabatically softened material ('adiabatic'), and a material undergoing adiabatic shear localization ('localization'). Reproduced from Grujicic et al. [112].

These interfacial instabilities can also produce the second type of bonding in cold spray, which is *mechanical interlocking*. This may occur in the form of interfacial rollups, in which flow caused by differing viscosities increases the interfacial area, leading to material mixing [112,114,115]. Mechanical interlocking is often seen in dissimilar metal systems with large differences in materials properties, such as a hard particle on a soft substrate. In these cases, adiabatic shear instability is suppressed on the particle side, causing jetting of the substrate around the particle thus producing strong mechanical bonds [100].

A recent theory developed by Hassani-Gangaraj et al. [116,117] proposes that ASI is not necessary for adhesion in cold spray or, more specifically, that adiabatic softening is not needed to see the onset of jetting. Instead, they propose that jetting forms due to strong pressure waves interacting with the expanding edge of the particle, and material within the jet lip fragments under a spallation-like process. The argument is based on a series of finite element simulations in which thermal softening was intentionally excluded from the material model. The results showed that jetting was observed in Cu particles with and without the thermal softening term [116,117]. Regardless of the mechanism, most researchers agree that jetting is a necessary condition for bonding to ensure breakup of native oxide to produce intimate metallic contact of fresh interfaces [118,119].

1.3.4. Microstructural evolution in cold spray coatings

As particles impact sequentially to buildup thickness, compaction of the particles leads to viscoplastic deformation and metallurgical bonding over a large fraction of interparticle interfaces [100]. Kinetic energy and momentum from the incoming high velocity particles on impact with previously deposited particles form the basis for coating buildup [120]. Van Steenkiste et al. [120,121] proposed that coating buildup occurs in four stages, as shown schematically in Fig. 1.8: (i) substrate cratering and first layer buildup of particles; (ii) particle deformation and realignment; (iii) metallic bond formation between particles (interparticle bonding) and void reduction; and (iv) further densification and work-hardening of the coating. Incomplete bonding due to low particle velocity and/or kinetic energy may lead to deposits with high porosity and low cohesive strength.

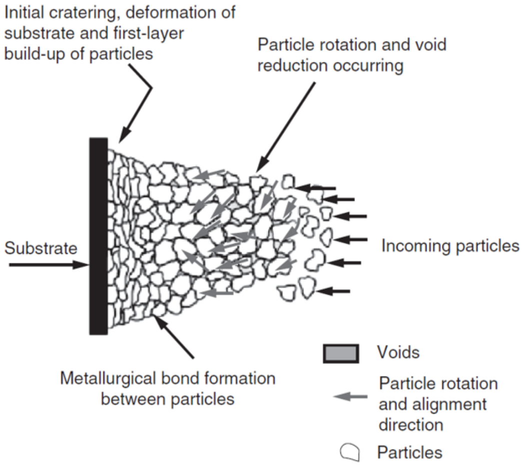

Fig. 1.8. Multi-stage coating formation in cold spray process, as proposed by Van Steenkiste et al. [121].

Microstructure of cold spray coatings evolves heterogeneously. Plastic deformation is typically restricted to the outer surfaces of the particles, allowing the center of the particle to retain its initial feedstock microstructure. Upon impact, pre-existing dislocations in the particle, as well as nucleation of dislocations due to high strain, results in dislocation entanglement. These dislocations then reorganize to form subgrains with *low-angle grain boundaries* (LAGBs) that can further elongate with deformation, in a process referred to as *continuous dynamic recrystallization* (cDRX) [122–125]. If the plastic strain and temperature are high enough, the subgrains may rotate and pinch off to form ultrafine equiaxed grains with *high-angle grain boundaries* (HAGBs) in a process known as *geometrical dynamic recrystallization* (gDRX) [115,122–124]. These ultrafine grains are typically only found in regions with the highest deformation due to the extremely high strain rates and the associated temperatures rises that are required.

Tiamiyu et al. [122] found gDRX grains in single Cu particles using the highest velocity conditions. Liu et al. [115] also found ultrafine grains on the order of 1-30 nm near cold sprayed Al particle boundaries. Additionally, they identified that these grains were aligned in small 100 nm perturbations, or "roll-ups", forming a zipper-like structure leading to nanoscale metallurgical interlocking, which they attributed to interfacial instability and velocity-induced centrifugal forces. Similarly, Zhou et al. [126] found that a large density of these ultrafine, recrystallized grains in cold sprayed Ti-6Al-4V could create "bridging connections," which strengthen adhesion through nanoscale metallurgical interlocking. This phenomenon was also shown using molecular dynamics simulations of Cu-on-Cu, in which metallurgically interlocking grains covered up to 76% of the interface [114]. Hence, it is clear that dynamic recrystallization along particle boundaries plays a major role in bonding.

1.3.5. Prior work on cold spray Cr coated Zr-alloy cladding development

At the University of Wisconsin-Madison, development of cold spray Cr coatings on Zr-alloy cladding has been ongoing for a number of years. Deposition of cold spray Cr coatings was investigated using a variety of Cr powders with unique microstructures [127,128]. These coatings were subjected to flowing steam tests in a temperature range of 1100-1300 °C to investigate growth kinetics and microstructure of surface oxide, and intermetallic compound formation at the coating-substrate interface [129]. Cr coatings were deposited on a cold sprayed Nb barrier interlayer to enhance the high temperature oxidation performance at temperatures above the Cr-Zr eutectic temperature [130]. Finally, the irradiation response of cold sprayed Cr coatings was investigated and showed acceptable resistance to irradiation damage, suggesting that the deformation-induced defects produced by the cold spray process may be beneficial for irradiation resistance [131].

Cold spray results in thick, dense, and adherent coatings to the substrate without any oxidation, phase changes, or degradation of the powder feedstock or substrate materials during deposition. Particles can be deposited directly onto the substrate without need of prior grinding or grit blasting steps. Coating deposition occurs with minimal thermal input to the substrate, which preserves its overall microstructure and properties. Cold spray coatings exhibit very high bond strength, high hardness, and have compressive surface residual stresses, which may provide improved mechanical behavior of the substrate during reactor operation. Finally, the high density and phase purity of the coatings combine to yield exceptional corrosion and oxidation properties. To summarize, the results show exceptional promise for cold spray coatings in nuclear energy systems [27].

1.4. Fabrication process for chromium powders

The main process for production of large quantities of chromium powders is the *electrolyte method*. In such method, the chrome alum sulfate method, trivalent chromium (Cr-III) is produced by leaching chromium metal from high-carbon ferrochrome in a bath of sulfuric acid (referred to as the *trivalent process*) [132]. Then, the chromium solution undergoes electrolysis for a period of ~72 h to transform Cr^{+3} into Cr^0. This produces brittle chromium metal at the cathode that is removed in large flakes about 20 mesh (850 µm) in size. In the another electrolytic process, the chromic acid method, hexavalent chromium (Cr-VI) is produced from chromium trioxide (CrO_3) obtained from sodium dichromate (referred to as the *hexavalent process*) [132]. The process is much more difficult to control than the first method, resulting in low yields of about 10%. However, the hexavalent process can produce a much higher purity chromium metal (<99.9%) on a consistent basis.

The chromium flakes are then blended with carbon, tin, and a polymeric binder and formed into small briquettes, where they are placed into a resistance-heated vacuum oven [132]. The oven is heated at a slow ramp rate up to 1400 °C and held at constant pressure to allow for degassing. The briquettes are then slowly cooled under flowing argon gas followed by a final hydrogen degassing step. During the high temperature anneal, the chromium metal is purified of nitrogen, lead, sulfur, and oxygen and the mechanical properties of the Cr flake are improved. Additional degassing steps can be performed to remove iron impurities leftover from the original chromite ore. Other processes to produce chromium powder include electroslag remelting and aluminum reduction (i.e., aluminothermic Cr) [132].

High purity electrolytic Cr flakes are still too large for traditional coating deposition. Therefore, powder manufacturers crush the flake into smaller sizes using either ball milling or impact milling techniques [133]. Ball milling utilizes a rotating cylinder containing large balls made of metal or ceramic that grind powder to a specified particle size distribution. Particle size is reduced through friction and impact with the tumbling balls. Impact mills are a class of attrition mills that pulverizes powder upon contact between two surfaces, where particle size is reduced through friction and shear. Specialized materials can be used in the mills to minimize trace element contamination, and the process can be carried out in an inert atmosphere to reduce oxygen contamination. After the milling process, particles are blended into a homogenous size distribution. This process produces non-spherical particles due to the fracture of particles along pre-existing defects.

Chromium flake can also be turned into spherical powders through gas atomization and plasma spheroidization techniques. Gas atomization involves melting a material in a crucible, where the liquid flows down a refractory metal nozzle and becomes atomized into fine molten droplets using a pressurized inert gas [134]. The molten droplets solidify into spherical particles while falling through an inert gas chamber. Plasma spheroidization involves injecting solid particles into a high-temperature plasma (3000-

10,000 K) to be melted under an inert atmosphere [135,136]. The surface tension reshapes the particles into spheres while the particles fall through the chamber under gravity and solidify at high cooling rates (~10^6 K/s). In both processes, several parameters including tube size, gas flow rates, and cooling rates can be tuned to control the particle size distribution. Additionally, careful control of the atomization (and spheroidization) environments would be beneficial for minimizing oxidation of the feedstock particles.

Spherical gas atomized Cr powders were initially used to deposit Cr coatings on Zr-alloy cladding [34]. The process produced relatively ductile Cr particles with low hardness and low defect density, allowing for buildup of thick coatings. The issue with gas atomization is that Cr vapors can cause volatilization of hexavalent Cr, which is a known carcinogen, and the high melting temperatures makes the process expensive. Plasma techniques may be a more economical approach for further spheroidizing of Cr powder. Another issue observed by Maier, Yeom, and Dabney et al. [34,137] was that large concentrations of helium in the carrier gas must be used to fully seal interparticle boundaries, which also makes cold spray process expensive. Hence, mechanically milled powders appear to be the more economical option so long as the milling process is carefully controlled to avoid excess work-hardening of the particles. Cold spray of electrolytic hard Cr powders led to deposition of a single layer of Cr particles [34], however annealing of the electrolytic hard Cr powder led to appreciable improvement in microstructure and ductility, allowing for thicker deposits [137]. The electrolytic soft Cr powder used in this research was carefully fabricated in specially designed ball mills to limit work-hardening and maintain ductility for cold spray deposition.

1.5. Plastic deformation in metals

Since plastic deformation is an essential feature in cold spray and governs deposition characteristics and microstructure, this chapter concludes with a brief overview of plastic deformation. *Plastic deformation* introduces permanent strain that occurs when a material is subjected to tensile, compressive, bending, or torsion stresses that exceed its yield strength [138]. *Flow stress* is a term used to describe the stress necessary to continue deformation during any stage of plastic straining. The primary carriers of plastic deformation in metals are *dislocations*, which are accumulations of point defects known as *line defects* in crystals. Dislocations are often simply represented by an extra plane of atoms in the lattice. Two distinct types of dislocations in crystalline solids are *edge* and *screw* dislocations, which are distinguished by the direction of their *Burgers vectors*, which represents the distortion of the periodic atomic arrangement of the defects. Edge dislocations have Burgers vector perpendicular to the dislocation line, and screw dislocations have Burgers vector parallel to the dislocation line. While the direction of dislocation motion is always parallel to the Burgers vector, the relationship between an applied shear stress, the direction of dislocation movement, and plastic strain generated is different for the two types of dislocations [138].

Plastic deformation occurs by slip or sliding of planes of atoms over one another by movement of dislocations along *slip planes* in *slip directions* that are unique to a material's crystal structure [139]. Slip in FCC materials occurs on {111} (close packed) planes along <110> directions, for a total of 12 independent slip systems. Slip in BCC metals occurs on {110} close packed planes along <111> directions, for a total of 48 independent slip systems. While slip in HCP materials can occur on the basal, pyramidal, and prism planes along prismatic or pyramidal directions, slip typically occurs on the basal plane {0001} for two independent slip systems.

The resistance of materials to plastic deformation is determined by the *shear stress* that is required to make the dislocations glide in their slip planes [139]. Plastic deformation and flow occur when the *resolved shear stress* acting on the plane and in the direction of slip reaches a critical value, known as the *critical resolved shear* stress, and is determined by the *Schmid factor*. The critical resolved shear stress is dependent on the strain rate and temperature of the material. If deformation is caried out at low and moderate temperatures (i.e., below a materials recrystallization temperature), the process is known as *cold working*. As crystalline materials continue to deform plastically, they become more resistant to deformation in a process called *work-hardening* [139]. The homogeneous nucleation of a dislocation occurs by the rupture of atomic bonds of a material along a certain direction. If the dislocation encounters an obstacle (a grain boundary, precipitate, etc.) its motion will be hampered. Subsequent dislocations will *pile up* behind the leading dislocation, increasing the stress. Thus, deformation is related to the number of dislocations that move and the distance traveled by them.

Parabolic work-hardening behavior can generally be represented by Eqn. 1.9, where σ is the stress, σ_0 is the flow stress, ε is the applied strain, K is a constant, and n is the work-hardening coefficient that depends on the nature of the material and typically varies between 0.2-0.5 [139]. Typically, the flow stress increases with strain rate and can be represented by Eqn. 1.10, where $\dot{\varepsilon}$ is the strain rate, m is the strain rate sensitivity, and K is a constant that differs from the one shown in Eqn. 1.9. The flow stress also increases with decreasing temperature. Johnson and Cook developed a comprehensive equation that relates a materials stress to its strain, strain rate, and temperature using Eqn. 1.11, where $K, n, C,$ and m are materials parameters, T_m is the melting temperature, and T_r and $\dot{\varepsilon_0}$ are reference temperatures and strain rates, respectively. BCC metals exhibit a greater temperature and strain rate sensitivity than FCC metals due to differences in mechanisms controlling the rate of dislocation motion.

$$\sigma = \sigma_0 + K\varepsilon^n \qquad \textit{Eqn. 1.9}$$

$$\sigma = K\dot{\varepsilon}^m \qquad \textit{Eqn. 1.10}$$

$$\sigma = (\sigma_0 + K\varepsilon^n)(1 + C\, ln\frac{\dot{\varepsilon}}{\dot{\varepsilon_0}})(1 - \left(\frac{T - T_r}{T_m - T_r}\right)^m) \qquad \textit{Eqn. 1.11}$$

For example, BCC metals are prone to having a *ductile-to-brittle transition temperature* (DBTT) that sharply changes plasticity from ductile deformation to brittle fracture [140]. DBTT can be traced back to nucleation and gliding of screw dislocations that are difficult to operate at low temperatures. A few researchers have traced the origin of DBTT to impurities in BCC metals (such as C, N, or O) that act as pinning sites for dislocation motion [84,141,142]. Other planar defects in a material, including *grain boundaries* and *twin boundaries*, can influence the mechanical properties of a material. The preferential orientation of grains in a material refers to its *texture*, which may also influence the preference of slip during deformation. The *Hall Petch* equation describes a material's yield strength to be inversely proportional to the square root of its grain size. At low temperatures, grain boundaries act as effective obstacles to dislocation motion, causing dislocation pileup and strengthening. At higher temperatures, grain boundaries can become a source of weakness due to grain boundary sliding, leading to plastic flow or opening of voids.

2. Experimental Methods and Methodologies

2.1. Cold spray coating deposition process

Cold spray coatings were deposited using a commercial Cold Gas Technologies (CGT) Kinetiks 4000/34 unit located in the Cold Spray Deposition Laboratory (within the Nuclear and Applied Materials Research Group, NAMRG) at the University of Wisconsin-Madison. The system is controlled by the equipment shown in Fig. 2.1 (a). The Kinetiks system provides control over the process gas parameters (pre-heat temperature, pressure or gas flow rate, and ratio of nitrogen/helium mixture) as well as control over the operational aspects of the powder feeder (feeder disk rotation speed, carrier gas flow rate). Twelve size 300 cylinders are connected to a manifold with a single regulated outlet to provide the pressure and quantities of gases required for the cold spray process. Industrial grade (99.998% purity) propellant gases of nitrogen and helium were procured from the company, AirGas. The gas lines run from the gas cylinders to the inside of a sound-resistant spray booth, where they connect to the gas pre-heater and main cold spray gun.

While most of the equipment is contained within the spray booth, operational control of the Kinetiks system, the robot program, and miniature lathes (when applicable) are positioned outside the booth for safety considerations. The spray booth serves to dampen the noise of the entire spray operation, as well as to contain the expelled gas and powder stream. The expelled gas is captured in a filtered ceiling vent that removes fine particles before the gas is exhausted by the building ventilation. The oxygen levels inside and outside the booth were constantly monitored to maintain a safe working environment before, during, and after a spray run. The sample holders were mounted individually on a downdraft table containing several layers of filters to collect the excess (rebounded or over-sprayed) powder. The entire booth, downdraft table, and powder feed equipment were cleaned with ethanol-dampened wipes to prevent cross-contamination whenever changing the feedstock powder. A specialized explosion-proof vacuum cleaner designed to prevent static discharge was also used to clean up pyrophoric powders.

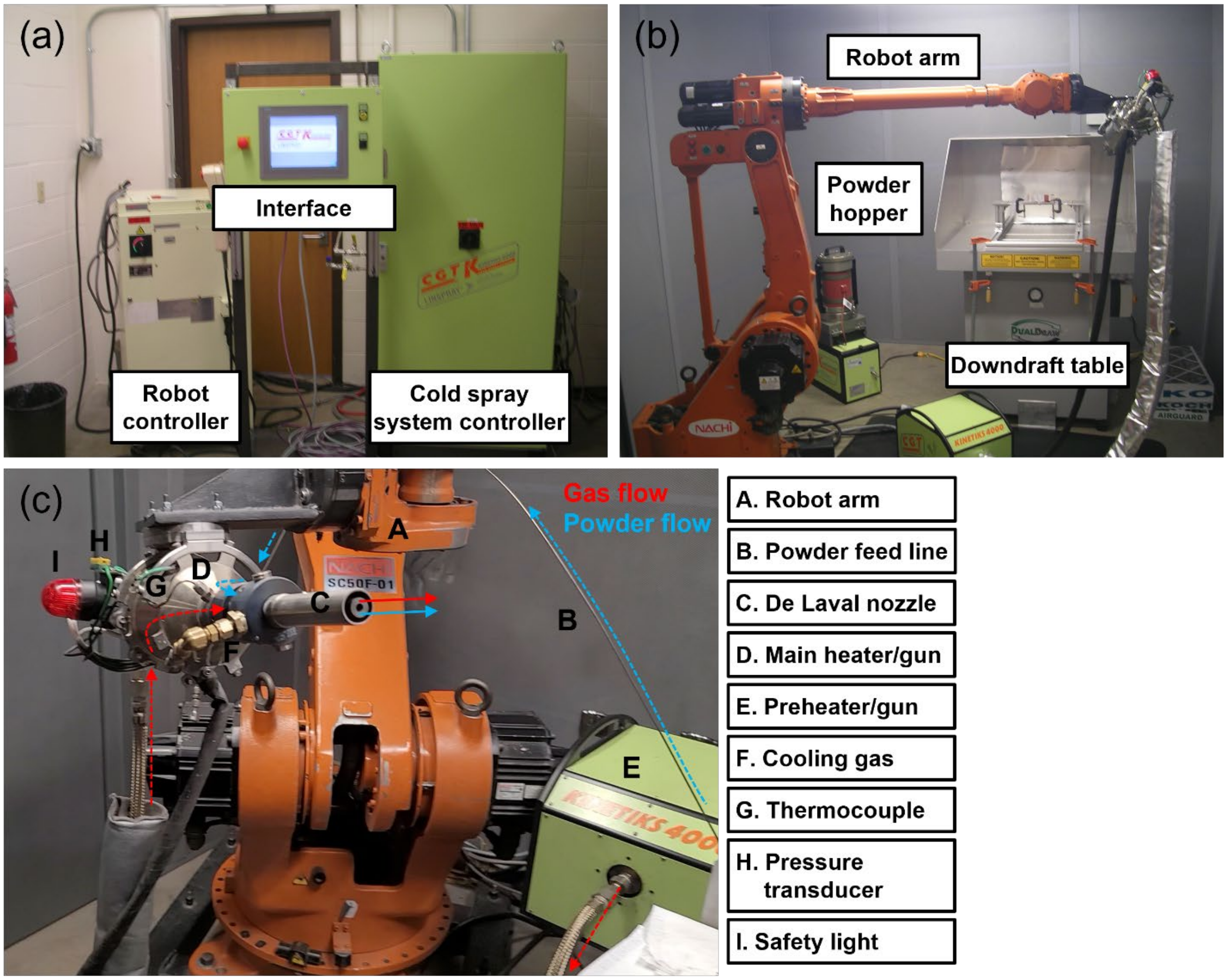

Fig. 2.1. Photographs of the cold spray system located in the Cold Spray Deposition Laboratory at the University of Wisconsin: (a) CGT Kinetiks 4000/34 controller and Nachi SC60F-01 robot controller, located outside of the spray booth; (b) Inside the spray booth, showing 6-axis robot, powder hopper, and downdraft table; (c) Closeup of the important components (labeled) comprising the cold spray system, with the paths of the carrier gas (red) and powder flow (blue) shown with arrows.

Fig. 2.1 (b) provides a look inside the spray booth, showing the cold spray gun mounted to a Nachi SC50F-01 6-axis robot that was pre-programmed with vertical and horizontal nozzle configurations, depending on the sample geometries to be sprayed. Fig. 2.1 (c) provides an overview of the various parts of the cold spray assembly. The converging-diverging nozzle is made of tungsten carbide with a Type-24 design. During a spray run the gas flows through the booth and into a pre-heater, where the pressurized gas can be heated up to 450 °C. The gas then passes through the cold spray gun (main heater) where it can be heated up to 800 °C. Meanwhile, inside the hopper the feedstock powder sits atop a disk containing small holes, rotating at 2 rpm. A small amount of powder is gravity-fed through the holes and into the feedline, where it is carried by nitrogen gas flowing at 4 m^3/h unless otherwise stated. The feedstock powder flows from the hopper through the feedline and into the cold spray gun just before the converging section of the nozzle, classifying this as a high-pressure cold spray process. A schematic of the cold spray process is shown in Fig. 2.2. Both powder and gas flow through the converging-diverging de Laval nozzle, where they accelerate in velocity towards the substrate. Upon impact with the substrate at high velocities the particles plastically deform and deposit to form a continuous coating.

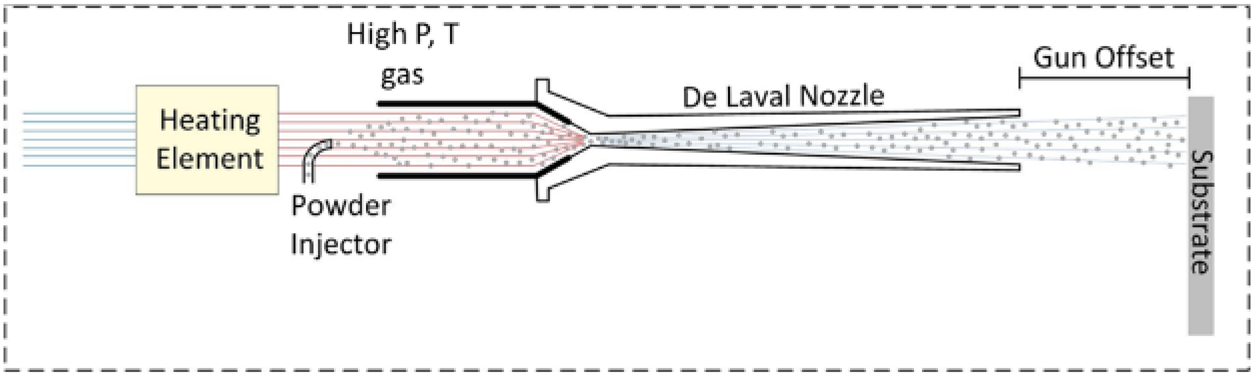

Fig. 2.2. Schematic illustration of the cold spray process, showing powder feed into the cold spray gun. The carrier gas flows through the heating element into the converging section of the nozzle. After reaching the throat, the gas and particles together accelerate in velocity through the diverging section, out of the nozzle and towards the substrate, where upon impact the particles plastically deform to form a coating.

For coating deposition, flat substrates were held vertically on an aluminum bridge using threaded rods and nuts to clamp the substrate between washers, as shown in Fig. 2.3 (a). The nozzle, held perpendicular to the substrate surface, was rastered horizontally across the sample face at a specified speed with the path incrementally raised vertically by a step size of 0.5 mm each pass. Tube geometries were held in a Sherline (Vista, CA) miniature lathe using a 3-jaw chuck and live center to rotate the cladding tube substrates, as shown in Fig. 2.2 (b). The miniature lathe can rotate cylindrical geometries (rods and tubes) from 2 mm to 38 mm (3/32” to 1-1/2”) in diameter. The rotational speed ranged from 70 - 2800 rpm and was varied by electronic speed control. The exact rotational speeds were measured using a handheld optical tachometer aimed at the lathe chuck. The gun, in vertical position normal to the tube surface, was traversed from left to right across the tube. With both configurations, the tip of the nozzle was held at a constant distance of

26 mm (1”) from the substrate surface unless otherwise noted. This distance is often referred to as the standoff distance.

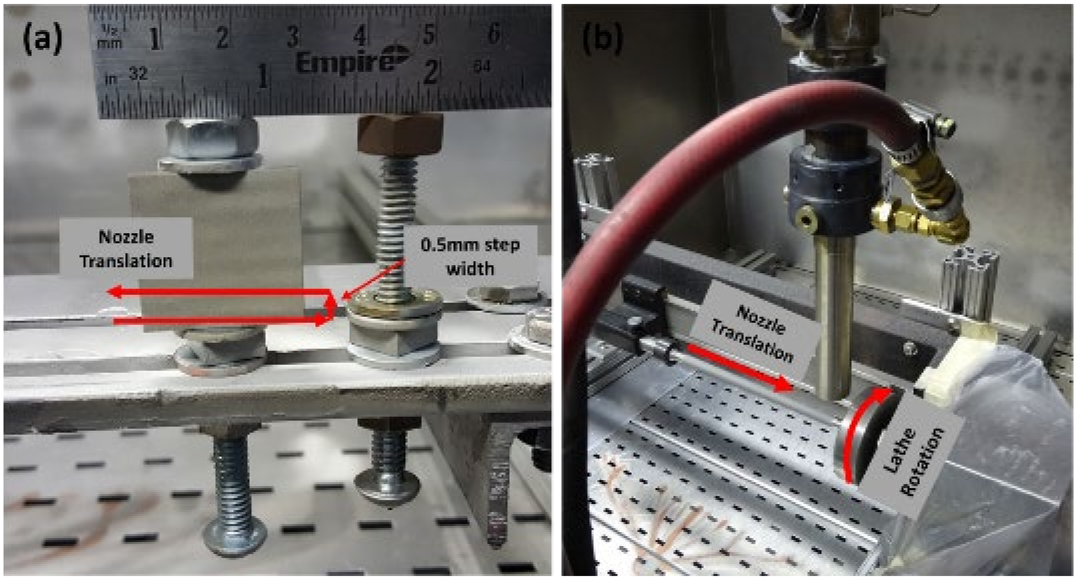

Fig. 2.3. Photographs of the sample holders in the cold spray laboratory, with nozzle translation paths indicated by the arrows: (a) horizontal bridge for coating flat substrates; (b) miniature lathe system for coating tubular cladding substrates.

The equivalent robot translation speed, V_R (required for tubular cladding geometries) was determined by first calculating the arc length of a helix S using Eqn. 2.1:

$$S = \sqrt{r^2 + c^2} * t \qquad \text{Eqn. 2.1}$$

where r is the radius of the cladding tube, c is the pitch per rotation (mm/Rad) using a pitch P of 0.5 mm, and t is the degree of rotation in radians. The degree of rotation t is then converted to helical velocity, V_H, using Eqn. 2.2:

$$t = \frac{V_H}{\sqrt{r^2 + c^2}} \qquad \text{Eqn. 2.2}$$

Finally, the spindle rotation speed V_S (rpm) and robot translation speed V_R (mm/s) for cylindrical geometries was determined via Eqn. 2.3 and Eqn. 2.4:

$$V_S = t(1\, rotation/2\pi)(60 s/min) \qquad \textit{Eqn. 2.3}$$

$$V_R = t(1\, rotation/2\pi) * P \qquad \textit{Eqn. 2.4}$$

To summarize, helical velocity V_H is chosen such that it matches the robot linear translation speed used for spraying flat substrates. Then, this velocity is converted into V_R and V_S components when programming the robot for cold spray deposition on cladding tubes. This way, similar parameters could be used for comparative studies of coatings deposited on flat and tubular (cladding) geometries.

2.2. Cold spray feedstock and substrate materials

2.2.1. Zirconium-alloy substrates

A variety of Zr-alloy substrates were procured for this research. Flat Zircaloy-4 (Zry-4) substrates were procured from ATI Wah Chang (Albany, OR) and were certified in accordance with ASTM B352 [143], the international standard for zirconium and zirconium alloy strip, sheet, and plate material. The 10.5” x 24.0” as-received Zr-4 plates were 0.104” thick and cut into manageable 1” x 10.5” strips with electrical discharge machining. Flat ZIRLO^{TM} substrates were acquired from Westinghouse Electric Company (WEC, Cranberry Township, PA). The 12” x 12” as-received ZIRLO^{TM} plates were 0.031” thick and cut into manageable 1” x 6” strips with electrical discharge machining. Additionally, Zry-4 cladding tubes were provided by Idaho National Laboratory, and ZIRLO^{TM} and Optimized ZIRLO^{TM} (OPZ) cladding tubes were provided by WEC. Nominal compositions of various Zr-alloy substrates used in this research are summarized in Table 2.1. The differences in these alloys arise from relatively small variations in concentrations of alloying elements, such as Sn, Nb, and Fe. All Zr-alloy substrates were ground using 600-grit SiC abrasive paper and cleaned with ethanol to remove surface oxide films and other residue from previous processing, and to slightly roughen the surface before deposition. The thickness of the substrates was measured with a Mitutoyo digital micrometer before and after deposition to provide an immediate onsite approximation of the maximum coating thickness.

Table 2.1. The nominal composition (in wt.%) of the Zr-alloy substrates used in this research.

Substrate	Zr	Sn	Nb	Fe	Cr	Si*	C*	O*	N*
Zircaloy-4	Bal.	1.34	--	0.22	0.11	9.5**	15**	1200	3.6**
ZIRLO®	Bal.	1.0	1.0	0.11	--	--	--	1200	--
Optimized ZIRLO™	Bal.	0.6-0.79	0.8-1.2	0.09-0.13	--	--	--	900-1600	--

Impurities: * parts per million (ppm); ** parts per billion (ppb).

2.2.2. *Electrolytic soft chromium powder*

Two lots of electrolytic soft chromium powder, procured from a commercial source, were produced for the University of Wisconsin-Madison research: Lot 1 included 15 lbs. of 635 mesh (-20 μm) powder, and Lot 2 included 15 lbs. of 325 mesh (-44 μm) powder. Nominal composition of the Cr powder provided by the supplier is summarized in Table 2.2.

Table 2.2. Nominal composition (ppm) of commercial Cr powder used in this study.

Mesh	Size (μm)	Cr	Fe	Ni	Si	C	N	O	S
635	-20	Bal.	1700	20	135	337	48	429	35
325	-45	Bal.	1800	25	91	177	52	1380	35

Particle size distribution for the two lots of Cr powder was determined using image analysis. First, Cr powder was placed in ethanol and allowed to mix thoroughly. Then, two droplets of the powder/ethanol solution were placed on conductive carbon tape, whereafter the ethanol was allowed to evaporate, leaving behind only the Cr particles. The particles were then imaged by scanning electron microscopy (SEM) at several specified magnifications, as shown in Fig. 2.4 (a,b). The images were analyzed using the Analyze Particles feature in ImageJ software, which uses thresholding to isolate individual particles, as shown in Fig. 2.4 (c,d). At least 100 particles were analyzed per lot of powder. Particle size was determined using Feret's diameter, which is the longest distance between two points along the particle.

The resulting particle size distributions are shown in Fig. 2.4 (e,f). D_{50} represents the median diameter of the particles, or the value of particle diameter at 50% in the cumulative distribution. The D_{50} values for the 635 mesh and 325 mesh lots of powder were 15 μm and 17 μm, respectively. In general, particle size distributions that are narrow are beneficial to the cold spray process, leading to more uniform powder flow through the powder feedline and thus ensuring a more even deposition. Since all particles in 635 mesh were < 30 μm, and to avoid having to perform additional sieving of the powder, 635 mesh (-20 μm) powder was used exclusively for all Cr coating depositions in this research unless otherwise stated.

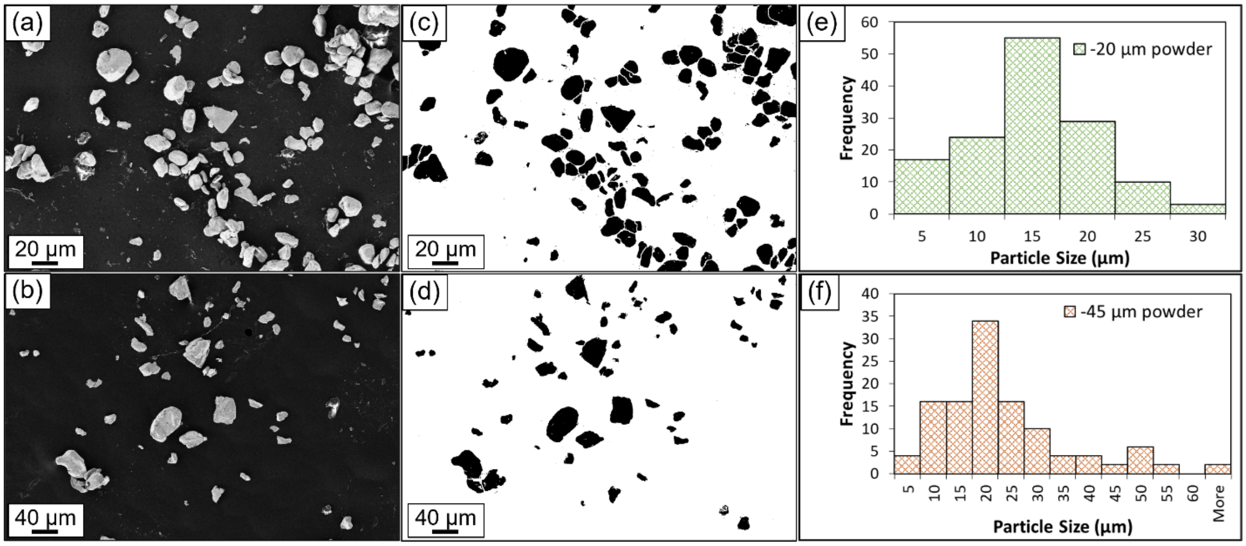

Fig. 2.4. SEM plan-view images of Cr particles from (a) 635 mesh (-20 μm) and (b) 325 mesh (-45 μm) lots; Image analysis used to identify individual particles from (c) 635 mesh (-20 μm) and (d) 325 mesh (-45 μm) lots; Particle size distributions for (e) 635 mesh (D_{50}~15 μm) and (f) 325 mesh (D_{50}~17 μm) lots.

2.3. Cold spray deposition parameters

An extensive amount of cold spray chromium deposition was performed in this research, including over 100 individual spray runs resulting in over 300 individual Cr coatings. These spray runs involved varying different cold spray parameters to ascertain their effects on coating quality, including coating thickness, density, surface roughness, interfacial roughness, and bonding, among others. Independent cold spray process variables and their corresponding dependent process variables include [96]:

a) Carrier gas temperature, pressure, and molecular weight – influence particle velocity

b) Powder feed-rate, standoff distance, and gun translation speed – influence deposition efficiency

c) Particle size, morphology, and microstructure – influence bonding quality

A selection of cold spray deposition runs that involved development, optimization, and testing of Cr coatings on Zr-alloy cladding will be described in the following subsections. This list is not exhaustive; however, Cr coatings deposited for other purposes (i.e., side projects) remain outside the scope of this research.

2.3.1. Initial deposition of electrolytic soft Cr powder on Zr-alloy substrates

Three standard parameter sets were used to deposit Cr coatings on Zr-alloy substrates using electrolytic soft Cr powder. This allowed for comparison of several carrier gas compositions and their effects on coating quality. The gas parameter combinations used to deposit Cr coatings is summarized in Table 2.3. While this study mainly focused on electrolytic soft Cr powder, previous work involving different Cr feedstock powders could be directly compared by using these cold spray parameters. An estimation of the particle velocity is also included in Table 2.3 and are based on computational fluid dynamics simulations that will be detailed in Section 2.4.1.

Table 2.3. Summary of the initial process gas conditions investigated for Cr deposition on Zr-alloy.

Condition	Process gas composition, He/N_2 (% volume flow rate)	Gas preheat temperature (°C)	Estimated particle velocity (m/s)
“Cr-N2”	0% He, 100% N_2	750	670
“Cr-75He”	75% He, 25% N_2	550	770
“Cr-He”	95% He, 5% N_2	500	870

Much of the development, characterization, and testing of the cold spray Cr coatings was focused on comparing “Cr-N2” and “Cr-He” coatings, which represent the maximum gas compositions and preheat temperatures achievable with the CGT Kinetiks system. Unless stated otherwise, all other cold spray parameters for the Cr-N2 and Cr-He conditions were kept constant between spray runs and are listed in Table 2.4. The results from these initial deposition runs are discussed in Section 3.

Table 2.4. Constant process parameters for the Cr-N2 and Cr-He conditions.

Process parameter	Value
Inlet gas pressure	4.0 MPa (Cr-N2); 3.8 MPa (Cr-He)
Carrier gas flow rate	80 ± 10 m^3/h (Cr-N2); 180 ± 10 m^3/h (Cr-He)
Nozzle traverse speed	200 mm/s
Nozzle standoff distance	26 mm
Powder feeder disk rotation	2 rpm
Powder flow rate	4 m^3/h

2.3.2. *Single-particle Cr impact experiments on Zr-alloy and pure Cr substrates*

In this study, single-particle impact experiments were performed to simulate each coating deposition stage separately to elucidate their specific critical velocity, deposition efficiency, and associated deformation mechanisms. To achieve this, Cr particles were impacted separately on both Zry-4 and bulk Cr substrates at various velocities. The former allowed for the understanding of interfacial bonding while the latter simulated interparticle bonding that would occur during the coating buildup phase of cold spray deposition.

Prior to single-particle deposition, the Zry-4 and Cr substrates were polished progressively down to a finer 1200 grit SiC abrasive grit to facilitate clear microscopic examination and analysis of the bonded particles and impact craters. Powder feed rates were minimized (1 m^3/h) and gun translation speeds were maximized (2000 mm/s) to allow only individual particles impacting on the selected substrates. Propellant gas pressure was maintained in the range of 3.5-4.0 MPa. While a wide range of particle velocities were investigated, three were chosen for extended characterization and details are provided in Table 2.5.

Table 2.5. Cold spray deposition parameters for single Cr particle impact experiments.

Condition	Propellant Gas Composition	Propellant Gas Temperature (°C)	Estimated Particle Velocity (m/s)
Low velocity	100%-N_2	350	580
Medium velocity	100%-N_2	750	680
High velocity	95%-He/5%-N_2	500	880

2.3.3. Cold spray shot peening for surface roughness reduction

Cold spray Cr coatings must meet minimum uniform thickness (<30 µm) and surface roughness (<0.2 µm) requirements to be considered for nuclear service. Shot peening of cold spray Cr coatings was investigated as an alternative to the conventional mechanical grinding process used to reduce surface roughness and possibly the thickness the as-deposited coatings. Because the cold spray gun is essentially a feedstock particle accelerator, it was used as an improvised shot peening device. Two cold spray shot peening experiments were performed over the course of the research, and the parameters of each experiment are provided in Table 2.6, and the results are discussed in Section 5.2.2.

Table 2.6. Cold spray shot peening parameters.

Parameter	Experiment A	Experiment B
Shot media	Spherical, gas atomized Cr	Non-spherical, electrolytic soft Cr
Particle size (µm)	25-44	-44
N_2 gas temperature (°C)	25	100
N_2 gas pressure (MPa)	0.7	1.0
Powder flow rate (m^3/h)	4	4
Standoff distance (mm)	30	30
Gun translation speed (mm/s)	100	100

2.3.4. Dual-layer Cr coatings on Zr-alloy for interfacial roughness reduction

Cold spray deposition produces an inherently rough interface due to high velocity particle impact and associated plastic deformation of the substrate. This is typically preferred, as jetting of the substrate produces the necessary conditions for metallurgical bonding, and the interface roughness promotes mechanical interlocking. However, interfacial roughness also limits the minimum thickness achievable with post deposition grinding treatments. Therefore, several experiments were designed to assess the effects of particle velocity and gun translation speed (i.e., “spray speed”) on interfacial roughness. Details of the experiments are provided in Table 2.7. Experiments A-C involved depositing a dual-layered coating: the first layer (a.k.a., “seed layer”) was deposited using low particle impact velocity followed by the second layer (a.k.a., “top layer”) which was deposited using high particle impact velocity. All seed layers were deposited using 100%-N_2 carrier gas preheated to a range of 100-500 °C. Top layers were deposited using either 100%-N_2 or 95%-He process gas compositions at the maximum preheat temperatures of 750 °C and 500 °C, respectively. Experiment D involved depositing a single layer using increasing spray speeds. The results from these experiments are described in Section 5.3.

Table 2.7. Cold spray parameters for reduction of interfacial roughness.

	Seed layer		Top layer	
Experiment	Particle velocity (m/s)	Spray speed (mm/s)	Particle velocity (m/s)	Spray speed (mm/s)
A	560-610	200	680-880	200
B	520-560	100	680-880	200
C	520-560	50	680-880	200
D	--	--	680	200-600

2.3.5. Deposition of Cr coatings on Zr-alloy using larger particle sizes

Typically, a tight particle size distribution (635 mesh) is used to deposit Cr coatings as it has been shown to improve particle flow characteristics. However, using larger particle size distribution (325 mesh) may be a more cost-effective approach. Therefore, one cold spray experiment was performed to assess the feasibility of using larger particle sizes (-44 µm) and their effects on particle velocity, interfacial roughness, and coating thickness. Details of the experiment are provided in Table 2.8. Coatings were deposited using 100%-N_2 gas preheated to 750 °C. The larger particle size distribution results in particle velocities ranging from 500-680 m/s. Process parameters that were varied include nozzle stand-off distance and spray speed. The results from the experiment are described in Section 5.1.1.

Table 2.8. Cold spray parameters for deposition of larger particles.

Spray run	Standoff distance (mm)	Spray speed (mm/s)
1	25	200
2	25	500
3	50	200
4	50	500

2.3.6. Deposition of Cr coatings on Zr-alloy for ion irradiation testing

Cold spray Cr coated Zr-alloy were subjected to high-energy heavy ion irradiation experiments to assess their overall resistance to irradiation damage. Cr-He coatings on Zry-4 were deposited using a spray speed of 400 mm/s, producing a coating thickness of 75 ± 10 μm. Coatings were then mounted to a metal puck and hand-polished using 600 grit SiC paper to reduce the coating thickness. The samples were polished in such a way that resulted in a gradient in coating thickness from zero (on the uncoated side) to about 50 μm on the coated side. The entire sample surface was then polished using progressively smaller polycrystalline diamond suspensions down to 0.05 μm, the final step being 0.02 μm colloidal silica to obtain a pristine surface finish. Further details about the test are provided in Section 2.12, and the test results are described in Section 6.

2.3.7. Deposition of Cr coatings on Zr-alloy for mechanical testing

Cold spray Cr coated Zr-alloy were subjected to unique mechanical and micro-mechanical tests to assess their mechanical performance. For mechanical testing in conjunction with synchrotron X-ray diffraction performed at Argonne National Laboratory (ANL), Cr-He coatings were deposited onto 800 μm thick ZIRLO^{TM} flat substrates using 400 mm/s spray speed. The approximate coating thickness was 75 ± 10 μm. After deposition, a portion of the samples was polished using 600 grit SiC abrasive paper to reduce surface roughness inherent to cold spray deposition. The final coating thickness was approximately 60 μm.

For mechanical testing using the micro-cantilever beam bending approach performed at Los Alamos National Laboratory by the author, Cr-N2 and Cr-He coatings were deposited onto cylindrical Zry-4 cladding tubes (~9.0 mm OD, 200 mm length) using 200 mm/s helical spray speed (~3.4 mm/s equivalent linear speed). The as-deposited coating thickness was 44.5 ± 2.8 μm and 101.3 ± 4.1 μm for Cr-N2 and Cr-He coatings, respectively. Coated cladding was mounted to a miniature lathe and gently hand polished using 600 grit SiC abrasive paper to reduce the surface roughness. Cr-He coatings were then polished using 320 grit SiC abrasive paper to further reduce the coating thickness, followed by one finishing pass using 600 grit paper. The coatings were consistently lubricated with ethanol during the polishing process, and coating thickness measurements were taken periodically using a handheld micrometer. Final coating thickness measurements were 20.5 ± 2.7 μm and 26.6 ± 4.1 μm for Cr-N2 and Cr-He coatings, respectively, averaged from 6 axial positions and 3 circumferential positions along the cladding tube for a total of 18 individual measurements. A photograph of a polished tube with thickness measurement locations is shown in Fig. 2.5.

Individual sample coupons were sectioned using a low-speed saw to an approximate thickness of 1.5 mm. Designated samples were then subjected to several annealing treatments described in Section 2.11. The cross-sectional faces of the sample coupons were then manually grinded to achieve flat, parallel faces and a total thickness of 1.28 ± 0.02 mm. Further details on this test are provided in Section 2.9, and the test results are described in Section 8.

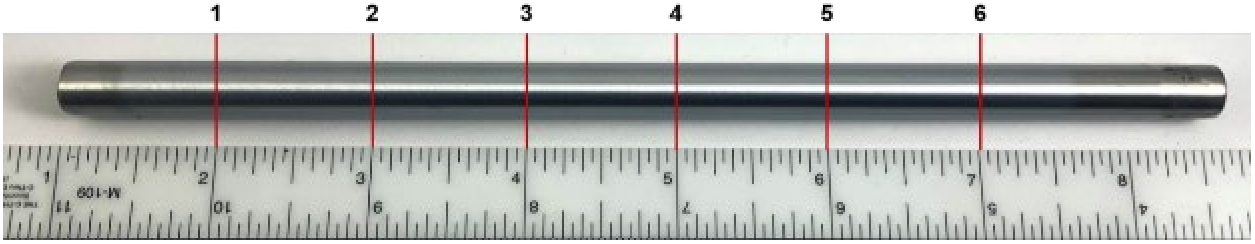

Fig. 2.5. Photograph of a polished Cr coating on Zry-4 cladding tube. Micrometer thickness measurements were taken at 6 axial positions along the tube, approximately 1" apart. At each position, thickness measurements were taken at 120° increments circumferentially around the tube, for a total of 18 thickness measurements.

2.3.8. Deposition of Cr coatings on Zr-alloy for hydrothermal corrosion testing

Cold spray Cr coatings on Zr-alloy cladding were subjected to pressurized water autoclave testing to assess the hydrothermal corrosion resistance in simulated PWR conditions. Cr-N2 and Cr-He coatings were deposited onto flat Zry-4 substrates using the typical spray parameters, producing an as-deposited coating thickness of 44.5 ± 2.8 μm and 101.3 ± 4.1 μm, respectively. Cr-coated and uncoated Zry-4 and Optimized ZIRLO^{TM} samples were prepared by removing the native oxide layer on all sides of the sample surface using SiC abrasive paper (successive grits from 320 to 1200 grit), followed by cleaning via ultrasonication in acetone and ethanol and air drying. Further details about the test are provided in Section 2.10, and the test results are described in Section 9.

2.3.9. Deposition of Cr coatings on Zr-alloy for high temperature oxidation testing

Cold spray Cr coated Zr-alloy were subjected to high temperature oxidation in air and steam environments to assess their performance in simulated LOCA conditions. Cr-He coatings were deposited onto flat Zry-4 substrates using a spray speed of 400 mm/s, producing an as-deposited coating thickness of 75.7 ± 7.6 µm. The surfaces of Cr coatings were then polished to remove inherent roughness resulting from the cold spray process, reducing the coating thickness to about 50 µm. The coatings were then cleaned via ultrasonication in acetone and ethanol and air drying. Further details about the test are provided in Section 2.11, and the test results are described in Section 9.

2.4. Modeling and simulation of the cold spray process

The experimental work was supported by a strong modeling component to predict coating formation characteristics as a function of process parameters. Through simulation of the cold spray process, a vastly expanded parameter space could be explored to gain a more fundamental understanding of the cold spray process, something that is difficult to achieve by experimentation alone. The modeling was performed primarily by using the licensed ANSYS software.

Cold spray deposition involves two distinct but interrelated parts: the first involves dynamics of particle and gas flow prior to particle impact on the substrate, and the second involves particle deformation and bonding upon impact. As the propellant gas is heated, compressed, expanded, and accelerated through the converging-diverging nozzle, feedstock powder particles are introduced into the gas stream and accelerate along with the gas. Thus, it is important to model both gas flow and particle flow from the inlet to the outlet of the nozzle to calculate the temperature and the velocity.

Once the particles exit the nozzle and accelerate towards and impact the substrate, they plastically deform at high strain rates to bond with each other and to the substrate. An adiabatic shear mechanism is generally assumed to play a role in the bonding process. Thus, it is important to simulate a transition from gas-flow dynamics to high velocity particle impact. Material properties such as elastic modulus and Poisson ratio, as well as deformation variables such as Johnson-Cook strength and equations of state become important. Using the particle temperature and velocity obtained from the first simulation, particle impact was simulated to obtain valuable information such as extent of deformation, strain rate, temperature rise, critical velocity, bonding criterion, and even multiple particle impacts. A description of the two facets of modeling is provided in the following sections, including validations and comparisons to literature.

2.4.1. Modeling supersonic gas and particle flow

Supersonic gas flow through a converging-diverging nozzle was simulated using computational fluid dynamics, with simulations being performed using ANSYS software Fluent package. The flow of the carrier gas through the nozzle was modeled as a 1-dimensional, isentropic, single-phase flow along the nozzle axis. The dimensions of the tungsten carbide nozzle used for conducting cold spray depositions were replicated in the nozzle geometry used for this simulation. Particle acceleration and heating in the gas flow within the nozzle was estimated by solving equations of motion and heat transfer and using the following assumptions: (i) the particle is spherical with negligible internal temperature gradients, (ii) specific heat is independent of temperature, (iii) interaction between particles are ignored, and (iv) the influences of particles on the gas flow are neglected [92].

First, simulation of the gas flow through the nozzle was performed. At the nozzle inlet, gas composition, temperature, and pressure were specified, and the simulation was allowed to converge. Then, a single chromium particle was introduced into the gas stream to predict its temperature and velocity as it flowed through the nozzle. The particle accelerates through momentum exchange with the carrier gas via fluid drag forces, as shown in the following equation:

$$m_p V_p \left(\frac{dV_p}{dx}\right) = \frac{C_D A_p \rho_p \left(V_g - V_p\right)^2}{2} \qquad \textit{Eqn. 2.5}$$

where V_p is the velocity of the particle (V_g the velocity of the gas), m_p, ρ_p, and A_p are the mass, density, and cross-sectional area of the particle, respectively, and C_D is the drag coefficient for a sphere [93]. Convective heat transfer between the carrier gas and particle is also considered:

$$m_p c_p V_p\left(\frac{dT_p}{dx}\right) = h_{gp}A_p\left(T_g - T_p\right), \qquad \textit{Eqn. 2.6}$$

where T_p is the particle temperature (T_g the gas temperature), c_p is the heat capacity of the particle, and h_{gp} is the convective heat transfer coefficient [144]. The temperature and velocity of the particle were collected along all stages of travel through the nozzle.

The model was also benchmarked against results reported in literature. Results from this study produced contour plots of gas temperature and velocity as shown in Fig. 2.6 that aligned closely with Osman et al [145]. Next, a sensitivity study was performed to quantify the impact of each variable on the simulation results by changing one variable at a time. Results from this study led to the selection of second-order spatial discretization using least-squares method to provide better accuracy. Gas density was assumed to be that of an ideal gas for helium. Viscosity of helium gas was estimated using kinetic theory. Real-Gas-Augier-Redlich-Kwong density model was used for N_2 gas and Sutherland model was used for the viscosity. Spatial discretization was utilized using second order and least-squares techniques, and AUSM for the flux to provide exact resolution of contact and shock discontinuities. Full definitions of the specific models used can be found in the ANSYS user guide [146].

Mixtures of N_2/He gases were modeled using the species model in Fluent coupled with species transport model and volumetric reaction. Since the mixture flow has fluctuations, eddy dissipation model was also included. Results from the gas mixture study showed that nearly all solutions converged, and results were in good agreement with published data.

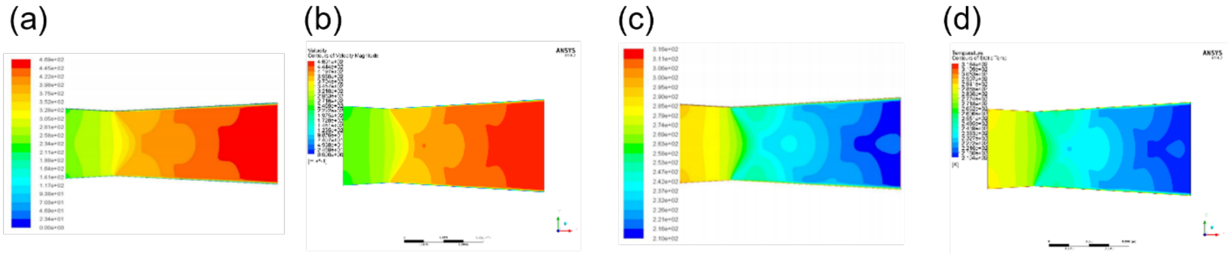

Fig. 2.6. Contours of air flowing through a nozzle at 9 bar and 320 K: (a) velocity contour plot from Osman et al. [145]; (b) velocity contour plot from simulations in the present research; (c) temperature contour plot from Osman et al. [145]; (d) temperature contour plot from simulations conducted in the present research.

Next, a single particle was injected into the nozzle and tracked using the discrete phase model. Two-way turbulence coupling was selected to consider the interaction between the particle and the gas stream. Spherical drag law was used for the spherical particles; however, morphology of the particles plays an important role in the acceleration of particles [147]. Another sensitivity study was performed to examine the accuracy of the predicted gas and particle velocities. Fig. 2.7 shows simulation results from Hulton [144] compared to the simulations in the present research. The comparison confirms the reliability of the velocity and temperature profiles for both gas and particles developed in the present research.

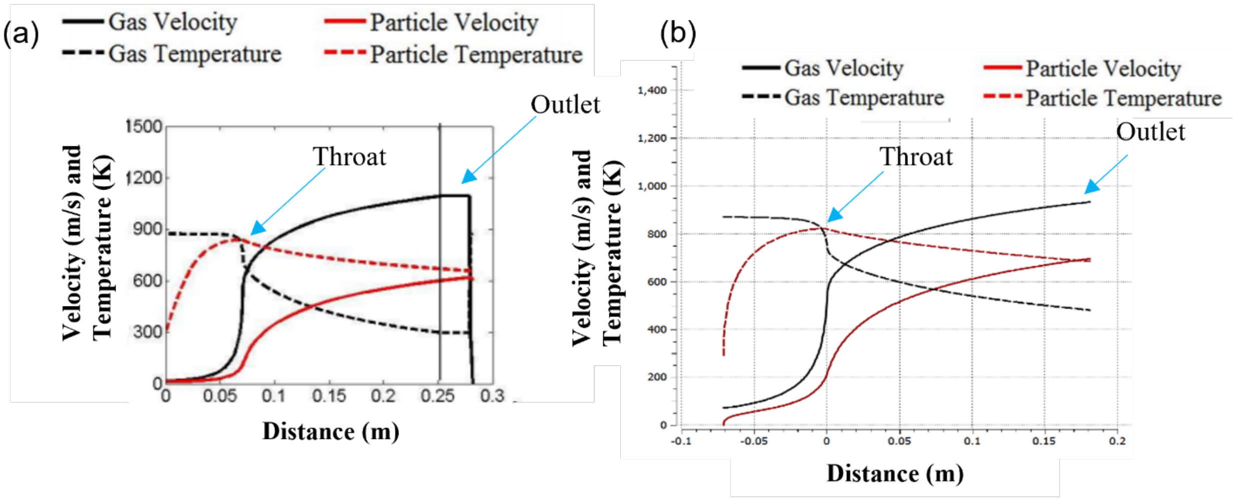

Fig. 2.7. Velocity and temperature of the gas and particle as a function of distance from the nozzle inlet to the exit. (a) Results from Hulton [144], with nozzle throat at x=0.07; (b) Results from the present study, with nozzle throat at x=0.

Effects of particle shape on particle temperature and velocity was also investigated to simulate the non-spherical electrolytic Cr powders. *Sphericity* (ψ_s) is defined as the ratio of the surface area of a spherical particle of equivalent volume to the surface area of the particle under investigation, hence, non-spherical particles will have $\psi_s < 1$. Researchers have used 3D CFD modeling to show that particles with $\psi_s = 0.4$ can accelerate up to 200 m/s faster than particles with $\psi_s = 1$ [96]. Thus, non-spherical particles can accelerate to much higher velocities compared to perfectly spherical particles. In ANSYS, this involves deviating from the *spherical* drag model to specifying a *shape factor*, which is defined the same as sphericity. For example, a pear-shaped and a cube-shaped particle were simulated because the shape factor model does not allow the complex sphero-conical geometry of electrolytic Cr particles. Nevertheless, the results shown in Table 2.9 revealed that increased velocity and decreased temperature can be achieved at the outlet of the nozzle with non-spherical particles. While the shape factor effect warrants further study, spherical particles were used for the remainder of the simulation work for simplicity.

Table 2.9. Simulated particle velocity and temperature at the nozzle outlet using particles with different shape factors (sphericity).

Particle shape	Shape factor	V_p at nozzle outlet (m/s)	T_p at nozzle outlet (K)
Spherical	1.00	595	550
Pear	0.96	610	546
Cube	0.80	698	522

After performing the verification of the University of Wisconsin's CFD model, actual cold spray process parameters were used as input variables in the simulation, including nozzle geometry, gas mixture compositions, temperature, pressure, particle size and material constants. The simulation allowed us to predict gas and particle temperature and velocity. Finally, these output values were then fed into the particle impact simulations to get the full picture of a typical cold spray process for a given set of processing parameters.

Fig. 2.8 shows a typical output from the supersonic gas flow CFD simulation. Velocity and temperature contours of the carrier gas (95%-He / 5%-N_2) and a Cr particle traveling through a nozzle are shown. The temperature of the carrier gas decreases as it moves through the nozzle, as expected. Meanwhile, the temperature of the Cr particle increases as it travels towards the throat of the nozzle, then slightly decreases in the diverging section. Both particle and gas velocity increase rapidly after flowing into the throat and traveling down the diverging section towards the nozzle outlet. The particle velocity at the outlet is reasonable for the input conditions and within the typical range of particle velocities during cold spray deposition (300 - 1300 m/s). Based on these results, simulations were recreated using a variety of Cr particle sizes and process gas conditions.

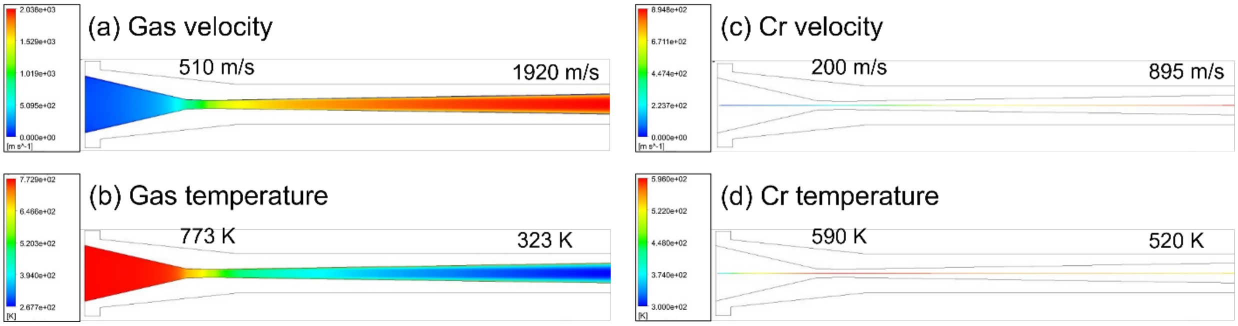

Fig. 2.8. Simulated velocity and temperature contours in de Laval nozzle for (a,b) 95%-He / 5%-N_2 *carrier gas mixture, and (c,d) Cr particle. Indicated values are at the nozzle throat and nozzle outlet.*

The particle velocity at the nozzle outlet is shown in Fig. 2.9 (a) for several Cr particle sizes within a carrier gas of 100%-N_2 composition. The results for velocity predictions of a 20 μm particle as a function of helium content in the gas mixture is shown in Fig. 2.9 (b). The plot also shows gas preheat temperatures that can be achieved with the reported He/N_2 gas mixture using the Kinetiks system. Interestingly, the gas dependence of particle velocity is more pronounced as the particle size decreases. Changing the gas from pure N_2 to pure He gas increases the particle velocity of a 40 μm diameter Cr particle by about 200 m/s, while the particle velocity increases by about 500 m/s for a 10 μm diameter Cr particle. This is significant as there is a range of particle sizes included in the hopper for a typical cold spray run. Particle velocities were also comparable for a 20 μm Cr particle and a 20 μm stainless steel particle (not shown). However, much thicker coatings were achieved with stainless steel powder than pure Cr powder, indicating that deposition efficiency is closely related to the feedstock powder microstructure and mechanical properties rather than just particle velocity – these effects are elaborated in the next section on particle impact modeling.

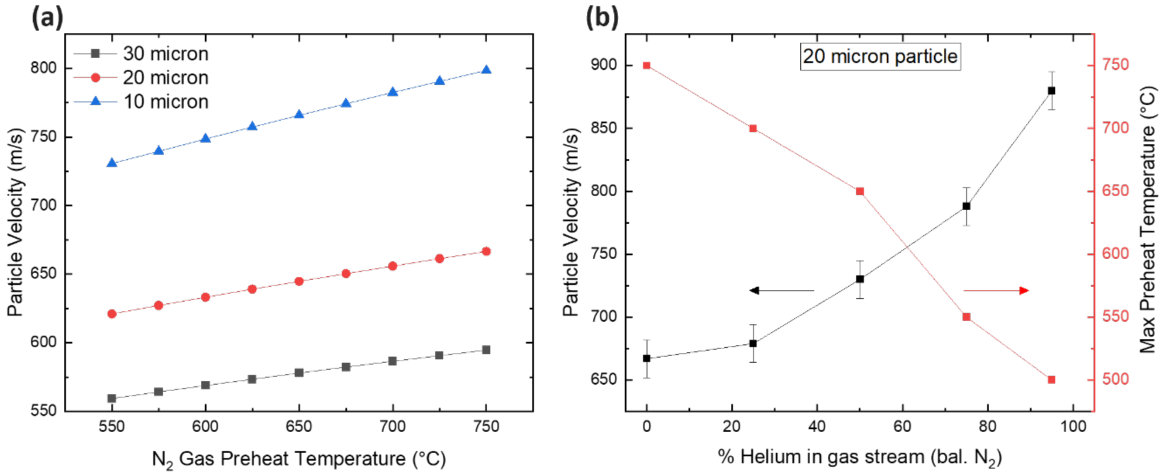

Fig. 2.9. Results from CFD simulation of Cr particles flowing through converging-diverging nozzle: (a) particle velocity at the nozzle outlet vs. N_2 *gas preheat temperature, as a function of particle size; (b) particle velocity at the nozzle outlet vs. gas mixture composition for 20 μm sized Cr particle.*

A small study was performed to investigate the effect of process gas pressure on particle temperature and velocity. Fig. 2.10 shows particle temperature and velocity as a function of the input gas pressure. Particle temperature is very comparable no matter the input gas pressure, while particle velocity increases by less than 100 m/s as the pressure is increased from 15 bar to 35 bar. This shows that the inlet pressure of the gas is mainly used to accelerate the particles up to the speed of the gas before the converging section of the nozzle.

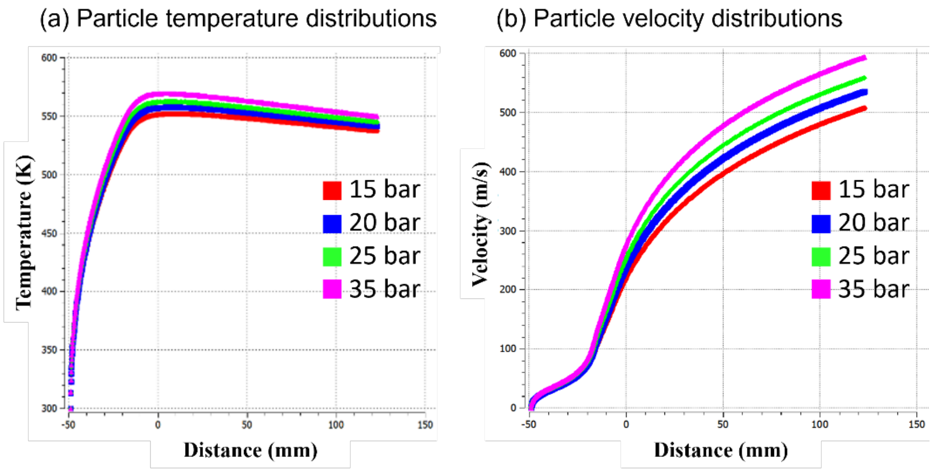
(a) Particle temperature distributions
(b) Particle velocity distributions

Fig. 2.10. Studies on the effect of carrier gas pressure for a 20 μm Cr particle deposited using 500 °C N_2 *gas showing particle temperature (a) and particle velocity (b) at varying pressures: 15 bar (red), 20 bar (blue), 25 bar (green), and 35 bar (purple).*

Velocity in cold spray is influenced by "bow shock effect," which occurs when the cone of supersonic gas extends to the substrate. Fig. 2.11 shows the various phenomena that occur when a supersonic gas reaches a substrate [148], with the bow shock region and stagnation bubble at the gas jet/substrate interface. This effect can occur when the stand-off distance is less than the length of the potential core, i.e., increasing the stand-off distance should decrease the size of the bow shock region. The shock waves act to decrease the gas velocity outside of the nozzle and effectively decrease the particle velocity due to pressure buildup at the substrate. The model assumes no bow shock effect at the substrate surface, which can attenuate the velocity of the gas and particles as they approach the substrate [148,149]. The moderately wide standoff distance (30 mm), combined with the relatively high density of Cr (7.19 g/cm^3), and the average particle size (15 µm) used in this research, result in the particles seeing minimal deceleration due to the bow shock effect while approaching the substrate surface.

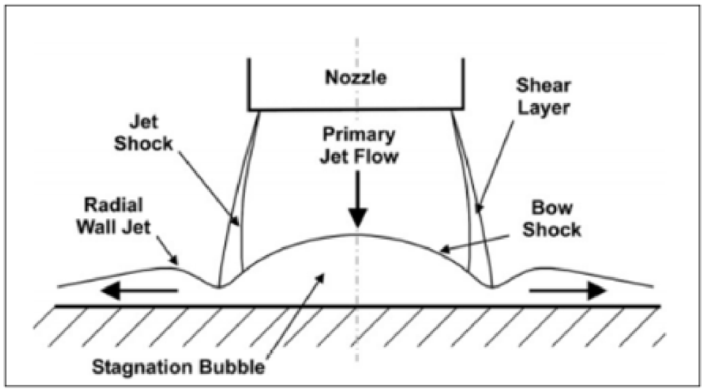

Fig. 2.11. Schematic diagram of the bow shock effect emanating from a supersonic gas interacting with a substrate surface [148].

2.4.2. Modeling high velocity particle impact and high strain rate deformation

High velocity particle impact was modeled using ANSYS software Autodyn package to create finite element modeling (FEM) simulations using the Explicit Dynamics module. Particle and substrate geometries were generated using commercial SolidWorks software for use in 2D or quasi-2D simulations. The substrate was designed to be at least 5x larger than the particle diameter for an accurate description of the problem but not too large to increase computational time. After both particle and substrate were mated, the computer aided design (CAD) assembly was imported into ANSYS workbench.

One important aspect of the simulation is meshing, and because of this a lot of time was devoted to determining the best mesh for this situation. A *mesh* contains a set of nodes which define unique locations where the *physical* equations are evaluated. These nodes connect to form a collection of *elements* that satisfy a *shape* (i.e., a particle). Elements can either be *structured* and contain uniform elements (i.e., self-repeated pattern of shapes), or *unstructured* and contain no element pattern, which is very memory intensive. These elements can be arranged in various ways to create different types of meshes.

The first method investigated is referred to as a *Lagrangian* mesh. This mesh contains maximized structured elements and is probably the most common type of mesh used in simulation work. However, a Lagrangian mesh may become too distorted to track during high strain rate deformation. In some cases, the simulation never solves to the desired end time due to error associated with the conversion of structured elements to unstructured elements (i.e., the element shape drastically changes over the course of the simulation). Fig. 2.12 (a) shows a simulation with a Lagrangian mesh that failed at 0.007 μs due to the formation of unstructured elements.

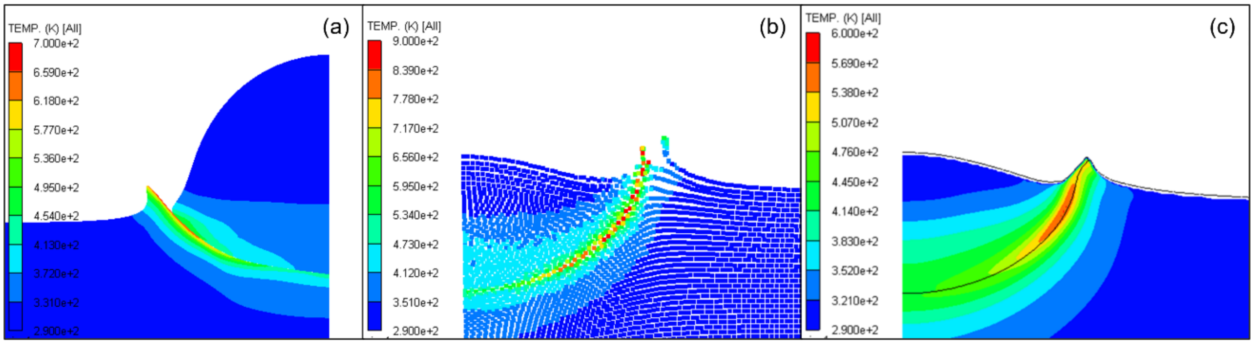

Fig. 2.12. Still images from a simulation of a 10 μm Al particle impacting a 50 × 50 μm Al substrate at a particle velocity of 550 m/s. (a) Lagrangian mesh; (b) SPH mesh; (c) Euler mesh.

The second method investigated is referred to as *Smooth Particle Hydrodynamics*, or SPH. This is a mesh-free Lagrangian technique for modeling a continuum media. This method is advantageous for high strain rate deformation as it avoids mesh distortion errors and does not need to include erosion controls as in the case of a Lagrangian mesh. Thus, in this simulation the material would move through the nodes as it is being deformed. Two issues arose in implementing the SPH method. The first is that boundary conditions are very difficult to implement in this method and because of this, nodes arranged in high density will diverge into unlikely states, yielding unrealistic results (e.g., temperature values well exceeding the melting temperature of the material). Fig. 2.12 (b) illustrates a simulation with a SPH mesh at 0.025 µs. The mesh shows many gaps between elements and reaches temperatures approaching or exceeding the melting point of aluminum. The second issue is a significantly high computational cost when using this method.

The third method investigated is referred to as Euler, where a *void part* is created with dimensions that encompass the particle and substrate. The element density in the void will translate to the element density in all objects. In Euler meshing, the elements do not move with the material, thus eliminating node distortion issues (i.e., a mesh-free part). Fig. 2.12 (c) illustrates a simulation with an Euler mesh at 0.025 µs, revealing that local heating and plastic flow contributed to particle-substrate bonding.

Different studies have agreed that using Eulerian or Coupled Eulerian-Lagrangian reduces the error and yields more accurate results in this type of simulations compared to the lone Lagrangian method, which also produces computation termination when elements are distorted significantly [150]. However, results from this research revealed that using the Eulerian method for explicit dynamics produced inaccurate calculations and misrepresentations of the deformation suffered by the particles compared to real experiments. Therefore, the Lagrangian mechanics method was optimized and used for all simulations. The geometries of the particles were processed with a tetrahedral mesh, while the substrate used a cartesian mesh with element sizes between 1-3 µm to account for the possible errors from unrestructured or highly deformed elements generated during the simulations that would lead to the termination of the process.

The Johnson-Cook (JC) model is widely used in FEM to predict the plasticity and flow behavior of a material when subjected to high strain rates and temperatures [151]. This model primarily calculates the energy and interactions between stress and strain as the material deforms while accounting for strain hardening and thermal softening [152]. The JC model in Eqn. 2.7 describes a materials equivalent stress σ

as it relates to the plastic strain ε, strain rate $\dot{\varepsilon}^*$ (Eqn. 2.8), and its homologous temperature T^* (Eqn. 2.9) [151]:

$$\sigma = (A + B\varepsilon^n)(1 + C \ln \dot{\varepsilon}^*)(1 - T^{*m}) \qquad \text{Eqn. 2.7}$$

$$\dot{\varepsilon}^* = \frac{\dot{\varepsilon}}{\dot{\varepsilon}_{ref}} \qquad \text{Eqn. 2.8}$$

$$T^* = \frac{T - T_{ref}}{T_m - T_{ref}} \qquad \text{Eqn. 2.9}$$

where A is the initial (reference) yield stress, B is the strain hardening constant, n is the strain hardening coefficient, C is the strengthening coefficient of strain rate, m is the thermal softening coefficient, $\dot{\varepsilon}$ is the strain rate, $\dot{\varepsilon_{ref}}$ is the reference strain rate, T_m is the melting temperature, T is the material temperature, and T_{ref} is the reference temperature typically set to 298 K [153]. Along with the JC parameters, density, specific heat, shear modulus, and equations of state and parameters from the Mie–Grüneisen model were required to process the simulations. These values were obtained directly from the materials database in ANSYS. JC parameters were obtained from literature for several common and uncommon materials used in cold spray, including aluminum, copper, nickel, steels, molybdenum, tungsten, tantalum, niobium, and zirconium and their alloys (including Zircaloy-4). Unfortunately, after an exhaustive search it was discovered that the JC parameters for Cr are not currently available. Instead, Fe was used as a surrogate for Cr given that it also has a BCC crystal structure.

Using the finished model, FEM simulations of high velocity particle impact were compared to experiments performed in the literature. Fig. 2.13 shows images of single-particle impacts from LIPIT experiments performed by Hassani et al. [101] alongside images from particle impact modeling performed by this research. The experiment demonstrated that differences in materials properties manifest in the deformation mechanisms of dissimilar materials systems. Fig. 2.13 (a-b) demonstrates splatting behavior due to the low hardness and dynamic yield strength of the soft Al particle compared to the harder Ni substrate. Fig. 2.13 (c-d) demonstrates co-deformation behavior between Al particles and Al substrate, having similar materials properties. Fig. 2.13 (e-f) demonstrates penetration behavior of a harder Ti particle on a softer Cu substrate at high particle impact velocities. Fig. 2.13 (g-h) shows severe penetration behavior of a hard, dense W particle impacting a softer Cu substrate at lower particle impact velocities due to the extreme mismatch of materials properties. The results from the simulations in Fig. 2.13 align closely with the particle morphologies shown experimentally, indicating that FEM simulations can be a powerful tool for predicting the deformation behavior of mismatched materials systems, so long as JC parameters are available.

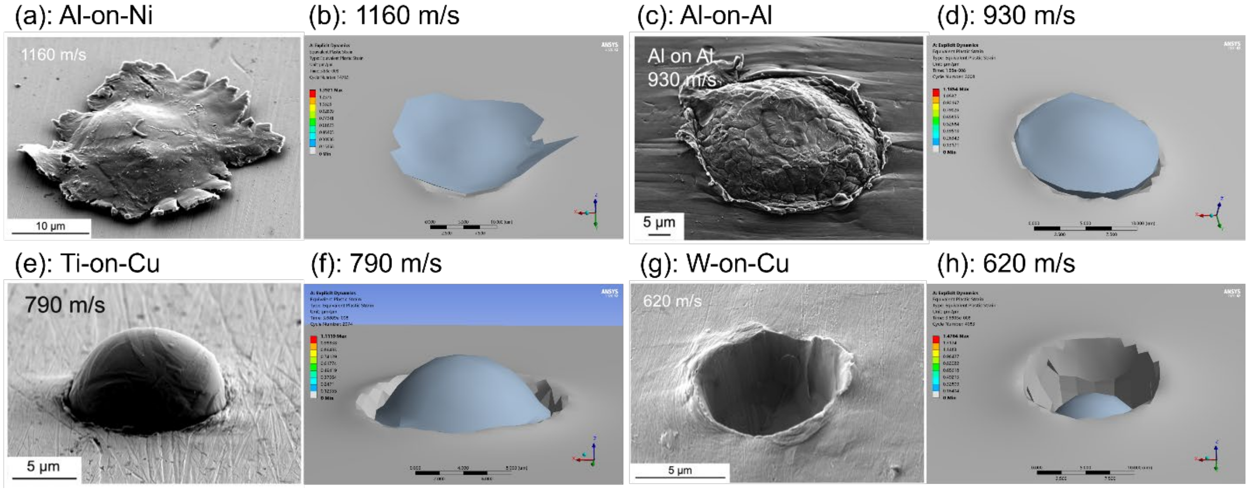

Fig. 2.13. Side-by-side images of single-particle impact morphologies from LIPIT experiments (left) and single-particle impact modeling performed by this research (right) for the following material-velocity conditions: (a-b) 11 µm Al particle impacting Ni at 1160 m/s, showing splatting behavior; (c-d) 10 µm Al particle impacting Al substrate at 930 m/s, showing co-deformation behavior; (e-f) 12 µm Ti particle impacting Cu at 790 m/s, showing penetration behavior; (g-h) 8 µm W particle impacting Cu substrate at 620 m/s, showing deep penetration behavior. Images reproduced from Hassani et al. [101].

2.5. Microstructural characterization, compositional analysis, and phase identification

Characterization of relevant materials was carried out in the Wisconsin Centers for Nanoscale Technology at the University of Wisconsin, Madison. Characterization of powder morphology and cross-sectional microstructure of Cr feedstock powders and cold spray deposited coatings were performed using scanning electron microscopy (SEM). Multiple SEMs were used in this work, including a Zeiss LEO 1530-1 field emission SEM and a Zeiss Gemini 450 field emission SEM, shown in Fig. 2.14 (a). Images were taken using the secondary electron (SE) imaging mode. Both microscopes contain energy dispersive X-ray spectroscopy (EDS) for compositional analysis of the as-deposited coatings and coatings after testing. For high-resolution imaging, SE imaging mode with 3-5 keV accelerating voltage was used. For EDS analysis, 12-15 keV accelerating voltage was used to ensure the criteria that the energy used exceeds twice the value of the characteristic X-ray energies of the majority elements present in the sample (Cr Kα ~5.4 keV, Zr Lα ~2.0 keV).

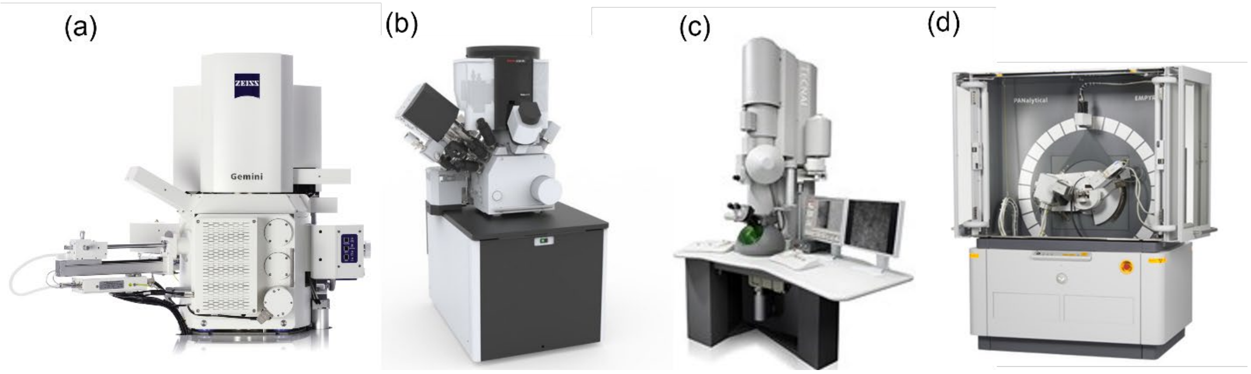

Fig. 2.14. Photographs of instruments used for materials characterization of powders and cold spray coatings: (a) SEM; (b) FIB; (c) TEM; (d) XRD.

One limitation of EDS chemical analysis is that quantification of light elements (Z<11) is difficult. Light elements typically generate weaker signals that are easily absorbed by the sample itself and are greatly affected by the condition of the sample surface (i.e., contamination). Additionally, principal Kα emission energies of lighter elements may overlap with principal Lα and Mα lines of heavier elements, for example O-Kα (0.525 keV) and Cr-Lα (0.572 keV). Quantification of oxygen and nitrogen using EDS can only be done if the elements are present in stoichiometric oxide and nitride compounds. To overcome this issue, relevant materials were analyzed using a Cameca SXFive field emission electron probe micro-analyzer (EPMA) located in the Department of Geology at UW-Madison. EPMA can perform quantitative analysis at high resolution using wavelength-dispersive X-ray spectroscopy (WDS), which separates elements based on wavelengths of X-rays rather than energies. The EPMA is equipped with multiple crystal spectrometers and can analyze up to five elements per scan. The samples were polished to mirror-finish and then vibratory polished for several hours to achieve a defect-free surface, then sputter-coated with a 1 nm layer of iridium to improve conductivity. WDS scans were acquired using 10-20 keV and 20-100 nA current depending on the required resolution, with a dwell time of 30 ms and a step size of 0.1-0.5 μm depending on the size of the map. The types of scans acquired included spectral element maps and point and line-scans. Correction of the continuous spectrum was performed using the off-peak background correction method.

The microstructure of Cr feedstock powders and deposited coatings were also characterized in cross-section using Electron Backscatter Diffraction (EBSD) on a Zeiss Gemini 300 field emission SEM with an Oxford Instruments Symmetry S3 detector. The samples were tilted to 70° with respect to the electron beam at a working distance of 8-10 mm, and data was acquired using an accelerating voltage of 30 keV and a step size of 30-70 nm. EBSD was used to acquire a variety of critical information including phase, grain orientation and size, intragranular misorientation, plastic strain, and dislocation density within Cr powders and coatings.

For samples requiring higher magnification imaging, thin foils were fabricated using a FEI Helios Plasma Focused Ion Beam (PFIB), shown in Fig. 2.14 (b). The PFIB uses a Xe^+ ion beam and operates at high milling currents in excess of 1 μA, allowing for fast milling of material. The first step involves depositing a protective Pt/C cap (3-5 μm thick) on the surface of the sample in the area of interest, which was done using an ion voltage and current of 12 kV and 100 pA, respectively. For surface-sensitive samples, this step was preceded by applying a thin (<500 nm) layer of Pt using the electron beam at 5 kV and 6.4 nA. The sample was then oriented normal to the ion beam (52° sample tilt) and rough milling steps were performed at 30 kV using milling currents of 60 nA, 15 nA, and 4 nA to create a cross-section approximately 2-3 μm thick. Next, 4 nA current was used to detach the sides and bottom of the lamella from the bulk sample, as shown in Fig. 2.15 (a). At this stage, the EasyLift micromanipulator was carefully moved next to the sample and attached with a Pt weld. Material on the remaining side was milled away and the sample was extracted from the bulk. Finally, the sample was moved to the Cu grid and welded using Pt, as shown in Fig. 2.15 (b), and then the probe was detached from the sample by milling through the Pt weld using 4 nA current. The final lamella was stable in the center of the Cu grid, as shown in Fig. 2.15 (c).

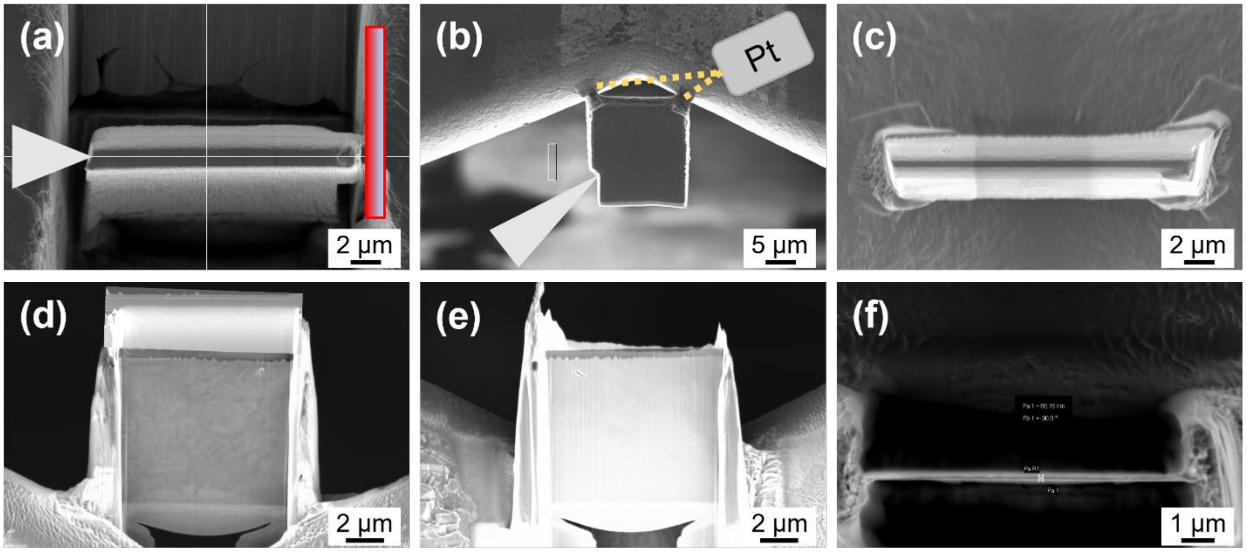

Fig. 2.15. The process for creating a thin foil lamella using (P)FIB: (a) A cross-section is milled from the material of interest, followed by attaching a microprobe to the side and detaching the cross-section from the bulk; (b) The sample is welded to a conductive Cu grid using Pt and the microprobe is detached; (c) Initial lamella has thickness of 2-3 µm. The sample is then thinned using successively lower milling currents from its initial state (d) to its final state (e) of electron transparency, where the final thickness (f) is less than 100 nm.

The Cu grid was transferred to a Zeiss Auriga Focused Ion Beam (FIB), which uses a Ga^+ ion beam for more precise milling at lower currents. The sample was tilted between 54-56° to become normal to the ion beam. Thinning steps were performed at an accelerating voltage of 30 kV using successively lower milling currents of 1 nA, 600 pA, 300 pA, and 140 pA until the contrast from the SE beam (Fig. 2.15 d) became electron transparent (Fig. 2.15 e) at ~7 kV. A final cleaning step was conducted at 5 kV and 100 pA for even gentler milling and to remove any surface damage that may have occurred during the higher energy milling steps. The final thickness of the thinned lamella was typically less than 100 nm, as shown in Fig. 2.15 (f).

Thin foil samples were primarily characterized in a Tecnai TF-30 transmission electron microscope (TEM), as shown in Fig. 2.14 (c), using an accelerating voltage of 300 keV. For conventional imaging, bright field (BF) and dark field (DF) imaging modes were used to characterize microstructure and to obtain selected area electron diffraction patterns (SAED). BF and high-angle annular dark field (HAADF) imaging was performed in scanning TEM (STEM) mode to characterize grain structure, particle boundaries, and to obtain higher phase contrast. EDS was also performed under STEM imaging mode by tilting the sample to 17° towards the EDS detector, which has a short working distance of 1 mm. High resolution TEM (HRTEM) was performed at extremely high magnifications (>900 kX) to characterize nanoscale features, such as particle-substrate and particle-particle interfacial structure.

EBSD was used to characterize samples mounted in cross-section and on samples lifted out by FIB and gently cleaned but not thinned to electron transparency, while transmission Kikuchi diffraction (TKD or t-EBSD) was performed on samples thinned to electron transparency. TKD data was acquired using a working distance of approximately 3 mm, an accelerating voltage of 30 keV and a step size of 30 nm, while the samples were tilted to -20° with respect to the electron beam. TKD is often used to improve the spatial resolution compared to conventional EBSD. Scans were taken with an exposure time between 0.25-0.35 ms or set to a minimum value while the Kikuchi patterns were still visible. After correcting for background, the indexed patterns were optimized by selecting a region of interest that minimized the mean angular deviation of the bands, i.e., maximized the goodness of fit, and the solutions were refined. The final EBSD/TKD maps were cleaned up by removing wild spikes and zero solutions using nearest neighbor correlation set to no more than 5 neighboring pixels.

EBSD and TKD were used to characterize the grain structure (using band contrast maps, or BC) of the electrolytic soft Cr powder before and after impact, as well as to evaluate the changes in the grain structure of the substrate in the interfacial regions after impact. Inverse pole figure (IPF) maps give information on grain size, orientation, and texture according to a bcc or hcp crystal structure. Grain orientation spread (GOS) and grain reference orientation deviation (GROD) maps were used to assess the average misorientation within grains of the Cr coating and Zr-alloy substrate [107,154,155]. GOS maps were generated by displaying the average of the misorientation angles to the grain mean orientation, so grains in GOS maps are displayed as one color representing the extent of misorientation. The GROD maps were generated by first selecting a reference orientation within each individual grain and plotting the misorientation (in degrees) from the reference. Blue pixels show regions within the grain that are close to the reference orientation, while a gradient from green to yellow to red indicates higher levels of misorientation within the grain, revealing increased levels of strain and plastic deformation. Grains that are uniformly blue represent recrystallized grains.

Kernel average misorientation (KAM) maps were used to assess plastic deformation within deformed particles and mechanically tested samples. KAM maps were generated by selecting the average misorientation between each data point and its nearest neighbors. KAM is higher in deformed grains due to local lattice distortion, deformation, and high dislocation density, and is restricted to misorientations less than 5°. Geometrically necessary dislocation (GND) maps were generated from the KAM maps by including the Burgers vector for bcc Cr, a/2 <111>. The GND maps were analyzed to obtain a mean and maximum value for the estimated dislocation density within the particles and coatings. In the case of Cr particles impacting Cr substrates, the Cr substrates were separated from the maps so that the dislocation density represented that of only the Cr particles.

A Malvern Panalytical Empyrean X-ray diffractometer (XRD) with Cu-Kα radiation, shown in Fig. 2.14 (d), was used to identify phases in feedstock powders, as-deposited coatings, and coatings after high temperature oxidation and autoclave corrosion tests. Diffraction peaks are produced during X-ray radiation of a material if the Bragg condition ($n\lambda = 2dsin\theta$) is satisfied, where n is the diffraction order, λ is the X-ray wavelength (1.54 Å for Cu-Kα), d is the inter-planar spacing of the crystal lattice, and θ is the incident angle between the X-ray and the scatter plane. Diffraction peaks were acquired from 20° to 120° in coupled 2θ mode using a scanning line 1D detector. DIFFRAC.EVA software (Bruker, USA) was used to analyze the diffraction data by removing background and using its phase matching capabilities.

2.6. Residual stress measurements

Typically, compressive residual stresses exist in cold spray coatings primarily due to mechanical (peening) effects. Several techniques have been used by researchers to characterize residual stresses including XRD, hole drilling, wafer curvature, or neutron diffraction. In this research, XRD using the $\sin^2\psi$ method was employed using the Malvern Panalytical Empyrean XRD shown in Fig. 2.14 (d).

A strain-free material is associated with a certain inter-planar spacing (i.e., *d-spacing*) that will produce a characteristic diffraction pattern using XRD [156], as defined by Eqn. 2.10 for cubic materials. When a material is strained, elongations or contractions are produced within the crystal lattice which changes the inter-planar spacing of the {hkl} lattice planes. This induced change in d will cause a shift in the diffraction pattern, shown in Eqn. 2.11, and by precise measurement of this shift the strain within the material can be deduced.

$$\frac{1}{d^2} = \frac{h^2 + k^2 + l^2}{a^2} \qquad \textit{Eqn. 2.10}$$

$$\varepsilon_{\phi\psi} = \frac{d_{hkl} - d_0}{d_0} \qquad \textit{Eqn. 2.11}$$

Assuming a plane-stress condition, i.e., $\sigma_z = 0$, residual stresses can be determined from measured residual strains using Hooke's law: $\sigma_y = E\varepsilon_y$. In the $\sin^2\psi$ method, strains are considered in terms of inter-planar spacing and can be used to evaluate residual stresses according to Eqn. 2.12:

$$\sigma_\phi = \frac{E}{(1+\nu)\sin^2\psi}\left(\frac{d_\psi - d_n}{d_n}\right) \qquad \textit{Eqn. 2.12}$$

where E and ν are the Young's modulus and Poisson's ratio, respectively, of the material, ϕ is an angle in the plane of the sample between a fixed direction and the diffraction plane normal, and ψ is an angle between the normal of the sample and the normal of the diffracting plane. Therefore, by measuring the d-spacing of the material at multiple ψ-tilts (positive and negative) and at least three directions ($\phi = 0°, 45°, 90°$), one can calculate the full stress tensor for the sample. For a simpler analysis, Eqn. 2.12 can be simplified to analyze the stress near the coating surface:

$$\sigma_\phi = \left(\frac{E}{1+\nu}\right)m \qquad \textit{Eqn. 2.13}$$

where m is the slope of the d *vs.* $\sin^2\psi$ curve.

Residual stress measurements of cold spray Cr coatings on Zry-4 were performed using the sin$^2\psi$ technique by closely mirroring the procedure outlined by Fitzpatrick et al. [156] and in accordance with ASTM standards on aligning the diffractometer [157], determining X-ray elastic constants [158], and measurement of stresses [159]. XRD scans were taken at $\phi = 0°, 45°, 90°$, where $\phi = 0°$ represents the spray direction and $\phi = 90°$ is normal to the spray direction in the plane of the coating. At least five ψ-tilts were used, both positive and negative, ranging from 0 to 0.4. Thus, a total of 30 measurements were performed for each sample. Measurements were taken using Cu Kα radiation and the {220} plane in Cr. Higher d-spacing planes are desirable for the sin$^2\psi$ method because they are more sensitive to shifts in inter-planar spacing.

Following acquisition, the data was analyzed using a specially written code in MATLAB for residual stress analysis. Each of the 30 peaks was smoothed using Pearson VII fitting profiles, the Kα_2 doublet was stripped, and corrections were performed for Lorentz polarization and absorption effects [156]. Following this, *d vs. sin*$^2\psi$ plots were generated and the slopes of the three curves were used in Eqn. 2.13 to calculate residual stresses in the three principal directions. A snapshot of this process is shown in Fig. 2.16.

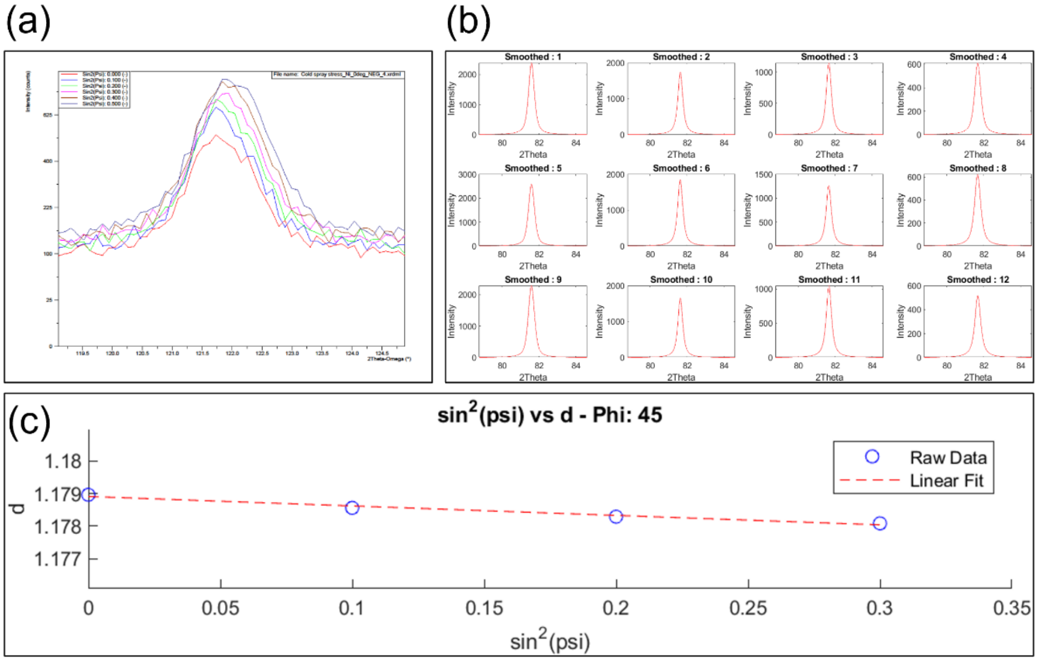

Fig. 2.16. Process of measuring residual stress in cold spray Cr coatings: (a) acquiring diffraction peaks at different ψ-tilts represented by the differently colored curves; (b) peak fitting, smoothing, and polarization corrections; (c) plotting d vs. $\sin^2\psi$ to get the slope used to calculate residual stress.

2.7. Hardness testing

Hardness testing (both microhardness and nanoindentation) was performed on feedstock Cr powders, cold spray Cr coatings, and associated substrate materials mounted in cross-section for an initial assessment of mechanical properties, and in the case of coatings also as a measure of work-hardening and densification. Microhardness indents were made using a Buehler Micromet II indenter equipped with a Vickers indentation tip and a 50-100 gf load, after calibrating with on a standard steel block of pre-calibrated hardness provided by Buehler. Indents were made in the middle of the coating thickness and in compliance with ASTM E92 [160] and E384 [161] standards.

Hardness measurements of the Cr feedstock particles, Cr coatings, and Zr-alloy substrates mounted in cross-section were also performed via nano-indentation using a Bruker Hysitron TI 950 TriboIndenter. Nano-hardness values were collected using a standard Berkovich diamond tip with a constant area function and a standard load transducer. All indentations were performed using constant segment times, following a trapezoidal load function with a maximum load of 10 mN. Hardness values were corrected for compliance of the mounting material according to the method proposed by Slagter et al. [162]. Nano-indentation of the Cr coatings often resulted in pile-up, a phenomenon in which material plastically deforms and “piles up” along the sides of an indent resulting in an increase in indentation area. In these cases, the indents were observed in the SEM to acquire the real contact area, which was used to correct hardness and modulus values after testing. A full description of the nano-indentation procedure, including corrections and study of pile-up phenomenon, can be found in the work by Quillin et al. [163].

2.8. Mechanical test methods

High energy synchrotron X-ray diffraction in the transmission mode was performed *in situ* during uniaxial tensile testing to understand the deformation and cracking behavior of cold spray Cr-coated Zr-alloy specimens in both the as-deposited and annealed conditions. Testing was performed at the Advanced Photon Source (APS) facility located at Argonne National Laboratory (ANL). The technique was deemed particularly useful for the present study because of the importance of a holistic understanding the deformation behavior of the bimetallic system, particularly the effects of the Cr coating on the deformation behavior of the Zr-alloy cladding. In light of this, it is noted that testing the deformation of the coating and the substrate separately would not yield realistic results for the coated cladding application due to the relief of stresses in coating and the exclusion of effects of coating-substrate adhesion on the overall deformation behavior. The fracture surface of the specimens was examined using SEM. Both elastic and plastic deformation mechanisms during tensile deformation were quantified using detailed X-ray line profile analysis. More details of the experiment and results from this study are described in Section 7.

2.9. Micro-mechanical test methods

Cold spray Cr coatings on Zr-alloy cladding were subjected to post-deposition treatments to simulate various microstructures the coating may experience during prototypical reactor environments and potential accident exposures. Microcantilever beams with a pentagonal cross-section were fabricated at the Cr-Zr interface in the as-deposited, low-temperature annealed, high-temperature annealed, and ion irradiated conditions using PFIB and FIB milling techniques. The cantilevers were subjected to beam bending tests at Los Alamos National Laboratory using a picoindenter contained inside of an SEM with *in situ* video capabilities. Cantilever beams were bent to failure or until a maximum displacement was reached. Deformation, cracking, and fracture behavior were qualitatively assessed using *in situ* and *ex situ* SEM imaging as well as EBSD mapping. More details of the experiment and results from this study are described in Section 8.

2.10. Autoclave corrosion testing in simulated PWR environments

Hydrothermal corrosion testing was performed on Cr-coated and uncoated Zr-alloy cladding using a Parr Instruments 4650 autoclave pressure vessel. A photograph of the pressure vessel, heater, and sample holder is shown in Fig. 2.17 (a). The pressure vessel and sample holder are Inconel 625 (a high strength, corrosion resistant nickel-based alloy), while the heater is comprised of conducting coils insulated by a graphite layer. Various components of the autoclave and pressure vessel are shown in Fig. 2.17 (b). The pressure vessel can reach a pressure of 34.5 MPa at a temperature of 500 °C, which is measured by a pressure transducer and a B-type thermocouple, respectively. The entire autoclave setup is enclosed by a safety shield during testing and is operated by the reactor controller connected to a computer that could be monitored remotely (Fig. 2.17 c).

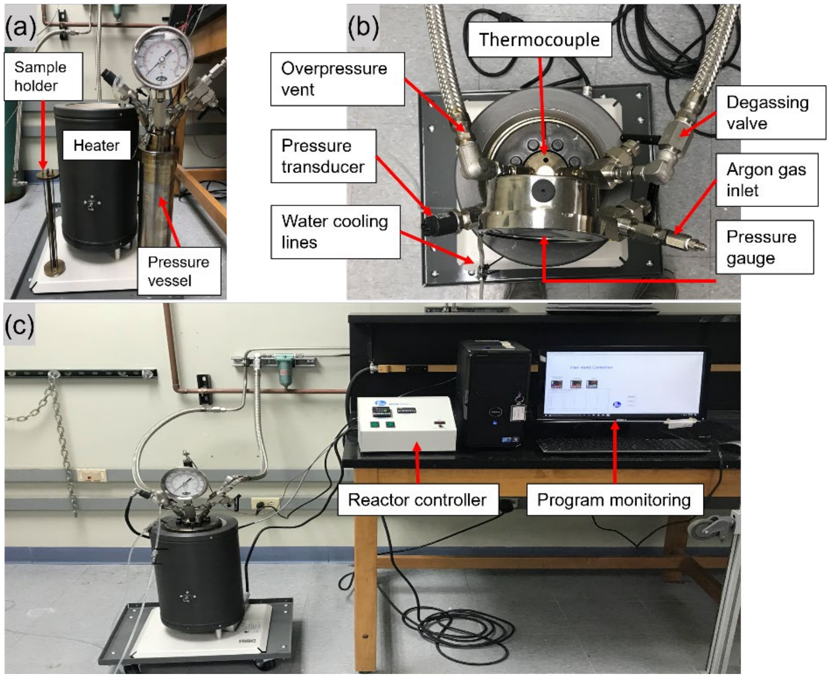

Fig. 2.17. Photographs of the pressurized water autoclave assembly: (a) disassembled heater, pressure vessel, and sample holder; (b) top-down view of the pressure vessel assembly, with relevant components labeled; (c) Entire assembly, including reactor controller and program monitor.

The autoclave test for a water environment followed the ASTM-G2 standard [164], using static (non-refreshing) deionized water and running at a temperature and pressure of 360 °C and 18.6 MPa, respectively, for a minimum of 72 hours and up to 30 days. Dissolved oxygen content in the deionized water was measured according to ASTM [165] and US-EPA [166] standards. Water was placed in an approved 300 mL biochemical oxygen demand (BOD) bottle and dissolved oxygen content was measured using a luminescent dissolved oxygen (LDO) sensor with an integrated stirring system, in accordance with ASTM

Method C [165]. Pure water placed in the autoclave has less than 5 ppm dissolved oxygen. At the start of each corrosion test, the water is heated to just below boiling (93 °C), where it is degassed further by bubbling argon gas for roughly 6 minutes. Measurements performed after the degassing step showed less than 1.5 ppm dissolved oxygen. With a volume of 1000 mL, the pressure vessel could hold up to 24 samples at a time. The samples were placed in Inconel 625 baskets connected to the sample holder, both of which were conditioned in the autoclave (prior to sample insertion) to passivate the surface.

The length, width, and thickness of each sample was measured using a digital micrometer (0.001 mm resolution). The samples were weighed before and after the autoclave test with a high-accuracy scale (1×10^{-6} g resolution) to determine the mass change due to corrosion. The weight change of the samples was determined by normalizing the mass change with respect to the exposed surface area of the sample (i.e., mg/dm^2). For Cr coated samples, only one side was coated. Therefore, uncoated Zr-alloy coupons were included in the autoclave tests to isolate the weight change induced by the Cr coating alone. Weight change of the Cr coating was calculated using the following equation:

$$\Delta W_{Cr} = \Delta W_{sample} - \left(\frac{\Delta W_{Zr-alloy}}{A_{Zr-alloy}}\right)(2lt + 2wt + lw)_{Zr-alloy} \qquad \textit{Eqn. 2.14}$$

where ΔW is the weight change (in mg), $A_{Zr-alloy}$ is the surface area of Zr-alloy (in dm^2), and $l, w,$ and t represent the dimensions of the coated Zr-alloy coupon. ΔW_{Cr} is then determined by dividing by the surface area of the coated surface to calculate the weight change per unit area.

Weight change of the cold spray Cr coatings were compared to the Zr-alloy substrates to assess the enhanced performance of the coating in simulated PWR conditions (360 °C, 18.6 MPa) using pure water chemistry. To more accurately simulate the PWR water chemistry, similar tests were performed with uncoated and Cr-coated Zr-alloy in the autoclave facility at WEC. These tests were performed at 360 °C, 18.6 MPa for 30 days in static (non-flowing) water within a stainless steel 316 autoclave. The water contained 70 ppm of dissolved Li and its dissolved oxygen concentration was estimated to be <3 ppb. In both tests, incremental weight change measurements and photographs were taken to produce at least three data points for each sample. A total of 30 samples were tested, 15 in pure water (UW) and 15 in elevated lithium water (WEC). The results from this experiment are described in Section 9.

2.11.High temperature oxidation testing and annealing treatments

High temperature oxidation tests for Cr-coated Zr-alloy cladding were conducted in both air and steam environments at temperatures ranging from 1100 to 1330 °C (for exposure times up to 60 minutes) to evaluate the stability of the coatings during a LOCA-type scenario. Preparation of the samples was described in Section 2.3.9. High temperature steam oxidation testing was performed in an alumina tube furnace (MTI, model GSL1600X) shown in Fig. 2.18, with a schematic diagram of the testing procedure shown in Fig. 2.19. The samples were placed in a quartz boat attached to a NiCr wire (Fig. 2.20 a), which was moved to Zone 1 (Fig. 2.19) within the furnace. The furnace was then heated to the desired temperature while Ar (g) flowed through the furnace to prevent any oxidation during the heating stage. Once heated, the temperature was checked by inserting a K-type thermocouple into the center of the heating zone. After the desired temperature was achieved, the steam generator was turned on. Steam was generated using deionized water flowing through stainless steel coil surrounded by heater tapes. This produced steam flowing at a velocity of ~64 cm/s and a temperature of ~500 °C. At this stage, the sample was moved to Zone 2 (hot zone in Fig. 2.19) by pulling the NiCr wire. The Ar (g) valve was closed and the steam valve was opened, allowing steam to flow through the furnace. At the end of the desired exposure time, the samples were moved to Zone 3 (Fig. 2.19), the steam valve was closed and the Ar (g) valve was re-opened to prevent further oxidation and heating of the sample while the furnace cooled to room temperature.

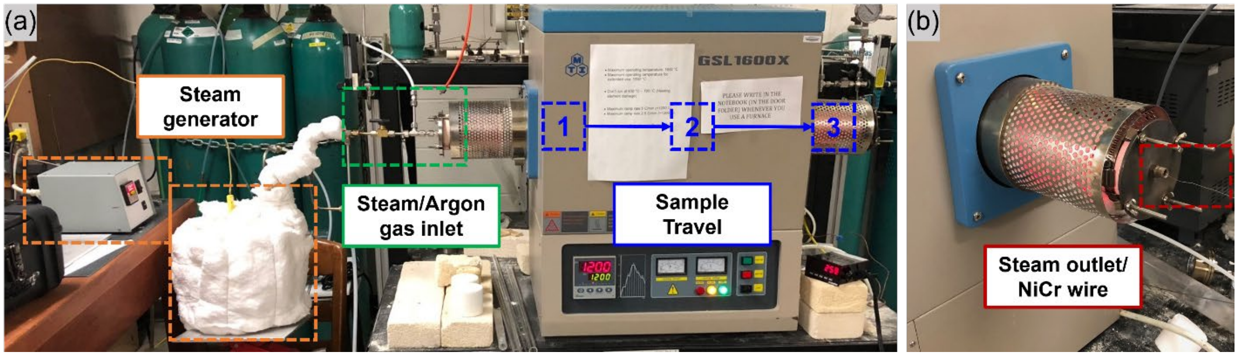

Fig. 2.18. (a) Photograph of high temperature steam oxidation test facility with components labelled; (b) Photograph of tube furnace exit, showing the red-hot alumina tube, steam outlet, and NiCr wire used to pull sample through tube furnace.

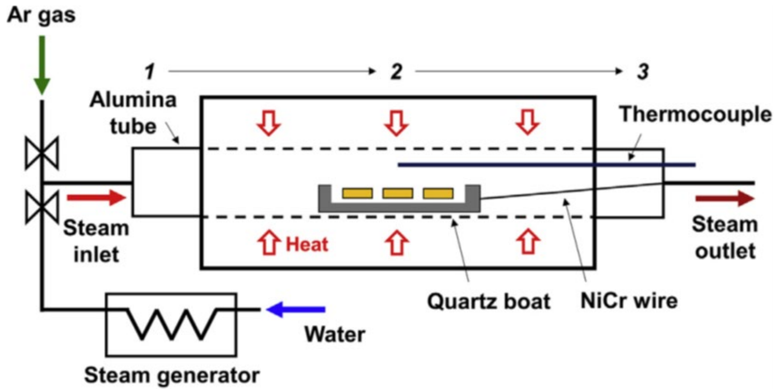

Fig. 2.19. Schematic diagram of the high temperature steam oxidation testing process. The numbers on the top indicate the different sample positions within the furnace.

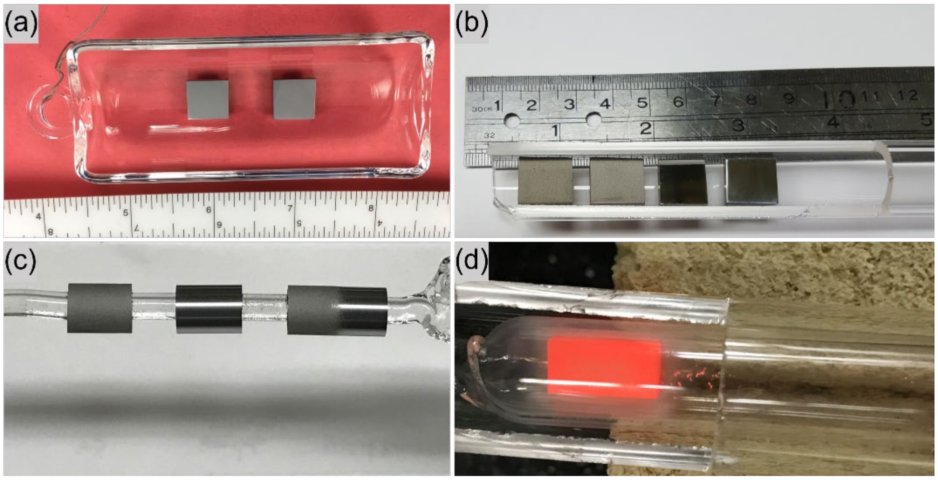

Fig. 2.20. Photographs of Cr-coated Zr-alloy test coupons placed in sample holders for high temperature testing: (a) quartz boat used for steam testing of flat and tube coupons; (b) quartz holder used for air testing flat coupons; (c) quartz holder used for air testing tube coupons; (d) encapsulated flat coupon in a quartz tube showing red-hot surface immediately after removal from furnace.

Using the same furnace, oxidation tests in ambient air environment were also conducted using a slightly different procedure. Flat coupons were placed in a custom quartz sample holder, as shown in Fig. 2.20 (b), while tube coupons were placed on a quartz rod connected to a quartz sample holder, as shown in Fig. 2.20 (c). Once the furnace reached the desired temperature, the quartz sample holder was inserted into the furnace and placed within the hot zone. After the desired exposure time, the quartz holder was removed from the furnace and the samples were allowed to air-cool.

For investigating microstructural changes in the coating and interdiffusion effects at the coating-substrate interface with minimal oxidation effects, the sample coupons were first encapsulated in a quartz ampule, as shown in Fig. 2.21. The system features a two-compartment system, one for Ti sponge oxygen getter and the other for the test samples. The two chambers are interconnected but separated by a thin slice of quartz rod with a slit that allowed gases (i.e., oxygen and argon) to pass through either side. The quartz tube was connected to vacuum, evacuated of air, and then backfilled with Ar (g) until reaching slightly below atmospheric pressure. This process was repeated at least ten times to ensure adequate oxygen removal. Then the quartz tube was sealed just before the vacuum fitting using an acetylene torch. An image of an encapsulated sample immediately after removal from the furnace is shown in Fig. 2.20 (d), illustrating the severity of the high-temperature exposure through the red hot color.

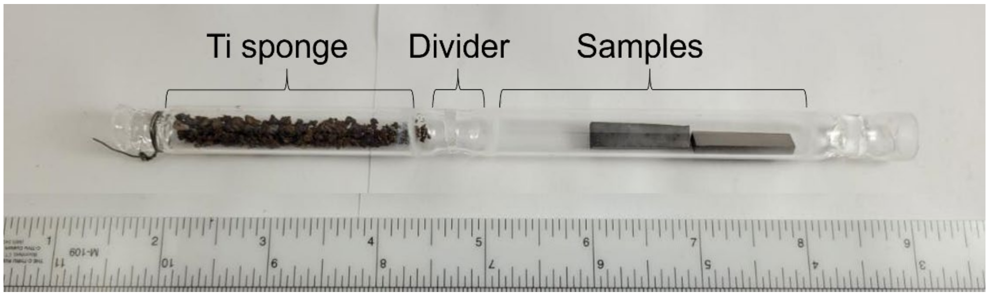

Fig. 2.21. Cr-coated Zr-alloy sample coupons encapsulated in a quartz ampule evacuated of oxygen and backfilled with argon gas. A chamber of titanium sponge was used to getter any residual oxygen in the ampule. A sliver of quartz rod with a slit was used as a divider between the two compartments.

After high temperature exposures in steam, air, or inert environments outlined above, the samples were metallographically prepared by mounting in cross-section. Material characterization using techniques including SEM, EDS, and EBSD were used to assess changes in microstructure, including porosity, grain growth, texture, thickness, composition/phase, morphology of surface oxide layers developed, and the composition gradient and width of inter-diffusion layers.

2.12.Ion irradiation testing

Cold spray Cr coatings on Zr-alloy cladding were subjected to high-energy heavy ion irradiation experiments to assess their overall resistance to irradiation damage. Preparation of the Cr-He coatings on

Zry-4 was described in Section 2.3.6. A photograph of the prepared coating is shown in Fig. 2.22 (a), revealing separate uncoated Zry-4 and Cr coated regions. The Cr coatings were irradiated in the Argonne Tandem Linac Accelerator System (ATLAS) beamline located at ANL. The sample was mounted in a fixture with an attached thermocouple (Fig. 2.22 b) and then loaded into the path of the ion beam (Fig. 2.22 c). The sample was heated to 350 °C and irradiated with 80 MeV Xe^{26+} ions, with an average ion flux of 2.13×10^{12} ions/cm^2/s. Total irradiation time was about 2 hours. The damage accumulation in the materials was predicted to be 30 dpa at a depth of 5.0-5.5 μm from the sample surface using SRIM simulations. Fig. 2.22 (d) shows a photograph of the sample after irradiation with the ion beam profile circled in red, revealing four unique zones of which to perform microstructural characterization.

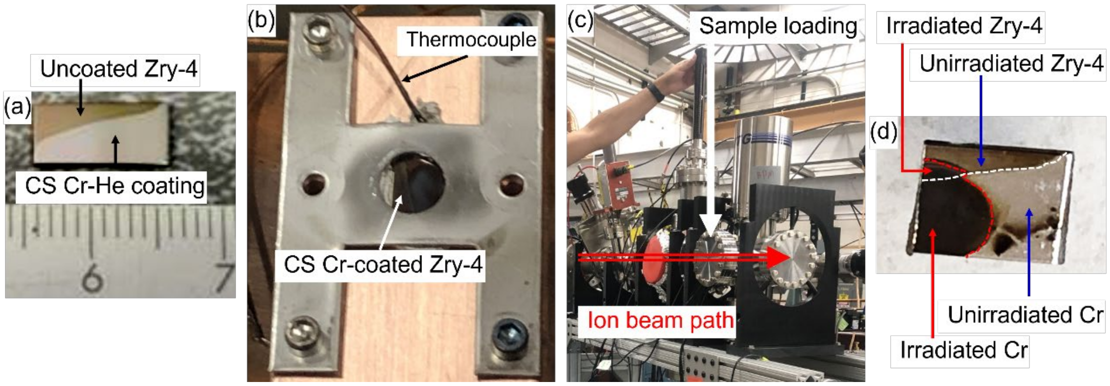

Fig. 2.22. Photographs from the ion irradiation experiment at the ATLAS facility in Argonne: (a) Sample surface, showing region of uncoated Zry-4 and cold spray Cr-He coating; (b) Sample secured to the fixture with an attached thermocouple; (c) Loading the sample into the ion beam path; (d) Sample after experiment, showing four regions that could be used for microstructural characterization.

FIB was used to extract lamellae from four unique locations about the sample, generating four distinct microstructural conditions: unirradiated and irradiated Cr/Zr interface, and unirradiated and irradiated bulk Cr coating. It is worth noting that the unirradiated samples were subjected to the same thermal history as their irradiated counterparts, making for a better comparison than using standard as-deposited coatings. The samples were characterized on the TF-30 using TEM brightfield imaging and STEM BF/HAADF imaging modes to identify irradiation-induced changes in the microstructure and interfacial mixing effects. EDS was performed in the TEM to map elemental composition qualitatively and quantitatively. Nanoindentation was also performed to assess any differences in mechanical properties due to irradiation. The results of radiation damage response in the aforementioned samples are discussed in Section 6.

3. Deposition of Cr Coatings on Zr-alloys by Cold Spray Technology

3.1. Analysis of feedstock Cr powders

Cold spray is a low temperature, solid-state deposition process. As a result, the coating generally retains much of the feedstock powder's microstructure except the effects of plastic deformation. Another attribute of the cold spray process is that the powder itself does not undergo any thermal decomposition or phase transformations (including oxidation) during the coating deposition. Thus, the coating remains compositionally consistent with the starting powder feedstock material. Characterization of the feedstock Cr powder is critical for predicting how the particles will deform, and for predicting how the coating microstructure will develop during high strain rate deformation. Additionally, the characteristics of the feedstock powder particles (i.e., morphology, grain size, hardness, etc.) are strongly related to the powder manufacturing and processing history.

The manufacturing process for the Cr powders used in this study were largely proprietary and, based on the information available, they are referred to as *electrolytic soft* Cr powders. Information provided in this paragraph relating the origins of the microstructure to the manufacturing processing steps should be viewed in general terms. Plan-view SEM images of the as-received Cr powder particles are shown in Fig. 3.1 (a). Higher magnification imaging revealed the particles to be non-spherical, but they displayed rounded edges and a flakey appearance, as shown in Fig. 3.1 (b). Some of these flakes can be seen in cross-section as shown in Fig. 3.1 (c), indicated by the red arrows near the particle edges. The particles were etched using Murakami's reagent (10 g NaOH, 10 g $K_3Fe(CN)_6$, 100 mL H_2O) to reveal microstructural features. A higher magnification image of the particle interior microstructure is shown in Fig. 3.1 (d), taken from the region encompassed by the blue colored box in Fig. 3.1 (c). Within the interior of the particle (lower right of Fig. 3.1 d), the microstructure shows a larger grain with an apparent subgrain structure as well as some micro-porosity (<200 nm diameter). Moving towards the particle edge (upper left of Fig. 3.1 d), these subgrains start to resolve into individual grains as indicated by the darker contrast around the grain boundaries. It is believed that these nanoscale grains formed due to a milling process involved in the powder manufacturing process. The roundness of the particles, however, indicates that the milling process was not severe but repetitious in nature, so as to yield fine grains in the peripheral regions of the particle. The presence of larger grains in the particle interior are reflective of an electrolytic process followed by a high temperature annealing and degassing treatment. For the purposes of this research, it is important to note that the Cr particles contain a heterogeneous grain size distribution with fine grain size on the periphery and coarser grains in the interior of the particle.

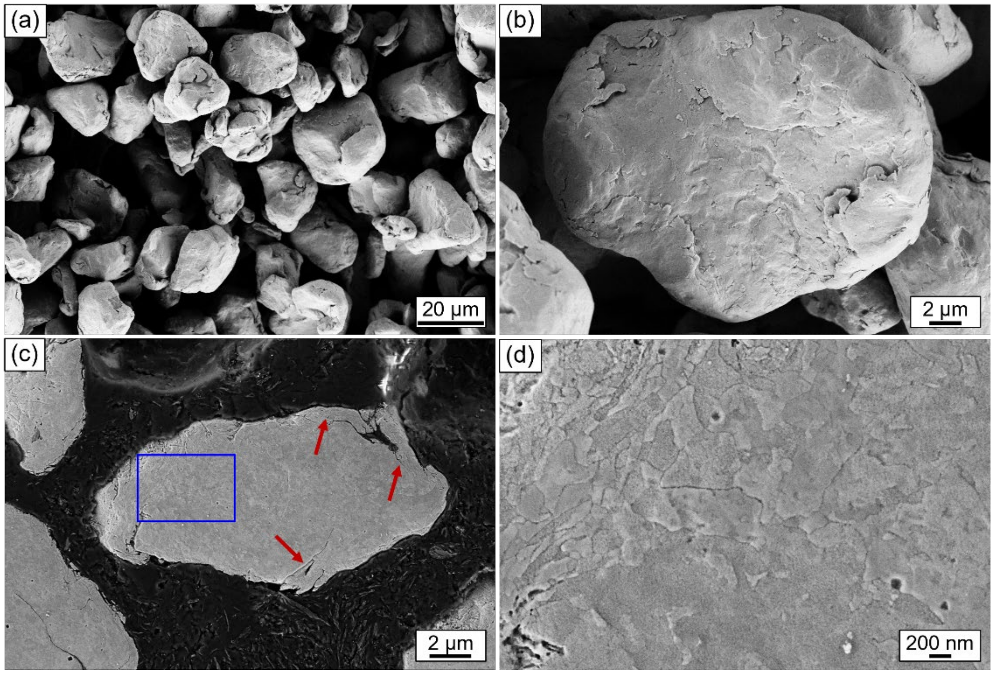

Fig. 3.1. SEM images of electrolytic soft Cr powder used in this research, showing (a) plan-view of non-spherical Cr particles, (b) higher magnification plan-view of Cr particle showing rounded and flakey exterior; (c) cross-section of a Cr particle, with red arrows indicating flakes; (d) high magnification cross section (blue square), showing non-uniform grain size.

3.2. Microstructure of cold spray Cr coatings

3.2.1. SEM characterization of as-deposited Cr coatings

Cold spray deposition of Cr powder on flat Zry-4 substrates was performed to investigate the effects of specific cold spray parameters on coating thickness. Three process gas conditions were selected for this study: (a) 750 °C, 100%-N_2 gas, (b) 550 °C, 75%-He/25%-N_2 gas, and (c) 500 °C, 95%-He/5%-N_2 gas. The gas temperatures reflect the maximum achievable preheat temperature for the specified gas composition. Additionally, two robot traverse speeds were selected for this study: 400 mm/s and 200 mm/s. The rest of the parameters were kept constant, as listed in Section 2.3.1. It was hypothesized that gas temperature, gas composition, and gun traverse (spray) speed had the most influence on coating thickness.

Low-magnification SEM images for the three conditions sprayed at 400 mm/s are shown in Fig. 3.2. All three conditions resulted in full coating coverage over the Zry-4 substrates. The coatings appear very dense with only minor defects and porosity visible at this magnification. No evidence of cracking or delamination along the interface was observed, indicating good adhesion with Zry-4. Fig. 3.2 reveals that gas composition has a large influence on coating thickness. The coating thickness for 100%-N_2 process gas was about 25 μm, and thickness increased by a factor of 2 and 2.5x with the addition of 75%-He and 95%-He to the gas stream, respectively. Increased concentrations of He in the process gas produced markedly higher particle velocities, which resulted in a greater number of particles reaching the critical velocities needed for particle bonding and cohesion, resulting in higher coating thickness. A plot of coating thickness versus particle velocity is shown in Fig. 3.3 for the mentioned gas compositions. A decrease in the gun traverse speed by a factor of 2 also led to roughly doubling of coating thickness for each gas condition. This is due to greater residence time at a given location which results in more particles being deposited per unit area and per unit time.

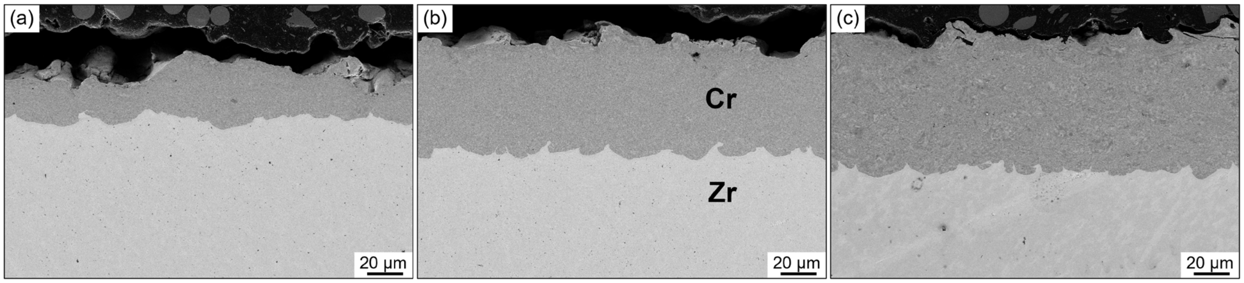

Fig. 3.2. Low magnification SEM images of Cr coatings deposited on Zry-4 using a gun traverse speed of 400 mm/s and the following gas compositions: (a) 100%-N_2, (b) 75%-He/25%-N_2, (c) 95%-He/5%-N_2.

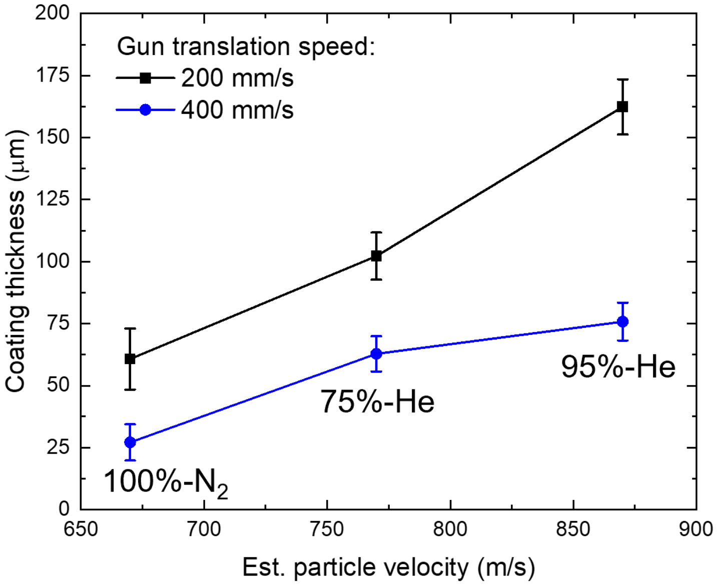

Fig. 3.3. Plot of coating thickness vs. estimated particle velocity for Cr coatings on Zry-4. The data points (left to right) represent the three gas compositions: 100%-N_2, 75%-He/25%-N_2, 95%-He/5%-N_2, respectively.

For a more detailed examination of microstructure, the coatings mounted in cross-section were etched using Murakami's reagent to reveal additional features including porosity, grain size, and inter-particle boundaries. Higher magnification SEM images of the Cr coating deposited using 100%-N_2 gas (henceforth referred to by *Cr-N2*) are shown in Fig. 3.4 (a-b). A continuous Cr-Zr interface is seen in Fig. 3.4 (a), with no cracking or delamination. Etching of the coating revealed inter-particle boundaries (IPBs), faintly highlighted in yellow in Fig. 3.4 (a) to preserve the image contrast. These boundaries are presented as line defects made up of nanoscale porosity surrounding bonded particles. Fig. 3.4 (b) shows an IPB in greater detail within the coating interior, where a graded microstructure is revealed with submicron-sized grains contained within the boundaries and larger grains away from the boundary. It is hypothesized that the interfaces of the colliding particles (which experience the most shear strains) underwent the highest plastic deformation and dynamic recrystallization, leading to grain refinement in the vicinity of these boundaries.

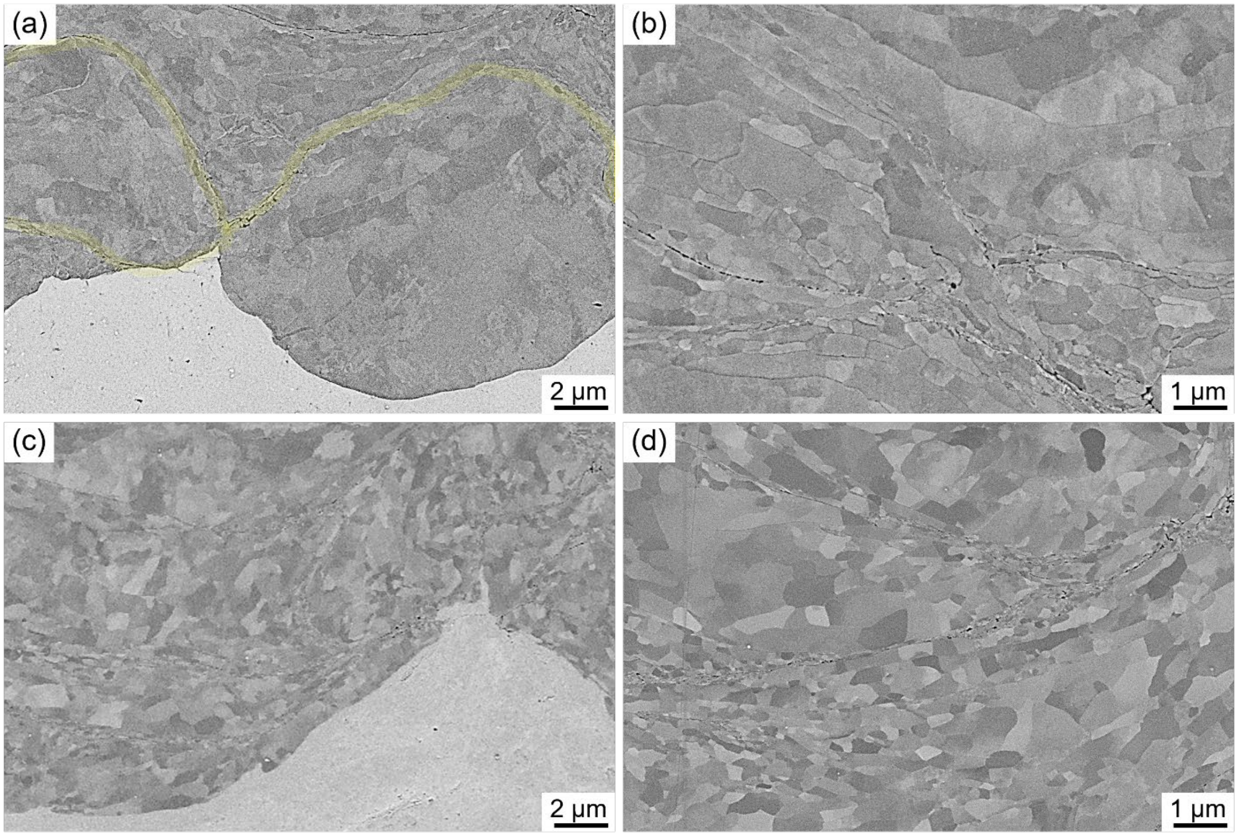

Fig. 3.4. High magnification SEM images of Cr coatings (etched with Murakami's reagent) deposited on Zry-4 using a gun traverse speed of 200 mm/s and the following gas compositions: (a-b) 100%-N_2 a.k.a. Cr-N2, (c-d) 95%-He/5%-N_2 a.k.a. Cr-He. A faint highlighting of inter-particle boundaries is shown in (a).

Higher magnification SEM images of the Cr coating deposited using 95%-He gas (henceforth referred to by *Cr-He*) are shown in Fig. 3.4 (c-d). The coatings sprayed with helium gas also show no evidence of cracking or delamination. Compared to the nitrogen coating, the helium coating reveals a denser microstructure with particle boundaries obscured and more difficult to resolve, an indication of more intimate interparticle bonding and greater grain deformation effects. Fig. 3.4 (d) also reveals a heterogeneous microstructure in terms of grain size. These differences in microstructure stemming from different carrier gases are due to the higher particle velocities achieved with He gas. Firstly, higher particle velocities lead to increased plastic deformation, leading to higher shear strains that can more effectively bond particle boundaries. Secondly, higher velocities mean more particles reach the threshold critical velocity for deposition, per unit area. This results in a "tamping effect" that further deforms and densifies the coating as more particles are deposited. It should be noted that tamping effect in nitrogen cold spray can be enhanced by reducing the gun traverse speed.

3.2.2. STEM characterization of as-deposited Cr coatings

FIB lamellae were extracted from the top surface of the coatings and thinned to electron transparency for higher resolution imaging in the TEM. Fig. 3.5 (a) shows a BF-STEM image of the as-deposited Cr-N2 coating. The heterogeneous microstructure is even more resolved as evidenced by grains up to 2 µm in diameter with a high density of dislocations (Fig. 3.5 b). A few IPBs are observed within the coating, and Fig. 3.5 (c) shows one of these boundaries consists of strained and elongated grains up to 1 µm in length but under 300 nm in width. Fig. 3.5 (d) shows the tail-end of one of these particle boundaries, revealing dynamically recrystallized grains less than 100 nm in diameter. No porosity was found within the thin lamellae, suggesting a very dense Cr-N2 coating with well bonded interparticle interfaces.

Fig. 3.6 (a) shows a BF-STEM image of the as-deposited Cr-He coating, revealing a similar heterogeneous, highly strained microstructure. Fig. 3.6 (b) shows a higher magnification image near an IPB, which clearly shows the transition from the evolution of larger equiaxed grains to elongated grains to dynamically recrystallized grains as one moves towards the center of the boundary. This is also illustrated in the selected area electron diffraction (SAED) patterns shown in Fig. 3.6 (c-e), taken from regions encompassed by the blue circles shown in Fig. 3.6 (b). The SAED pattern from area (c) shows several spots that indicate the beam interacted with only a few grains (i.e., larger grains). The spots are roughly 5 nm^{-1} away from the center of the pattern which corresponds to an interplanar spacing of 0.208 nm and the (110) family of planes for Cr [167]. The spots become more frequent and align themselves into rings in area (d), indicating that more grains were captured by the electron beam (i.e., nanocrystalline grains). Even more spots were observed in the SAED pattern from area (e), indicating a high density of ultrafine grains. This clearly indicates substantial grain refinement as the area of beam interaction was the same for all three locations, and the distance of the spots and rings from the center of the pattern did not change, confirming that the diffraction pattern corresponds to bcc Cr and no other phases.

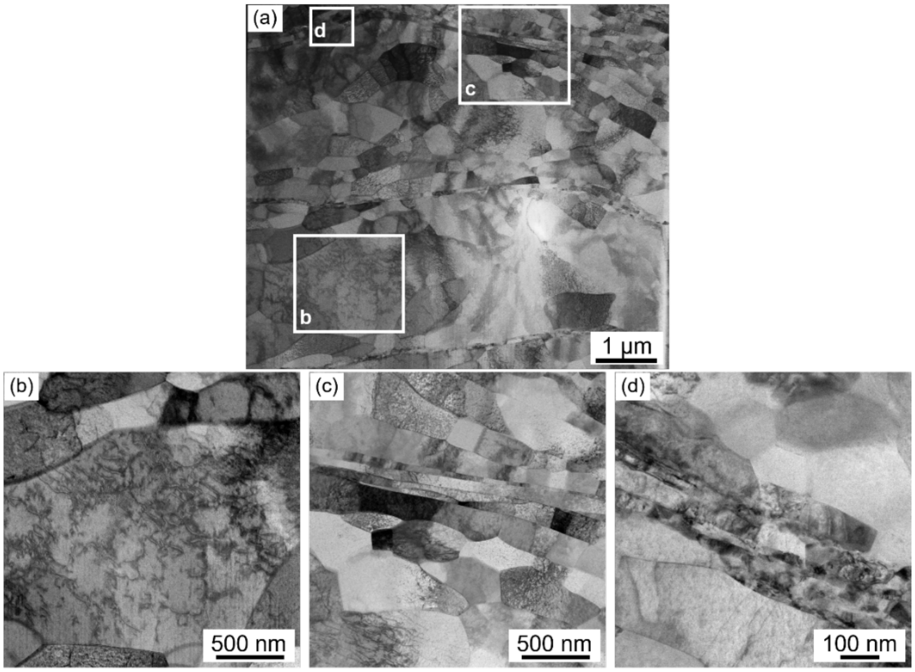

Fig. 3.5. (a) BF-STEM image of the Cr-N2 coating, with selective areas of the coating imaged at higher magnification: (b) large grain containing high density of dislocations; (c) strained and elongated grains located at an inter-particle boundary; (c) dynamically recrystallized grains located at the tail end of an inter-particle boundary. The images illustrate the heterogeneous nature of the cold spray Cr coating microstructure.

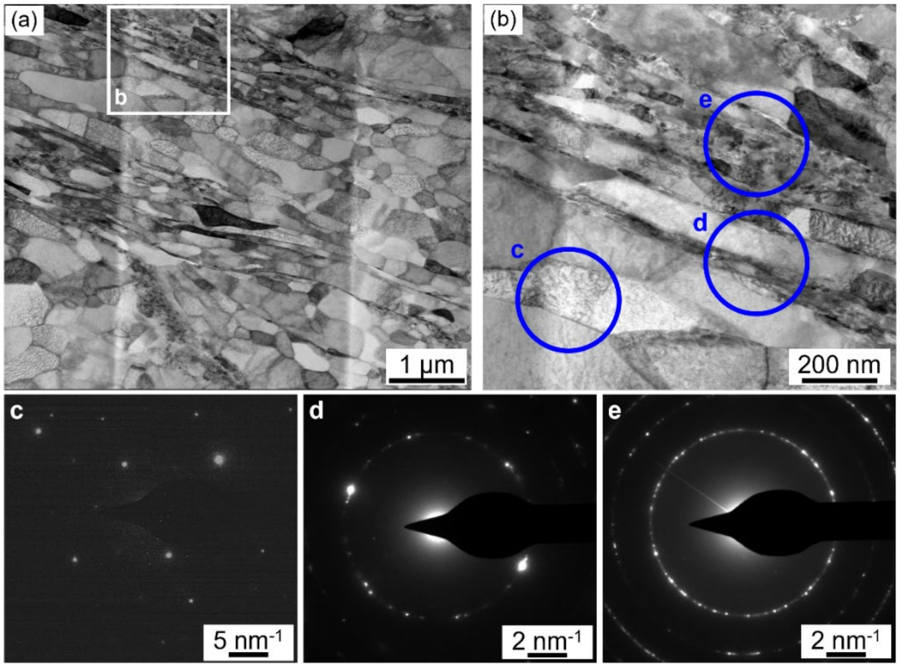

Fig. 3.6. (a) BF-STEM image of the Cr-He coating showing a similar heterogeneous microstructure in terms of grain size. (b) Higher magnification BF-STEM image near an IPB. (c-e) SAED patterns illustrate the evolution of grain refinement across the boundary, transitioning from spots (c) to sparsely populated rings (d) to heavily populated rings (e).

A FIB lamella was also lifted out from the Cr-Zr interface for TEM analysis. Fig. 3.7 (a) shows a BF-STEM image of the Cr-Zr interface for a Cr-He coating deposited on Zry-4. The interface is clearly observed demarcating the Cr coating (lighter contrast) and Zry-4 substrate (darker contrast) bonded in intimate contact. Two regions were selected for higher resolution imaging. Fig. 3.7 (b) shows a high magnification image captured within a particle boundary, showing ultrafine dynamically recrystallized grains less than 100 nm in diameter, but a heterogeneous distribution of grain sizes. The associated SAED pattern indicates many grains were sampled by the electron beam in this region. Fig. 3.7 (c) shows a high magnification image of the Zry-4 substrate near the interface, also showing ultrafine dynamically recrystallized grains less than 100 nm in diameter. However, the grains in the Zry-4 show a more equiaxed microstructure, likely due to more uniform high strain rate plastic deformation over a larger contact area. The associated SAED pattern shows more rings due to the lower symmetry of hcp Zr planes and many more spots, indicating sampling of many grains [167]. It is interesting to note that such level of refined grains was not observed within the Cr side of the interface (Fig. 3.7 a), and this finding will be explored further in Section 4.

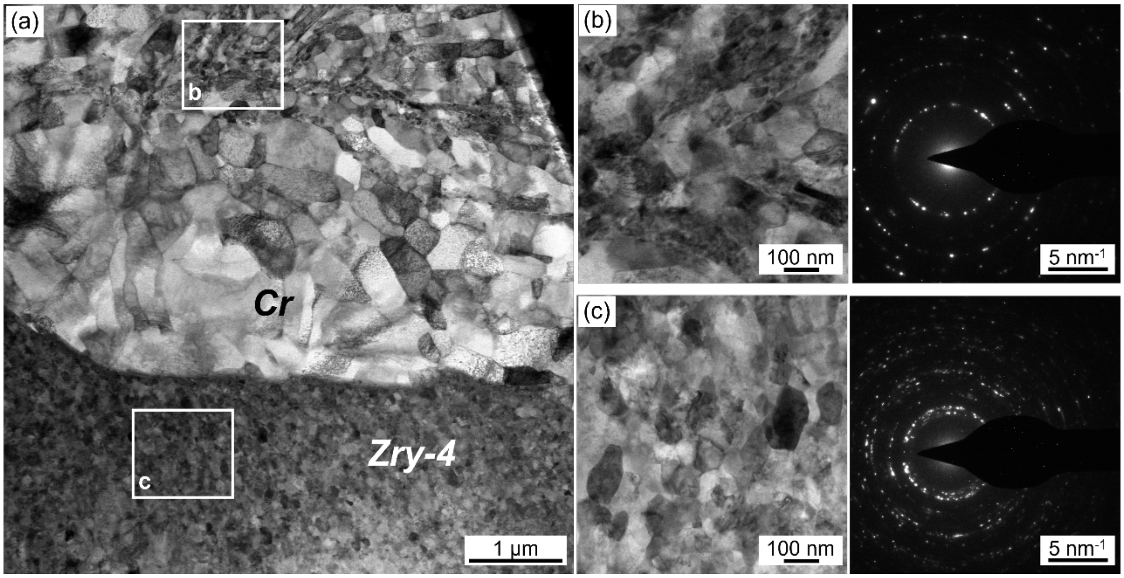

Fig. 3.7. (a) BF-STEM images of the Cr-Zr interface for a Cr-He coating deposited on Zry-4, with selected areas imaged at higher magnifications showing; (b) recrystallized grains in the Cr coating, with associated SAED pattern; (c) recrystallized grains in the Zry-4 substrate, with associated SAED pattern.

3.3. X-ray diffraction of feedstock powder and deposited Cr coatings

XRD was performed to confirm no phase change or oxidation of the feedstock powders occurred during cold spray deposition. Fig. 3.8 shows XRD scans of the electrolytic soft Cr powder and cold spray deposited coatings, revealing pure bcc Cr peaks and no additional oxide phases, indicating that deposition occurred at relatively low particle temperatures. A slight peak shift was observed in the coatings with respect to the standard d-spacings of Cr, indicating that some residual strain was present. Peak broadening, which can arise from non-uniform micro-strains and small crystallite size [168], was observed in both powder and coatings; however, the magnitude of broadening did not increase with increasing gas velocity. In past experiments, peak broadening was observed after depositing coatings with gas-atomized [34] and annealed electrolytic [137] Cr particles, which contained very low internal strain. Higher resolution measurements of residual stresses within the electrolytic soft Cr coatings are discussed in Section 3.5.

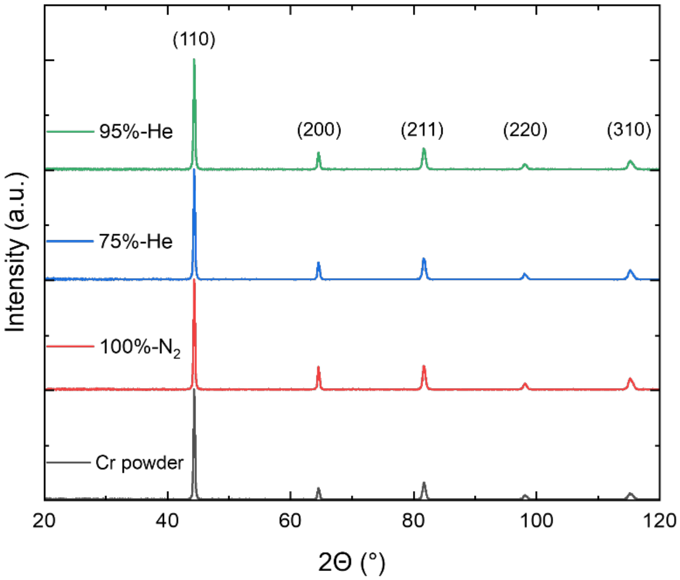

Fig. 3.8. XRD of the electrolytic soft Cr powder and corresponding cold spray Cr coatings, showing no phase changes occurred during the deposition process. All patterns matched to pure bcc Cr.

3.4. Hardness of feedstock Cr powder and deposited Cr coatings

Hardness measurements of the feedstock Cr powder, Zr-alloy substrates, and resultant Cr coatings were performed to assess the extent of plastic deformation resulting from cold spray deposition, and the results are shown in Table 3.1. The cold spray Cr-He coating and Zry-4 had hardness values of 384 $HV_{0.1}$ and 180 $HV_{0.1}$, respectively. Although not a focus of this study, this result suggests that the hard Cr coating can potentially increase the grid-to-rod fretting resistance Zr-alloys. Previous studies (by other members of the author's group) on pin-on-disk wear testing of cold spray Cr coatings showed 70% reduction in wear track width and 85% reduction in wear track depth compared to uncoated Zr-alloy cladding [169].

Table 3.1. Hardness testing results of feedstock Cr powder, Zry-4 substrate, and cold spray Cr-He coating.

Sample	**Microhardness ($HV_{0.1}$)**	**Nano-hardness (GPa)**
Electrolytic soft Cr powder	n/a	3.9 ± 0.2
Zry-4 substrate	184 ± 5	1.8 ± 0.1
Cr-N2 coating	363 ± 17	5.0 ± 0.8
Cr-He coating	384 ± 20	6.4 ± 1.1

Table 3.1 also shows results from nano-indentation testing. Hardness of the coatings increased to 5.0-6.4 GPa from the initial hardness of the Cr powder (3.9 GPa), indicative of work-hardening. These finding confirm that the as-fabricated feedstock Cr powder contained appreciable capacity for plastic deformation. Cr powders can show a wide range in hardness depending on the manufacturing route and using a softer Cr powder (with hardness much lower than the coating) increases the deformation capacity and deformability of the particles, allowing denser coatings to be achieved. The larger standard deviation for the Cr coatings compared to the feedstock Cr powder results from the heterogeneous nature of coating microstructure. Therefore, the nanoindentation results provide a reasonable representation of the average hardness of the Cr coatings. Fig. 3.9 shows a cross-sectional SEM image of the nano-indents within the Cr-He coating. Particle boundaries were harder compared to particle interiors (due to the deformation being concentrated at the boundaries), resulting in smaller indents. Meanwhile, nano-indents within particle interiors were larger and showed more evidence of pile-up, indicating higher ductility [163]. Thus, nano-indentation is another technique that can demonstrate the heterogeneous nature of cold spray coatings.

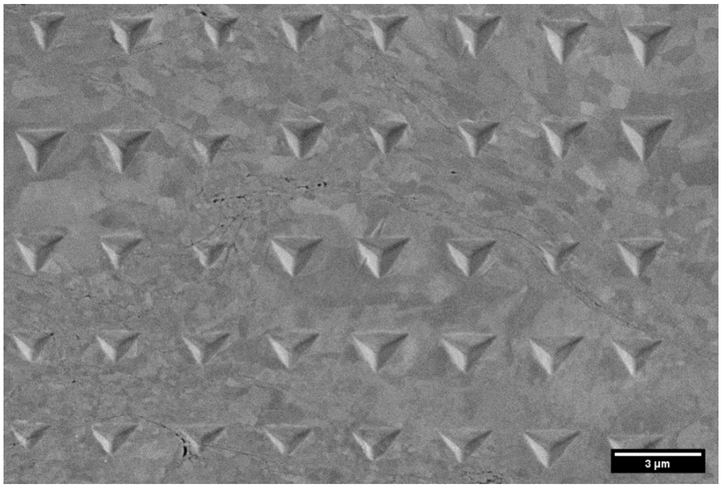

Fig. 3.9. SEM image of the Cr-He coating in cross-section with nano-indentations. Some of the indents have "rounded" edges, evidence of pile-up. Indentation size also varies depending on location, indicating a heterogeneous coating microstructure.

3.5. Residual stress measurements of deposited Cr coatings

Compressive residual stresses in cold spray coatings arise from the tamping effect of the particles [170]. These stresses are generally beneficial as they delay the initiation of cracks during straining events. Residual stresses in the coatings deposited using 100%-N_2, 75%-He, and 95%-He carrier gas compositions were measured using the XRD $\sin^2\psi$ method described in Section 2.6, and the results are shown in Table 3.2. Values represent stresses at the surfaces of the coatings and are limited by the penetration depth of the X-rays (<5 µm) in Cr. Compressive residual stresses in the as-deposited Cr coatings increased from 329 MPa to 400 MPa, indicating increasing helium gas (i.e., higher particle velocities) can enhance the compressive residual stress state of the Cr coatings. The results also show that the XRD $\sin^2\psi$ method is more sensitive to revealing residual stresses than analyzing peak shift from standard 2θ scans.

Table 3.2. Surface residual stresses in cold spray Cr coatings, measured using the XRD $\sin^2\psi$ method.

Process gas condition	**Surface compressive residual stresses (MPa)**
100%-N_2	329 ± 21
75%-He	397 ± 35
95%-He	400 ± 21

4. Coating Formation and Bonding Mechanisms in Cold Spray Deposition of Cr on Zr-alloy

4.1. Single-particle impact experiments of Cr on Zr-alloy and pure Cr substrates

4.1.1. Experimental description

An important aspect of understanding coating formation in cold spray is the impact velocity of the particles [95,108]. Particles must attain a critical velocity to sufficiently deform and adhere during impact with the substrate. The fraction of particles that get deposited vs. those that rebound off the substrate (i.e., the deposition efficiency, or *DE*) is estimated via, $DE = \Delta m_s / M_p$, where Δm_s is the change in mass of the substrate and M_p is the mass of all particles that have interacted with the substrate [90]. Alternatively, deposition efficiency can be measured using the expression $DE = n_p/(n_p + n_c)$, where n_p is the number of deposited particles and n_c is the number of impact craters from rebounded particles. This can be accomplished in cold spray by using a low powder feed rate and increasing the gun traverse speed to deposit individual particles on the substrate.

Single particle impact experiments are insightful as both critical velocity and deposition efficiency can be directly measured, and the deformation behavior and bonding characteristics of the impacted particles can be subsequently characterized individually [101–107]. For example, Hassani et al. [101] investigated a number of metallic particle/substrate combinations and identified three primary deformation behaviors, namely splatting, co-deformation, and penetration. Collectively, these deformation behaviors can result in metallurgical or mechanical bonding, or a combination thereof [111]. In that experiment, the former was typically favored for mechanically similar materials, while the latter was common with mechanically dissimilar materials [101]. According to these studies, hardness and density were the initial metrics for mismatch and, generally, smaller differences in these properties leads to improved particle-substrate bonding [100].

For the Cr cold spray deposition on Zry-4, we envision a two-stage process. First, high velocity bcc Cr particles impact an hcp Zry-4 substrate (i.e., the Cr-Zr system) resulting in high strain rate plastic deformation at the colliding interfaces, which promotes adhesion of the particles to the substrate. Second, subsequent high-velocity Cr particles impact on the initially deposited and work-hardened Cr layer (i.e., the Cr-Cr system) resulting in interparticle cohesion and coating buildup.

Nanoindentation of the feedstock Cr powders and microhardness measurements of the Zry-4 and bulk Cr substrates were performed in accordance with the procedure described in Section 2.7. STEM and HRTEM were used to characterize the cross-sectional microstructure of the feedstock Cr particles, as well as the interfacial bonding between the coatings and the substrates. After single particle impact experiments, characterization of the bonded Cr particles was performed using a PFIB with SEM and EDS. Plan-view SEM images of the impacted single particles were captured for each velocity condition at five unique standardized locations taken about 2.5 mm from the center of the spray plume. For the Cr particles deposited on Zry-4 substrates, EDS was used to distinguish the bonded Cr particles from impact craters on the Zry-4 substrate surface. For the Cr particles deposited on Cr substrates, individually bonded particles and craters were counted for each image using ImageJ software. The deposition efficiency was calculated as the ratio of the total number of bonded particles to the sum of the total number of bonded particles and impact craters.

PFIB was also used to section out individually bonded Cr particles on the Zry-4 and bulk Cr substrates. The particles were lifted out and attached to a conductive Cu grid where they were lightly thinned on the FIB using successively lower ion-beam milling currents to create a smooth cross-sectional surface. EBSD was used to characterize the impacted single particles and substrates, while TKD was used to characterize a feedstock Cr particle and a Cr-He coating, both of which were previously thinned to electron transparency for STEM analysis. The procedures for EBSD and TKD mapping were described in Section 2.5 along with a description of the various mapping techniques.

4.1.2. Characterization of feedstock Cr powder

A BF-STEM image of a Cr particle (Fig. 4.1 a) shows the presence of large grains in the center of the particle with contrast coming from a dislocation forest (Fig. 4.1 b). Smaller, deformed grains were observed at the particle edges (Fig. 4.1 c), likely due to a mechanical milling process involved in manufacture of the powders. Fig. 4.1 (d) shows a thin (<10 nm) native oxide layer on the particle surface. While the presence of this oxide layer can potentially hinder bonding during deposition, it is thought that reaching sufficient impact velocities could fracture and eject the oxide layer upon impact to create the clean metallic surfaces necessary for bonding [111].

The TKD maps shown in Fig. 4.1 (e-g) further reveal the grain structure of the Cr particle. The IPF shows a graded microstructure, with a large grain (>5 μm) in the center of the particle and smaller grains closer to the particle edges. The GROD map in Fig. 4.1 (f) highlights ultrafine grains along the particle surface with GROD < 1°, indicating that these grains resulted from recrystallization during mechanical milling. The GROD map also reveals misorientation gradients within the slightly larger grains, with a maximum GROD of 35°. The KAM map in Fig. 4.1 (g) shows low levels of strain in the grain interiors and increasing levels of strain closer to grain boundaries. These boundaries align with areas of higher dislocation contrast observed in the STEM images.

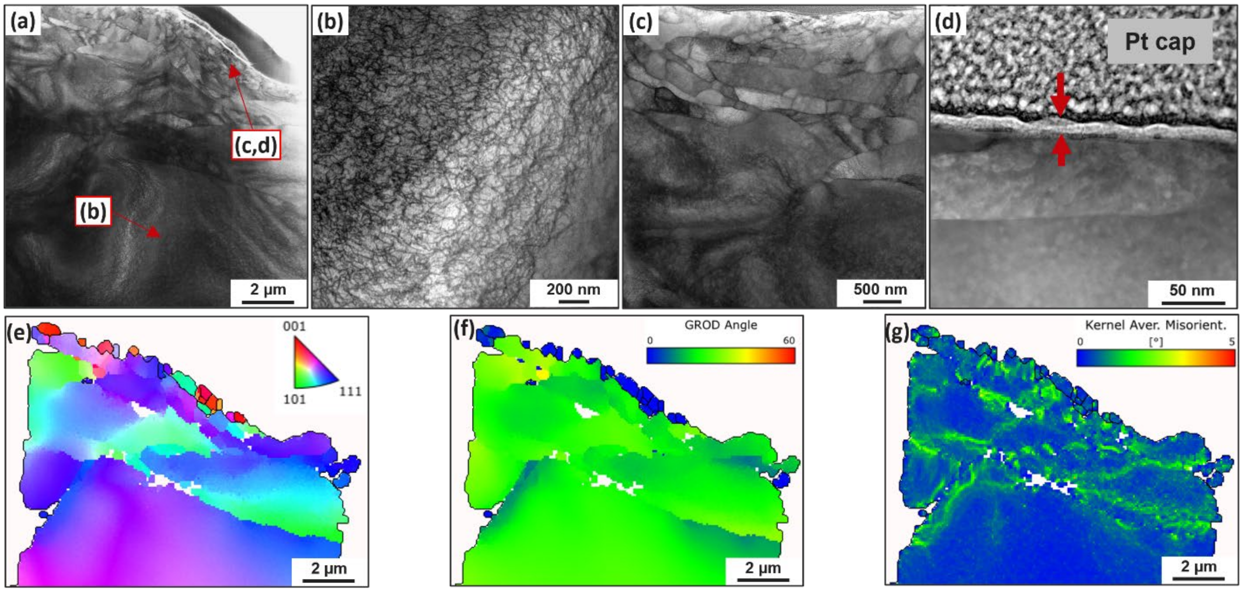

Fig. 4.1. (a) BF-STEM image of Cr particle in cross-section; (b) BF-STEM image within large interior grain, showing a dislocation forest; (c) BF-STEM image showing deformed, submicron grains near particle surface; (d) HAADF STEM image showing native oxide layer (<10 nm) on particle surface, as indicated by the red arrows; on the bottom row, TKD mapping of a Cr particle showing (e) IPF, (f) GROD, and (g) KAM.

Nanoindentation measurements of the Cr particles revealed an average hardness of 4.1 ± 0.2 GPa. The Vickers microhardness values of the Zry-4 and bulk Cr substrates were determined to be 180 ± 4 and 145 ± 6 $HV_{0.1}$, respectively.

4.1.3. Single-particle impacts: deposition efficiency and critical velocity

SEM plan-view images of deposited Cr particles on Zry-4 substrates for increasing impact velocities are shown in Fig. 4.2 (a-c). All velocity conditions resulted in plastic deformation of the substrate, as evidenced by deformation bands on the substrate surface surrounding the particle. EDS mapping (shown in Appendix A) revealed some of the craters contained remnants of impacted Cr particles, possibly from the detachment of flakes near the surface of Cr particles. At the low velocity condition ($v_p \sim 580\ m/s$), it is believed that a fraction of the kinetic energy was consumed in the detachment of flakes upon impact, resulting in less energy for bonding and low deposition efficiency. Hassani et al. [101] observed similar effects in the deposition of single Ti particles on Cu, in which partial detachment occurred due to suspected elastic rebound forces breaking the bonds near the critical velocity [118,119]. This phenomenon is discussed in more detail in Appendix A.

Fig. 4.3 (a) shows a plot of deposition efficiency vs. particle velocities for both the Cr-on-Zr and Cr-on-Cr systems. The DE of Cr on Zry-4 is about 25% at the lowest velocity condition ($v_p \sim 580\ m/s$), and signs of localized jetting was observed in various regions around the bonded particle. As the particle velocity increased to the medium condition ($v_p \sim 680\ m/s$) the DE approached 100%, meaning no impact craters were observed above this impact velocity. At this point, jetting of the Zry-4 substrate was present along most of the periphery of the particles and the magnitude of the jetting increased with particle velocity. This would both enhance metallurgical bonding at the Cr-Zr interface and promote mechanical interlocking. This observation with the Cr-on-Zr system is consistent with other dissimilar metal systems consisting of a hard particle and a relatively soft, lower density substrate [100,101].

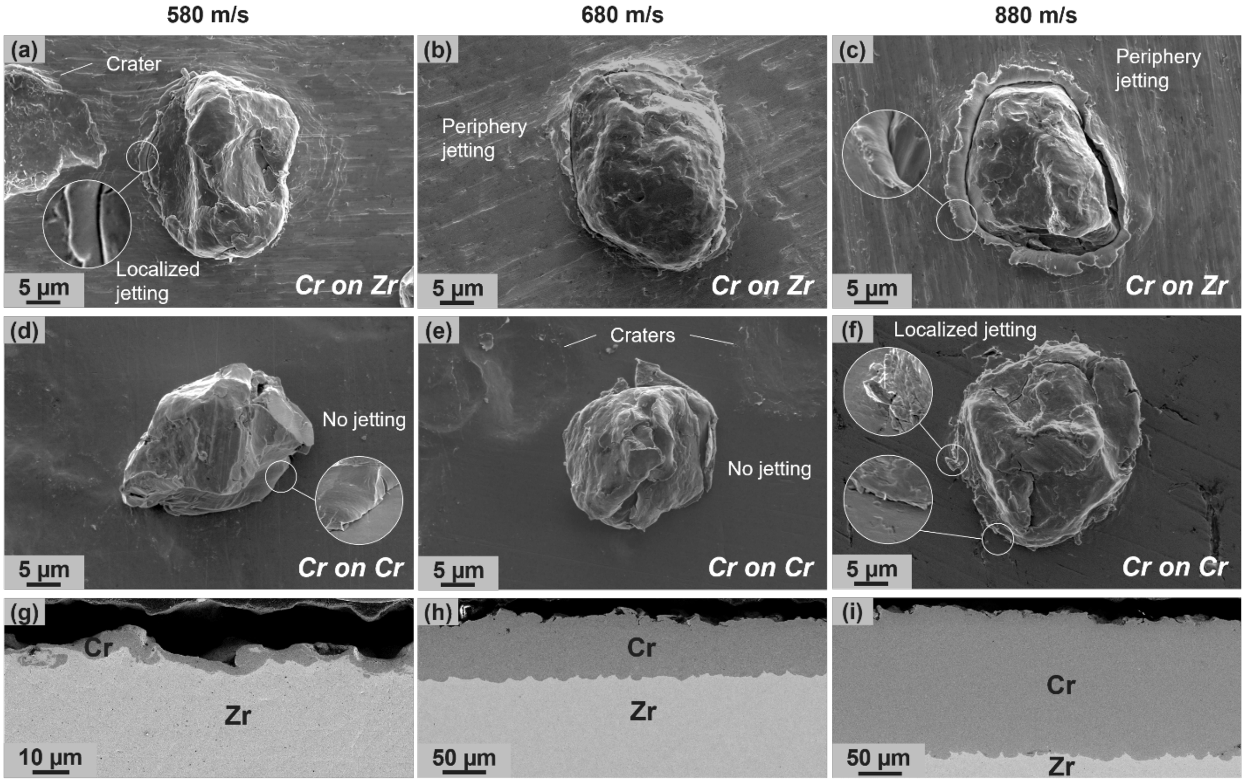

Fig. 4.2. SEM images of single Cr particle deposition at 580, 680, and 880 m/s (using 2000 mm/s gun translation speed): (a-c) Cr particle impacts on Zry-4 substrates; (d-f) Cr particle impacts on bulk Cr substrates; (g-i) cold spray Cr coatings on Zry-4 substrates deposited using 200 mm/s gun translation speed. A few craters captured in the images are labeled. Insets in (a-f) show magnified images of jetting at the periphery of the particles.

The Cr-on-Cr system revealed a different particle morphology after impact. Plan-view SEM images of Cr particles deposited on pure Cr substrates using increasing velocities are shown in Fig. 4.2 (d-f). The low and medium velocity conditions revealed little to no plastic deformation of the bulk Cr substrate, while some deformation bands indicative of plastic deformation appear on the substrate at the highest velocity. The inset in Fig. 4.2 (d) shows the particle resting atop the substrate with no visible particle or substrate jetting ($v_p \sim 580\ m/s$). Meanwhile, signs of localized jetting of either the particle, substrate, or both were observed in Fig. 4.2 (f) for the high velocity condition ($v_p \sim 880\ m/s$). The impact craters on the pure Cr substrates were smoother than those observed on the Zry-4 substrates and no partially bonded Cr particles were observed. The maximum DE for Cr-on-Cr was 35%, which was achieved at a velocity of 880 m/s.

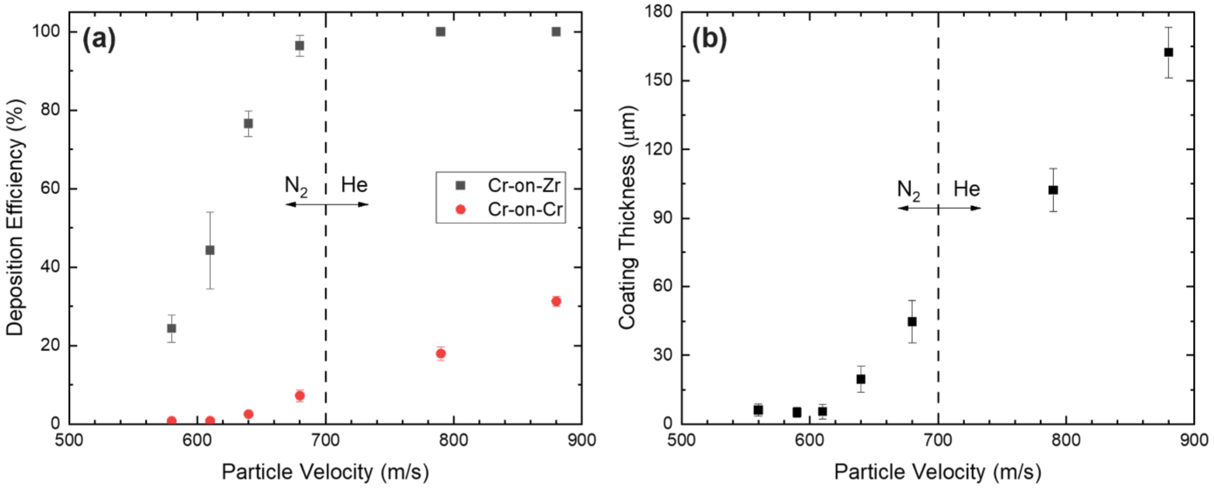

Fig. 4.3. (a) Plot of deposition efficiency vs. particle velocity for Cr on Zry-4 and Cr on pure Cr; (b) Plot of coating thickness vs. particle velocity for Cr on Zry-4; The dotted line indicates a transition from 100%-N_2 carrier gas to a N_2/He carrier gas mixture.

4.1.4. Deformation microstructures in impacted Cr particles

Fig. 4.4 shows representative FIB cross-sections of bonded particles. Starting with the Cr-on-Zr system (Fig. 4.4 a-c), the Zry-4 substrate deforms more than the Cr particles, as indicated by the depth of particle penetration into the substrate. In the low velocity condition (Fig. 4.4 a), trans-particle cracking and incomplete bonding (marked by blue arrows) can be seen both within the Cr particle and along the Cr-Zr interface, respectively, indicating inadequate particle velocity. For the medium and high velocity conditions, no particle cracking nor substrate debonding was observed, indicating that complete bonding was achieved. As the Cr particle velocity increased, the Zry-4 substrate experienced enhanced plastic flow eventually leading to substrate jetting (indicated by red arrows in Fig. 4.4). While all conditions resulted in some amount of substrate jetting, increasing velocity led to a more robust mechanical interlocking of the particle and the substrate.

Fig. 4.4 (d-f) shows the Cr-on-Cr system after particle impact. In this case, shallow penetration depth of Cr particles and negligible jetting of the substrate indicate that the Cr particles deformed more than the pure Cr substrate. Although there is evidence of jetting at the highest velocity condition ($v_p \sim 880\ m/s$), as indicated by the red arrows in Fig. 4.4 (f), it was difficult to discern if this occurred in the particle or the substrate due to the intimate bonding at the interface. As the particle velocity increased a notable transition occurred between 680 and 880 m/s, resulting in deeper penetration of the Cr particle into the substrate leading to co-deformation and associated enhanced contribution from mechanical interlocking.

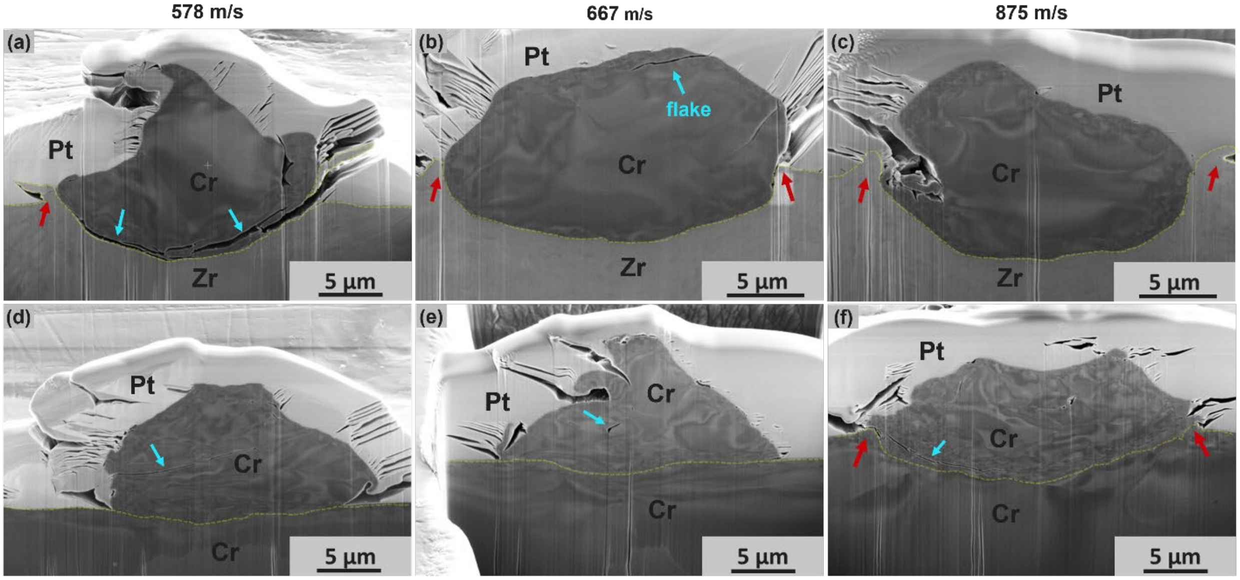

Fig. 4.4. SEM images of bonded particle cross-sections prepared by FIB, showing Cr-on-Zr (top row) and Cr-on-Cr (bottom row) for the following particle velocity conditions: (a,d) 580 m/s, (b,e) 680 m/s, (c,f) 880 m/s. The interface between particle and substrate is overlayed with a dotted yellow line. Red arrows indicate areas of substrate jetting, and blue arrows indicate defects within particles. The crack-like features above the particles represent discontinuities in the deposited protective Pt cap used for preparation of samples by FIB.

The results from EBSD mapping of lamellae lifted out from particles of the Cr-on-Zr system (the same particles shown in Fig. 4.4 a-c) are shown in Fig. 4.5. The IPF maps shown in Fig. 4.5 (a-c) reveal that, for all three velocity conditions, the center of the particles is composed of large grains, while the particle edges consist of smaller sized grains. This is comparable to the initial condition of the representative feedstock (as-received) particle shown in Fig. 4.1 (e). In contrast, the Zry-4 substrate within 2-5 µm of the particle/substrate interface generated rather poor Kikuchi patterns (indicated by white pixels, which could not be indexed) suggesting the occurrence of severe plastic deformation of the Zry-4 substrate. For all impact velocities, the GROD maps in Fig. 4.5 (d-f) reveal relatively low amounts of intragranular misorientation (< 30°) in the center of the particles, with higher misorientation (> 45°) near the edges. Fine recrystallized grains (GROD < 2°) were observed right along the edges of particles deposited at all three impact velocities. The indexed grains within the Zry-4 substrate also appear to be recrystallized, based on nearly all grains showing GROD less than 2°. The KAM maps in Fig. 4.5 (g-i) highlight the strained regions more clearly, with low strain indicated by KAM values below 1° in the central regions of the particles. Regions of higher strain are observed near the edges of the particle, which could be from the powder fabrication process or from the high velocity impact or a combination of the two. The regions of the Zry-4 substrate that were indexed show higher KAM, indicating the substrates were subjected to large amounts of plastic strain.

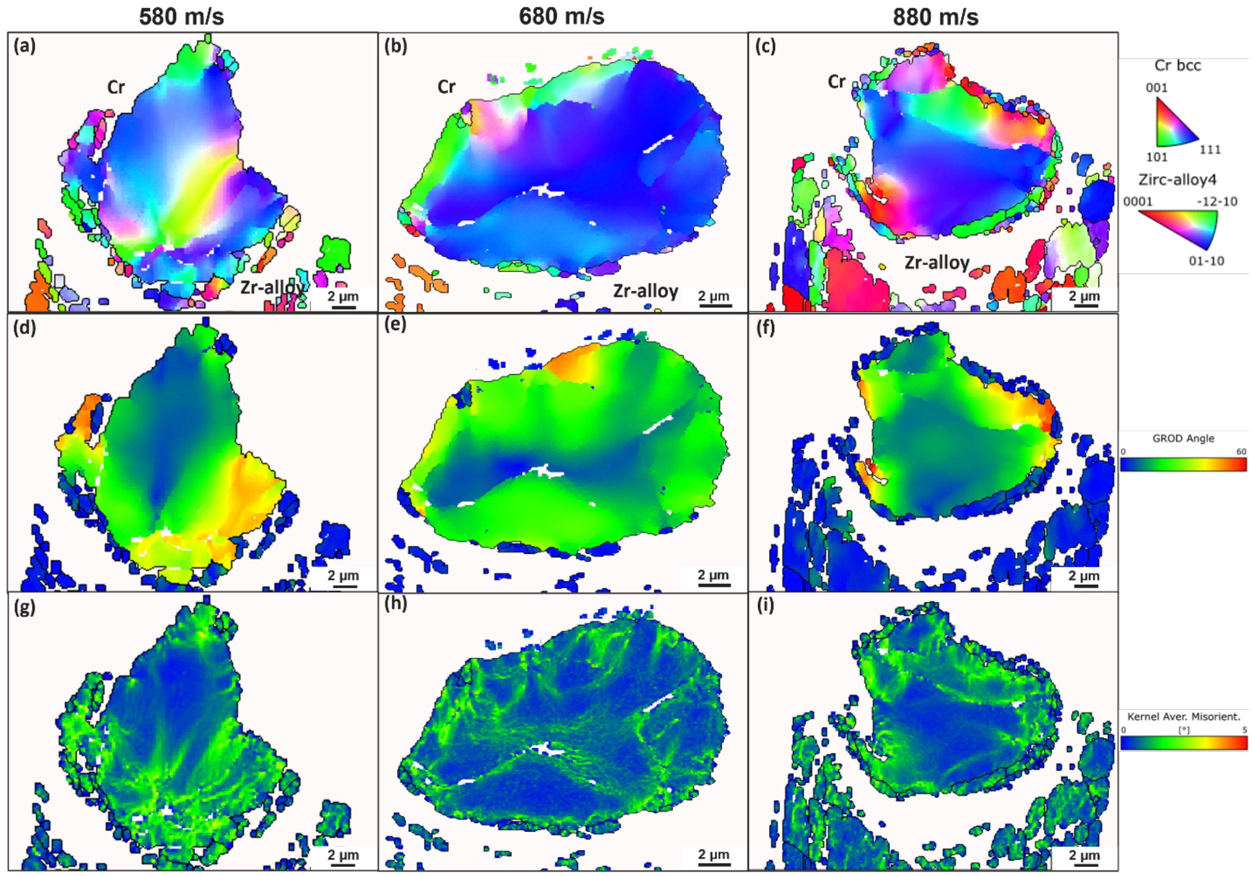

Fig. 4.5. EBSD mapping results for the Cr-on-Zr system deposited at 580 m/s (left column), 680 m/s (center column), and 880 m/s (right column). (a-c) IPFs; (d-f) GROD maps; (g-i) KAM maps.

EBSD maps for the Cr-on-Cr system (from the same particles shown in Fig. 4.4 d-f) are shown in Fig. 4.6. The IPF maps in Fig. 4.6 (a-c) reveal a remarkably different microstructure compared to the Cr-on-Zr system, most notably the grain size decreased within the center of the particles. The GROD maps in Fig. 4.6 (d-f) reveal varying levels of intragranular misorientation within the particles, and the level of maximum misorientation increased with increasing impact velocity. The KAM maps shown in Fig. 4.6 (g-i) reveal the strain within the particles also increases with impact velocity, with regions of KAM > 3° being present both within the particle interior and near the edges. The KAM is also more heterogeneous within Cr particles that impacted Cr substrates. IPF maps reveal that the pure Cr substrate initially contained large grains and low defect density near the surface, while the GROD and KAM maps indicate that a strain gradient began to emerge as the substrate was impacted with particles at higher velocities.

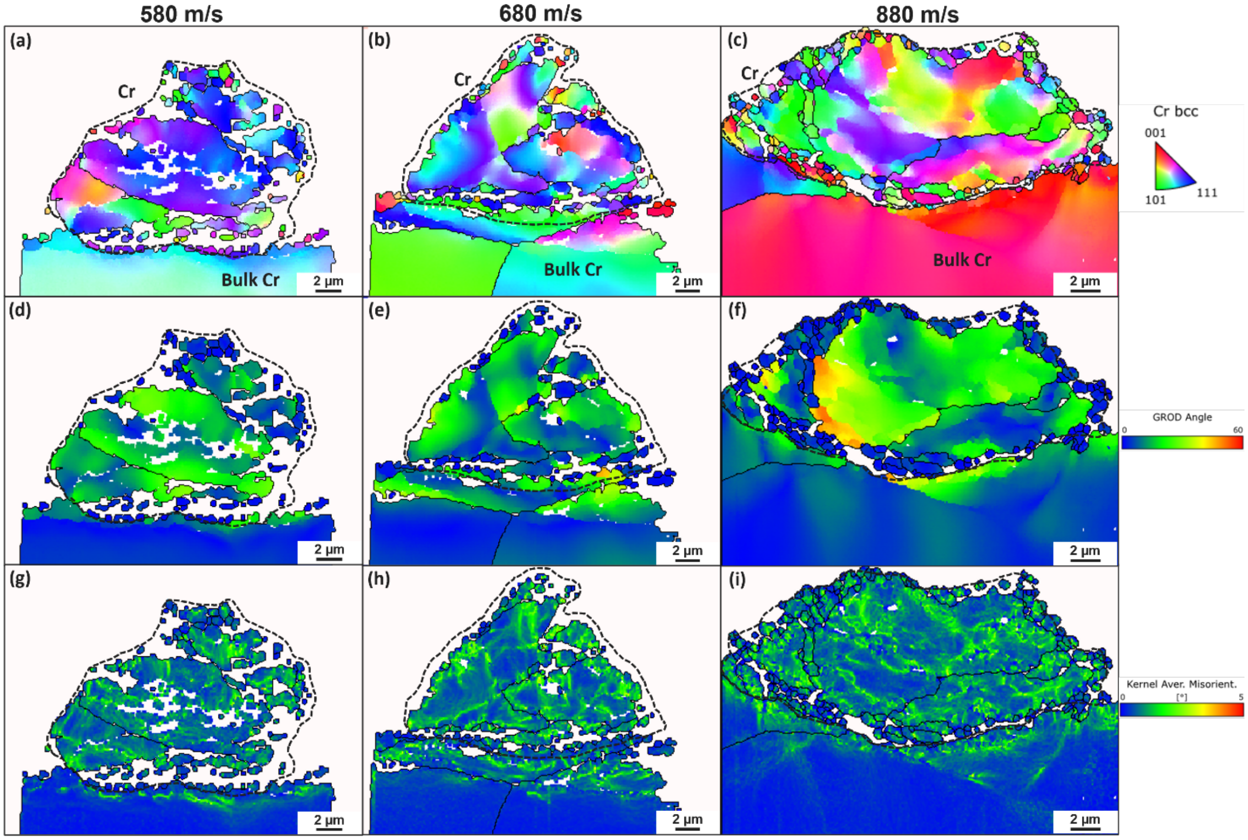

Fig. 4.6. EBSD mapping results for the Cr-on-Cr system deposited at 580 m/s (left column), 680 m/s (center column), and 880 m/s (right column). (a-c) IPFs; (d-f) GROD maps; (g-i) KAM maps.

GND maps were used to quantify dislocation densities within the Cr particles before and after impact, with the average and maximum values shown in Table 4.1. For the Cr-on-Zr system, the average dislocation density was about $1.3 \times 10^{15}/m^2$ and the maximum about $4 \times 10^{15}/m^2$, with no discernable trend with particle impact velocity. For the Cr-on-Cr system, both the average and maximum dislocation density increased with particle impact velocity, with the maximum dislocation density reaching $6.4 \times 10^{15}/m^2$ for the highest velocity condition. This further confirms that the Cr particles experienced greater strain hardening during impact with the pure Cr substrates.

Table 4.1. Dislocation densities (×$10^{15}/m^2$) tabulated for a feedstock (as-received) Cr particle and for Cr particles impacted at 580, 680, and 880 m/s.

	Cr-on-Zry-4		Cr-on-Cr	
Condition	Mean	Max	Mean	Max
As-received	1.27	3.24	1.27	3.24
580 m/s	1.24	3.78	1.26	4.92
680 m/s	1.32	4.62	1.52	5.16
880 m/s	1.27	4.17	1.88	6.38

4.1.5. Characterization of cold spray Cr coatings on Zry-4

Figure 4.7 shows results of TKD mapping for a Cr coating on Zry-4 substrate deposited using 880 m/s particle velocity. The band contrast image of the TKD measurement allows for a clearer visualization (in comparison to EBSD results presented above) of the extent of deformation in the Zry-4. Low band contrast can be seen in the Zry-4 within 1-2 µm of the interface, indicating either a highly strained or recrystallized microstructure, especially within the jet lip. The GROD map in Figure 4.7 (c) picks up some of these very fine (<200 nm) grains of very low misorientation (< 2°) near the interface, indicating that dynamic recrystallization of Zry-4 has occurred. This microstructure is consistent with the single particle EBSD maps shown in Fig. 4.5. This recrystallized microstructure in cold-sprayed Zr-alloy was also observed by Fazi et al. [89], who demonstrated that these grains may be partially recovered through thermal recrystallization via autoclave exposure at 415 °C [37]. Further away from the interface (2-5 µm), the KAM map in Figure 4.7 (d) also reveals a highly strained Zry-4 microstructure (KAM > 3°) but with a larger grain size (>1 µm). Within the Cr coating, the microstructure is also consistent with the EBSD maps shown in Fig. 4.6. Chromium grains near the Cr-Zr interface are larger and contain lower amounts of misorientation and strain compared to grains in the interior of the coating. The variation in grain size, sub-grain microstructure, misorientation, dynamic recrystallization, and strain throughout the Cr coating presents a heterogeneous microstructure, typical of cold spray coatings.

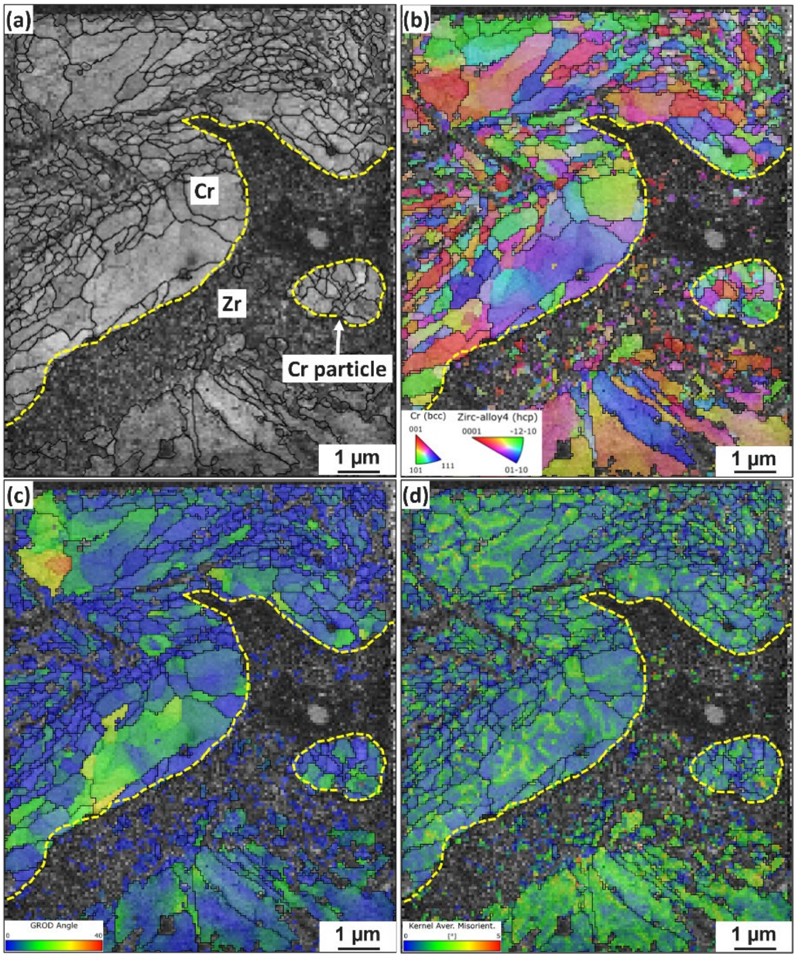

Figure 4.7. TKD mapping results for cold spray Cr coating on Zry-4 deposited at 880 m/s: (a) BC; (b) IPF; (c) GROD; (d) KAM.

Fig. 4.8 (a) shows an SEM image of the polished cross-section of the Cr-Zr interface for the 880 m/s condition (same as coating shown in Fig. 4.2 i), revealing a lightly etched microstructure within the coating. The Cr coating was well bonded to the Zry-4 substrate and there was no evidence of cracking or delamination. BF-TEM images were taken near the Cr-Zr interface, as shown in Fig. 4.8 (b). On the Zry-4 side of the interface, a fine-grained structure was observed, whereas the Cr side of the interface shows larger dislocation-containing grains. The high-resolution TEM (HRTEM) image shown in Fig. 4.8 (c) also reveals a heavily strained contrast which, coupled with the non-indexable regions within the Zry-4 (from EBSD/TKD maps in Fig. 4.5 and Figure 4.7), indicate the Zry-4 experienced dynamic recrystallization in the near-interface region. The HRTEM image also captured continuous planes of atoms across the interface, showing *crystallographic coherency* between the coating and substrate that is indicative of a metallurgical bonding. This suggests that as the near-interface regions of the Zry-4 experience dynamic recrystallization upon impact, the new grains orient themselves to achieve crystallographic coherency with the Cr lattice.

Fast Fourier Transform (FFT) analysis performed on the HRTEM image in Fig. 4.8 (c) confirm alignment of the {0002} basal planes in Zry-4 with the {110} planes in the Cr lattice, indicating a preferred orientation relationship between Cr and Zr. Burgers [171] demonstrated that there exists a crystallographic orientation relationship between bcc and hcp structures, namely, the {110} planes of the bcc lattice are parallel to the {0001} basal planes in the hcp lattice. Wenk et al. [172] demonstrated that the bcc phase can nucleate in highly deformed hcp grains with a heterogeneous microstructure (during the high temperature α↔β phase transformation), and can dominate the texture by preferential growth. Thus, it is plausible that during the high strain rate plastic deformation of Zry-4, in which dynamic recrystallization produced a fine-grained heterogeneous microstructure near the interface, the grains with {0001} orientation aligned themselves with the {110} planes in the Cr lattice. The FFT patterns indicated crystallinity across the entire interface with no evidence of amorphization.

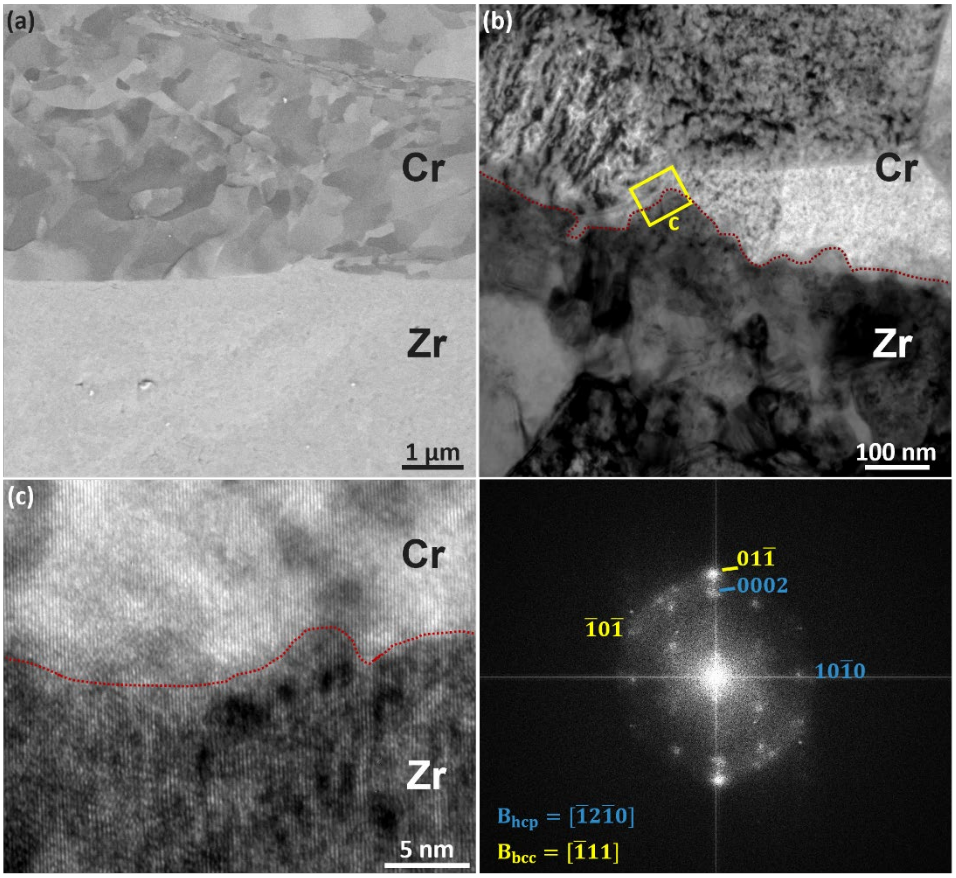

Fig. 4.8. (a) SEM image of Cr-Zr interface for a coating deposited at 880 m/s; (b) BF-TEM image of Cr-Zr interface, showing deformed and fine grains in Zry-4; (c) HRTEM image and associated FFT showing coherency between the Cr coating and Zry-4 substrate across the interface caused by reorientation of grains during dynamic recrystallization in the Zry-4 substrate.

Higher magnification TKD mapping was also performed within the interior of the as-deposited cold spray Cr coating, as shown in Fig. 4.9. The IPF map shown in Fig. 4.9 (a) reveals a heterogeneous microstructure, with grain sizes in the Cr coating ranging from less than 100 nm to 5 µm. The area weighted grain size statistics revealed that over 50% of the grains were below 300 nm in diameter. In Fig. 4.9 (b), over 50% of the grains show GROD below 1°, with a few grains peaking at 12° misorientation. The KAM map in Fig. 4.9 (c) shows much of the Cr coating microstructure contains similar amounts of plastic strain (< 2°), with the highest KAM located near sub-grain boundaries.

The TKD band contrast image in Fig. 4.9 (d) highlights two inter-particle boundaries (appearing as black unindexed points), with the thickness of these boundaries ranging from 400 nm to 1 µm. For a more in-depth examination of these inter-particle regions, BF-STEM imaging was performed in the regions indicated in Fig. 4.9 (d). Within these inter-particle boundaries, two features typical to cold spray deposition can be seen: Fig. 4.9 (e) shows a region with elongated grains originating from high strain rate plastic deformation and shear, while Fig. 4.9 (f) shows a region of dynamically recrystallized grains surrounded by larger, equiaxed grains. The IPBs are tightly bonded throughout the microstructure, indicating high levels of cohesion within the Cr coating.

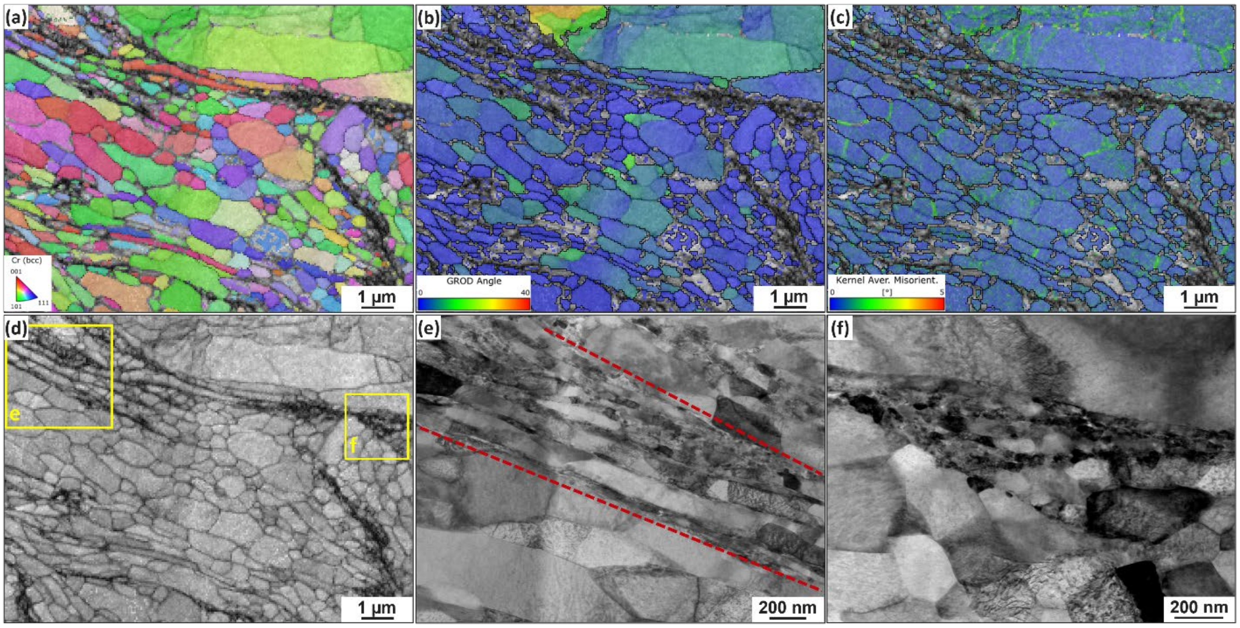

Fig. 4.9. TKD mapping results for cold spray Cr coating deposited at 880 m/s: (a) IPF; (b) GROD; (c) KAM; (d) Band contrast, which highlight inter-particle boundaries (black/low contrast). Selected areas were observed using BF-STEM imaging, highlighting (e) interparticle boundary (red lines) containing elongated grains surrounded by lesser deformed grains; (f) tail end of a particle boundary, showing dynamically recrystallized nano-scale grains.

4.2. Critical velocity and deposition efficiency

Critical velocity (v_{crit}) in cold spray has been defined as the point where either the DE rises from zero, or the DE reaches 50% for a powder with a normal size distribution [97]. Using the first definition of v_{crit}, experimental determination of DE through single-particle impact studies resulted in the identification of two critical velocities for bonding: $v_{crit}^{Cr-Zr}{\sim}540\ m/s$, and $v_{crit}^{Cr-Cr}{\sim}640\ m/s$, as shown in Fig. 4.3 (a), where v_{crit}^{Cr-Zr} was determined by extrapolating the fit to zero. Assadi et al. [100] developed an empirical relationship between a particle's mechanical and thermo-physical properties and the critical velocity for bonding of similar materials:

$$v_{crit} = \sqrt{a\sigma/\rho + bc_p(T_m - T_p)}, \qquad \textit{Eqn. 4.1}$$

where ρ is the density, c_p is the heat capacity, T_m is the melting temperature, T_p is the mean temperature of the particle upon impact, a and b are fitting constants, and σ is the temperature-dependent flow stress, approximated as:

$$\sigma = \sigma_{UTS}\left[1 - \left(\frac{T_p - T_{ref}}{T_m - T_{ref}}\right)\right], \qquad \textit{Eqn. 4.2}$$

where T_{ref} is a reference temperature set as 25 °C. The equation assumes linear thermal softening up to the melting temperature. This approach was used in this study to compare it to the experimentally determined critical velocity for Cr-on-Cr. The values used for Cr include melting temperature (1907 °C), density (7.19 g/cm^3), heat capacity (0.46 J/g°C), and measured particle hardness from nanoindentation (~418 HV from 4.1 GPa) in place of the tensile strength [98]. Using particle temperatures obtained from the particle flow simulations (discussed in Section 2.4.1), the estimated v_{crit}^{Cr-Cr} from Eqn. 4.1 and Eqn. 4.2 was calculated to be ~638 m/s for a maximum particle size of 20 μm. Fitting parameters a and b were chosen by correlating the experimental results with critical velocity calculations and were set to 4.1 and 0.3, respectively, which are reasonable for a standard particle size distribution [98,100].

Two considerations should be noted for these calculations. First, the dependence of particle size on critical velocity was not investigated, mainly due to the tight particle size distribution used in this study (-20+10 μm). It is generally accepted that the critical velocity increases with decreasing particle size [98,100]. In this experiment, the increase in v_{crit} for smaller particles could be compensated by the increase in impact velocity (shown in Section 2.4.1). Therefore, we used a 20 μm particle to represent the minimum v_{crit} needed for Cr-Cr bonding. Second, while particle temperature was included in these calculations, it was not a focus of investigation. The estimated particle temperatures from CFD simulations ranged from 150-450

°C for carrier gases preheated from 350-750 °C, respectively. While some bcc metals undergo a brittle-to-ductile transition (BDTT), these particle temperatures are low for refractory metals with high melting points such as Cr. Therefore, more weight was put on the mechanical fitting parameter over the thermo-physical parameter since it has been shown that initial Cr particle microstructure and hardness have a large effect on deposition efficiency [34,137].

A conservative critical velocity of 640 m/s for Cr-on-Zry-4 was proposed for this application. This critical velocity is slightly higher than the point where the DE of Cr-on-Zr reaches 50% ($DE_{615\ m/s}^{Cr-Zr}{\sim}50\%$) for a powder with a normal size distribution (second definition of v_{crit}) [97], but provides a good starting point for optimizing cold spray Cr coating deposition. Namely, this critical velocity represents the stage at which full Zry-4 substrate coverage can be attained ($DE_{640\ m/s}^{Cr-Zr}{\sim}77\%$) while *simultaneously* the Cr coating thickness begins to increase beyond the first layer of Cr particles (i.e., coating formation begins). It should be noted that Eqn. 4.1 cannot be used for dissimilar metals as the deformation mechanisms are more complex, though it is interesting that both definitions of v_{crit} can be used to obtain a conservative value for the Cr-on-Zr system.

4.3. Bonding at the Cr-Zr interface: role of particle/substrate mechanical property mismatch

From the EBSD and microscopy results, it is clear the Zry-4 substrate undergoes more plastic deformation than the Cr particles during impact. The EBSD maps shown in Fig. 4.5 did not indicate significant deformation of the impacted Cr particles when compared to as-received feedstock Cr particles (Fig. 4.1). These results indicate that the mismatched Cr-on-Zr metal system operates in the penetration-dominated mode of impact bonding. In this mode, as defined by Hassani et al [101], impact-induced plastic strain is mostly accommodated by the substrate, with no significant deformation of the particle.

At first glance, differences in deformation seem to be due to differences in hardness (4.1 ± 0.2 vs. 1.8 ± 0.1 GPa) and elastic modulus (280 ± 10 vs. 100 ± 10 GPa) for Cr and Zry-4, respectively [173,174]. The yield strengths for Cr and Zry-4 are difficult to compare as they can be influenced by impurities, microstructure, temperature, strain rate sensitivity, and other factors, but generally range between 200-500 MPa [60,141,175–177]. However, the bulk Cr substrate was softer than the Zry-4 (145 ± 6 vs. 180 ± 4 $HV_{0.1}$, respectively), and differences in deformation were substantial, indicating that hardness is not necessarily the only metric for predicting deformation during cold spray. Johnson [178] proposed that the controlling physical properties influencing impact-induced deformation can be represented by a dimensionless parameter: $\rho V^2/Y_d$, where ρ, V^2, and Y_d are the density, velocity, and dynamic yield strength, respectively, of the substrate and particle. Hassani et al. [101] expanded on this parameter by using material velocities of $V_{(p,s)}$, rather than the impact velocity. This term includes shock impedance (ρC_0), where C_0 is the Hugoniot shock velocity constant, which is related to a material's bulk modulus. The resultant impact-mode ratio, R, proposed by Hassani [101] should be similar to the one proposed by Johnson [178]:

$$R = \frac{\left(\frac{\rho V_s^2}{Y_d}\right)_s}{\left(\frac{\rho V_p^2}{Y_d}\right)_p} \cong \frac{\left(\rho C_0^2 Y_d\right)_p}{\left(\rho C_0^2 Y_d\right)_s}, \qquad \textit{Eqn. 4.3}$$

where the subscripts p and s refer to the particle and substrate, respectively. A value of R=1 indicates ideal co-deformation, whereas increasing values of R indicate a higher degree to which plastic deformation in the substrate increases.

Materials constants were taken from literature, including density (7190 vs. 6560 kg/m^3) and shock velocity constants (5200 vs. 3900 m/s^2) for Cr and Zr, respectively [179]. Dynamic yield strengths were calculated using data collected from plate and particle impact experiments on Zr and Cr [180–186]. Both ratios ($R^{Johnson}$ and $R^{Hassani}$) produced nearly identical values of 9.8, indicating that the Cr-Zr system is dominated by the penetration regime. This result can be linked to the higher shock impedance and dynamic yield strength of Cr (1550 MPa) compared to Zr (930 MPa), and in the tendency of bcc metals to work-harden with increasing strain rates [184,187]. Meanwhile, evidence of strain-rate softening has been observed in Zr during plate impact testing [182].

The microscopy and EBSD results also indicated that adhesion between Cr and Zr is facilitated by both mechanical and metallurgical bonding, the latter being defined by crystallographic coherency and/or elemental transport across the interface. Fig. 4.4 shows that some amount of mechanical interlocking is possible at all velocities above v_{crit}^{Cr-Zr}, though increasing velocity led to a transition from localized jetting to full periphery jetting around the Cr particles [106]. Due to the penetration-dominated mode discussed earlier, and because $v_{crit}^{Cr-Cr} > v_{crit}^{Cr-Zr}$, the velocities required for Cr coating buildup indicate that Cr-on-Zr impact will always result in interfacial jetting of Zr, leading to a strong metallurgical bond.

The experimentally determined critical velocity for coating buildup (640 m/s) produces minimal particle rebounds, particle penetration at the interface, and peripheral jetting in the Cr-Zr system. The combination of mechanical interlocking and metallurgical bonding should result in high adhesion strength between the Cr coating and Zry-4 cladding. Indeed, during scratch, axial and ring hoop tension, fatigue, pressurized water corrosion, thermal creep, and burst tests, no reported spallation or delamination of cold spray Cr coating has been reported for coatings sprayed above this impact velocity [188–192].

4.4. Coating formation mechanisms: necessity of dynamic recrystallization versus jetting

Cr particle impacts on Cr substrates showed transition from penetration-dominated to co-deformation-dominated impact bonding mechanism [101]. Below the critical velocity of 640 m/s, impacting Cr particles showed very little penetration into the bulk Cr substrates and most of the deformation was confined to the particle interior (Fig. 4.6 d). As particle velocity increased, IPFs and GROD maps in Fig. 4.6 (a-f) revealed grain refinement in the Cr particles after impact, and KAM maps shown in Fig. 4.6 (g-i) revealed a higher distribution of plastic strain and dislocation density within the Cr particles. At the highest velocity condition, deformation becomes more equitably shared between the Cr particle and the Cr substrate, resulting in localized particle/substrate jetting and an increase in penetration depth into the substrate (Fig. 4.4 f), which in turn would lead to stronger bonding.

The commonly held view in cold spray is that only adiabatic shear instabilities (ASI) upon impact lead to jetting and subsequent bonding, though this assertion has been challenged in recent years [99,116,117,193,194]. Hassani et al. [116] argued that jetting is predominantly a pressure-driven phenomenon and does not require ASI. However, the authors of that study and others [113,116] maintained that jetting is critical for solid-state bonding in cold spray as the large mechanical distortion/plastic strain associated with jetting produces the clean, oxide-free surfaces and high enough contact pressures needed for intimate contact and metal-to-metal bonding.

On the contrary, the current results for the Cr-on-Cr system at the intermediate velocity condition (Fig. 4.2 e, Fig. 4.4 e and Fig. 4.6 b, e, and h) suggest that bonding can be achieved with the occurrence of practically negligible jetting. In other words, the high plastic strains associated with jetting are not essential for bonding, at least for the Cr-on-Cr system. Instead, the nanoscale structural transformations occurring at the impact interface at the observed levels of plastic strain must be responsible for bonding. A distinct feature characteristic of the Cr-on-Cr system is that demarcation of particle-substrate interface becomes obscured due to the presence of fine recrystallized grains on either side of the interface (Fig. 4.9). In particular, the presence of fine, but elongated grains (Fig. 4.9e) resulting from continuous dynamic recrystallization (cDRX) and ultra-fine grains (<50 nm, Fig. 4.9f) resulting from geometrical dynamic recrystallization (gDRX) can be seen at the center and tail-ends of the particle boundaries, respectively [122,195]. This suggests the plausibility of dynamic recrystallization occurring during impact to be closely correlated with bonding.

In fact, prior research has shown that such a correlation between dynamic recrystallization occurring at the contacting particle interfaces and bonding does exist in Cu, Al and Ti-based alloy systems [107,115,122,126,196–198]. The fine-recrystallized structure at the interface has been described to provide a means for nanoscale interlocking through creation of bridging connections and nanoscale “zipper” like structures. The difference between those literature reports and the current observations, however, is the magnitude of strain at which dynamic recrystallization is observed. In Cu, Al and Ti-based systems, dynamic recrystallization is initiated at a stage where the system exhibits substantial jetting, i.e., high levels of plastic strain. On the contrary, in the case of the Cr-on-Cr system investigated in this study, dynamic recrystallization is initiated at much lower strain values, where no significant jetting has been initiated.

The most common measurement used to quantify recrystallization fraction in the microstructure is grain orientation spread (GOS) [199–202]. The procedure used by Ayad et al. [202], in which the criteria included selecting grains containing both GOS < 2.5° and normalized GOS/D_i < 1.5°, where D_i is the maximum ferret diameter, was used in this study. Additionally, the subset of grains used in the analysis were confined to within 1 μm of the interface to prevent sampling of prior recrystallized grains from the powder fabrication process. Quantification of the extent of this dynamic recrystallization during single particle Cr impacts on bulk Cr substrates using the EBSD results are shown in Figure 4.10. The results reveal two important findings: (i) internal misorientation, grain size, and grain aspect ratio decrease with increasing particle velocity; (ii) the number of recrystallized grains along the interface increases with increasing particle velocity. This suggests that during higher velocity impacts, a larger number of finer and more equiaxed recrystallized grains are generated along deforming interfaces. Despite the statistical variations in Figure 4.10 (which can be attributed to the low number of resolved interfacial grains in the EBSD maps), the results are consistent with the above stated hypothesis that bonding in this system is dependent on the extent of dynamic recrystallization, regardless of the occurrence of jetting.

It can be concluded that the nanoscale interlocking resulting from dynamic recrystallization at the particle-particle interface is effective in realizing intimate bonding in the Cr-on-Cr system, even if the strain is not sufficient to initiate jetting. The critical localized plastic strain for triggering dynamic recrystallization in Cr, rather than that strain essential for causing jetting, dictates bonding. In the case of Cr, dynamic recrystallization occurs at a lower plastic strain than that required for jetting, compared to other softer fcc metals such as Cu and Al. Consequently, jetting is naturally associated with bonding in fcc metals such as Cu and Al, while it appears to be not strictly necessary for bonding in Cr and perhaps other less deformable metals.

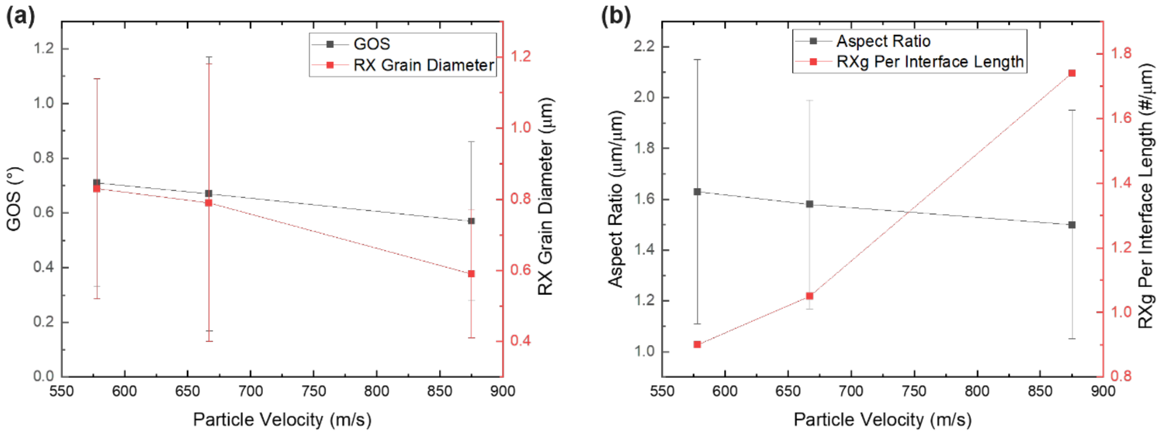

Figure 4.10. Plots of dynamically recrystallized grain statistics for the single-particle Cr impacts on pure Cr substrates, calculated from EBSD results: (a) GOS and recrystallized (RX) grain diameter vs. particle velocity; (b) Grain aspect ratio and number of recrystallized grains (RXg) per interfacial length vs. particle velocity.

4.5. Influence of feedstock Cr particle microstructure on coating formation

Aside from reaching the critical velocity for Cr-on-Cr, it appears the main factor influencing coating formation in cold sprayed Cr is the propensity of the feedstock Cr particles to work-harden. GND density increased with increasing impact velocity for the single Cr particles (Table 4.1) as well as for the deposited Cr coating. Nanoindentation measurements taken within the highest velocity coating showed a hardness of 6.4 ± 1.1 GPa, a 56% increase in hardness from the undeformed Cr particles (4.1 ± 0.2 GPa). STEM imaging and EBSD mapping of the feedstock Cr powder, shown in Fig. 4.9, revealed a large grained and low defect density particle able to undergo significant work-hardening during high strain rate deformation. In previous investigations by the author [34,137], three Cr feedstock powders produced by different methods were used to deposit coating via cold spray. These powders included: (i) electrolytic hard chromium followed by mechanical milling; (ii) electrolytic hard chromium followed by milling, followed by annealing in inert argon environment at 800 °C for 1 hour; (iii) gas atomized Cr powder; and (iv) electrolytic soft chromium (followed by milling) powder used in this study. These powders will henceforth be referred to as *electrolytic hard, annealed electrolytic hard, atomized, and electrolytic soft,* respectively.

Figure 4.11 gives an overview of the initial microstructure of the feedstock Cr powders and subsequent cold spray coatings: the first row shows IPFs generated using TKD, the second row shows KAM maps generated using TKD, and the third row shows cross-sectional SEM images of the deposited Cr coatings using identical cold spray parameters ($v_p \sim 780\ m/s$). Native oxide thickness measured using HAADF-STEM imaging, particle hardness measured using nanoindentation, and Cr coating thickness measured using SEM imaging are also included in Figure 4.11.

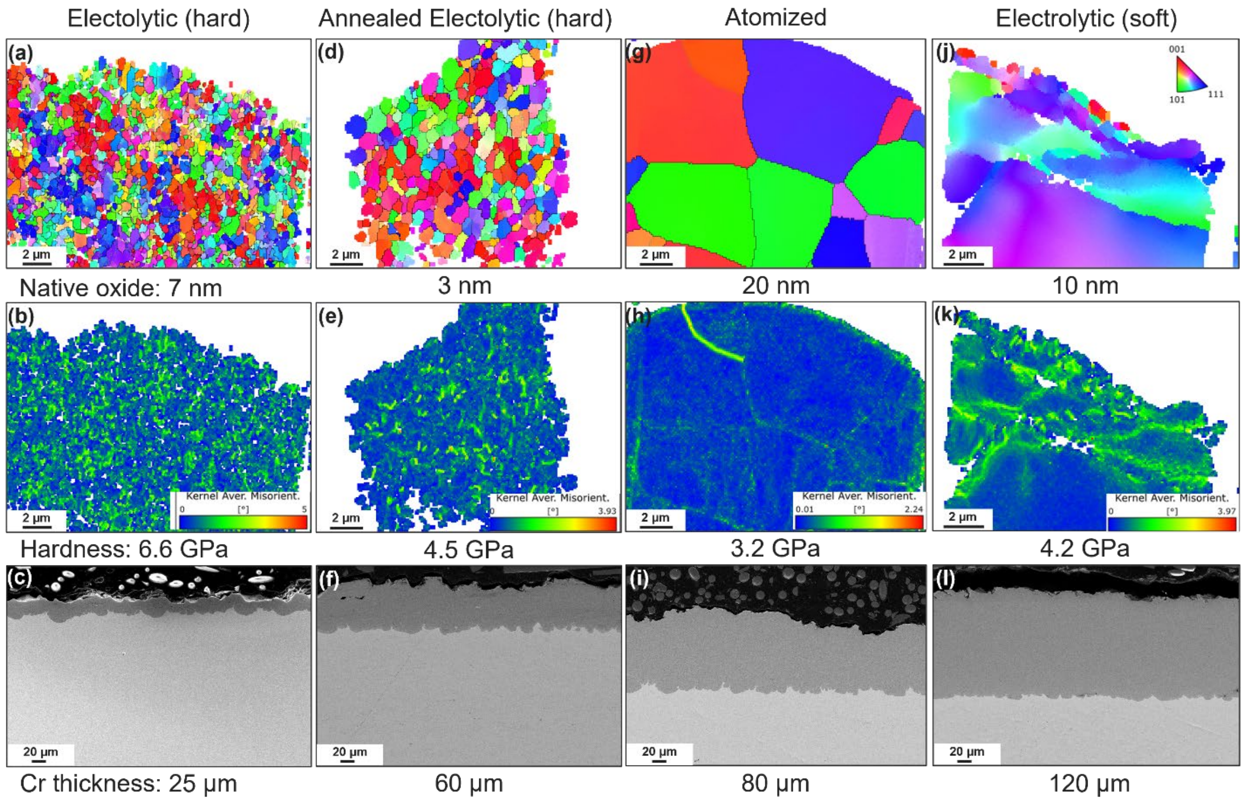

Figure 4.11. TKD-produced IPF maps (first row) and KAM maps (second row), and cross-sectional SEM images of cold spray Cr coatings (third row) sprayed using the following Cr particles: (a-c) electrolytic hard Cr; (d-f) annealed electrolytic hard Cr; (g-i) spherical gas atomized Cr; (j-l) electrolytic soft Cr used in this research. The figure also contains HAADF-STEM measurements on native oxide scale on the particles, nanoindentation measurements of particle hardness, and SEM image measurements of coating thickness.

The electrolytic hard powder (Figure 4.11 a-c) contained very fine, submicron-sized grains and a large amount of internal strain, which resulted in a coating thickness of only ~25 µm. After annealing the electrolytic hard Cr powder (Figure 4.11 d-f), recovery and recrystallization resulted in stress relief, which led to a coating thickness increase to ~60 µm. The atomized Cr powder (Figure 4.11 g-i) showed an average grain size of about 3 µm and very low internal strain, resulting in a coating thickness of ~80 µm. Finally, the electrolytic soft powder used in this study (Figure 4.11 j-l) produced the highest coating thickness of ~120 µm. Based on the TKD and SEM results shown in Figure 4.11, it appears the main factors governing coating buildup and cohesion for Cr particles, in order of importance, are hardness, grain size, and particle morphology.

Hardness of the feedstock Cr particles appears to be the dominant factor governing coating formation. The electrolytic hard Cr powder shown in Figure 4.11 (a) had the highest hardness and most internal stresses, which produced the thinnest coating containing only the first layer of deposited Cr particles. The other three powders showed much lower hardness and internal stress levels, leading to a buildup of coating thickness not achievable with the electrolytic hard powder. Despite the initial hardness of the feedstock particles, all Cr coatings reached an average hardness between 6-7 GPa, which indicates that in each case Cr reaches a maximum capacity of work-hardening during deposition. Therefore, low hardness and low internal stress of the feedstock Cr powder are important factors that govern the ability to build up thickness.

The second important factor for Cr coating formation is grain size. Given that hardness is closely linked to grain size via the Hall-Petch relationship, slight grain growth of the annealed hard electrolytic powder resulted in buildup of a thicker coating. Still, the annealed hard electrolytic Cr powder built up half the total coating thickness compared to the electrolytic soft Cr powder used in this research, despite having comparable hardness. The difference here mainly comes from grain size as both the atomized and soft electrolytic Cr powder contained grains larger than 1 µm in size.

Interestingly, the electrolytic soft Cr powder used in this research produced thicker coatings than the atomized Cr powder, despite showing higher hardness, higher internal strain gradients, and lower average grain size. This finding leads to the third important factor in Cr coating formation, which is particle morphology. Maier et al. [34] showed that for spherical Cr particles (Figure 4.11 g), lower particle velocities can lead to inadequately bonded inter-particle boundaries, since bonding of these spherical particles requires high enough kinetic energy for plastic deformation and associated adiabatic shear instabilities across particle interfaces. Meanwhile, Yeom et al. [137] showed that for non-spherical particles, interlocking along sliding/shearing interfaces may produce weak frictional bonds if particles are properly aligned. In other words, alignment of these particles like "teeth in a wheel" coupled with microscopic sliding and associated dynamic recrystallization discussed earlier may provide the necessary inter-particle cohesion in lieu of large-scale adiabatic shear.

The electrolytic soft Cr powder used in this research has the "best of both worlds", so to speak. On the one hand, its low hardness, low defect density, and large grain size allow it to undergo plastic deformation at the colliding interface, resulting in high shear strains and associated metallurgical bonding. On the other hand, if the particle does not have sufficient kinetic energy for plastic deformation (i.e., lower impact velocity due to slight differences in particle size), it may still become trapped within the coating upon impact due to frictional interlocking. After entrapment, the tamping effect of successive particle impacts will continue deforming the particle, allowing it to flow, fill in any gaps, and densify the coating. In contrast, the spherical atomized powder may only rely upon plastic deformation and shear for bonding and cohesion. Therefore, the added benefit of an irregular shape results in additional coating thickness.

As previously discussed in Section 4.4, cohesive bonding between particles occurs on a very localized level, restricted to about 1 μm between colliding interfaces. Therefore, the surface characteristics of the feedstock particles are very important. Native oxide films on the four Cr particles shown in Figure 4.11 measured between 5-30 nm in thickness, but the fact that coating formation occurred for all particles indicates that this thickness range is acceptable and film breakup should occur so long as sufficient particle velocities are achieved. Fine grains at the particle surface do not appear to significantly inhibit bonding so long as this grain size distribution does not make up the entire particle, as is the case for electrolytic hard chromium powder. This analysis demonstrates the complex interactions that exist between microstructural features contained within a single chromium particle, and how these features influence coating formation and cohesion mechanisms.

5. Advancing Cold Spray Cr Coating for Nuclear Reactor Cladding Application

This section focuses on steps towards advancing the understanding of Cr cold spray deposition on Zr-alloy for PWR cladding application, including an assessment of process parameters, application of particle flow and particle impact models for the effective deposition of coatings, and engineering of coating surface and coating-substrate interfaces.

5.1. Examination of the effects of cold spray parameters on coating quality

5.1.1. Effects of gas preheat, particle temperature, and particle size on critical velocity

As discussed in Section 4.2, the critical velocity of Cr-on-Cr was determined experimentally and verified using an empirical relationship between the mechanical and thermal properties of chromium to its critical velocity. Fig. 5.1 shows a plot of critical velocity vs. gas preheat temperature for Cr-on-Cr bonding, which shows that the critical velocity for the formation of Cr coatings decreases with increasing gas preheat temperature. It is possible that this is due to particle heating in the gas stream. The JC equation (Eqn. 2.7) explains that the flow stress of a material decreases with increasing temperature; therefore, particles experiencing higher temperatures upon impact are more likely to plastically deform and bond, thus decreasing their critical velocity. The empirical equation used to estimate the critical velocity of Cr in Section 4.2 is reproduced here for clarity: $v_{crit} = \sqrt{a\sigma/\rho + bc_p(T_m - T_p)}$, which reiterates that the critical velocity decreases with increasing particle temperature.

However, researchers have shown that smaller particles have higher heating and cooling rates than larger particles [120,203]. This means that, while small particles heat up rapidly in the converging section of the nozzle, they quickly cool down with the expanding gas at they move towards the nozzle exit. This feature was revealed in the CFD simulations shown in this work and others [120,203]. In CFD simulations previously shown (Fig. 2.8), the particles are injected very close to the converging section of the nozzle, whereas in experimental conditions the particles are injected further back in the cold spray gun where they have longer time to acquire heat through convection. Regardless, the narrow size distribution of the Cr particles used in this research should result in minimal differences in particle temperature between particles of slightly different sizes.

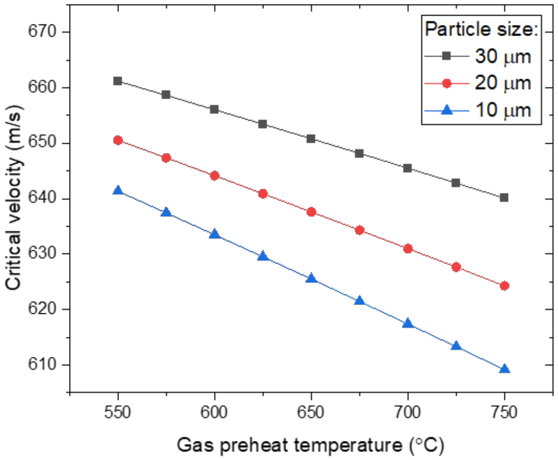

Fig. 5.1. Plot of critical velocity of Cr-on-Cr bonding vs. gas preheat temperature, with respect to particle size. The results show critical velocity decreases with increasing temperature.

The effect of particle size and nozzle stand-off distance were investigated by depositing electrolytic soft Cr powder in the larger size distribution (325 mesh, -44 µm) and varying the standoff distance between 26 mm and 50 mm using Cr-N2 gas conditions. The study was also performed using gun traverse speeds of both 200 and 500 mm/s. The cross-sectional images of the deposited coatings are shown in Fig. 5.2. The results show that at the typical standoff distance of 26 mm, the thickness of Cr-N2$^{-44\mu m}$ coatings was 20 µm and 10 µm (Fig. 5.2 a, c) while the thickness of Cr-N2$^{-20\mu m}$ coatings (shown later in this section) was 54 µm and 45 µm, deposited using spray speeds of 200 mm/s and 500 mm/s, respectively. Increasing the standoff distance from 26 to 50 mm resulted in thicker coatings and improved coating uniformity, as shown Fig. 5.2 (b, d) for the Cr-N2$^{-44\mu m}$ coatings.

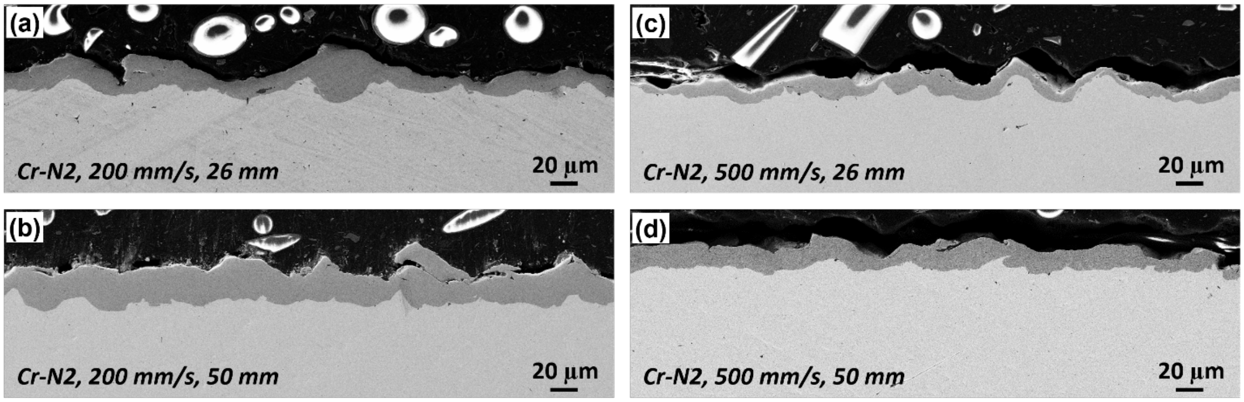

Fig. 5.2. Cross-sectional SEM images of cold spray Cr coatings on Zry-4, deposited using larger electrolytic soft Cr particles (-44 µm) and Cr-N2 gas conditions. Two spray speeds and two standoff distances were used: (a) 200 mm/s, 26 mm; (b) 200 mm/s, 50 mm; (c) 500 mm/s, 26 mm; (d) 500 mm/s, 50 mm. The images show reduced coating thickness when spraying with larger particle size distribution.

In this research, CFD simulations report the particle velocity at the nozzle outlet. During experimental conditions, however, particles continue to accelerate between the nozzle outlet and the substrate surface. When the nozzle standoff distance is too short, the bow shock at the substrate surface effectively slows down the velocity of the particles (as discussed in Section 2.4.1). The fact that the smaller Cr particles were able to deposit double the thickness compared to the larger Cr particles indicates the bow shock effect is not very significant at a standoff distance of 26 mm. If it was, the smaller Cr particles would be much more affected due to their smaller mass.

The more likely reason for the improvement in coating quality for the Cr-N2$^{-44\mu m}$ coatings at longer (50 mm) standoff has to do with particle acceleration and momentum. The particle velocity measurements from CFD calculations (Fig. 2.9 a) showed that a 30 µm particle exits the nozzle between 80-200 m/s slower than a 10-20 µm particle. Larger particles also have more mass, meaning they require higher kinetic energies to plastically deform at the substrate. The low particle velocity at the nozzle exit combined with the short 26 mm standoff distance resulted in limited acceleration of the larger Cr$^{-44\mu m}$ particles, leading to low deposition efficiency (Fig. 5.2 a). Doubling of the standoff distance to 50 mm provided more time for the larger Cr particles to accelerate and build up momentum (i.e., kinetic energy) to achieve plastic deformation at the substrate (Fig. 5.2 c).

5.1.2. CFD and FEM simulations of particle impact and coating formation

Coating quality may be expressed as a function of a dimensionless parameter, η, defined as the ratio of the particle impact velocity to the critical impact velocity ($\eta = v_p/v_{crit}$). Researchers have found that the quality of cold spray coatings (i.e., thickness, density, bond strength, etc.) increases with higher values of η [100]. In this research, assessment of η as a function of independent cold spray parameters (namely, gas preheat temperature, pressure, and composition) was performed. Fig. 5.3 (a) shows a contour plot of η as a function of nitrogen gas preheat temperature and pressure, which reveals that η has a weak dependence on pressure but increases with temperature. Fig. 5.3 (b) shows a contour plot of η as a function of preheat temperature and He composition in the carrier gas, showing η has a stronger dependence on the amount of He in the gas stream than gas preheat temperature. Fig. 5.3 (c) further illustrates this point, showing that for Cr coatings η can reach values of 1.04 and 1.37 using 100%-N2 and 95%-He gas compositions, respectively. The previous sections have demonstrated that the density and thickness of cold spray Cr coatings improves with He in the carrier gas, and this can be directly tied to particle velocity through η.

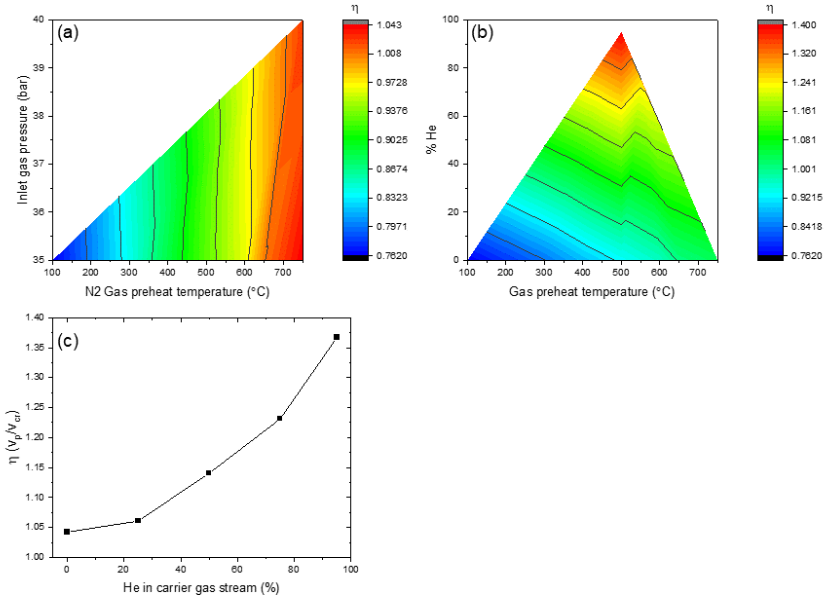

Fig. 5.3. (a) Contour plot of dimensionless parameter 'η' as a function of N_2 gas preheat temperature and pressure; (b) Contour plot of 'η' as a function preheat temperature and carrier gas composition (%-He); (c) Plot showing η increases with increasing He in the carrier gas.

FEM was used to simulate high velocity particle impact on a substrate. Since the materials parameters for Cr (relating to Johnson-Cook deformation) are not available, a pure Fe particle was used as a surrogate to simulate Cr particle deformation. Fig. 5.4 shows a simulation of a 20 µm Fe particle impacting Zry-4 at a velocity of 600 m/s. The impact lasts for approximately 30 ns, during which the evolution of stress and strain increases primarily within the Zry-4 substrate near the interface. The strain within the Fe particle remains relatively low over the course of impact, which aligns well with the microstructure of the single Cr particles shown in Section 4.

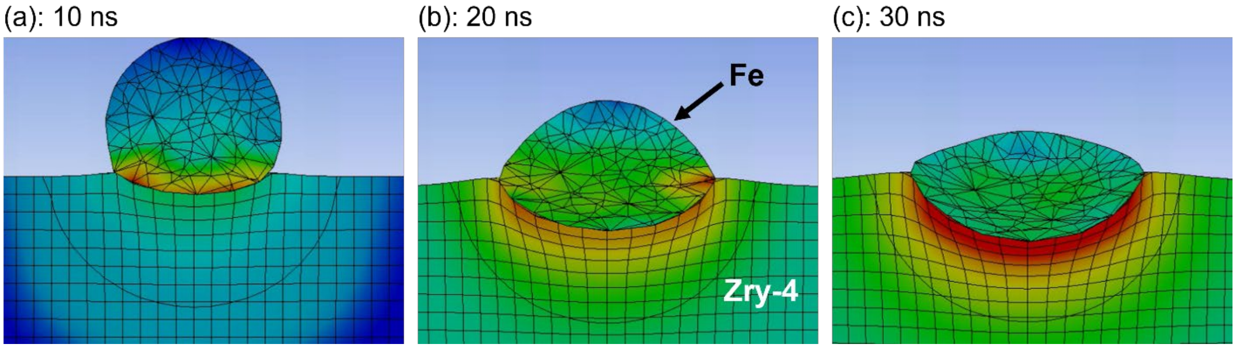

Fig. 5.4. FEM simulation of a 20 µm Fe particle impacting a Zry-4 substrate at 600 m/s impact velocity, showing the evolution of plastic strain at (a) 10 ns, (b) 20 ns, and (c) 30 ns.

Fig. 5.5 shows a single Fe particle impacting an Fe substrate at increasing particle velocities. At 670 m/s (η~1), deformation of both the particle and substrate can be seen, especially near the interface, which also aligns with the single particle Cr-on-Cr impact results discussed in Section 4. Fig. 5.5 (a) also shows a temperature spike near the interface of the colliding particle which may promote better bonding and dynamic recrystallization. At higher particle velocities (η~1.2), the simulation shows significant deformation and jetting of the particle becomes more severe (Fig. 5.5 b). At the highest velocity (η~1.6), the particle begins to experience erosion (Fig. 5.5 c). These simulations are useful for predicting the deformation behavior of single Cr particles.

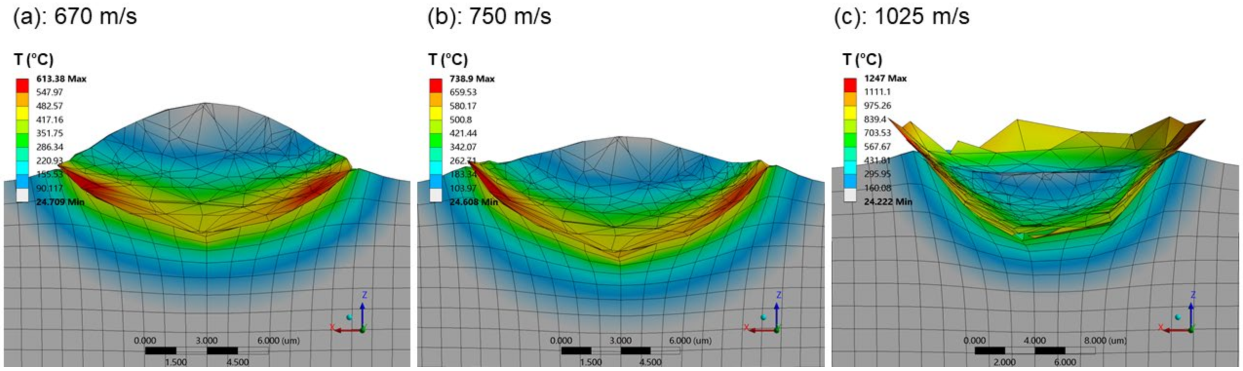

(a): 670 m/s

(b): 750 m/s

(c): 1025 m/s

Fig. 5.5. FEM simulation of single particle Fe impacting Fe with particle velocities set to 670, 750, and 1025 m/s, respectively, displaying temperature output (in °C).

Fig. 5.6 shows an FEM simulation of multiple Fe impacts on Zry-4, impacting at a velocity of 600 m/s. The images show the plastic strain at the particle-substrate interface increases when the first particles impact (Fig. 5.6 b), and then remains relatively constant as coating begins to buildup thickness (Fig. 5.6 c). The plastic strain is significantly high along inter-particle boundaries, indicating severe deformation and bonding. The simulations provide a useful illustration of coating buildup through interparticle cohesion and align well with the results shown in the previous sections.

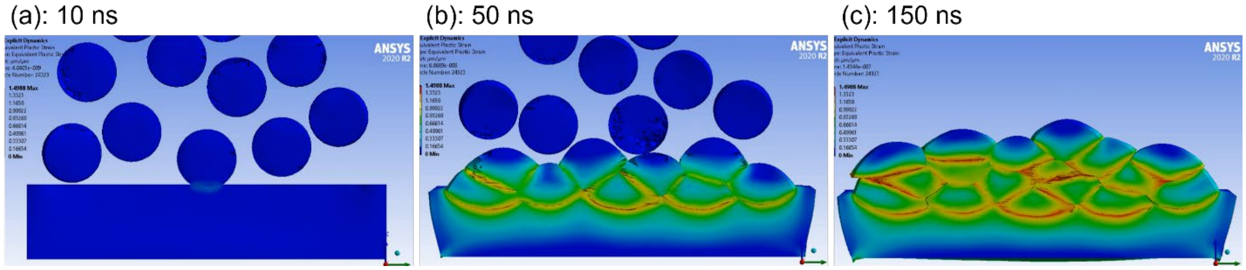

(a): 10 ns

(b): 50 ns

(c): 150 ns

Fig. 5.6. FEM simulation of multiple particle impacts of Fe on Zry-4. The particle velocity was set to 600 m/s. The simulation shows the evolution of plastic strain at the substrate, within particles, and along interparticle boundaries over (a) 10 ns, (b) 50 ns, and (c) 150 ns.

5.2. Addressing surface roughness in cold spray Cr coatings

Cold spray coatings inherently have a high surface roughness due to lesser deformed particles on the topmost layer of the coating, as shown in Fig. 5.7 (a). While this rough surface can provide the necessary corrosion and oxidation resistance, from a practical standpoint a smoother surface may be desirable to minimize CRUD deposition. Additionally, while rougher surfaces provide more efficient heat transfer, they can also increase pressure drops across the cladding length. However, these considerations are outside the scope of this research. Cr coatings are polished using mechanical grinding to reduce the coating thickness and to replicate the surface roughness of traditional Zr-alloy cladding. An image of a polished Cr coating on an OPZ cladding tube is shown in Fig. 5.7 (b), which illustrates that the minimum thickness of the coating is limited by the interfacial roughness. The rest of this section will explore select experiments that were performed to arrive at practical methods to mitigate surface roughness and interfacial roughness of cold spray Cr-coated Zr-alloy.

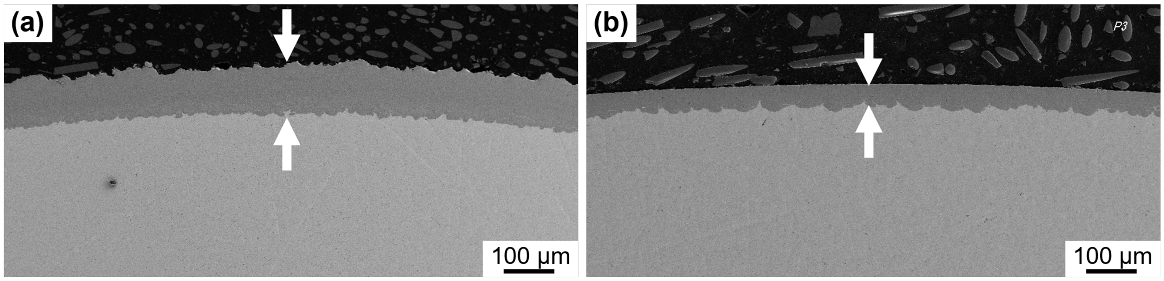

Fig. 5.7. (a) SEM image of an as-deposited Cr coating on OPZ cladding tube, showing high levels of surface roughness and interfacial roughness; (b) SEM of a polished Cr coating on OPZ cladding, showing that uniform coating thickness is limited by the interfacial roughness.

5.2.1. Conventional shot peening to reduce surface roughness

Shot peening (SP) is a type of severe surface plastic deformation technique in which high-energy spherical shots are propelled towards materials' surface to induce plastic deformation in the near-surface regions of the material. There are many studies that have parametrically investigated shot peening and to elucidate the effects on residual stress, hardness, and fatigue and corrosion performance [204]. If a surface is initially smooth, shot peening will increase the surface roughness, especially with increasing shot diameter and/or velocity [205–212]. However, shot peening has been shown to reduce surface roughness of thermal spray and cold spray coatings [213–215], and the induced hardening and nanocrystalline layer densified the coatings while improving oxidation and corrosion resistance.

The goal of this set of experiments was to study the effect of SP on the surface roughness of cold spray coatings. Six Cr-He coatings on Zry-4 substrates were shot peened for 5 to 25 seconds using 1 mm spherical steel shots. A standoff distance of 3 inches and 20 psi of air pressure was used based on optimization from a previous investigation involving shot peening of pre-roughed 316 stainless steel. Results of characterization of the Cr coatings using SEM and optical profilometry are shown in Fig. 5.8, as a function of peening duration. The cross-sectional SEM image of the as-deposited surface (Fig. 5.8 a) illustrates some macroscopic peaks and valleys on the coating surface, while the plan-view SEM image (Fig. 5.8 g) illustrates local roughness due to lesser deformed particles. The average roughness of all Cr-coated Zry-4 substrates before peening was measured to be 5.5 ± 0.3 μm using optical profilometry.

The cross-sectional SEM images in Fig. 5.8 (a-f) show a qualitative decrease in roughness with increasing peening time. The plan-view SEM images in Fig. 5.8 (g-l) reveal the rough surface morphology of the as-sprayed Cr coating begins to flatten out with increasing peening time, transitioning from a crater-like morphology to a flatter, compressed surface. Improvements in the surface reflectivity can be seen in the 3D surface plots in Fig. 5.8 (m-r), as increasing SP exposure led to further deformation and consolidation of local irregularities on the coating surfaces.

Fig. 5.9 shows a plot of the average surface roughness (Ra) of the Cr coating surface as a function of peening time, quantified using optical profilometry measurements (from Fig. 5.8 m-r) and using MALAB via cross-sectional image analysis (from Fig. 5.8 a-f). Five seconds of peening led to a factor of 2 decrease in Ra to 3 μm, with a minimum roughness of 2-2.3 μm achieved after 15 seconds. The results show good agreement between the two measurement techniques. A slight increase in roughness for longer peening times suggests that 15 s is the threshold before peening begins to roughen the surface.

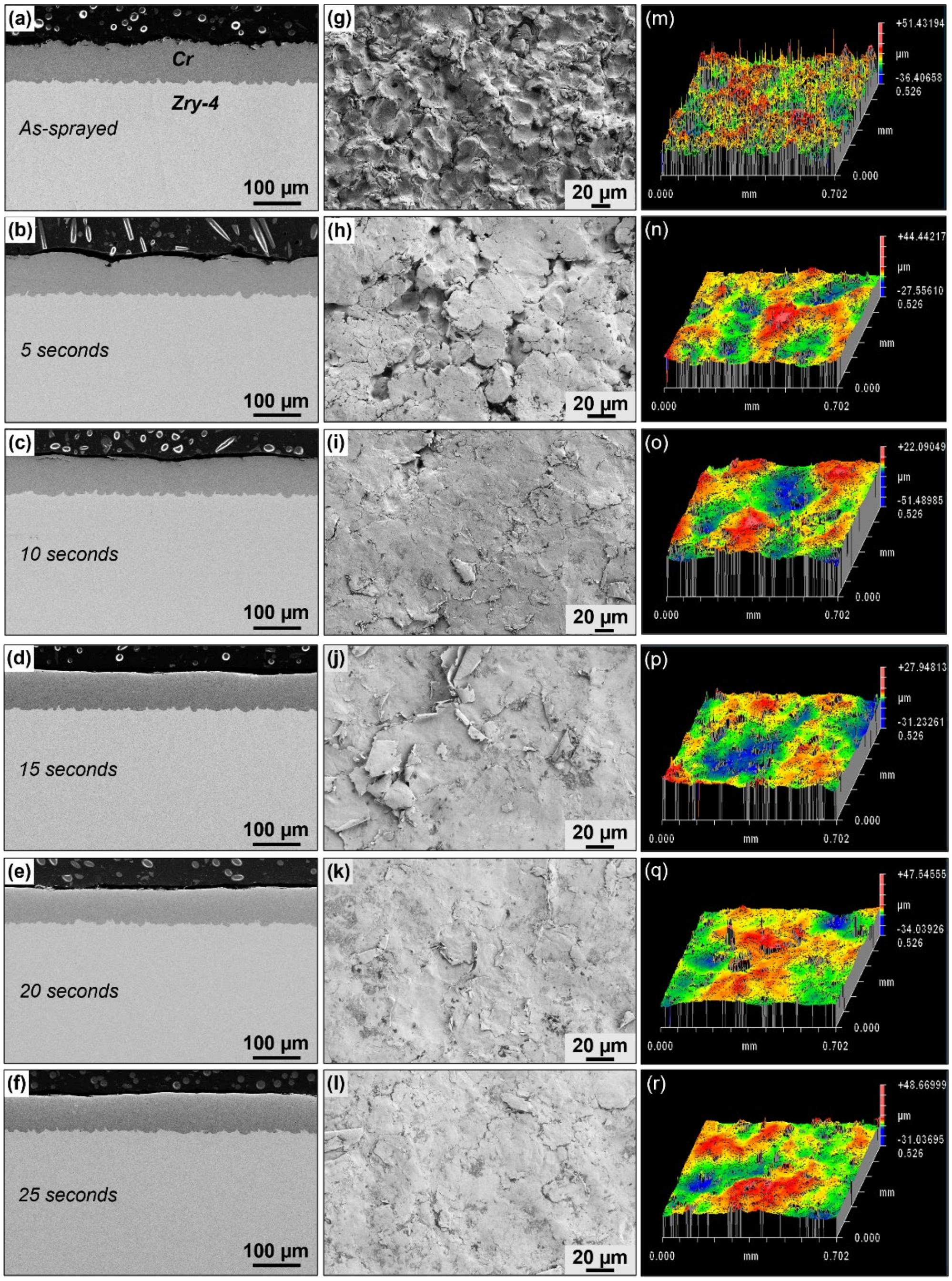

Fig. 5.8. Images of cold spray Cr-He coatings from the as-sprayed condition (top row) up to 25 s peening time (bottom row): (a-f) Cross-sectional SEM images; (g-l) Plan-view SEM images of Cr coating surface; (m-r) Optical profilometry 3D surface plots of Cr coating surface.

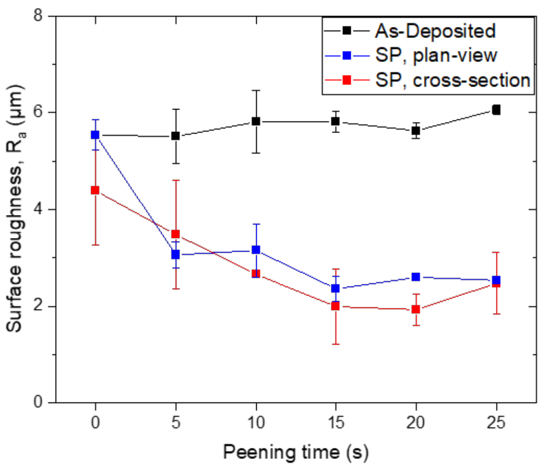

Fig. 5.9. Plot of average surface roughness (Ra) vs peening time for the as-deposited Cr-He coatings (black) and SP samples measured using plan-view optical profilometry (blue) and cross-sectional SEM images (red).

5.2.2. Cold spray peening to reduce surface roughness

An innovative and potentially economical approach for reducing surface roughness is to use cold spray peening, wherein the cold spray gun itself is used as for shot peening [16, 20-23]. Previous studies have used peening (shot) media different from that of the coating material. This research investigates the use of Cr particles (under a set of conditions different from the ones used for depositing coating) to induce peening effects. The Cr particle size used for peening is larger and the spray conditions are adjusted to achieve lower velocities so that tamping and rebound are favored. This approach, referred to as cold spray shot peening (CSSP), is particularly favorable for LWR cladding and other nuclear applications as it does not introduce a new material into the system and avoids any possibility of cross-contamination.

In the first experiment, CSSP was performed on a variety of coating/substrate conditions. Spherical gas atomized Cr powder particles (~3.2 GPa) greater than 44 µm in size (Fig. 5.10) were used as the shot media for two reasons: (i) to explore a softer shot media than that used for coating deposition to impose a gentler, near-surface tamping, and (ii) to effectively utilize larger sized powders that would otherwise be discarded as being unsuitable for typical cold spray coating deposition, thus making the process economical and sustainable. Peening parameters were provided in Table 2.6 and in the experimental Section 2.3.3.

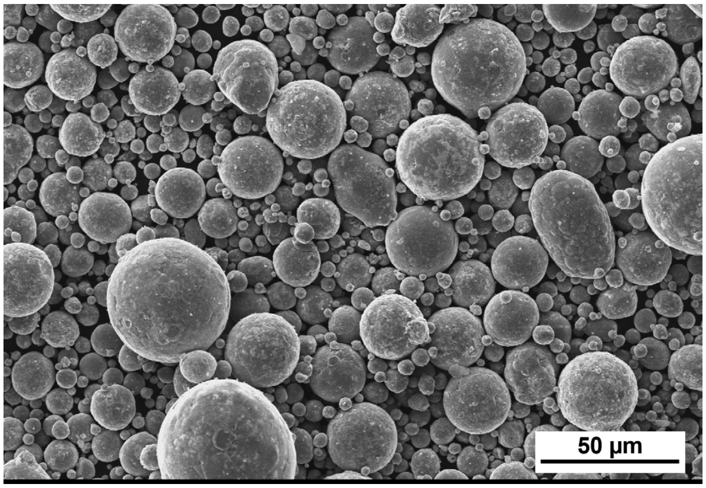

Fig. 5.10. Plan-view SEM image of spherical, gas atomized Cr particles. The larger particles were sieved out and used as shot media during CSSP.

Table 5.1 lists the three different cold spray coatings and two substrates selected for this study. Note that in addition to cold spray Cr coatings, a cold spray FeCrAl alloy coating and two bare substrates of Zry-4 and 316 stainless steel (SS316) were selected to demonstrate the universality of this approach. The Zry-4 and SS316 substrates were intentionally roughened by grit blasting with 36 grit (30 mesh, -762 µm) alumina particles for 30 seconds. The Ra of the starting coating/substrate surfaces (measured using optical profilometry) are also included in Table 5.1.

Table 5.1. Samples and corresponding surfaces conditions used for CSSP experiment. Average roughness (Ra) was measured using optical profilometry.

Sample type	Coating or substrate	Surface treatment	Ra (µm)
Cr-N2	Coating	As-sprayed	6.0 ± 0.7
Cr-He	Coating	As-sprayed	5.4 ± 1.2
Fe10Cr5Al	Coating	As-sprayed	5.1 ± 0.3
Zry-4	Substrate	Grit blast	9.4 ± 1.4
SS316	Substrate	Grit blast	8.6 ± 1.3

Photographs of the SS316 and Zry-4 substrates after grit blasting and following CSSP are shown in Fig. 5.11 (a,b) and Fig. 5.11 (e,f), respectively. A noticeable change in reflectivity, surface morphology, and topography was observed after CSSP with spherical Cr particles. Plan-view SEM images of the SS316 and Zry-4 substrate surfaces (Fig. 5.11 c and g, respectively) show a very rough appearance after grit blasting. A noticeable improvement in roughness was observed after CSSP (Fig. 5.11 d and h), and individual dimples from the impacted Cr particles can be resolved. This result was interesting given the low hardness of the feedstock Cr media and gentle peening conditions, but this can be attributed to the repetitious tamping effects of cold spray and the high density of Cr itself (i.e., high mass/momentum).

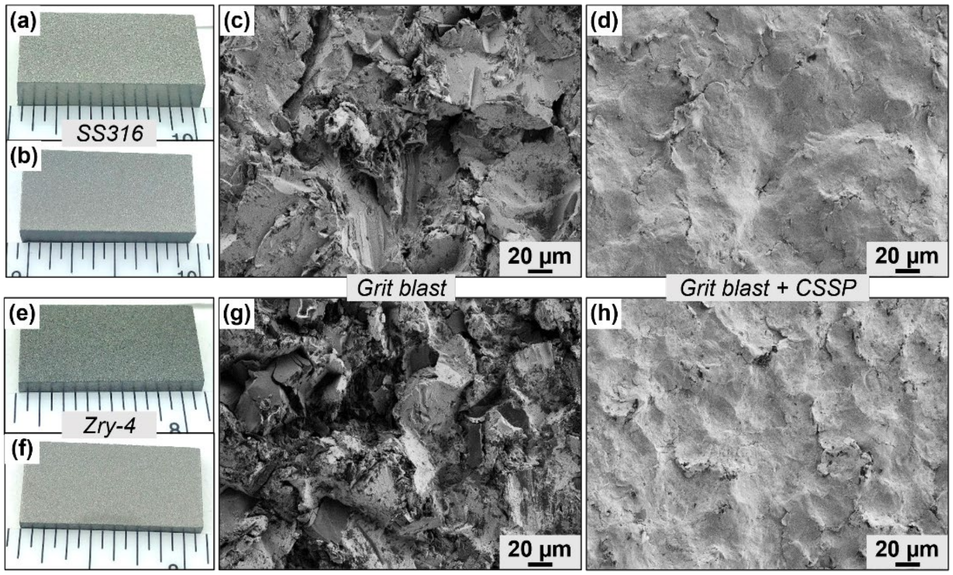

Fig. 5.11. (a,b) Photographs and plan-view SEM images of grit blasted substrates before and after CSSP: (a-d) 316 stainless steel and (e-h) Zry-4.

Cross-sectional SEM images of the CSSP substrates are shown in Fig. 5.12. These images confirm the micro-roughness of the grit blasted substrates was nearly eliminated. Alumina grit blast particles were observed embedded in the surfaces of both substrates which are effects of the aggressive parameters used to roughen the surfaces. Fragments of embedded Cr particles were also observed at the near-surface of both substrates (also an artifact of the experiment) but in greater abundance in Zry-4, possibly due to the hardness of the substrates (180 HV vs. 194 HV for Zry-4 and SS316, respectively). Nevertheless, the results show promise for using CSSP in conjunction with larger Cr particles (than required for coating deposition) and lower particle velocity to reduce the roughness of pre-roughened substrates.

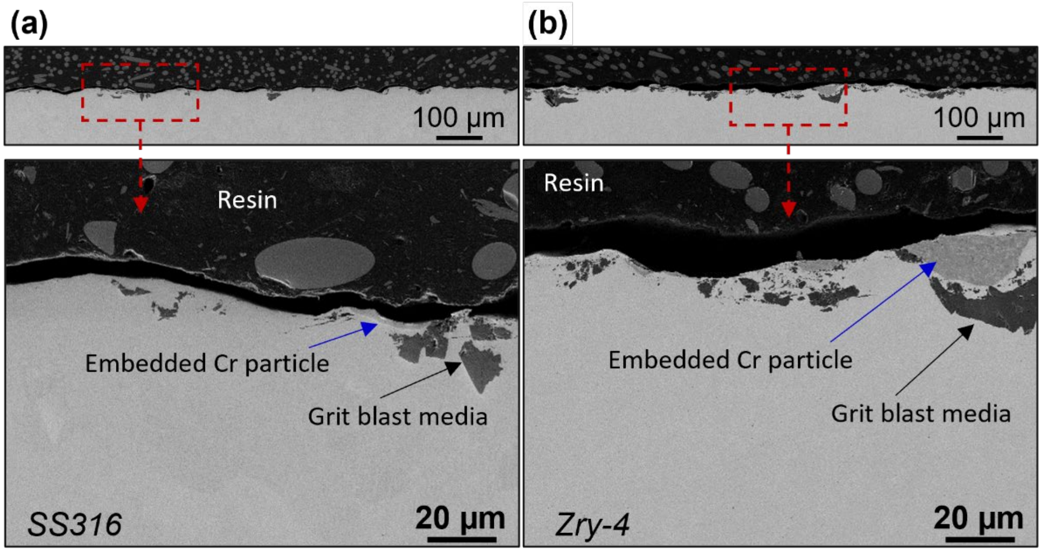

Fig. 5.12. Cross-sectional SEM images of grit blasted (a) 316 stainless steel and (b) Zry-4 after CSSP. Both samples show local areas where grit blast media (black arrows) became embedded in the substrate before peening. During peening, some Cr shot particles (blue arrows) were also deposited on the substrates.

Photographs of the FeCrAl, Cr-N2, and Cr-He coatings before and after CSSP are shown in Fig. 5.13 (a-b, e-f, i-k, respectively). The surfaces of the three coatings exhibited roughness after cold spraying but showed notable differences in reflectivity, topography, and surface morphology after CSSP. The FeCrAl coatings (Fig. 5.13 c) displayed very undeformed spherical particles on the surface after spraying (Fig. 5.14 a). CSSP resulted in deformation and flattening of the particles on the coating surface (Fig. 5.13 d), but micro-roughness remained in the form of particle flakes that are visible in cross-section (Fig. 5.14 b).

The surface of the as-deposited Cr-N2 coating contained some undeformed particles (Fig. 5.13 g), but mostly exhibited a network of partially deformed and consolidated particles. Again, CSSP of the Cr-N2 coating resulted in a noticeable decrease in roughness (Fig. 5.13 h). The surface morphology of the as-sprayed Cr-He coating was similar to the Cr-N2 coating, but showed even greater qualitative improvement in micro-roughness after CSSP (Fig. 5.13 k-l). The cross-sectional images of the Cr coatings before and after peening (Fig. 5.14 c-f) confirm these observations. The macroscopic surface roughness (in the form of undulations and waviness) was also reduced after CSSP.

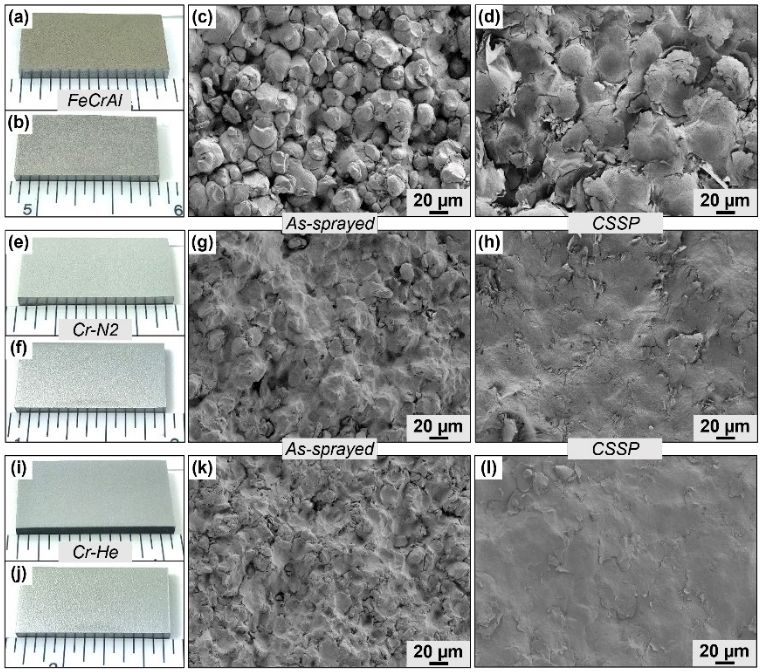

Fig. 5.13. Photographs and plan-view SEM images of cold spray coatings on Zry-4 substrates before and after CSSP: (a-d) FeCrAl; (e-h) Cr-N2; (i-l) Cr-He.

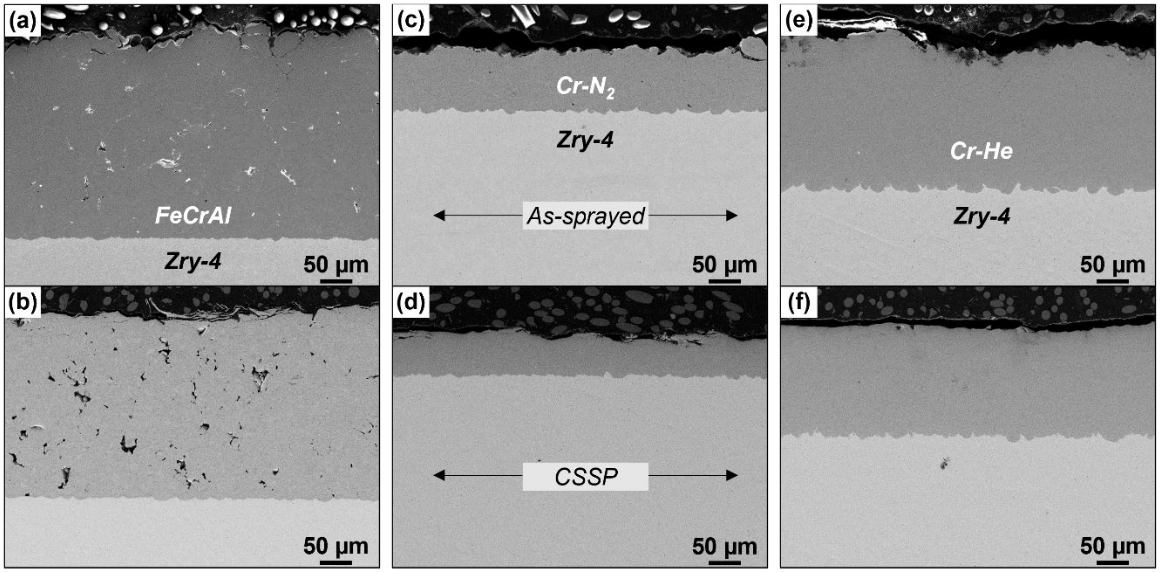

Fig. 5.14. Cross-sectional SEM images of cold spray coatings on Zry-4 substrates before and after CSSP: (a,b) FeCrAl; (c,d) Cr-N2; (e,f) Cr-He.

Roughness measurements from cross-sectional image analysis are shown in Fig. 5.15. The FeCrAl coating remained the roughest at 3.9 µm, and the Zry-4 and SS316 substrates were comparable at 3.7 µm. The roughness of the CSSP Cr coatings decreased from 6.0 and 5.4 µm (Cr-N2 and Cr-He, respectively) to ~3.3 µm for both coatings, near 2x reduction in roughness.

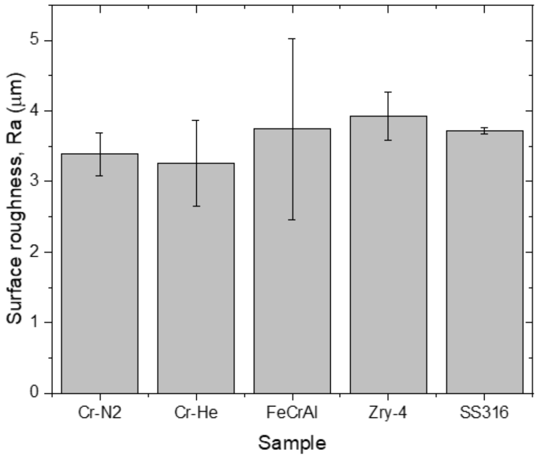

Fig. 5.15. Average micro-roughness (Ra) of the CSSP samples measured from cross-sectional SEM images

Given the effectiveness of CSSP to reduce the roughness of as-deposited cold spray Cr coatings using spherical, soft Cr powder, further experiments were conducted to advance this concept to more prototypical manufacturing conditions for the coated cladding application. This focused on Cr-N2 cold spray coatings (which are favored by industry on account of the high cost of helium) and on using electrolytically soft Cr powders rather than the more expensive gas atomized powders. Electrolytic soft Cr powders are also used to deposit coatings in industry, so this would essentially entail using the larger mesh cut of the same type of powders that would otherwise be designated as scrap. The electrolytic soft Cr powders have a higher hardness (~4.1 GPa) than gas atomized powders (~3.2 GPa), as measured using nano-indentation.

CSSP of Cr-N2 coatings on Zry-4, deposited using 300 and 500 mm/s gun translation speed, was performed using electrolytic soft Cr particles (-44 µm) and a gas temperature and traverse speed set to 100 °C and 100 mm/s, respectively (Table 2.6). Cross-sectional SEM images of the Cr-N2 coating deposited at 300 mm/s before and after CSSP are shown in Fig. 5.16 (a,b). As before, CSSP was successful in reducing micro-roughness at the coating surface. Cross-sectional SEM images of the Cr-N2 coating deposited at 500 mm/s before and after CSSP are shown in Fig. 5.16 (c,d), and exhibited the same phenomenon.

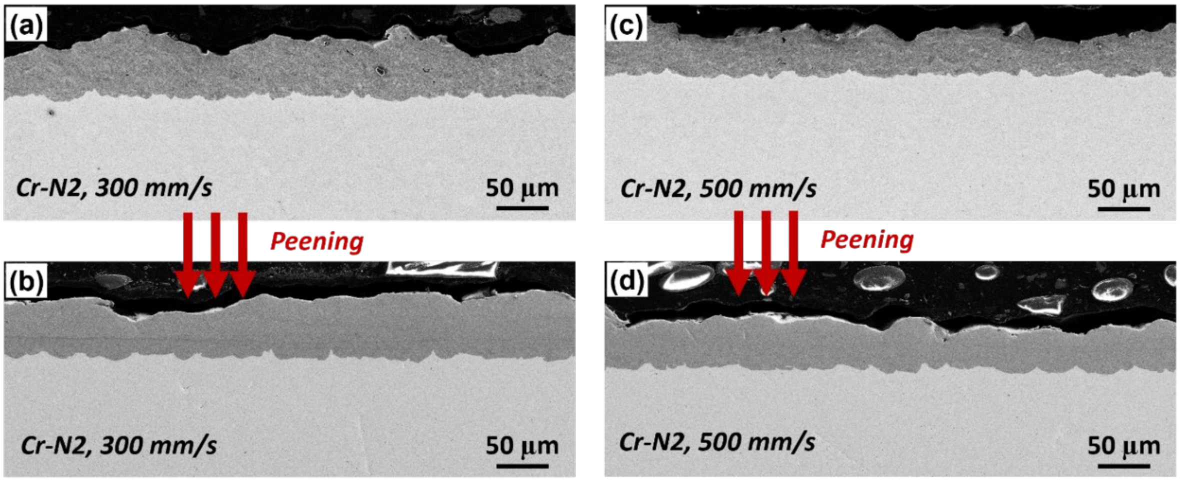

Fig. 5.16. Cross-sectional SEM images, showing: Cold spray Cr-N2 coatings on Zry-4 deposited using 300 mm/s spray speed, before (a) and after (b) CSSP; Cold spray Cr-N2 coatings on Zry-4 deposited using 500 mm/s spray speed, before (c) and after (d) CSSP. Peening was performed using -44 μm electrolytic (soft) Cr particles.

Fig. 5.17 shows several EBSD maps of the Cr-N2 coating deposited using 500 mm/s spray speed in its near-surface regions, after CSSP. The band contrast map in Fig. 5.17 (a) illustrates a very high indexing rate for the Cr coating, and individual Cr particles and particle boundaries were resolved. The IPF map (Fig. 5.17 b) and KAM map (Fig. 5.17 c) of the peened coating reveal the typical strained cold spray microstructure. The maps do not reveal any major differences in microstructure or strain at the coating surface compared to the rest of the bulk Cr coating, indicating that the peening treatment was rather gentle. Majority of the coating exhibited no chipping or delamination, indicating peening is an effective way of compacting the undeformed surface particles without compromising coating integrity.

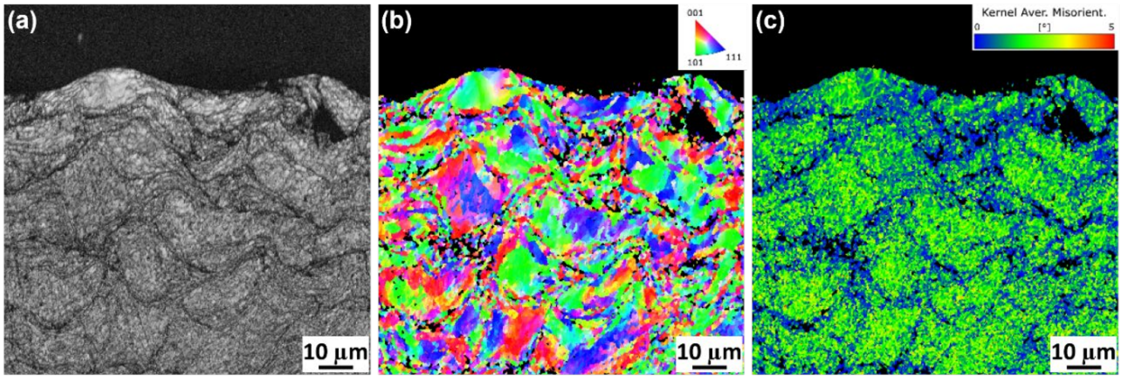

Fig. 5.17. EBSD results for the Cr-N2 coating on Zry-4 sprayed at 500 mm/s after CSSP: (a) band contrast map; (b) IPF map; (c) KAM map.

It may be possible to use CSSP to achieve a coating that meets thickness specifications (<30 µm) and thereby minimizes or even eliminates post-deposition grinding or polishing treatments. Fig. 5.18 shows a Cr-N2 coating deposited using 600 mm/s spray speed, after CSSP. The minimum as-deposited coating thickness was about 28 µm and CSSP of this region resulted in a coating thickness between 5-20 µm. The compacted surface has the potential to provide protection in both normal operating and high temperature accident environment while avoiding spallation of loose particles, respectively.

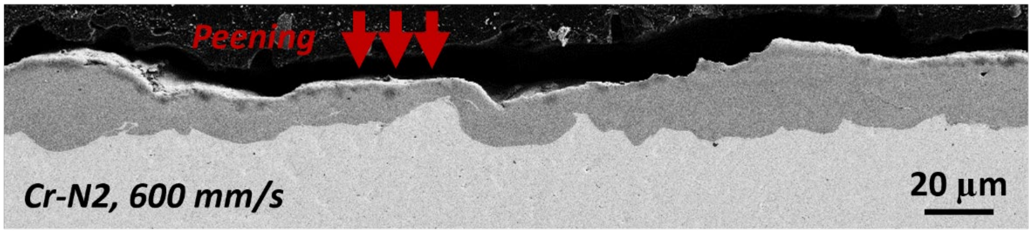

Fig. 5.18. Cross-sectional SEM image of a Cr-N2 coating on Zry-4 sprayed at 600 mm/s, after CSSP. This demonstrates a thin coating <20 µm thickness can be achieved with CSSP.

5.3. Addressing interfacial roughness in cold spray Cr coatings

5.3.1. Low velocity cold spray and dual-layered coatings

This research is unique in that it involves a hard and less deformable particle material (Cr, hardness for electrolytic soft powders: 4.1 GPa) impacting a softer substrate (Zr-alloy, hardness: 1.8 GPa). This combination can give rise to notable interfacial roughness. To investigate the possibility of reducing interfacial roughness, a two-step deposition approach involving deposition of an initial layer at low particle velocities (referred to as *seed layer*, postulated to yield low interfacial roughness) followed by deposition at high particle velocities to create a top layer. The goal was to lower the interfacial roughness while at the same time achieving good bond strength between the coating and substrate. A schematic illustration of this concept in Fig. 5.19.

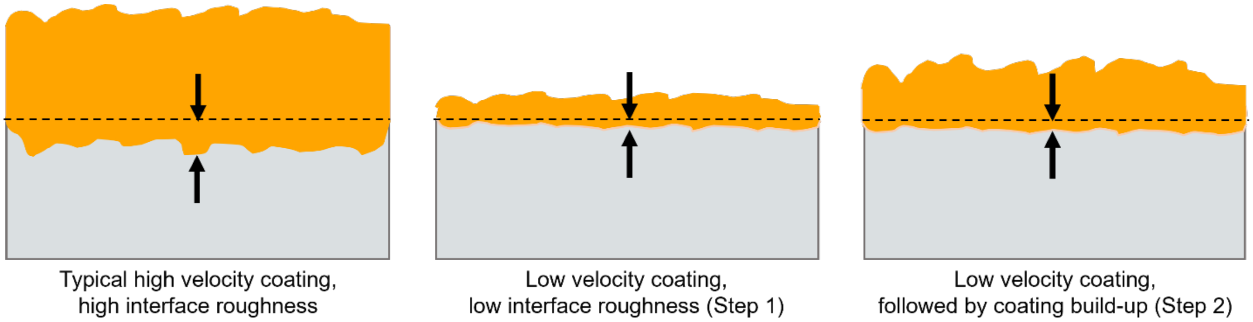

Fig. 5.19. Schematic illustration of the interfacial roughness of a typical high velocity coating (left). The proposed concept involves spraying a low velocity seed layer to minimize interfacial roughness (center), and then build up coating thickness with a second pass top layer sprayed at a higher velocity (right).

The cross-sectional SEM images of seed layers deposited using different conditions of Cr-N2 are shown in Fig. 5.20. Three experimental campaigns were undertaken, each with a different gun traverse speed (Table 2.7). For Campaign 1, the seed layer sprayed at gas preheat temperature of 300 °C qualitatively showed the lowest interfacial roughness (Fig. 5.20 a). Campaign 2 was designed to spray at temperatures below 300 °C and reduced translation speed to enhance surface coverage. The images in Fig. 5.20 (d-f) revealed that full coverage was still not achieved for all conditions. Campaign 3 repeated the temperatures of Campaign 2 but decreased the translation speed further to 50 mm/s to improve seed layer coverage (Fig. 5.20 g-i). Similarly, the 300 °C gas preheat temperature resulted in low roughness. The average thickness of the seed layer was about 5 µm and the average interfacial roughness was about ~1.9 µm.

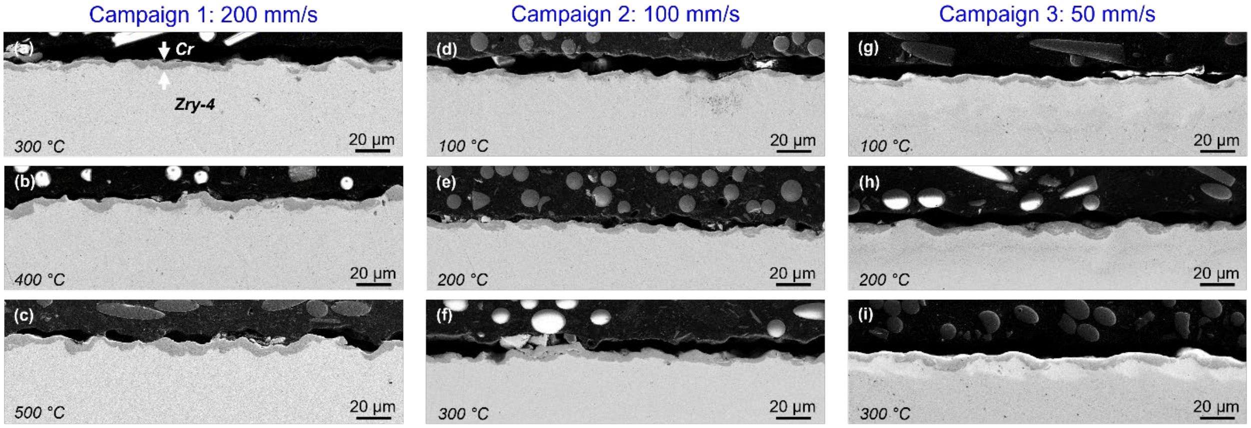

Fig. 5.20. Cross-sectional SEM images of the Cr/Zry-4 interface from three low velocity seed layer deposits. Carrier gas preheat temperatures are noted on the bottom left of each image. Additionally, each column compares a different gun translation speed: (a-c) 200 mm/s; (d-f) 100 mm/s; (g-i) 50 mm/s.

Seed layers sprayed using 50 mm/s gun translation speed (campaign 3) were used as substrates for deposition of a top layer at high velocity. Fig. 5.21 (d-f) shows cross-sectional images of the three seed layers used. The leftmost column (Fig. 5.21 a-c) shows top layers sprayed using the high velocity Cr-N_2 gas conditions, and the rightmost column (Fig. 5.21 g-i) shows top layers sprayed using the high velocity Cr-He gas condition. Visual examination reveal both Cr-N_2 and Cr-He top layers exhibit a rough interface comparable to or rougher than coatings deposited without a seed layer, indicating that the underlying Zr-alloy substrate had significant deformation capacity remaining after the deposition of the seed layer.

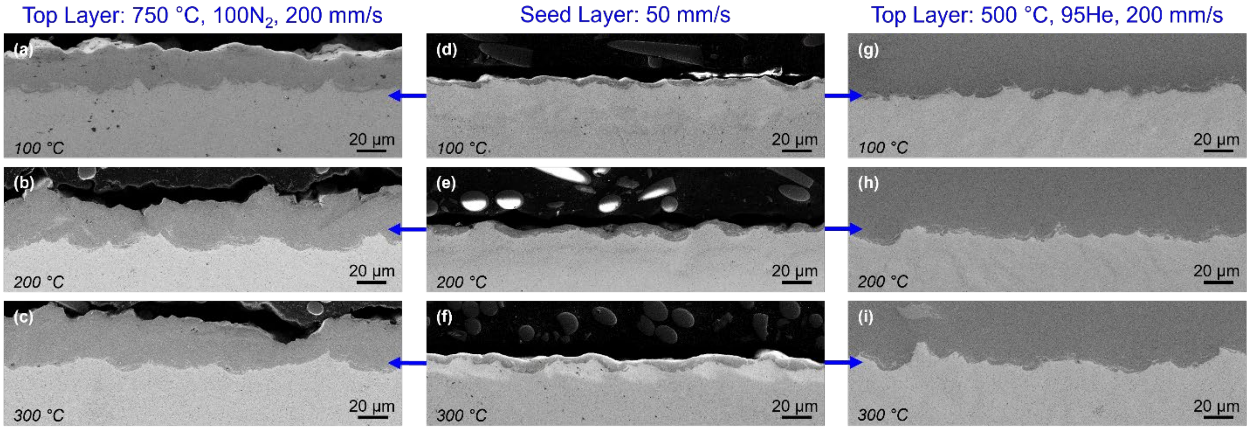

Fig. 5.21. Cross-sectional SEM images of three seed layers (temperature listed lower left) sprayed using 50 mm/s gun translation speed (d-f). Subsequently, a top layer was sprayed with high velocity N_2 gas (a-c) or high velocity He gas (g-i).

5.3.2. *Effects of delay time and surface activation*

With the knowledge gained from the single-particle impact experiments (discussed in Section 4), it is now understood that the seed layers were deposited using particle velocities $v_p \approx 520 - 610\ m/s$, which lie in the vicinity of the critical velocity for interfacial bonding ($v_{crit}^{Cr-Zr} \sim 550\ m/s$) but below the critical velocity for Cr coating buildup ($v_{crit}^{Cr-Cr} \sim 640\ m/s$).

It is worth briefly discussing the results of low velocity cold spray in the context of the research by Klinkov and Kosarev [216], who deposited aluminum particles on copper substrates using cold spray to understand deposition efficiency. They explained that, at lower velocities, particles first impact and rebound from the substrate, thus cleaning and deforming the surface. After a certain time, the surface is sufficiently activated (i.e., roughened) and particles begin to attach, rapidly forming a coating. This "delay time" for particle attachment and coating formation depends on particle impact velocity and critical velocity. The schematic shown in Fig. 5.22 illustrates this process, with associated plan-view and cross-sectional SEM images from seed layer coatings deposited in this research ($v_p \approx 540\ m/s$). As initial particles impact the substrate, they rebound and roughen the surface (Fig. 5.22 a). After sufficient activation time, particles begin to attach and form the first layer coating on the substrate (Fig. 5.22 b). Due to the low deposition efficiency of Cr-on-Cr (0%), the first layer coating is sufficiently flattened due to repeated particle rebounds (Fig. 5.22 c).

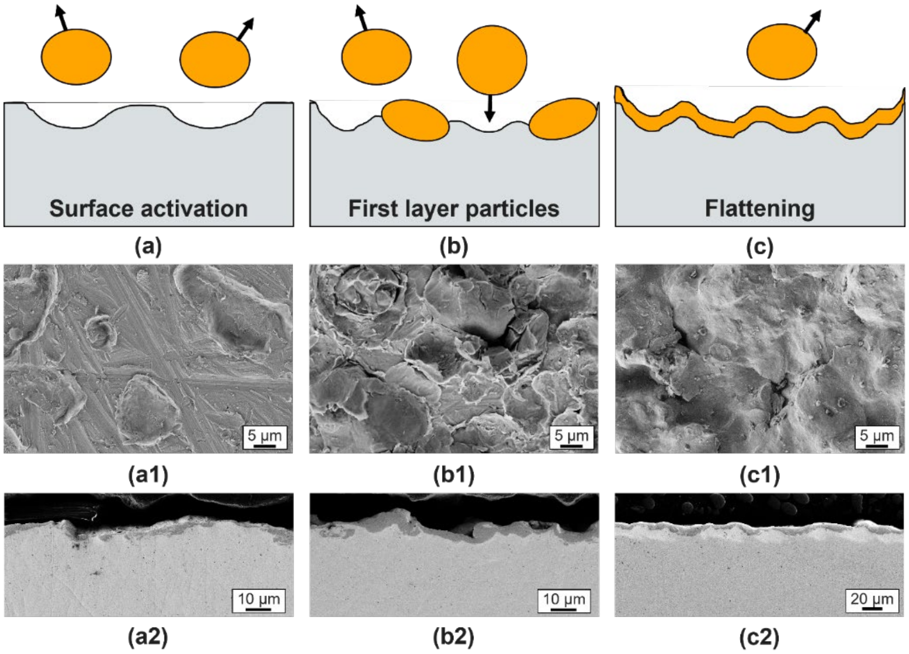

Fig. 5.22. Schematic illustration of low-velocity coating formation for Cr on Zr-alloy: (a) surface activation of the substrate caused by rebounded particles; (b) after sufficient surface activation, first layer of particles attach; (c) flattening of the first-layer coating due to rebounding caused by low deposition efficiency.

From this schematic, we can understand why the seed layers did not reduce interfacial roughness. Low deposition efficiency resulted in extreme flattening of the first layer coating, so much so that interfacial mechanical mixing occurred between the Cr particles and Zr-alloy substrate [217]. This essentially fused the Cr particles into the substrate, creating a new substrate with a roughened surface after surface activation.

The apparent work-hardening of the substrate due to repeated particle rebounds did not prevent roughness from increasing after high-velocity deposition of the top layer coating.

Klinkov and Kosarev [216] demonstrated that, at a certain critical velocity, particles may attach if the surface is sufficiently activated. They also demonstrated that the delay time decreases to zero at sufficiently high particle impact velocities, leading to particles bonding a non-activated surface. We've experimentally identified this velocity as $v_{DE=100}^{Cr-Zr} \sim 670\ m/s$, where the deposition efficiency of Cr-on-Zr reaches 100% (Fig. 4.3). Theoretically, eliminating the activation requirement (i.e., roughening of Zr-alloy) for first-layer coating formation should yield low interfacial roughness. However, this was not the case, which led to the examination of the effect of high velocity particles deposited per unit.

Fig. 5.23 shows FIB cross-sections of single Cr particles bonded to Zry-4 using increasing particle impact velocity (repurposed from Section 4 of this document). The measured particle penetration depth in Zry-4 ranged from 3.8 to 5.2 µm for Cr particles impacting from 620 to 880 m/s. This is a small change in penetration depth for a large change in particle velocity. The typical peak-to-valley interfacial roughness of Cr coatings deposited at similar particle velocities measured between 8 and 20 µm. It was hypothesized that the large number of particles impacting one specific area of the substrate at one specific time (during coating deposition) significantly increases the penetration depth and roughness of the coatings. A schematic illustration of this theory is shown in Fig. 5.24 (a-c).

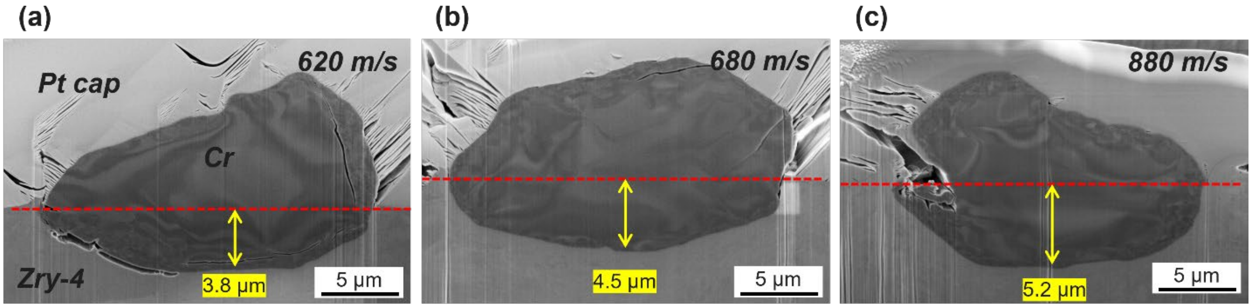

Fig. 5.23. SEM images of cross-sectioned Cr particles bonded to Zry-4 at different particle velocities: (a) 620 m/s; (b) 680 m/s; (c) 880 m/s; Measured particle penetration depths are shown in yellow. Cracks observed are in the Pt cap used for FIB sample preparation and not a part of the Cr-Zr system.

Alternatively, if the particle flow rate was reduced, we'd expect a situation as shown in Fig. 5.24 (d-f). Fewer particles impacting per unit area per unit time would reduce the momentum exchange to the substrate, and particle penetration would be influenced solely on the impacting particle velocity such as shown in Fig. 5.23. Additionally, the substrate would experience less deformation and work-hardening, so the tamping effect of additional particle impacts could potentially level out the interfacial roughness due to additional deformation capacity.

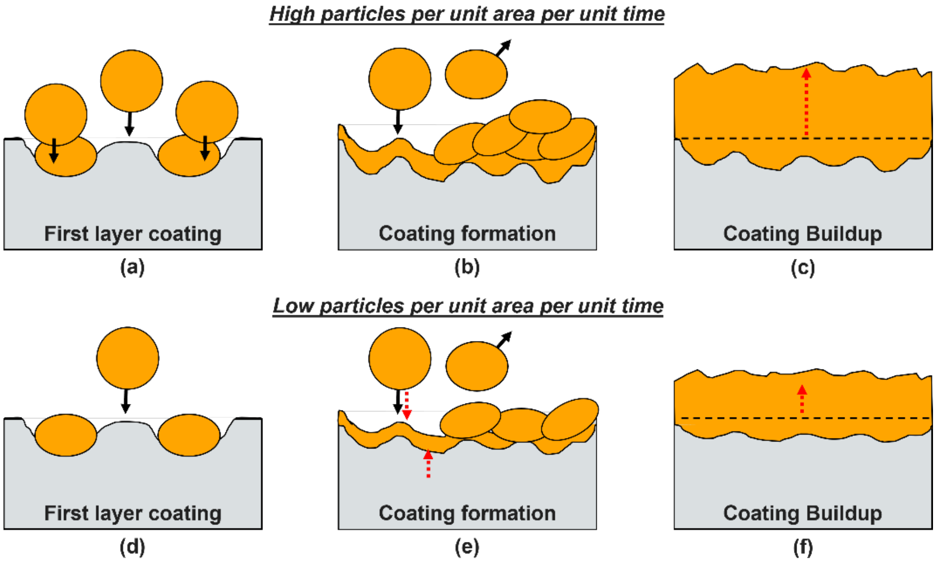

Fig. 5.24. Schematic illustration of the effect of particle flow/deposition rate on interfacial roughness. (a-c) High particle flow rate, causing multiple particles to impact one specific area at the same time, leading to increased roughness; (d-f) Low particle flow rate, which results in fewer particles impacting one specific at the same time, leading to reduced penetration and interfacial roughness.

A second cold spray experiment was performed with the goal of decreasing the interfacial roughness. To achieve uniform particle flow through the powder feed-line, the particle flow rate was maintained using the same typical parameters. However, the gun traverse speed was increased to reduce the number of particle impacts per unit area per unit time. One consequence with increasing this spray speed is reduced coating thickness, which may require additional passes to build up coating. Additionally, the operation of the cold spray gun was changed from pressure-control to gas-flow-control. This has the effect of reducing the input pressure of the gas by decreasing the gas flow rates while maintaining the same gas preheat temperature and results in a smoother gas flow.

Fig. 5.25 shows cold spray Cr-N2 coatings on Zry-4 deposited using (a) 200 mm/s gun speed and pressure-control (P.C.) mode, and (b-f) 200-600 mm/s gun speed and flow-control (F.C.) mode. There were some qualitative improvements in the roughness in terms of minimization of extrusion events, however, the peak-to-valley roughness remained high. It's possible the parameters used here were not aggressive enough to significantly lower the flow of particles impacting the substrate at the same time.

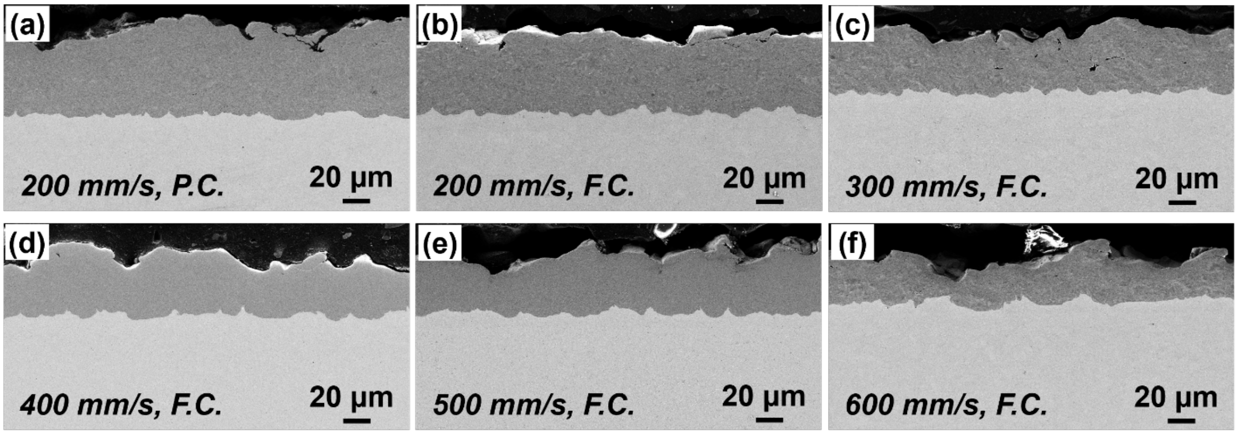

Fig. 5.25. Cross-sectional SEM images of cold spray Cr-N2 coatings on Zry-4 using the following gun speeds: (a) 200 mm/s in pressure-control (P.C.) mode; (b-f) 200, 300, 400, 500, and 600 mm/s in flow-control (F.C.) mode.

To conclude, this research attempted to use the insights gained from single-particle impact experiments and particle impact modeling to design experiments to improve cold spray Cr coatings on Zr-alloy substrates for the LWR application. While cold spray parameters have many competing effects that influence coating quality, the results in this chapter showed that improvements are possible, even with a mismatched materials system like Cr and Zr.

6. Microstructural Evolution in Ion Irradiated Cold Spray Cr Coated Zr-Alloy

6.1. Experiment description

This section of the research focuses on irradiation damage effects in cold spray Cr-coated Zr-alloy and represents the first in-depth investigation of this specific area. High energy Xe^{26+} ion irradiation was performed to understand irradiation effects in both in the bulk cold spray Cr coating and the Cr/Zr-alloy interface. High resolution TEM in conjunction with EDS was used to elucidate the effects of irradiation on interfacial mixing, compositional redistribution, and amorphization on a nanoscale, while the nanoindentation method was used to discern any irradiation-induced mechanical property changes.

For this study, cold spray Cr-He coatings were deposited on Zry-4 substrate using a gun traverse speed of 400 mm/s, producing a coating thickness of 75 µm ± 10 µm, as shown in cross-section in Fig. 6.1 (a). To prepare the sample, the Cr coating was polished in such a way that that there was a gradient in coating thickness ranging from zero to 50 µm as shown in Fig. 6.1 (b). For ion irradiation the samples were progressively ground culminating with a final grinding step with 1200 grit SiC paper. This was followed by polishing using progressively finer polycrystalline diamond suspensions down to 0.05 µm, culminating in a final polishing step with 0.02 µm colloidal silica. The samples were then ultrasonically cleaned using micro-organic soap, pure water, acetone, ethanol, and then allowed to dry in air.

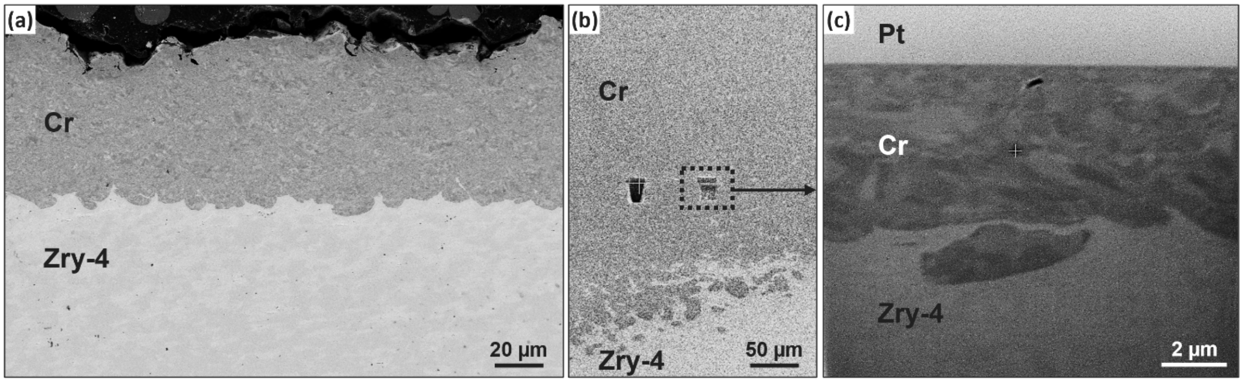

Fig. 6.1. (a) Cross-sectional SEM image of as-deposited Cr coating on Zry-4; (b) Plan-view SEM image of the coating after polishing, showing thin Cr coating and exposed Zry-4; (c) Cross-section of thin Cr coating (~5 µm) lifted out from (b) using FIB.

The Cr-coated Zry-4 samples were irradiated in the Argonne Tandem Linac Accelerator System (ATLAS) beamline at Argonne National Laboratory, and with the author participating in-person and collaboratively with personnel at ANL. The sample was heated to 350 °C and irradiated with 80 MeV Xe^{26+} ions, with an average ion flux of 2.13×10^{12} ions/cm^2/s. Total irradiation time was about 2 hours. The damage accumulation in the materials was estimated using SRIM software in conjunction with the Quick Damage Kinchin-Pease mode [218]. Displacement energies for Cr and Zr were set to 40 eV. This simulation indicated a maximum damage of 30 dpa at a depth between 5.0 to 5.5 μm from the Cr coating surface as shown in Fig. 6.2. The irradiation parameters used in this study are summarized in Table 6.1.

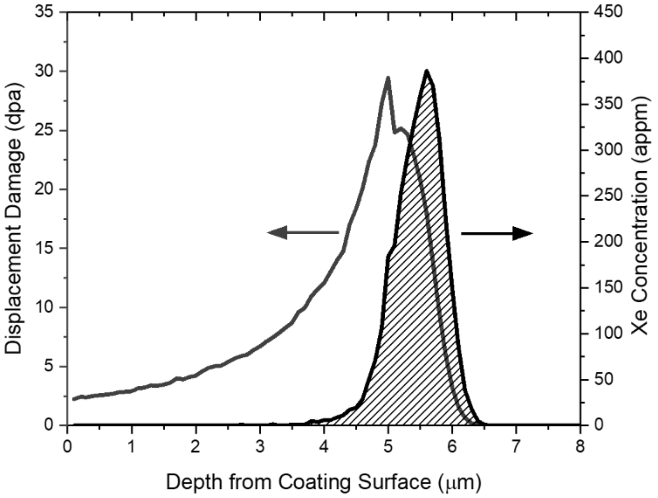

Fig. 6.2. SRIM simulation of damage (dpa) and Xe concentration in cold spray Cr coatings on Zry-4 after irradiation with 80 MeV Xe^{26+} ions.

Table 6.1. Summary of the irradiation parameters used in this study.

Sample	Ions	Energy (MeV)	Displacement damage		Total fluence (ions-cm^{-2})	Temperature (°C)
			depth (μm)	dpa		
Cr-coated Zry-4	Xe^{26+}	80	5.0-5.5	25-30	1.5×10^{16}	350

Two cross-sectional thin foil specimens for TEM analysis were taken from the irradiated sample in areas corresponding to the damage calculation. One sample was taken from an area where the Cr coating was approximately 5 μm thick (example shown in Fig. 6.1 c) so that the peak damage occurred at the Cr/Zr interface and the damage profile extended slightly into the Zry-4 substrate. The other sample was taken where the Cr coating was thicker (>10 μm), so the damage was confined to just the Cr coating. In addition, two thin foil samples were taken from the as-deposited (unirradiated) cold spray Cr coating on Zry-4, one encompassing the interface and one within the bulk Cr coating, to account for just thermal effects but not irradiation effects.

Microstructural characterization was performed using TEM, STEM, and HRTEM imaging techniques. EDS was performed on the samples in STEM mode using a Bruker QUANTAX 200 EDS equipped with XFlash7 detector, with analysis conducted using the ESPRIT2 software. Hardness measurements of the Cr coating before and after irradiation were performed by nanoindentation. The sample was indented both within and outside of the ion beam region, so that both regions experienced the same thermal history during irradiation. 140 indents were performed in a 20 × 7 grid using displacement control mode, with each indent spaced 40 μm apart. The programmed contact depth for each row of indents increased by 1 μm, up to 7 μm maximum depth for the last row. The peak indentation loads varied from 85 mN (at 1 μm depth) up to 2.5 N (at 7 μm depth). Optical microscopy and SEM were used to characterize the indents after testing, and atomic force microscopy (AFM) was used in tapping mode to characterize the surface topography and measure the pileup height for selected indents.

6.2. Interfacial characterization of the as-deposited and irradiated Cr-coated Zry-4

A BF-STEM image of a section of the cold sprayed Cr coating on Zry-4 near the interface is shown in Fig. 6.3 (a). The deformation of Zry-4 substrate around the impacted Cr particles during particle impact is evident. Fig. 6.3 (b) shows a higher magnification BF-STEM image of this interface, which reveals multiple insights into the particle impact/bonding process. First, the Zr-side of the interface contains very fine (<200 nm) nanoscale grains, which have formed from dynamic recrystallization of Zry-4 during high strain rate plastic deformation upon impact [111,219]. Second, the Cr grains near the interface are larger (>500 nm) and show contrast from dislocations and sub-grain boundaries, indicating that they experienced less plastic deformation than the near-interface regions of Zry-4. Away from the interface, the Cr coating shows a heterogeneous microstructure with larger grains in particle interiors and smaller grains near particle boundaries. The Cr coating microstructure will be discussed in detail in Section 6.3.

Further examination of the as-deposited Cr-Zr interface was carried out by HRTEM imaging as shown in Fig. 6.3 (c). Fast Fourier Transform (FFT) analysis of different regions of the image reveal bcc Cr phase on one side of the boundary (marked region 1), and a mixed signal corresponding to both bcc-Cr and hcp-Zr on the other side (marked region 2). It is insightful to note the presence of crystallographic coherency between the Cr coating and the Zry-4 substrate. A combination of mechanical interlocking from jetting of the substrate (shown in Fig. 6.3 a) and metallurgical bonding is evident from the strong crystallographic coherency between Cr and Zr (shown in Fig. 6.3 c), which ensures good adhesion of the Cr coating to the Zry-4 substate.

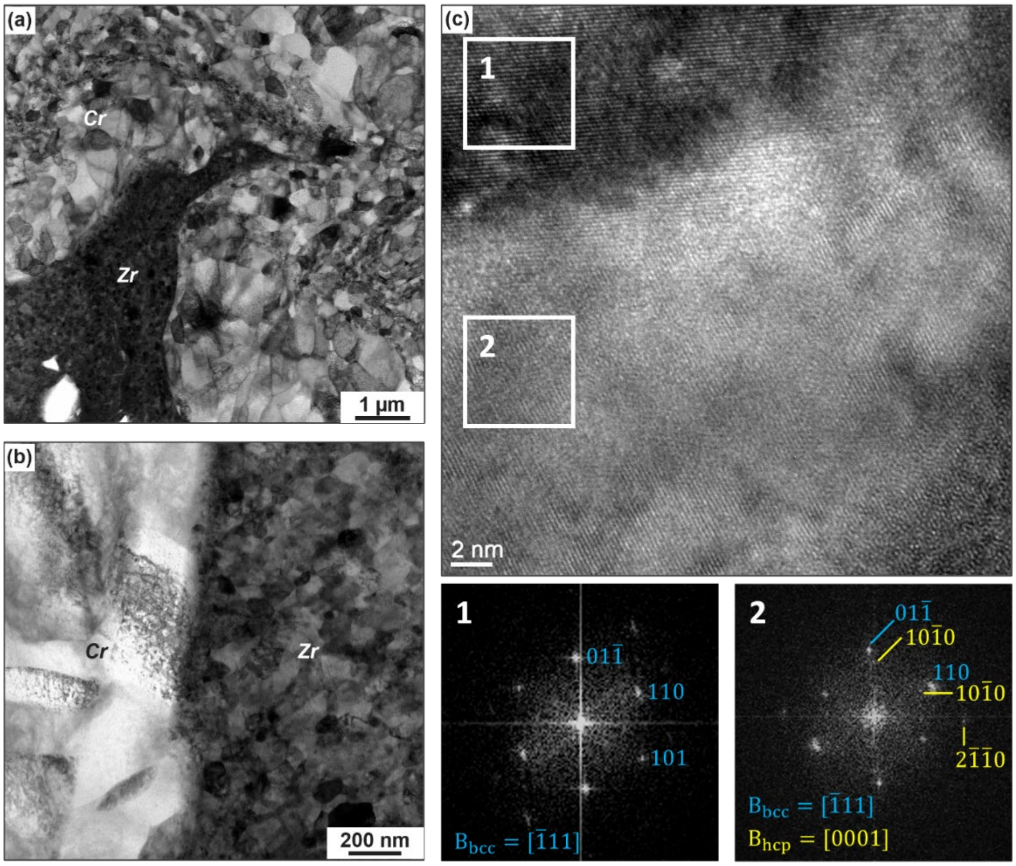

Fig. 6.3. (a, b) BF-STEM images of the unirradiated cold spray Cr-coated Zry-4 sample, with the higher magnification image (b) taken away from the jet lip; (c) HRTEM image of the unirradiated Cr-Zr interface with associated FFTs, showing crystallographic coherency between the lattices of the Cr coating and Zry-4 substrate.

Results of STEM-EDS measurements obtained from near the interface of the as-deposited Cr on Zry-4 sample are shown in Fig. 6.4. A distinct contrast variation delineates the Cr/Zry-4 interface in both the

HAADF image and the EDS spectral maps. However, EDS maps of Cr and Fe do not reveal such a sharp interface. Instead, co-segregation of Cr and Fe on the Zry-4 side up to 200 nm away from the interface can be observed. This suggests that the high strain-rate adiabatic shear deformation and associated thermal spike during cold spray impact may have caused the diffusion of Cr into the Zry-4 substrate, i.e., resulting in nano-scale compositional mixing. The observation of co-segregation of Fe is likely attributable to the 0.18-0.24 wt.% Fe that is inherently present in Zry-4 [220]. No other element besides Cr and Fe were found to segregate in the interfacial regions based on the EDS measurements. Additional EDS revealed that the presence of Fe was found mainly in regions where the Zry-4 substrate was highly strained, such as the jetted region shown in Fig. 6.3 (a).

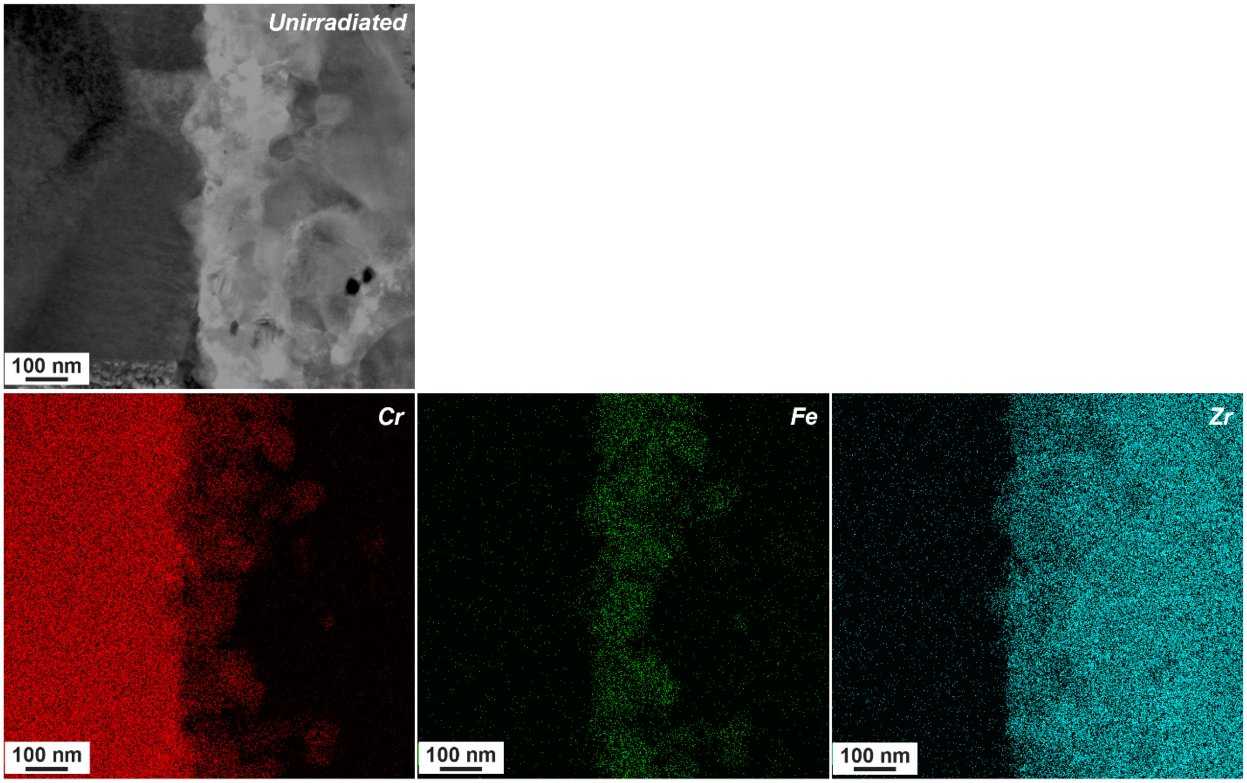

Fig. 6.4. HAADF-STEM image of the unirradiated Cr-Zr interface with associated EDS elemental mapping, including Cr (red), Fe (green), and Zr (blue), showing Cr and Fe co-segregation up to 200 nm within the Zr-side of the interface.

A BF-STEM image of the irradiated Cr coating on Zry-4 is shown in Fig. 6.5 (a). The FIB lamellae contained multiple Cr-Zr interfaces (indicating this was a region of the interface with pronounced jetting), which makes it useful for investigating irradiation damage effects at different irradiation damage (dpa) levels. Fig. 6.5 (b) shows a higher magnification STEM image taken at the interface, about 5 µm from the coating surface (~30 dpa). The Cr coating and Zry-4 substrate microstructure appear similar to the as-deposited structure near the interface, with a recrystallized nanograined Zry-4 microstructure and a larger grained, dislocation-intense Cr microstructure.

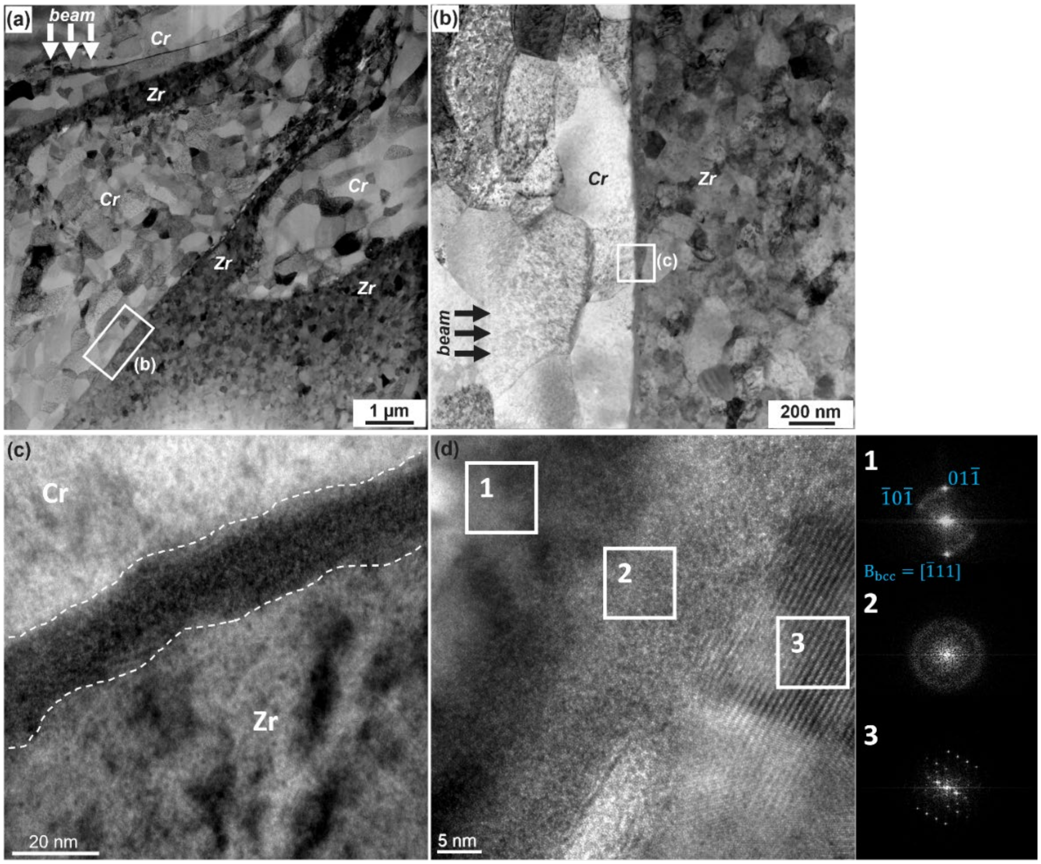

Fig. 6.5. (a, b) BF- STEM images of the cold spray Cr coating on Zry-4 after Xe^{26+} ion irradiation, with the higher magnification image (b) taken ~5 µm from the coating surface (up to 30 dpa). The arrows indicate the beam direction, or ion travel through the irradiated sample. (c) BF-TEM image of the irradiated Cr-Zr interface showing a dark band in-between the Cr and Zr regions; (d) HRTEM image with associated FFTs, showing an amorphous band (FFT-2) approximately 20 nm thick, with crystalline Cr (FFT-1) and Zr (FFT-3) phases on either side.

However, a clearly defined intermediate contrast exists at the interfacial boundary of the irradiated sample that was not observed at the coating-substrate interface of the as-deposited sample. A higher magnification BF-TEM image of the irradiated interface focusing on the intermediate contrast layer is shown in Fig. 6.5 (c). The average thickness of this layer was about 20 nm. HRTEM was performed to investigate the microstructure in the vicinity of the irradiated interface, as shown in Fig. 6.5 (d). On either side of this band, separate bcc-Cr (FFT-1) and hcp-Zr (FFT-3) phases were identified, while the band itself (FFT-2) was identified as amorphous, apparent from the diffuse intensity ring in the FFT. Thus, the heavy ion irradiation transformed about 20 nm of the crystalline cold spray Cr-Zr interface into an amorphous structure. This amorphous band was consistently present at all Zr-Cr interfaces that were between 4.5 to 5.5 μm below the surface of the Cr coating, which corresponded to the peak damage depths.

STEM-EDS of the same irradiated Cr-Zr interface is shown in Fig. 6.6. The lower magnification maps in Fig. 6.6 (a) do not reveal the same Fe segregation along the interface after irradiation (as seen in the as-deposited specimen), instead manifesting in certain spots or in precipitates within the Zry-4 substrate. Interestingly, some Fe segregation was found near interfaces closer to the surface (<4 μm) but was not widespread at the peak damage interface. The higher magnification EDS maps in Fig. 6.6 (b) show the distribution of Cr and Zr around the interface, with more Cr signal on the Zr side of the interface. This is consistent with what was shown for the as-deposited sample, in that Cr is more likely to diffuse into Zr than vice-versa.

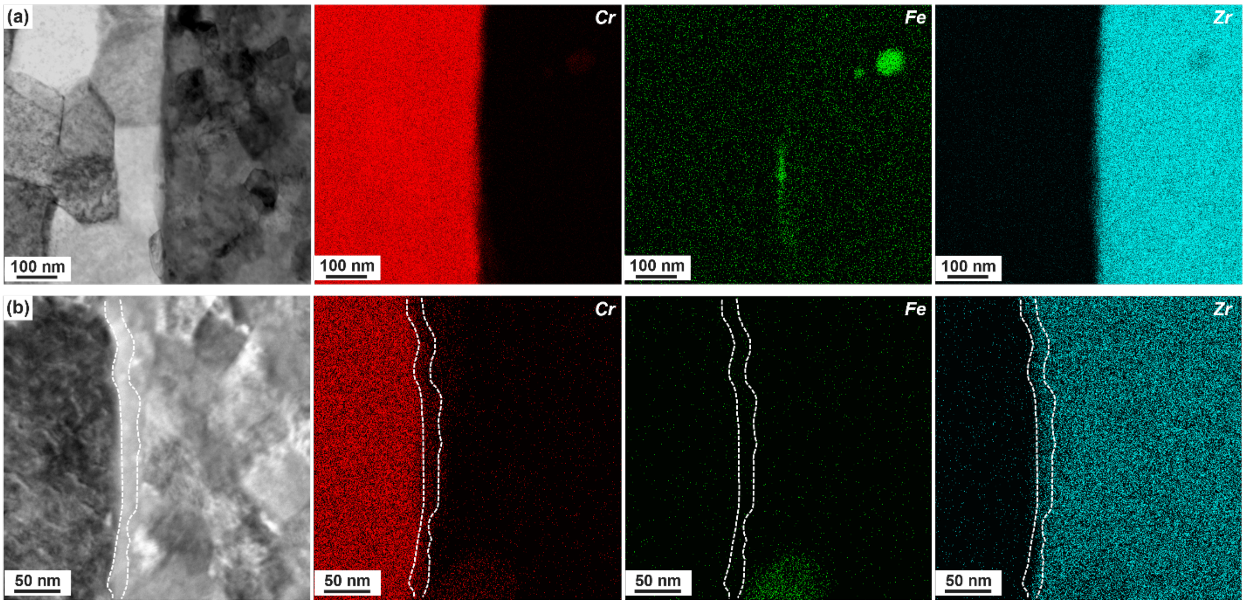

Fig. 6.6. (a) BF-STEM image of the irradiated Cr-Zr interface with associated EDS spectral mapping. (b) Higher magnification HAADF-STEM image of irradiated Cr-Zr interface with associated EDS spectral mapping, including Cr (red), Fe (green), and Zr (blue). The amorphous layer is located between the white dotted lines.

6.3. Microstructural characterization of the as-deposited and irradiated Cr coatings

BF-STEM imaging was used to compare the bulk microstructure of the as-deposited and irradiated cold spray Cr coatings, as shown in Fig. 6.7. The as-deposited Cr coating (Fig. 6.7 a) showed regions of elongated and dynamically recrystallized grains surrounded by lesser deformed, dislocation-intense grains. Dynamically recrystallized grains were typically sandwiched in between elongated grains or at the tail ends of particle boundaries, corresponding to regions of highest plastic strain. The irradiated sample (Fig. 6.7 b) presented a similar microstructure underneath the damaged region, showing a heterogeneous mixture of equiaxed and elongated grains. However, within the peak damage region (as indicated by the SRIM overlay), the inter-particle boundary at the top left of the image revealed more nanoscale, equiaxed recrystallized grains than a typical particle boundary found in the as-deposited coating. It is speculated that irradiation-induced recrystallization occurred at the interparticle boundaries of the irradiated sample, an effect that has been previously been observed in irradiation damage studies of heavily cold worked materials [81]. These fine recrystallized grains cross-over the original interparticle boundaries, partially obliterating them to create a stronger interparticle bonding.

Additionally, higher magnification TEM images were captured in a grain away from the interparticle boundaries, but still in the peak damage region (denoted by the white box in Fig. 6.7 b). This was done to avoid the contrast arising from high dislocation density in the IPB regions. The images shown in Fig. 6.7 (c-d) reveal nano-sized voids (1-3 nm) within a lesser deformed irradiated Cr grain, confirmed by using a common underfocus (Fig. 6.7 c) and overfocus (Fig. 6.7 d) TEM imaging technique.

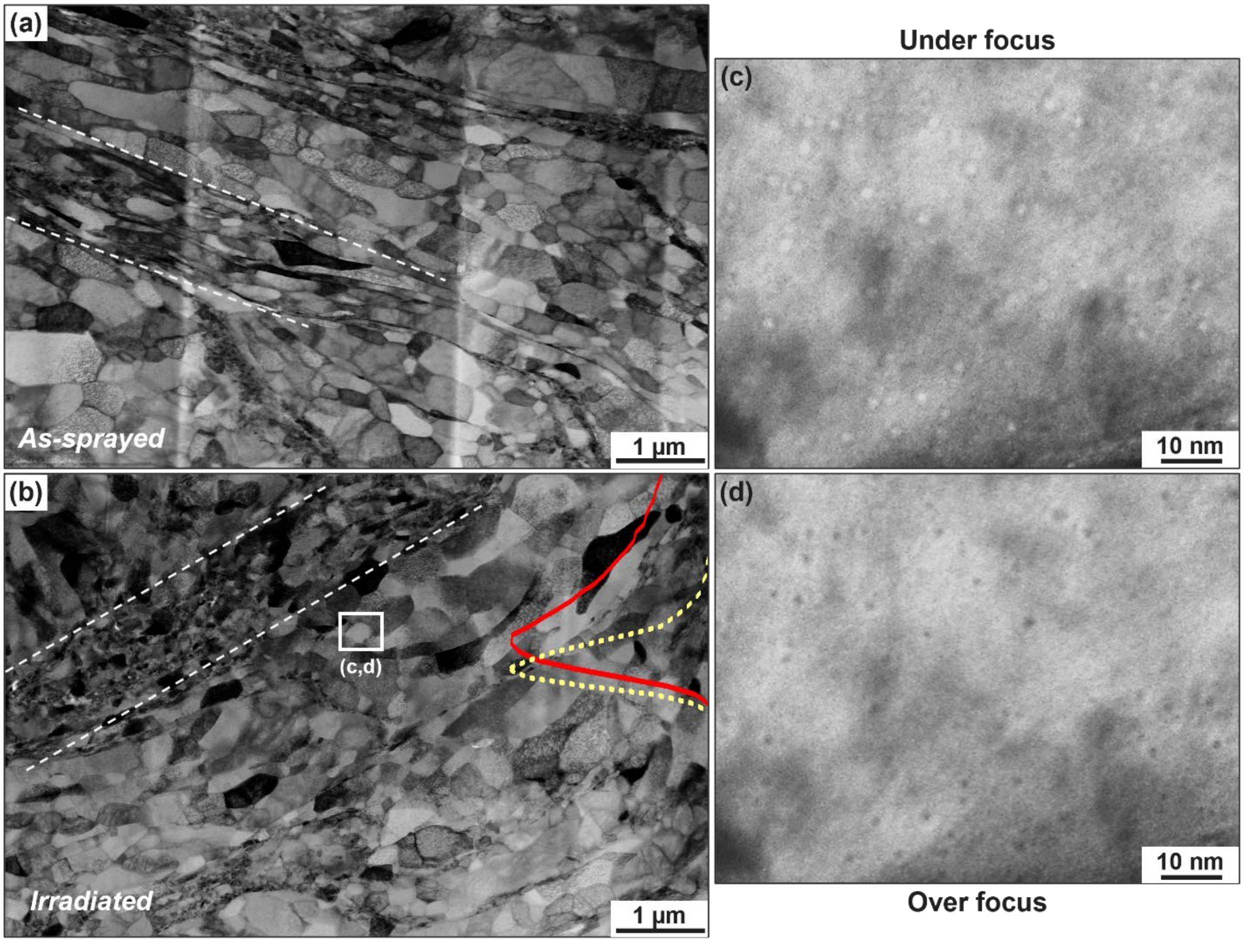

Fig. 6.7. BF-STEM images of the cold spray Cr coated samples: (a) as-deposited condition; (b) after Xe^{26+} *ion irradiation. SRIM damage vs. depth profile simulations are superimposed on the image for the irradiated sample that show dpa (solid red line) and Xe ion concentration profile (yellow dashed line). Notable inter-particle boundaries are marked between the white dashed lines. The region indicated in (b) was imaged using BF-TEM to reveal nano-scale voids in (c,d).*

Nanoindentation testing results of the unirradiated and irradiated Cr coatings are shown in Fig. 6.8. The mean contact depth was slightly lower than the maximum programmed depth, as shown in Fig. 6.8 (a). Hardness within 1 μm of the surface was about 5.9 GPa in the unirradiated (thermal effects only) and irradiated regions of the coating (Fig. 6.8 b). At the maximum contact depth, hardness dropped to 3.0 GPa and 1.9 GPa for the unirradiated and irradiated coatings, respectively. The reduction of hardness with indentation depth has been routinely observed due to the indentation size effect [221]. However, nanoindentation results reveal that the irradiated coating was consistently softer approaching the peak damage depth.

Fig. 6.8 (c-d) shows SEM images of indents on the surface of the unirradiated and irradiated coatings. Both coating conditions displayed a significant amount of pileup around the indents. Using AFM measurements, the average pileup of indents made at 1 and 7 µm peak depths were observed to be 260 and 970 nm, respectively for the unirradiated coating, and 130 and 1030 nm for the irradiated coating, respectively. Both samples showed higher pileup with increasing indentation depth, but no discernable trend was discovered between samples. The morphology of the Cr coating surface also changed during irradiation. The polished, unirradiated surface remained smooth on the side that experienced the same thermal history (Fig. 6.8 c), while the irradiated surface shows a rougher, textured surface with small (<500 nm) spherical features (Fig. 6.8 d), a product of energetic ion sputtering.

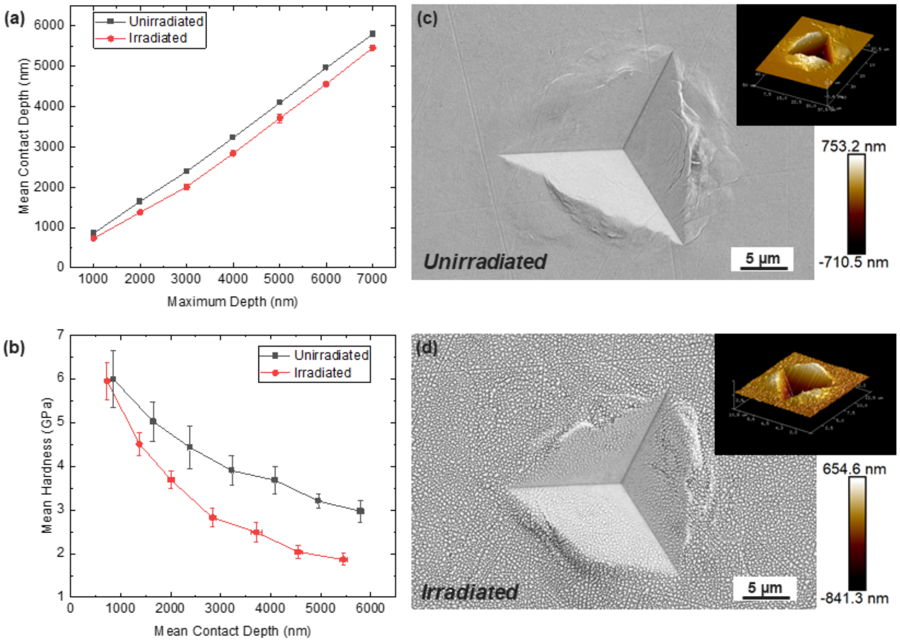

Fig. 6.8. Results from nanoindentation testing of the unirradiated and irradiated Cr coatings: (a) mean (actual) contact depth vs. maximum depth of indent penetration; (b) mean hardness vs. mean contact depth; Plan-view SEM images of indents with associated AFM 3D surface plots for the (c) unirradiated and (d) irradiated coatings. The indents correspond to 5 µm actual maximum depth penetration. AFM surface plots confirm the evidence of indentation pileup.

6.4. Fe segregation and amorphization at the irradiated Cr-Zr interface

STEM/EDS analysis of the as-deposited interface revealed higher concentrations of Cr and Fe near the interface (Fig. 6.4), up to 200 nm from the interface on the Zry-4 substrate side. Fazi et al. [89] used atom probe tomography (APT) to characterize the interface of cold spray Cr coating on Optimized ZIRLO^{TM}, where they identified segregation of Cr, Fe, and Nb near the interfacial region and up to 200 nm away from the interface on the OPZ side. The Fe concentration in that study reached up to 8% within 20 nm of the Cr-Zr interface. Optimized ZIRLO^{TM} contains up to 1.2% Nb and 0.13% Fe [5], whereas Zry-4 contains up to 0.24% Fe and negligible Nb. Fe concentration in this study reached up to 11% within 50 nm of the Cr/Zry-4 interface, and no Nb nor Sn segregation was observed. Additionally, the EDS spectral maps in Fig. 6.4 show Cr and Fe segregated within grains rather than along grain boundaries, which is in agreement with the work by Fazi et al. [89], which attributed the alloying element segregation from dissolution of second phase particles due to localized heat and shear during particle impact and plastic deformation.

For a more fundamental understanding of the phenomenon of Fe segregation, thermodynamic calculations were performed with assessed thermodynamic data corresponding to the Cr-Fe-Nb-Sn-Zr system [222] using Thermo-Calc v.2024(b) software [223]. Fig. 6.9 (a) shows an isothermal (at 300 °C), composition-dependent chemical potential map of Fe in an hcp Zr-Cr-Fe ternary solid solution. The data points overlaid on the map represent actual concentrations of Cr and Fe measured along the interface using STEM-EDS. The results indicate that the initial chemical potential of Fe in Zry-4 is about 13 kJ/mol (marked by the arrow in Fig. 6.9 a). During the initial impact of Cr on Zry-4, high strain rate deformation of the substrate is expected to produce temperature spikes that accelerate the diffusion of Cr into Zry-4. Iso-chemical potential contours from the map suggest that for the Cr concentration of 20-35 wt.% measured near the interface, an increase in the Fe concentration within the Zr-Cr-Fe solid solution up to 8-11 wt.% must occur to maintain the initial chemical potential of the Zr-alloy, i.e., equilibrium with the underlying substrate. In other words, the results demonstrate that a thermodynamic driving force does exist for the co-segregation of Fe with Cr along the interface during cold spray deposition.

Fig. 6.9 (b) also shows isothermal (at 300 °C) chemical potential curves of Fe, but along a section of the composition space depicted in Fig. 6.9 (a), i.e., at a fixed Cr composition of 35 wt. %, representative of a typical concentration dissolved in the Zry-4 substrate upon particle impact. In addition to the standard single-phase chemical potential, the chemical potential of an irradiated solid solution has also been plotted, by including an additional irradiation enthalpy of 13 kJ/mol (assumed to be contributed by irradiation-induced defects such as vacancies, interstitials etc.). This value of irradiation enthalpy was selected as a representative value, typical for the level of damage introduced into metallic materials, for illustration purposes [224]. For the Cr-content considered, a substantial decrease in Fe solubility from about 8 wt.% to 1.75 wt.% as a consequence of the introduction of the irradiation enthalpy can be observed. In other words, the introduction of the additional irradiation-induced enthalpy triggers a re-homogenization of the Fe concentration, which explains the STEM-EDS observations presented in Fig. 6.6. The approach does contain assumptions (e.g., does not consider kinetic driving forces), but nevertheless provides an initial explanation of compositional redistribution during irradiation.

It has also been observed that Fe undergoes faster diffusion in α-Zr at the irradiation temperatures and fluences used in this study, which could also explain the depletion of Fe in the interfacial region [225,226]. Wu et al. [88] used HRTEM to identify Fe at the interface of PVD Cr on Zr-alloy, and found up to 3.3 wt.% Fe in the form of C14 hexagonal close packed and C15 metastable face centered cubic $Zr(Fe,Cr)_2$ Laves phases. In contrast to the present study, they observed a slight increase in Fe concentration along the interface during irradiation, which increased stability of the C14 phase and led to the dissolution of the C15 phase.

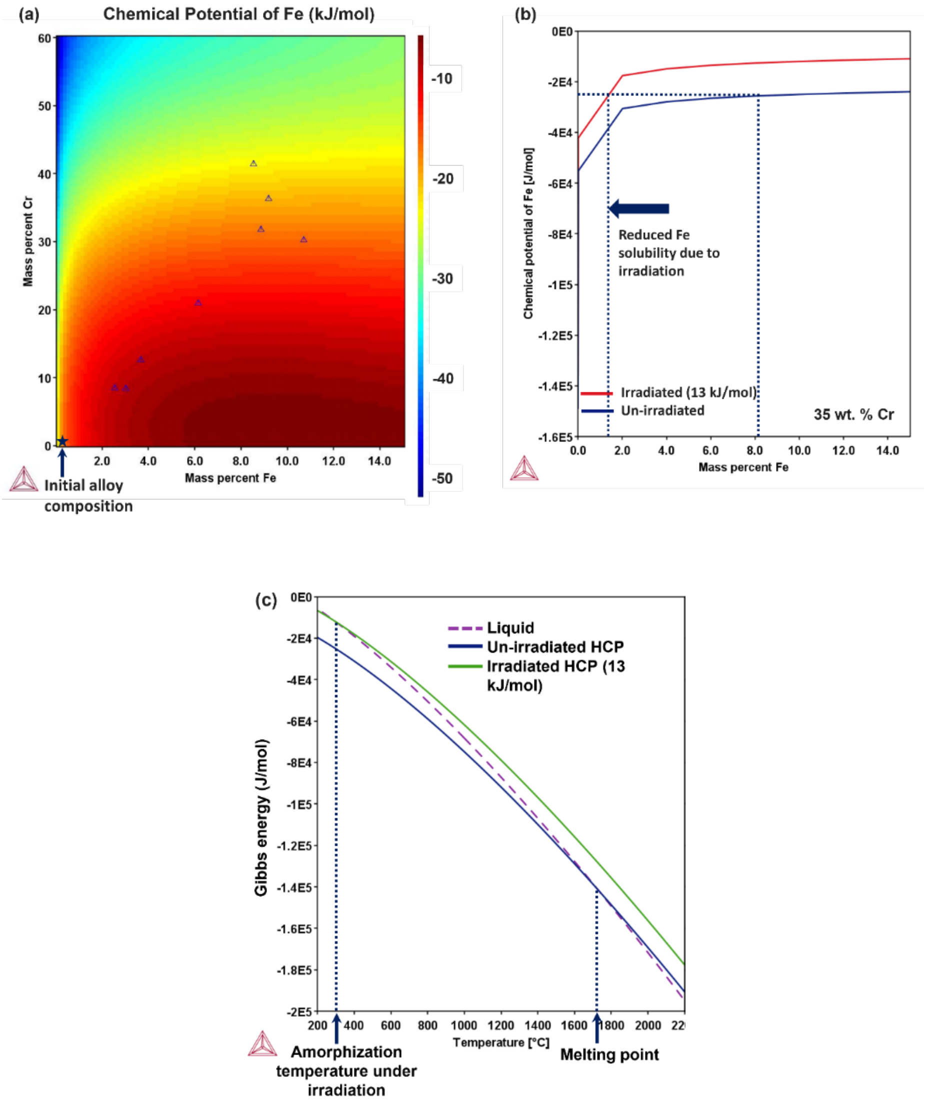

Fig. 6.9. (a) Standard isothermal (at 300 °C) chemical potential map of Fe in a ternary Zr-Cr-Fe solid solution as a function of Cr and Fe content in the unirradiated alloy. Measured EDS concentrations of Fe and Cr from Fig. 6.4 are shown as points on the map; (b) Chemical potential curves of Fe against mass percent Fe in the Zr-Cr-Fe solid solution for a fixed Cr content of 35 wt. %, in the standard condition and with the introduction of 13 kJ/mol of irradiation enthalpy. The results show reduced solubility of Fe due to irradiation. (c) Gibbs energy curves as a function of temperature for pure Zr in the liquid phase, standard hcp phase, and an irradiated hcp phase assuming an irradiation enthalpy of 13 kJ/mol.

The thermodynamics of amorphization on the Zr-rich side of the interface after irradiation was also evaluated using the thermodynamic data for pure Zr. Fig. 6.9 (c) shows Gibbs energy curves as a function of temperature for pure Zr in the liquid phase, standard hcp phase, and an irradiated hcp phase assuming an irradiation enthalpy of 13 kJ/mol. For these calculations, the formation of $ZrCr_2$ Laves phase and other intermetallic phases was not considered in view of the extremely slow long-range diffusion kinetics at the irradiation temperature [227]. With the introduction of an irradiation enthalpy of 13 kJ/mol, formation of the liquid (i.e., amorphous phase when extrapolated to low temperatures) becomes energetically favorable at the irradiation temperature of 300 °C. In other words, the calculations show that Zr is the primary driver for amorphization in this system. Griffiths et al. [226] demonstrated that amorphization of $Zr(Fe,Cr)_2$ precipitates depends on Fe and Cr concentration, and that depletion of Fe and increased Cr concentration stabilize the amorphous phase during irradiation between 520-600 K. It is possible that a similar phenomenon occurred here, with depletion of Fe from the interface into solid solution in Zr, and the increased Cr content from the coating promoted the stabilization of amorphous phase at the interface. Since the amorphous layer at the interface was quite thin (<50 nm), it is not expected to significantly affect adhesion of the Cr coating to the Zry-4 substrate as will be demonstrated in Section 8.3.5.

Again, the approach discussed here has built-in assumptions (for example, not including kinetics), but nevertheless provides an initial explanation of compositional redistribution and phase evolution during irradiation.

6.5. Recrystallization and microstructural effects in the irradiated Cr coating

For the as-deposited Cr coating, elongated grains exceeding 1 μm in length can be seen both within and between inter-particle boundaries (Fig. 6.7 a), with the width of these grains ranging from less than 100 nm to over 400 nm, respectively. Equiaxed, dynamically recrystallized grains less than 100 nm in diameter can also been seen in the center and at tail-ends of the inter-particle boundaries. Both elongated and dynamically recrystallized grains form during the high strain rate deformation and localized shear of Cr particles and aid in cohesive bonding [100,195,228].

After irradiation, a qualitative difference in microstructure and a quantitative difference in hardness was observed. Additionally, the absence of elongated grains at inter-particle boundaries within the peak damage region is notable (left side of Fig. 6.7 b). Instead, the formation of equiaxed grains at these sites that tend to obliterate the interparticle boundaries, with its associated beneficial effects. Some nano-scale porosity can also be seen within this inter-particle region, in the form of white contrast in the bright field image. In literature, similar elimination of elongated grains has been observed in 20% cold drawn steel after irradiation with 46 MeV Ni^{6+} ions up to 64 dpa [81], an effect that was attributed to grain boundary migration driven by dissolution of voids. Recrystallization and grain growth have also been observed in other bulk nanocrystalline materials subjected to ion irradiation, including pure metals (Ni, Zr, Pt, Cu, and Au) and high entropy alloys [229–231]. The observation of plastically deformed and cold-worked materials, including cold spray coatings, exhibiting innately greater resistance to irradiation damage and swelling may in part be attributable to irradiation-induced recrystallization [81]. In general, the closure of interparticle boundaries and recrystallization during irradiation may be beneficial from the standpoint of enhancing ductility and corrosion resistance.

Kaoumi et al. [230] identified three temperature regimes for ion irradiation induced grain growth in nanocrystalline thin films: (i) purely thermal regime (above bulk recrystallization temperature); (ii) thermally-assisted regime; (iii) low temperature/athermal regime. In regime (ii), thermal motion and irradiation effects combine to increase the rate of recrystallization and grain growth. They identified a typical homologous transition temperature between 0.14 and 0.22 T_m [230]. For an irradiation temperature of 623 K, the homologous temperature for Cr was ~0.28, slightly higher than the average range of regime (ii). However, it is generally known that the bulk recrystallization temperature for metals is between 0.3-0.5 T_m [232], and combined with the short irradiation time of two hours, it is more likely that recrystallization of cold spray Cr occurred in the thermally-assisted regime.

The average hardness at the surface of the unirradiated (~6.0 ± 0.7 GPa) and irradiated (6.0 ± 0.4 GPa) Cr coating are consistent with the hardness of other cold spray Cr coatings (~6-7 GPa) indented in cross-section using a standard load transducer and up to low indentation depth (<200 nm) [34,233]. The heterogeneous microstructure of cold spray coatings, i.e., differences in grain size, dislocation density, strain gradients, and other heterogeneities across the microstructure led to scatter in hardness values (Fig. 6.8 b). As the indentation depth increased, the irradiated sample produced more consistent indents with lower deviation in hardness than the unirradiated sample, suggesting a normalization of the microstructure. Since the indents were taken from the same sample, both unirradiated and irradiated regions experienced the same thermal history. The consistent reduction in hardness of the irradiated sample (~2 GPa over 2.5 μm contact depth) may be a result of irradiation-induced recrystallization, grain growth, and even void formation in the Cr coating [85].

Irradiation defects, such as voids and dislocation loops, were not observed within the interparticle boundaries outlined in Fig. 6.7 (b). This is likely due to the nanoscale grain size and possibly heavy defect contrast within the boundaries making it difficult to discern defects formed from irradiation in relation to those formed from plastic deformation. Alternatively, the large density of interfaces in the form of grain and sub-grain boundaries in the interparticle boundaries in the Cr coating may act as sinks for radiation-induced defects. Radiation-induced point defects produced within this region may readily migrate towards these interfaces, leading to a non-equilibrium environment that induces grain boundary migration and grain growth through a defect-driven mechanism [224]. In other words, an absence of defects could be due to recrystallization out-performing void production and growth.

A small concentration of voids <3 nm in diameter were observed in larger grains away from the particle boundaries (Fig. 6.7 c,d). Contrast from the STEM images of the Cr coating microstructure suggest that these large grains also contain dislocation networks and substructures. Gong et al. [86] correlated radiation hardening of Cr with the frequency and size of voids and crystallinity in the microstructure. They explained that a low number of larger voids may better resist dislocation motion, contributing towards hardening. Conversely, grains with inherent defect density clusters may increase the activation barrier to void growth, resulting in a larger population of smaller voids. During *in situ* Kr^{2+} irradiation of cold spray Cr, Maier et al. [36] observed a suppression of dislocation loop formation and overall reduction of defect size and number density in the as-deposited Cr coating compared to an annealed cold spray Cr coating. Thus, the inherent defect density of cold spray Cr imparts radiation resistance through recombination of point defects by sinks and associated grain boundary migration, leading to irradiation-induced deformation recovery.

7. In Situ Synchrotron Diffraction Studies on Mechanical Behavior of the Cr-Zr System

7.1. Experimental description

7.1.1. Motivation

This chapter of the research involves a fundamental investigation of the deformation behavior and failure mechanisms in cold spray Cr-coated Zr-alloy system using *in situ* synchrotron X-ray diffraction. This technique is being used in recent years to characterize the evolution of lattice strain, dislocation density and character distribution, and load partitioning phenomena during macro-scale deformation of a wide variety of materials [63–66]. The technique was deemed particularly useful for the present study because of the importance of understanding the deformation behavior of the coating-substrate system as a whole and particularly the effects of the Cr coating on the deformation behavior of the Zr-alloy cladding. In light of this, it is noted that testing the deformation of the coating and the substrate separately will not yield realistic results for the coated cladding application due to the relief of stresses in coating and the exclusion of coating-substrate adhesion effects on the overall deformation behavior [234]. The deformation characteristics of as-deposited and annealed cold spray Cr coatings on Zr-alloy substrates were investigated to achieve a holistic understanding of the mechanical deformation behavior of the bimetallic system [233].

7.1.2. Sample fabrication

Cold spray deposition of electrolytic soft chromium powder was used to deposit Cr using the Cr-He deposition conditions. The substrates were flat ZIRLO^{TM} cladding material provided by WEC. Cr coating of approximately 80 μm thickness was deposited onto an 800 μm thick ZIRLO^{TM} substrate. After deposition, a portion of the samples was polished using 600 grit SiC abrasive paper to reduce surface roughness inherent to cold spray deposition. The final coating thickness was approximately 60 μm.

The other portion of the sample was annealed at 750 °C for 30 minutes to induce a slight drop in hardness and stress relief in the coatings, similar to the levels that might be encountered in a reactor over multiple years. This temperature is also below the α↔β phase transition temperature of the Zr-alloy substrate [235]. The short annealing time was selected to avoid the possibility of any distortion or warping of the sample due to residual stresses present in the coating from the cold spray deposition process, which may interfere with the mechanical testing procedures. The surface of the annealed sample was also polished using 600 grit SiC abrasive paper to reduce the surface roughness, as well as to remove any surface oxide that formed during the annealing process.

The two types of Cr coated samples were then machined into miniature tensile specimens using electric discharge machining (EDM). Dimensions of the tensile dog-bone specimens used for these experiments are shown in Table 7.1, with the as-deposited sample corresponding to an SS-J3 tensile specimen, and the annealed sample slightly scaled up to fit the new fixturing that was installed in the APS during the course of the experiments. Three tensile specimens were tested for each condition (as-deposited/annealed), for a total of six tested specimens.

7.1.3. Synchrotron diffraction experiments

In situ tensile tests were performed at Sector 1-ID of the Advanced Photon Source (APS) at Argonne National Laboratory. The specimens were mounted on a stage with a transducer that captured load and displacement data. During tensile deformation, a monochromatic synchrotron beam with a square shape was used to illuminate the gauge region of the sample. A CeO_2 powder sample was used as a standard to calibrate the diffraction parameters (beam length, detector tilt, etc.). As the beam passed through the sample, the scattered signals were collected by a Hydra wide angle X-ray scattering (WAXS) detector array consisting of four GE-RT41 high-resolution (2048 × 2048 pixels) detectors. A schematic illustration of the synchrotron experimental system is shown in Fig. 7.1. During each tensile test, the top grip of the tensile device pulled a continuous displacement in the vertical direction (uniaxial tensile) while the bottom grip remained stationary. Simultaneously, the stage holding the device would translate through several axial positions along the gauge section while being scanned by the beam, with a step size equal to the size of the beam. This process was repeated until gauge failure. Specific information about the beam conditions is provided in Table 7.1.

The engineering stress was calculated using the sample dimensions and the load captured by the transducer. Because an extensometer was not used during the test, the cross-head displacement data does not accurately capture the engineering strain during the elastic portion of the tensile test [236]. Therefore, lattice strain in the Zr-alloy was used as a measure of the engineering strain up to the yield stress. The lattice strain was calculated using the captured diffraction data and is described further in Section 7.1.4. After yielding, the displacement data was used to approximate the engineering strain through the rest of tensile deformation. True stress and true strain were calculated from the engineering stress and strain via: $\sigma_t=\sigma(1+\varepsilon)$, $\varepsilon_t=\ln(1+\varepsilon)$, respectively.

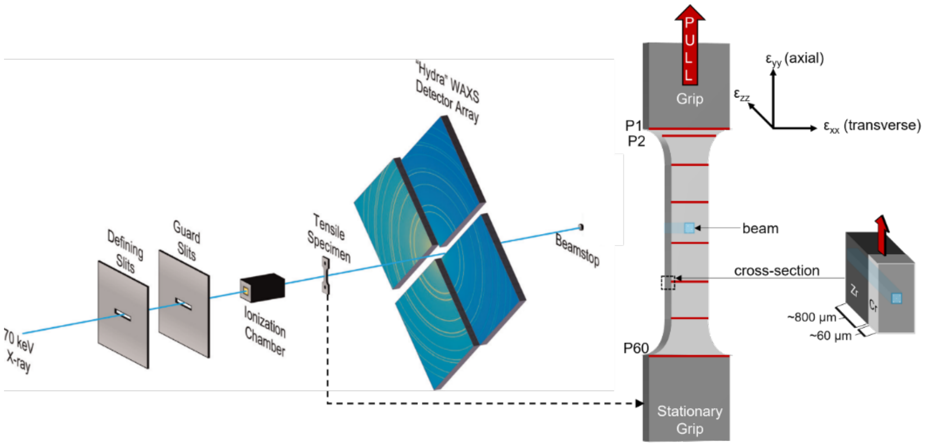

Fig. 7.1. Schematic illustration of synchrotron experimental system (left) with magnified schematic of dog-bone specimen (right). A cross-section of the Cr-coated Zr-alloy cladding (far right) illustrates synchrotron beam penetration through the entire gauge section.

Table 7.1. Parameters for tensile test and synchrotron beam used for this study.

Tensile Test Conditions	**As-Deposited Specimen**	**Annealed Specimen**
Gauge Length (mm)	5.00	12.0
Gauge Width (mm)	1.15	2.50
Gauge Thickness (mm)	0.86	0.86
Strain Rate (s^{-1})	1.20×10^{-5}	1.66×10^{-5}
Synchrotron Conditions	**As-Deposited Specimen**	**Annealed Specimen**
Beam Energy (keV)	80.7	71.7
Beam Wavelength (Å)	0.154	0.173
Beam Size (µm x µm)	100 × 100	200 × 200
No. Positions along Gauge	57	63

7.1.4. Diffraction data analysis

For each of the four GE detectors, six 10° azimuthal intervals (denoted by ϕ) of Debye-Scherrer diffraction rings were obtained from the WAXS signals. Each of these intervals was integrated into one-dimensional diffraction data for each gauge position and strain step of the tensile test. After performing background corrections, the 1D data was fitted to pseudo-Voigt peak functions using an analytical program to obtain lattice spacing, full width at half max (FWHM), intensity, integrated intensity, and peak shape information. Diffraction data analysis was performed at the gauge location nearest to necking and macroscopic failure of the specimens.

Elastic deformation of the specimens was investigated by examining the lattice strain evolution during the tensile tests. Measurements of lattice strains in a composite or a bimetallic material were made based on the development of Debye-Scherrer rings during the tensile tests. When an external load is applied, the radii of the rings decrease along the loading direction and increase in the perpendicular direction due to Poisson's effect. First, the lattice spacings of the 24 different azimuth angles (6 azimuthal intervals × 4 detectors) were fitted to the following equation to obtain lattice strains [66]:

$$d(\phi) = \frac{d_y - d_x}{2}\cos(2\phi) + \frac{d_y + d_x}{2}, \qquad \textit{Eqn. 7.1}$$

where ϕ is the azimuthal angle, d_y is the lattice spacing in the tensile/axial direction (ϕ =0° and 180°), and d_x is the lattice spacing in the transverse direction (ϕ =90° and 270°). For each material (Cr and Zr in this case), the lattice strains of specific *hkl*-reflections were calculated using:

$$\varepsilon_{yy}^{hkl} = \frac{d_y^{hkl} - d_0^{hkl}}{d_0^{hkl}}, \qquad \textit{Eqn. 7.2}$$

$$\varepsilon_{xx}^{hkl} = \frac{d_x^{hkl} - d_0^{hkl}}{d_0^{hkl}}, \qquad \textit{Eqn. 7.3}$$

where $\varepsilon_{xx}^{hkl}$and ε_{yy}^{hkl} are the lattice strains of the {hkl} reflection in the transverse and axial directions, respectively. The reference lattice spacing, d_0^{hkl}, was determined by finding the intersection of d_x and d_y curves plotted as a function of applied strain during the elastic portion of tensile deformation.

To gain a comprehensive understanding of the lattice strain, the average bulk lattice strain from each material was calculated from the individual lattice strains using the weighted average of each reflection, as proposed by Daymond [237]:

$$\bar{\varepsilon} = \frac{\sum_{hkl} \alpha_{hkl} \varepsilon_{hkl}}{\sum_{hkl} \alpha_{hkl}}, \qquad \textit{Eqn. 7.4}$$

where the weight coefficient, α_{hkl}, is defined as

$$\alpha_{hkl} = \frac{T_{hkl} \rho_{hkl} E_{hkl}}{\bar{E}}, \qquad \textit{Eqn. 7.5}$$

where ρ_{hkl} and E_{hkl} are the multiplicity and Young's modulus of the reflections, respectively, and $\bar{E}$ is the average Young's modulus of the matrix material. The Harris texture index, T_{hkl}, is defined as [238]:

$$T_{hkl} = \frac{I_{hkl_i}/R_{hkl_i}}{\frac{1}{n}\sum_{j=1}^{n} I_{hkl_j}/R_{hkl_j}}, \qquad \textit{Eqn. 7.6}$$

which is the ratio of the integrated intensity I_{hkl} to the theoretical integrated intensity R_{hkl}, defined as:

$$R_{hkl} = \frac{1}{V^2}\left[|F|^2 \rho \left(\frac{1+\cos^2 2\theta}{\sin^2\theta \, cos\theta}\right)\right], \qquad \textit{Eqn. 7.7}$$

where V is the volume of the unit cell, F is the structure factor, ρ is the reflection multiplicity, and the inside term is the Lorentz-polarization factor as a function of the diffraction angle, θ. Thus, by calculating the average bulk lattice strain, the elastic behaviors of the coating and substrate materials could be compared *in situ* during the tensile test.

Plastic deformation of the specimens was investigated by examining the breadth, or broadening, of the diffraction peaks during the tensile tests. The Williamson-Hall (WH) method assumes diffraction peak broadening represents the sum of crystallographic domain size and micro (internal) strain:

$$\beta cos\theta = \frac{K\lambda}{D} + C\varepsilon sin\theta, \qquad \text{Eqn. 7.8}$$

where β is the integral breadth of the diffraction peak, θ is the diffraction angle, λ is the wavelength of the synchrotron beam, D is the average crystallite size, ε is the internal strain due to plastic deformation, and K and C are two adjustable parameters set to 0.9 and 4.0, respectively. The breadth data of diffraction peaks was first corrected for instrumental broadening effects, followed by plotting against the diffraction angle and then fitted using linear regression to obtain the internal strain.

If the internal strain is assumed to be attributed to dislocations, the modified Williamson-Hall (mWH) approach can be used to quantify the evolution of dislocation density in the material [239,240]:

$$\frac{\beta cos\theta}{\lambda} = \frac{0.9}{D} + \left(\frac{\pi A b^2}{2}\right)^{\frac{1}{2}} \rho^{\frac{1}{2}} \left(K\bar{C}^{\frac{1}{2}}\right), \qquad \text{Eqn. 7.9}$$

where b is the Burgers vector of dislocations, ρ is the dislocation density, $K = 2sin\theta/\lambda$, $\bar{C}$ is the average contrast factor for dislocations, and A is an adjustable constant used to set the initial dislocation density. The average dislocation contrast factor $\bar{C}$ characterizes the "visibility" of dislocations in diffraction experiments and depends on the crystal structure of the material [241]. In cubic crystals, as is the case for the Cr coating, the average contrast factor can be represented by the following equation:

$$\bar{C} = \bar{C}_{h00}(1 - qH^2), \qquad \text{Eqn. 7.10}$$

where $\bar{C}_{h00}$ is the average contrast factor corresponding to the *h00* reflection, q is a material-specific parameter depending on the elastic constants of the crystal, and H^2 is a fourth-order invariant of the *hkl* indices [242]. Since both edge and screw dislocations are present in the crystal, they must be represented by the equation:

$$\bar{C} = \left[v_s\bar{C}_{h00,s} + (1 - v_s)\bar{C}_{h00,e}\right]\{1 - [v_s q_s + (1 - v_s)q_e]H^2\}, \qquad \text{Eqn. 7.11}$$

where v_s is the fraction of screw dislocations, (1-v_s) represents the fraction of edge dislocations, and for all other terms the subscripts *s* and *e* represent screw and edge dislocations, respectively [64]. Values for these constants were chosen for Cr (listed in Table B.1. in Appendix B) based on the method developed by Ungár [242]. When fitting Eqn. 7.9, v_s was represented as a row vector of one thousand evenly spaced points between zero and one, and the value that maximized the coefficient of determination (R^2) was chosen as the optimized fraction of screw dislocations in the Cr coating. Then, Eqn. 7.9 was refitted with the optimized v_s values to obtain the dislocation density in the coating.

In cubic crystals, there is only one main slip system, so the Burgers vector for BCC crystal can be represented by $b = (a/2) < 111 >$. The same cannot be said for the Zr substrate, as its HCP structure has three main slip systems (basal, prismatic, and pyramidal), which are further divided into 11 sub-slip-systems with three different Burgers vectors that can coexist: <*a*>, <*c*>, and <*a*+*c*>. Thus, Eqn. 7.9 must be re-written to consider the complex contrast-Burgers factor, $\overline{b^2C}$:

$$\frac{\beta cos\theta}{\lambda} = \frac{0.9}{D} + \left(\frac{\pi A^2}{2}\right)^{\frac{1}{2}} \rho^{\frac{1}{2}} K \overline{(b^2C)^{\frac{1}{2}}}, \qquad \text{Eqn. 7.12}$$

in which the complex contrast-Burgers factor is represented by [241]:

$$\overline{b^2 C_{hk.l}}^{(m)} = \sum_{i=1}^{3} h_i \bar{C}^{(i)} b_i^2, \qquad \text{Eqn. 7.13}$$

where h_i is the fraction of the three Burgers vector types (h_a, h_c, and h_{a+c}) and $\bar{C}^{(i)}$ is the average over the sub-slip-systems corresponding to the same Burgers vector type. As in the case of Cr coating, the fraction of h_i was represented as a row vector of one thousand points between zero and one when fitting Eqn. 7.12 and the values of h_a, h_c, and h_{a+c} that maximized the fitting confidence parameter R^2 were chosen to represent the dislocations in the Zr substrate. Then, Eqn. 7.12 was refitted using linear regression to obtain the dislocation density in the substrate. The specified parameters used to calculate the contrast-Burgers factor for Zr are included in Appendix B in Table B.2. and Table B.3. The parameters in Table B.3. were separated into three groups based on the Burgers vector notation, and then averaged for use in Eqn. 7.13.

7.1.5. Microscopy and materials characterization

Characterization of feedstock chromium powders and the fracture surface of strained tensile specimens was performed using SEM. Cr cold spray coated samples (both as-deposited and annealed) were characterized using SEM as well as by using a PFIB to mill out small cross-sections in desired regions of the samples to assess the grain structure before and after annealing. The fracture surface morphology was examined to understand the failure mechanisms of the Cr coating and underlying Zr-alloy substrate and to correlate this with data from the synchrotron experiments. Finally, hardness testing of the Cr powder mounted in cross section was performed using nano-indentation, and hardness testing of the Cr coatings and Zr-alloy substrates were performed using Vickers micro-hardness. The procedure for hardness testing was described in Section 2.7.

7.2. Microstructure and hardness of Cr powder and Cr-coated Zr-alloy

Hardness of the electrolytic soft Cr powder (measured using nano-indentation) was 3.9 ± 0.2 GPa. Higher magnification SEM imaging of the as-deposited Cr coating cross-section (Fig. 7.2 a) revealed details of the as-deposited coating microstructure. In particular, the regions of severe plastic deformation produced from the high-velocity impact and subsequent high strain rate deformation can be observed (represented by arrows in Fig. 7.2 a). A heterogeneous microstructure exists due to the edges of Cr particles deforming more than the particle interior, resulting in a gradation in grain size varying from the sub-micron scale at the interparticle boundaries to over a few microns in the particle interiors. Nano-indentation measurements within the coating revealed a hardness of 6.38 ± 1.10 GPa, indicating the particles underwent strain-hardening during deformation associated with coating formation. The relatively higher standard deviation in the coating hardness values is due to the heterogeneous nature of the coating containing interparticle boundaries, subgrain structures, and dynamically recrystallized grains.

Similar cross-sectional secondary electron imaging of the annealed sample revealed a substantially different initial microstructure of the Cr coating. The grain size increased with a notable annihilation of the regions of severe plastic deformation (Fig. 7.2 b). This was also reflected in a reduction of the microhardness of the annealed Cr coating to 330 ± 10 $HV_{0.05}$, from an initial hardness of 384 ± 19 $HV_{0.05}$ in the as-deposited Cr coating. Meanwhile, the hardness of the Zr-alloy substrate did not exhibit any variation due to cold spray or annealing (184 ± 4 $HV_{0.05}$ vs. 180 ± 4 $HV_{0.05}$ for as-deposited and annealed conditions, respectively). This is consistent with previous reports in literature which have indicated that the Zr-alloy substrate microstructure is largely unaffected by the cold spray process, with its deformation being largely restricted to the first few microns near the interface [37,89].

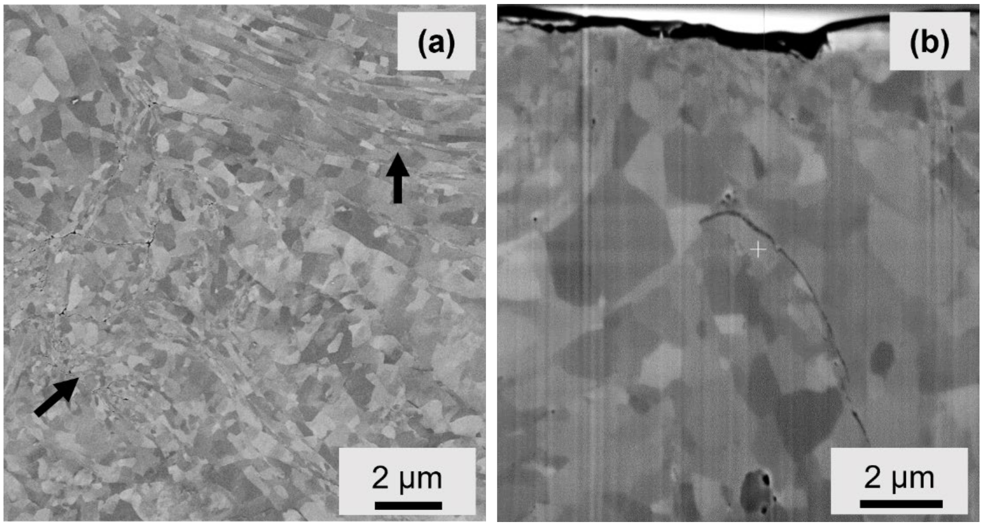

Fig. 7.2. High magnification cross-sectional SEM images of the internal microstructure of (a) as-deposited Cr coating, with arrows showing deformed, elongated, and dynamically recrystallized grains; (b) annealed Cr coating, showing more equiaxed and recrystallized grains.

7.3. Tensile test and fractography of tested samples

The engineering stress-strain curves from the tensile tests for as-deposited and annealed specimens are shown in Fig. 7.3 (a), and their conversion to true stress-strain curves are shown in Fig. 7.3 (b). The respective tensile properties of the as-deposited and annealed samples are summarized in Table 7.2. The yield strength and ultimate tensile strength of the two samples were quite similar, and comparable to those reported in ASTM B352 Standard for similar Zr-alloys [143]. Both samples experienced about 8% uniform elongation. The total elongation for the as-deposited samples was 2% greater than that of the annealed samples, though this could be due to the difference in gauge length between specimens. The measured elastic moduli for the as-deposited and annealed samples were 110 and 96 GPa, respectively, which are closer in magnitude to an uncoated Zr-alloy (Cr~270 GPa [243], Zr~90 GPa [174]). Nonetheless, a detailed analysis of the modulus of a coated cladding (bi-metal system) was not undertaken this study. Although there was a small difference in sample size between as-deposited and annealed materials, both materials' specimens had length-to-width ratios of greater than 4 as recommended by ASTM [244–246]. Therefore, it is unlikely that specimen geometry had a significant effect on the values of yield strength, ultimate tensile strength, and uniform elongation. These values are in good agreement with those reported for a Zr-alloy close in composition with ZIRLO^{TM} [143], and are comparable to results from tensile testing of polycrystalline Zr [66,247,248] and Zr-alloys [249–252], suggesting that the Cr coatings have negligible effect on the macroscopic mechanical properties of the Zr-alloy substrates.

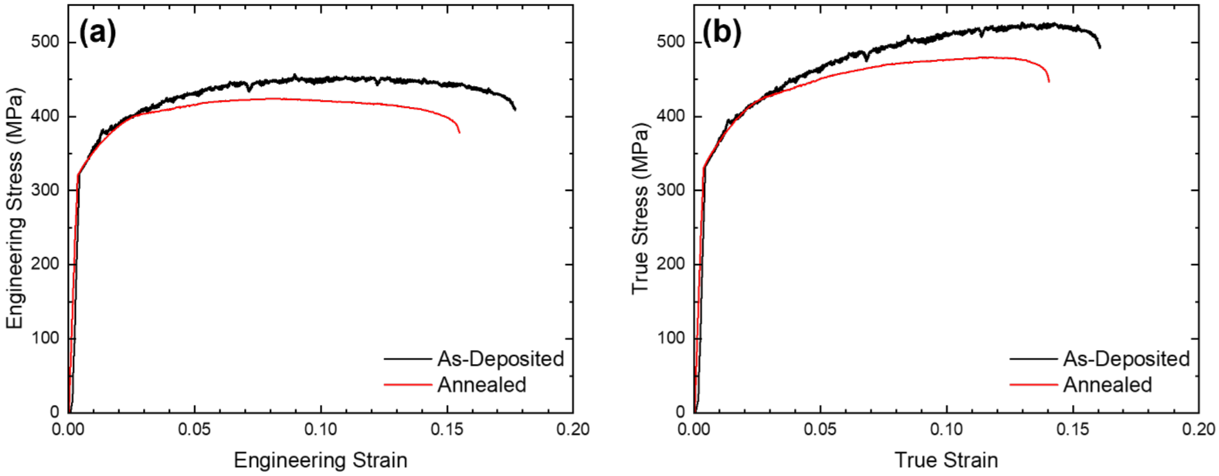

Fig. 7.3. (a) Engineering stress-strain curves for the as-deposited and annealed samples; (b) True stress-strain curves for the as-deposited and annealed samples.

Table 7.2. Values for Young's modulus (E), yield strength (YS), ultimate tensile strength (UTS), uniform elongation (UE), and total elongation (TE), as determined from the engineering stress-strain curves. Reference values for uniaxial tensile tests for uncoated Zr-alloy have been included [143].

Sample	E (GPa)	YS (MPa)	UTS (MPa)	UE (%)	TE (%)
As-deposited	110 ± 7	341 ± 24	433 ± 15	7.8 ± 2.0	15.2 ± 3.2
Annealed	96.2 ± 5.1	343 ± 16	436 ± 13	8.3 ± 0.6	13.0 ± 3.7
ZIRLO^{TM} [143]	--	346 ± 31	480 ± 35	--	17.5 ± 2.9

Images of the as-deposited coating surface after completion of the tensile test are shown in Fig. 7.4 (a). Apart from the main failure location, multiple cracks developed in the Cr coating perpendicular to the elongation direction throughout the gauge region. Fig. 7.5 (a–b) shows SEM images of the fracture surface of the as-deposited sample. The fractographs show evidence of brittle cleavage fracture in the Cr coating contrasted with typical dimples and micro-void coalescence in the Zr-alloy substrate. The reduced width of the specimen, particularly on the uncoated sides of the Zr-alloy substrate, indicates the occurrence of necking in the Zr alloy. The higher magnification SEM image shown in Fig. 7.5 (b) reveals that the Cr coating remained adhered to the substrate up to strain to failure.

Images of the annealed coating surface after the tensile test are shown in Fig. 7.4 (b). The SEM images again revealed multiple cracks in the Cr coating, but these cracks differ from those observed in the as-deposited specimen in two distinct ways. Firstly, the cracks are more circuitous and often terminate within the width of the gauge section, indicating the presence of microstructural features within the coating that impede crack propagation. For example, the blue arrow in Fig. 7.4 (b-inset) shows some cracks terminating in the middle of the gauge region. Secondly, some thin cracks (<5 μm) run nearly parallel to the elongation direction, shown by the red arrow in Fig. 7.4 (b-inset), indicating cracking was not restricted only to the transverse direction of the coating surface.

The cross-sectional SEM images of the main fracture surface of the annealed sample are shown in Fig. 7.5 (c–d). Similar to the as-deposited specimen, the coating surface reveals brittle cleavage fracture in the Cr coating with ductile micro-void coalescence failure in the Zr-alloy substrate. The annealed Cr coating also remained strongly adhered to the Zr-alloy substrate. A few instances of accumulation of voids at inter-particle boundaries due to reorientation of grains during annealing were observed before tensile strain (Fig. 7.2 b) and after tensile failure (Fig. 7.5 d), which sometimes appeared as micro-cracks suggesting either these cracks formed during the annealing process due to reorientation of grains, or they are not cracks but instead accumulation of voids at inter-particle boundaries. Regardless, both cohesion strength within the Cr coating and adhesion strength at the Cr/Zr interface remained high for both as-deposited and annealed samples throughout the duration of the tensile tests, as no spallation of the coating was observed in either case.

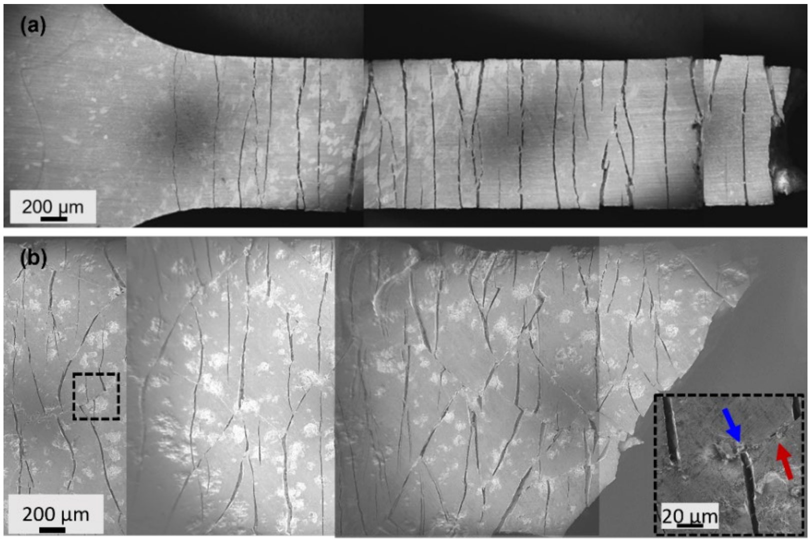

Fig. 7.4. (a) SEM images of cracking along the surface of the as-deposited Cr coating; (b) SEM image of cracking along the surface of the annealed Cr coating, with the inset showing a higher magnification SEM image of cracking in the axial direction (red arrow) and crack termination in the transverse direction (blue arrow). The lighter contrast areas ("white spots") on the surfaces of the coatings represent remnants of surface roughness left behind on the coating surface even after polishing.

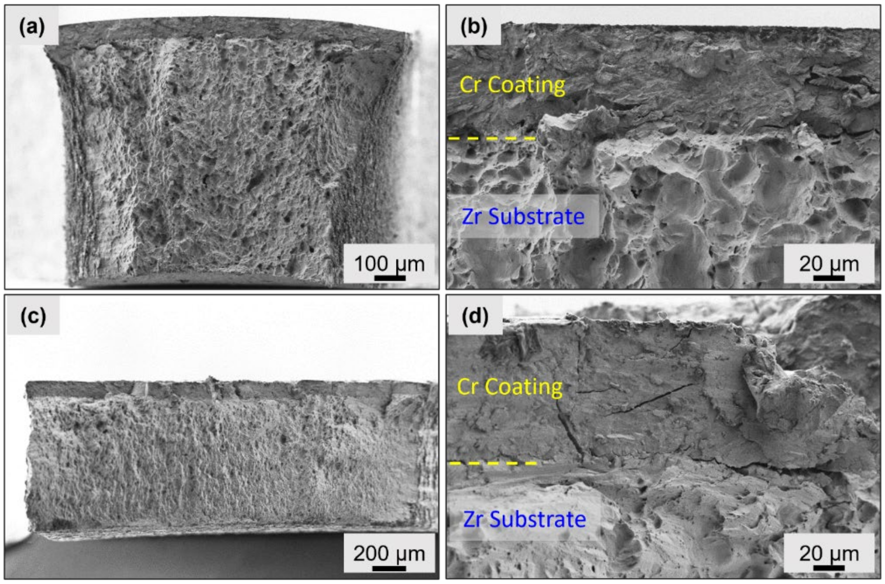

Fig. 7.5. (a, c) SEM images of the fracture surfaces of the as-deposited and annealed samples, respectively; (b, d) Higher magnification SEM images of the Cr/Zr interface of as-deposited and annealed samples, respectively. The images show Cr coating (dark contrast) and Zr-alloy substrate (light contrast) with interface marked with yellow line.

7.4. In situ synchrotron diffraction results

7.4.1. As-deposited specimen

Fig. 7.6 (a) shows the Debye-Scherrer rings measured for the as-deposited sample from one of the four detectors just before sample failure. The highest intensity Cr peak (b) and Zr peak (c) have been indicated on the plot. Pseudo-Voigt fitting was performed for five Cr peaks and fifteen Zr peaks to extract the d-spacing, intensity, FWHM, and integrated intensity of the peaks. Fitting of the Cr peaks was especially challenging for multiple reasons. First, Cr exhibits only a small number of peaks due to its high crystal symmetry compared to HCP-Zr. Second, the relatively small thickness of the Cr coating (~7% of total sample thickness) yielded relatively low peak intensities for Cr in comparison to Zr. Third, as the Cr peaks shifted and became broader during the course of the measurements due to elastic and plastic strains, respectively, some of the Cr peaks began to shift towards higher-intensity Zr peaks, making it difficult to fit a proper background. This is especially evident by observing the evolution of peak positions and peak broadening as a function of macroscopic strain, as shown in Appendix B, Fig. B.1. For example, texture evolution in Zr is evident by the presence of certain peaks in the GE-2 detector (see d~1.46 Å) but absent in the GE-1 detector, thus obscuring the {200} Cr peak. Nevertheless, care was taken when fitting Cr peaks to reduce the amount of error in the peak fitting outputs, which were used for the subsequent strain analysis.

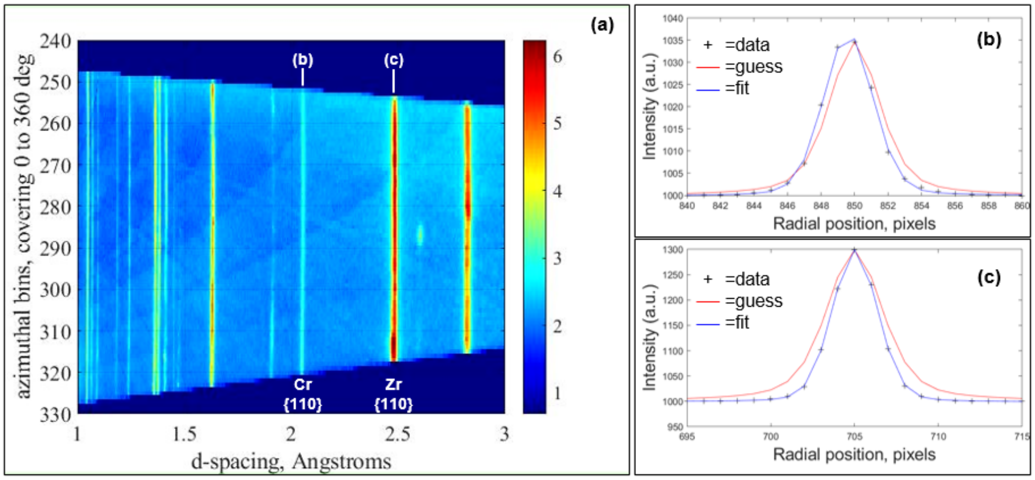

Fig. 7.6. (a) Transformed diffraction image for as-deposited sample showing Debye-Scherrer rings across detector azimuth; Pseudo-Voigt fitting of (b) Cr {110} peak and of (c) Zr {110} peak.

Calculated lattice strains for each *hkl* reflection and bulk lattice strains (defined by Eqn. 7.4-Eqn. 7.7) as a function of applied strain are presented in Fig. 7.7 (a-c). Before straining (i.e., in the as-deposited condition), the Cr coating exhibits a small amount of compressive lattice strain in the transverse direction (Fig. 7.7 b). This is due to compressive residual stresses inherently induced by the cold spray deposition process due to the peening effect. The Zr-alloy substrate also exhibits some initial non-zero lattice strain (Fig. 7.7 c), though it is centered about zero in the axial and transverse directions. It appears that Cr coating begins to yield at about 170 MPa of applied stress as the linearity of the Cr lattice strain curves begins to diverge (transition from regime I). However, the Zr-alloy substrate does not yield until the yield stress of 332 MPa (regime II). As the sample begins to plastically deform (regime III), the Cr lattice strain in the axial direction begins to substantially recover while that in the transverse direction reaches its maximum value of between $3\text{-}5 \times 10^{-3}$. It is plausible that cracks started to form in the coating during regime II before the Zr-alloy substrate yielded. Upon transition to regime III when the substrate began to undergo macroscopic yielding, the coating would have sufficiently cracked such that it could no longer continue sharing the load with the substrate. Further, after macroscopic yielding, the lattice strain evolution in Zr becomes highly anisotropic, with lattice strain in the longitudinal direction continuing to increase until reaching a maximum between 5 to 7×10^{-3} just before failure. In the transverse direction, the Zr reflections experienced mixed straining/relaxation behavior, indicating that the substrate is textured. The elastic modulus of each fitted reflection calculated from the slope of the lattice strain vs. applied stress during elastic deformation is presented in Table B.4. of Appendix B.

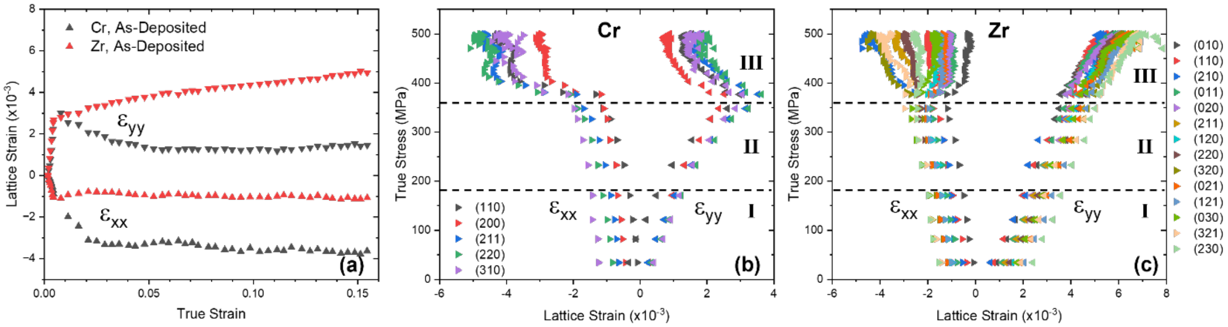

Fig. 7.7. (a) Bulk lattice strain evolution for as-deposited Cr and Zr; (b) Lattice strain evolution for Cr diffraction peaks; (c) Lattice strain evolution for Zr diffraction peaks. The axial and transverse directions are labeled as ε_{yy} *and* ε_{xx}*, respectively.*

Dislocation density evolution for as-deposited Cr and Zr, calculated from the modified Williamson-Hall (WH) fitting, is shown in Fig. 7.8. The initial state of the cold spray Cr coating consists of severe plastic deformation with a high density of dislocations of about $10^{16}/m^2$. On the other hand, the Zr-alloy substrate exhibits a lower density of dislocations of about $10^{14}/m^2$. This once again demonstrates that the bulk of the substrate is not affected by the cold spray process (Fig. 7.8 a,d). The dislocation density in the Cr coating increases to a maximum of about $3 \times 10^{16}/m^2$, while the dislocation density in the Zr-alloy continued to increase until reaching a maximum of about $5 \times 10^{16}/m^2$ near failure of the specimen.

The open symbols in Fig. 7.8 represent dislocation density values that were calculated using a slope generated from a modified WH fitting with lower fitting confidence ($R^2 < 0.8$). For Zr, there are relatively few open symbols indicating a high level of confidence. In other words, the internal strain evolution in the Zr-alloy substrate can be attributed to an increase in dislocations. Meanwhile for Cr, the level of confidence decreases at about 5% and 10% applied strain in the axial and transverse directions, respectively. It is likely that at 5% applied strain the cracking in the Cr coating (Fig. 7.4 b) was quite significant. Therefore, while still being bonded to the underlying Zr-alloy substrate (Fig. 7.5 b), it was no longer plastically deforming in the axial direction.

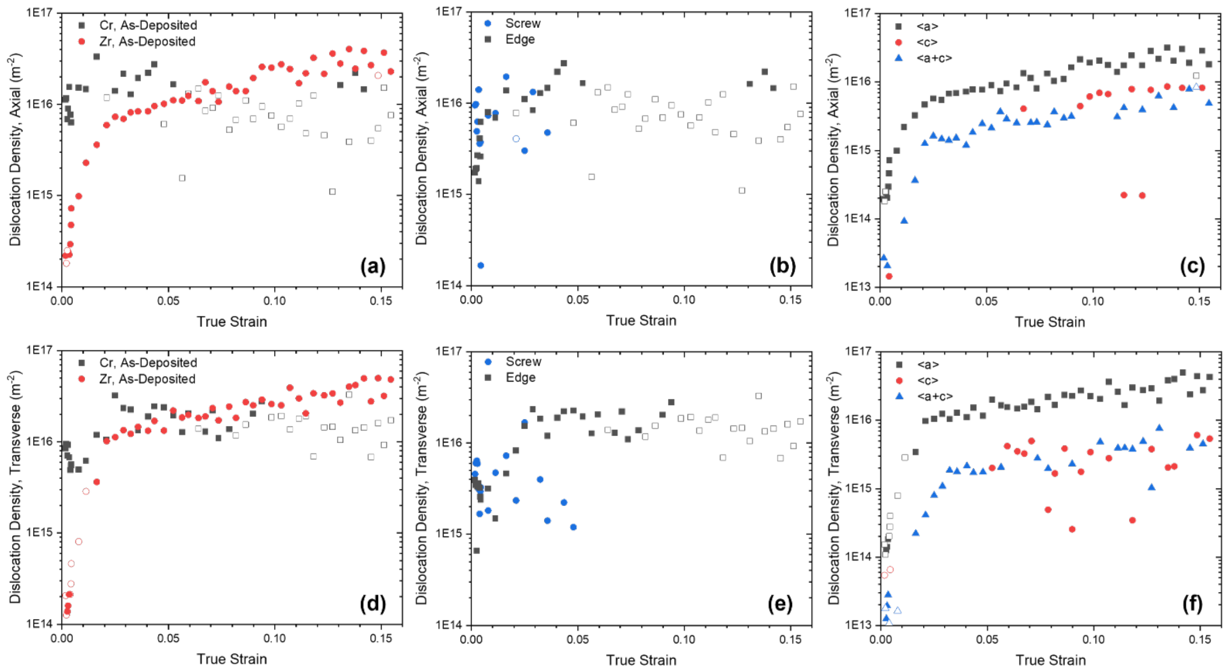

Fig. 7.8. (a) Dislocation density evolution for as-deposited Cr and Zr in the axial direction, with (b) Evolution of screw/edge dislocations in the Cr coating in the axial direction and (c) Evolution of various types of dislocations for Zr in the axial direction; (d) Evolution of dislocation density for as-deposited Cr and Zr in the transverse direction, with (e) Evolution of screw/edge dislocations in the Cr coating in the transverse direction, and (f) Evolution of various types of dislocations in Zr in the transverse direction. Any open symbols represent values with a coefficient of determination $R^2 < 0.8$.

Fig. 7.8 (b, e) shows the breakdown of screw and edge dislocation density evolution for the Cr coating using the contrast factors for the BCC system. It is interesting to note that in the as-deposited condition (i.e., at zero applied strain), the fraction of screw dislocations is slightly larger than the edge dislocation fraction in the Cr coating. Such a distribution of dislocation character is rather unusual for BCC metals/alloys deformed to such large strain values (as is the case in cold spray deposition) at room temperature. When subjected to conventional tensile loading, the edge dislocation fraction is expected to be dominant at comparable strain values [64]. Nevertheless, with increasing strain, the proportion of edge dislocations increases until it saturates at about $2 \times 10^{16}/\text{m}^2$, while the screw dislocation density remains largely constant. This is consistent with what is expected from the low relative mobility of screw dislocations in BCC alloys at room temperature. Fig. 7.8 (c, f) shows the evolution of the three types of dislocation systems (i.e., <*a*> type, <*c*> type and <*a*+*c*> type) that exist in the Zr-alloy substrate. As expected, the <*a*> type dislocations represent the largest fraction in Zr (~80%) while the <*a*+*c*> type dislocations are the next highest (<20%). It appears the <*c*> type dislocations are more active towards the later stages of plastic deformation.

7.4.2. Annealed specimen

The calculated lattice strain from the 2D diffraction data for annealed Cr and Zr is shown in Fig. 7.9 (a-c). The strain in both Cr and Zr lattices are centered around zero at the beginning of the tensile test, indicating annealing had a stress relieving effect in the Cr coating. The axial-direction lattice strain recovery in Cr at about 1% applied strain in regime I indicates the initiation of cracks in the Cr coating. Lattice strain in the transverse direction however continues to increase to an average of 4 $\times 10^{-3}$. Lattice strain in the Zr-alloy substrate shows typical behavior throughout the test, indicating it bore most of the load and was not impacted by cracking of the Cr coating. The calculated elastic moduli for certain reflections, is shown in the Supplemental Information (Table S4). Like the as-deposited sample, the Zr lattice planes display modulus values comparable to bulk values, while the moduli of the Cr planes are much lower in the axial direction.

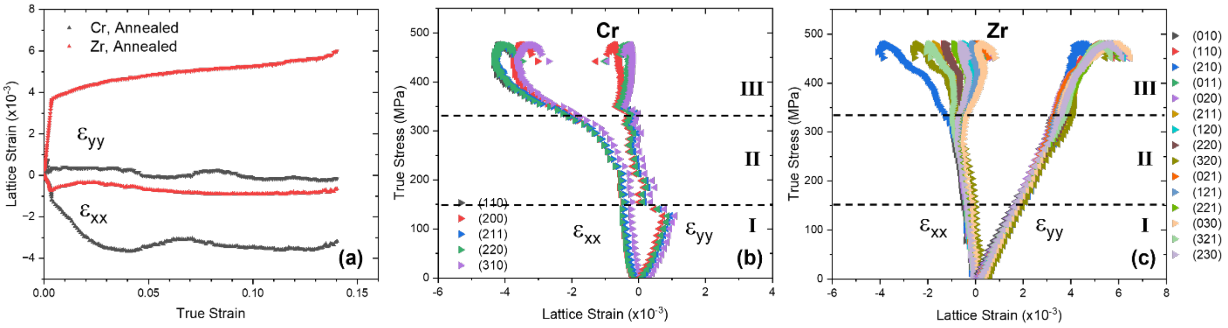

Fig. 7.9. (a) Bulk lattice strain evolution for annealed Cr and Zr, averaged using (b) Calculated lattice strain evolution for Cr diffraction peaks, and (c) Calculated lattice strain evolution for Zr-alloy diffraction peaks. The axial and transverse directions are labeled as ε_{yy} *and* ε_{xx}*, respectively.*

Dislocation density evolution for annealed Cr and Zr is shown in Fig. 7.10 (a, d). In the Cr coating, the initial dislocation density has dropped by about an order of magnitude to 10^{15}/m^2 after annealing, while for the Zr-alloy substrate it remains at about 10^{14}/m^2. Early in the tensile test (less than 1% applied strain), dislocation density in the Cr coating increases in the axial direction up to 3×10^{15}/m^2, after which it remains constant. This coincides with the lattice strain shown in Fig. 7.7 (a), further validating that cracking in the Cr coating began early and was no longer plastically deforming in the axial direction. In the transverse direction, however, the dislocation density in the Cr continues to increase up to 2 × 10^{16}/m^2, where the fitting confidence degrades at about 11% applied strain. This appears to be the saturation limit of dislocations for cold sprayed Cr. The dislocation density evolution in the annealed Zr-alloy behaved similarly to the as-deposited specimen, continuing to increase during tensile deformation until reaching a maximum at 3.5 × 10^{16}/m^2.

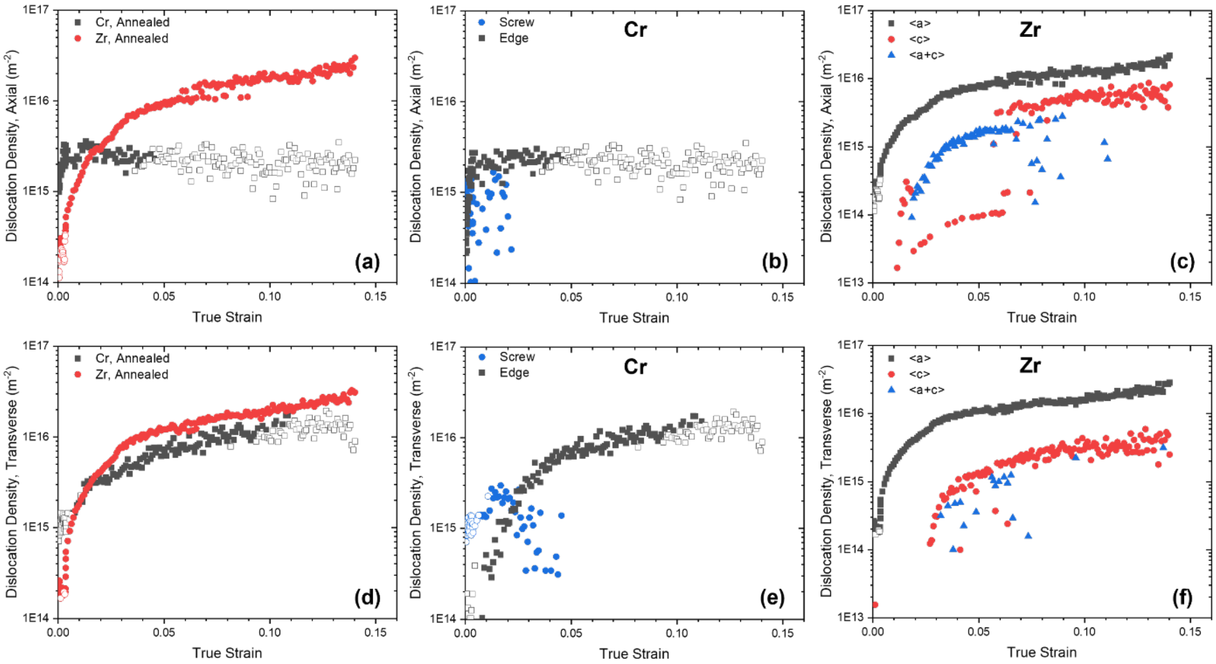

Fig. 7.10. (a) Dislocation density evolution for annealed Cr and Zr-alloy in the axial direction, with (b) Evolution of screw/edge dislocations in the Cr coating in the axial direction and (c) Evolution of various dislocation types in Zr-alloy in the axial direction; (d) Evolution of dislocation density for annealed Cr and Zr-alloy in the transverse direction, with (e) Evolution of screw/edge dislocations in the Cr coating in the transverse direction, and (f) Evolution of various types of dislocations in Zr-alloy in the transverse direction. Any open symbols represent values with a coefficient of determination $R^2 < 0.8$.

An interesting effect of the annealing treatment within the Cr coating can be observed in the edge and screw dislocation populations of the annealed sample at zero applied strain. It can be seen that while these populations have been measured to be roughly equal in the axial direction (Fig. 7.10 b), the edge dislocation density appears to be reduced by an order of magnitude in the transverse direction (Fig. 7.10 e). This has important consequences on the failure mechanism of the annealed Cr coating and has been discussed in detail in Section 7.6. With increasing strain, the edge dislocation density increases sharply in both the transverse and axial directions (Fig. 7.10 b&e). Interestingly, even after the coating starts to exhibit cracks at about 1% applied strain, the edge dislocation population continues to increase in the transverse direction until just before failure (Fig. 7.10 e). As the cracking in the Cr coating was discontinuous or circuitous in the annealed sample and there was no bulk sectioning of the coating (Fig. 7.4 d), the Cr coating continued to deform in the transverse direction thus increasing the population of edge dislocations. Meanwhile, the annealed Zr-alloy substrate contains mostly <*a*>-type dislocations (~85%) with mixed percentages of <c> and <a+c> becoming active during different stages of tensile deformation. Both <*c*> and <*a*+*c*>- type dislocations increase just after yield, with <*a*+*c*> type dislocations becoming more active at the start of plastic deformation in the axial direction (Fig. 7.10 c) and <*c*> type dislocations increasing in the transverse direction (Fig. 7.10 f).

The complete *in situ* diffraction data from this experiment are summarized for the Cr coatings and the Zr-alloy substrates in Table 7.3 and Table 7.4, respectively.

Table 7.3. Tabulated synchrotron diffraction data for as-deposited and annealed Cr coatings, including lattice strains (Eqn. 7.4), modified Williamson-Hall fitting results and dislocation densities (Eqn. 7.9). Dislocation densities and edge/screw components at fracture were taken from the axial direction. The values between 3-5% applied strain were averaged.

Parameter	**As-Deposited Cr (initial)**	**Annealed Cr (initial)**	**As-Deposited Cr (at fracture)**	**Annealed Cr (at fracture)**
Lattice strain, ε_{yy} ($x10^{-3}$)	0.23	0.18	1.7	0.99
Lattice strain, ε_{xx} ($x10^{-3}$)	0.72	0.08	4.3	3.3
mWH slope ($x10^{-3}$)	7.5± 0.1	2.5± 0.1	8.6 ± 0.1	3.7 ± 0.1
mWH intercept ($x10^{-3}$)	0.8± 0.1	1.6± 0.1	0.7 ± 0.1	1.4 ± 0.1
Dislocation density ($x10^{15}$ m^{-2})	10± 3	1.3 ± 0.2	20 ± 5	2.4 ± 0.1
Edge dislocations ($x10^{15}$ m^{-2})	3.8 ± 2.4	0.4 ± 0.1	20 ± 5	2.4 ± 0.1
Screw dislocations ($x10^{15}$ m^{-2})	6.7 ± 3.9	0.9 ± 0.2	0.01	0.01

Table 7.4. Tabulated data values for as-deposited and annealed Zr-alloy substrates, lattice strains (Eqn. 7.4), modified Williamson-Hall fitting results and dislocation densities (Eqn. 7.12).

Parameter	**As-Deposited Zr (initial)**	**Annealed Zr (initial)**	**As-Deposited Zr (at fracture)**	**Annealed Zr (at fracture)**
Lattice strain, ε_{yy} (x10^{-3})	1.7	0.3	6.7	6.0
Lattice strain, ε_{xx} (x10^{-3})	1.0	0.02	2.1	0.7
mWH slope (x10^{-3})	0.4± 0.01	0.4± 0.05	4.7 ± 0.1	4.9 ± 0.01
mWH intercept (x10^{-3})	1.3± 0.01	1.7± 0.01	0.1 ± 0.4	0.9 ± 0.2
Dislocation density (x10^{15} m^{-2})	0.2± 0.03	0.2 ± 0.04	30 ± 7	25 ± 4
<a> Dislocation density (x10^{15} m^{-2})	0.2 ± 0.03	0.2 ± 0.04	23± 6	19 ± 3

7.5. Deformation mechanisms in the Zr-alloy substrates

The synchrotron XRD data, particularly on the populations of various dislocation types (presented in Fig. 7.8 and Fig. 7.10) reveal important insights into the deformation mechanisms of both as-deposited and annealed Zr-alloy substrate. <*a*>-type screw dislocations in Zr alloys can undergo prismatic, basal as well as pyramidal slip [253–256]. Out of these, prismatic slip of these dislocations has been well known to be the primary slip mechanism in Zr alloys. The fact that <*a*>-type dislocations form a major part of the dislocation population in both the samples at all stages of deformation is in good agreement with the primary deformation mechanism agreed upon in the literature. For the major operational secondary deformation mechanism in Zr alloys, several competing slip mechanisms have been identified. These candidate mechanisms include basal slip of <*a*>-type dislocations, <*c*>-type dislocation slip, and pyramidal slip of <*a*>-type dislocations, which actually proceeds by decomposition of <*a*>-type dislocations into <*a*+*c*>-type dislocations [253–257]. The mechanism selection has been observed to be dependent on multiple factors including alloy composition and c/a ratio (which govern the critical resolved shear stress (CRSS) for different slip systems), magnitude of strain and strain rate, and finally crystallographic texture, which governs the Schmid factor distribution.

The results indicate that the major operational secondary deformation mechanism is different in the as-deposited and annealed samples, and also at different stages of deformation. In case of the as-deposited specimen, the dominance of <*a*+*c*>-type dislocations over <*c*>-type dislocations during the initial stages of deformation suggests that pyramidal slip of <*a*>-type dislocation is the secondary deformation mechanism at the corresponding strain levels. With increasing plastic strain, approaching the stage of necking, activation of <*c*>-type dislocation slip can be observed. <*c*>-type dislocation slip has been found to contribute towards maintaining mechanical compatibility between deforming grains [258]. For the annealed specimen, the dislocation populations appear to be significantly different when measured by the longitudinal and axial detectors. Moreover, they differ significantly from the behavior of the as-deposited substrate. The primary reason for this difference could be the evolution of crystallographic texture during the annealing treatment (see texture factors for as-deposited and annealed substrate in Table B.5. of Appendix B), resulting in a modification of the Schmid factor distributions for the different slip systems [259–261]. As a result, in the initial stages of deformation, <*a*+*c*>-type dislocations predominate over <*c*>-type dislocations in the axial detector results (Fig. 7.10 c) while the opposite is true in the transverse detector results (Fig. 7.10 f). In other words, the secondary slip system activation is not uniform across differently oriented grains in the alloy and depends on their respective Schmid factors. In the later stages of deformation, <*c*>-type dislocation activity takes over as the major secondary deformation mechanism, as in the as-deposited sample (Fig. 7.8 c&f). These differences in the secondary deformation mechanisms, resulting from the texture evolution during the annealing treatment, are speculated to be responsible for the minor differences in ductility and necking behavior observed between the two Zr alloy substrates. As a final point, it must be mentioned that these subtle differences in the deformation behavior of the two substrates do not affect the coating deformation behavior in any significant manner, which is discussed in the following section.

7.6. Deformation mechanism in the Cr coatings

In terms of its dislocation sub-structure, the as-deposited Cr coating (Fig. 7.8) appears to present a significant deviation with respect to literature reports on BCC Cr subjected to low strain-rate, room temperature tensile deformation. Early theoretical work [262] and recent experimental investigations [140] on the dislocation sub-structure of low strain-rate deformed Cr during the stages of work hardening and beyond have shown the dislocation network to be populated by a significantly higher fraction of edge component than the screw component. The theoretical basis for this observation has been detailed as follows. Screw dislocations have a mobility that is at least two orders of magnitude lower than edge dislocations at room temperature. This is due to the necessity of a thermally-activated double kink pair nucleation mechanism for their glide. Consequently, the rate of annihilation of screw dislocations entering within a critical proximity of each other by means of cross-slip becomes significant at these later stages of deformation (post macroscopic yielding). This leads to a saturation, or even decrease in the screw dislocation density with increasing deformation strain, which is accommodated by the increasing edge dislocation fraction. This theoretical understanding has also helped explain the sharp ductile-brittle transition temperature of BCC Cr [140].

However, it appears from the dislocation density results of the as-deposited Cr coating that the mechanisms of dislocation activity during the cold spray deposition-induced high strain-rate deformation of Cr differ significantly. Despite the as-deposited Cr coating being in an advanced stage of deformation (with significant dislocation multiplication and strain hardening), it can be seen from Fig. 7.8 (b & e) that the screw dislocation fraction is slightly higher than the edge dislocation fraction. While it may not be possible to experimentally verify the microscopic mechanisms occurring at such high deformation rates, some explanations could be offered. The first is based on the discussion of Essmann and Mughrabi on the effect of ‘correlated glide’ of screw dislocations on their annihilation rate [262]. If it is assumed that the high strain rate deformation facilitates correlated glide of groups of dislocations, annihilation of individual segments would not occur even if they were closer to each other than the critical annihilation distance. A significantly reduced annihilation rate could possibly explain the high screw dislocation density. Secondly, numerical simulations of cold spray particle impact and coating formation reveal that local temperature rise of contacting particle surfaces instantaneously during impact can range from 400 K up to 1000 K [111,108,263–265]. This localized transient heating could take the system locally, for short time periods, above the ductile-brittle-transition temperature [61,266,267]. Such local thermal spikes would result in a significantly higher mobility for screw dislocations contributing towards an enhancement in their population. In either case, theoretical investigations would be essential to clarify the occurrence and relative importance of either or both mechanisms.

The behavior of the as-deposited coating upon being subjected to tensile stress, however, is consistent with conventional understanding. A small amount of plasticity is facilitated by increasing edge dislocation density, with the screw dislocation density remaining either constant or decreasing. Cracks can then initiate homogeneously within the coating at a strain level close to 1%, apparent from the relaxation in lattice strain shown in Fig. 7.7 (a) when the dislocation density is high enough for crack nucleation. Considering that there are no other microstructural features to resist crack propagation, trans-particle cracks propagate readily. This is reflected in the form of linear cracks, propagating over the entire width of the gauge cross-section transverse to the loading direction.

The behavior of the annealed sample on the other hand differs significantly from the as-deposited sample. In fact, it presents another unique dislocation sub-structure in BCC Cr by virtue of its unique processing history. Notably, it is a significantly screw dislocation-dominated structure and, importantly, the reduction in edge dislocation density is particularly pronounced in the transverse direction in comparison to the axial direction (Fig. 7.10 e & b, respectively). This difference in dislocation density along different diffraction directions once again implies that the distribution of edge dislocation density is not uniform across all grains in the annealed coating microstructure. Upon comparison of grain sizes (Fig. 7.2), dislocation densities (Fig. 7.8 & Fig. 7.10) and the texture factors (calculated from Eqn. 7.6 and shown in Table B.6. in Appendix B) for the annealed and as-deposited coatings, it is apparent that the microstructural evolution in the course of annealing is a rather complex phenomenon. Occurrence of the processes of recovery, recrystallization, and grain growth, each to a different extent of completion can be inferred. Therefore, a separate investigation is essential to understand the exact processes occurring during annealing. However, the observed heterogeneity in dislocation density distribution among different grains in the annealed microstructure can explain the enhanced resistance of the annealed coating to the propagation of the localized cracks. Initiation of cracks possibly occurs in those grains with a higher dislocation density and low Schmid factor. However, resistance to the propagation of these cracks is facilitated by the presence of low dislocation density grains in the microstructure, which still have a potential to exhibit plasticity. In other words, when these low dislocation density grains are encountered by the crack tips, they undergo plastic deformation (predominantly in the transverse direction) and thus impose a back stress on the growing crack. This would hinder the occurrence of linear propagation of the cracks, thus imparting toughness to the coating.

It must be mentioned that the plasticity of the low dislocation density grains – which is facilitated by rapid multiplication of the edge dislocation segments (over an order of magnitude, as seen in Fig. 7.10 e) – is not always observed in BCC metals/alloys [268]. In fact, increasing brittleness has been observed in some BCC alloys with decreasing initial edge dislocation density [269]. However, the rapid multiplication in this case could be resulting from the pre-existence of a relatively high fraction of screw dislocation segments, which is rather unique to the annealed coating microstructure. Due to their low mobility, the screw segments would act as efficient pinning sites for edge dislocations. A large number of these screw segments would imply the operation of a large number of edge dislocation sources, leading to rapid multiplication. In conclusion, it can be said that although initiation of cracks occurs in the annealed coating at almost the same macroscopic strain as in the as-deposited coating, their overall propagation length is much more circuitous, making the coating tougher and more effective in serving as an environmental barrier under the influence of external stress.

8. Annealing Treatments and Micromechanical Testing of Cold Spray Cr-coated Zr-alloy

Post-deposition annealing has historically been used on cold spray coatings to improve the microstructure and mechanical properties of work-hardened deposits. However, in the PWR application, the cladding is exposed to elevated temperature for extended periods of time which will lead to annealing of the coating with associated effects of softening and stress relief. In the case of high temperature transients or LOCA, the temperatures could exceed 700 °C or even 1000 °C and result in very rapid stress relief, softening, and grain reorientation in the coating. Additionally, this research has shown that irradiation itself can potentially lead to recrystallization and softening. Therefore, it was deemed important to understand the annealing response of the coatings, particularly as it relates to change in mechanical properties.

Section 8.1 will explore several different annealing conditions and their effects on microstructure and local mechanical properties of Cr-coated Zr-alloy cladding. Section 8.2 will discuss results from annealing experiments that are intended to simulate potential microstructural changes that the cold spray Cr coating may undergo in nuclear service. Section 8.3 will discuss the results of micro-cantilever beam bending testing of annealed samples to assess the microstructural effect on adhesion at the Cr-Zr interface.

8.1. Low temperature annealing of cold spray Cr coatings

Previous annealing treatments of Cr coatings deposited with electrolytic hard Cr powder (different than the powder in this research) were performed between 350-650 °C for 8 hours at each temperature [169]. Microhardness measurements from this experiment revealed a relatively small change in hardness (~75 $HV_{.05}$) up to 550 °C, which could indicate recovery within cold spray Cr. Recovery is the process of annihilation and rearrangement of defects within a deformed metal without migration of high angle grain boundaries, and is often used to reduce residual stresses [270]. At 650 °C, the hardness dropped an additional 125 $HV_{.05}$ which could represent the start of recrystallization in chromium. 650 °C represents a homologous temperature (T/T_m) of 0.42, and it is well known that the recrystallization temperature for most metals initiates in the range of 0.3 to 0.5 T_m (expressed in deg. K) [270]. Increasing cold work in the metal increases the driving force for recrystallization [232], which is an important consideration in annealing of cold spray coatings. Previous published data on bulk chromium metal showed that higher temperatures (>750 °C) could rapidly recrystallize rolled chromium (<1 h) [271–273].

Using our previous experiment as a benchmark, microhardness measurements from several annealing treatments performed throughout the course of this research are shown in Fig. 8.1. Cr-N2 and Cr-He coatings were annealed at several temperatures and times and later used for testing purposes. Annealing at 350 °C (T/T_m ~0.28) for 24 hours to 168 hours showed no significant change in hardness, suggesting that significantly longer times may be required to induce recrystallization and softening.

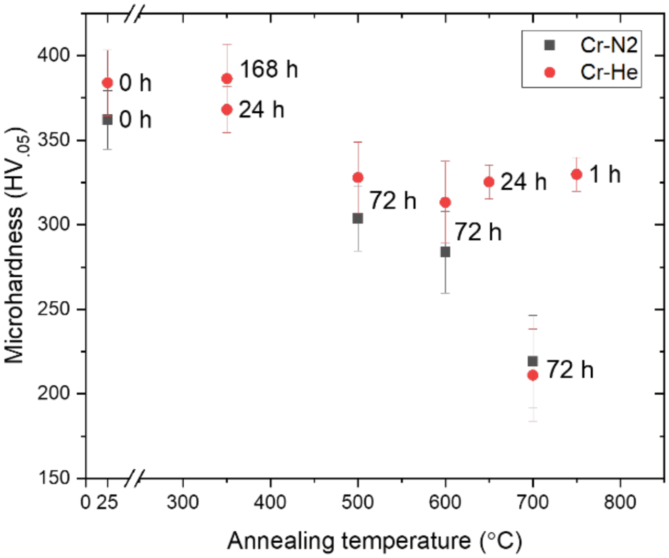

Fig. 8.1. Microhardness measurements from as-deposited and annealed cold spray Cr-N2 and Cr-He coatings, deposited using the electrolytic soft Cr powder used in this research. The hardness at 25 °C represents the as-deposited coating hardness. Annealing times are listed next to their respective data points.

To understand long-time annealing effects on the Cr coating microstructure during in-reactor service, Cr-N2 and Cr-He coatings were annealed at 350 °C for a total of 90 days (~1500 hours) with samples being removed for cross-sectional EBSD analysis at increments of 30 days. Fig. 8.2 shows EBSD results for the as-deposited Cr-N2 coating before and after annealing for 60 days. The IPF and KAM maps (a, c) reveal the typical microstructure of cold sprayed Cr, with larger grains representing the interior of strained particles (KAM >2°) that are surrounded by nano-scale grains showing KAM <1°, indicative of dynamic recrystallization. The KAM maps reveal even more reduction of local strain (KAM <1°) after annealing, especially within particle interiors (Fig. 8.2 d). This indicates that annealing has reduced the dislocation density within the Cr-N2 coating, suggesting that recovery is taking place.

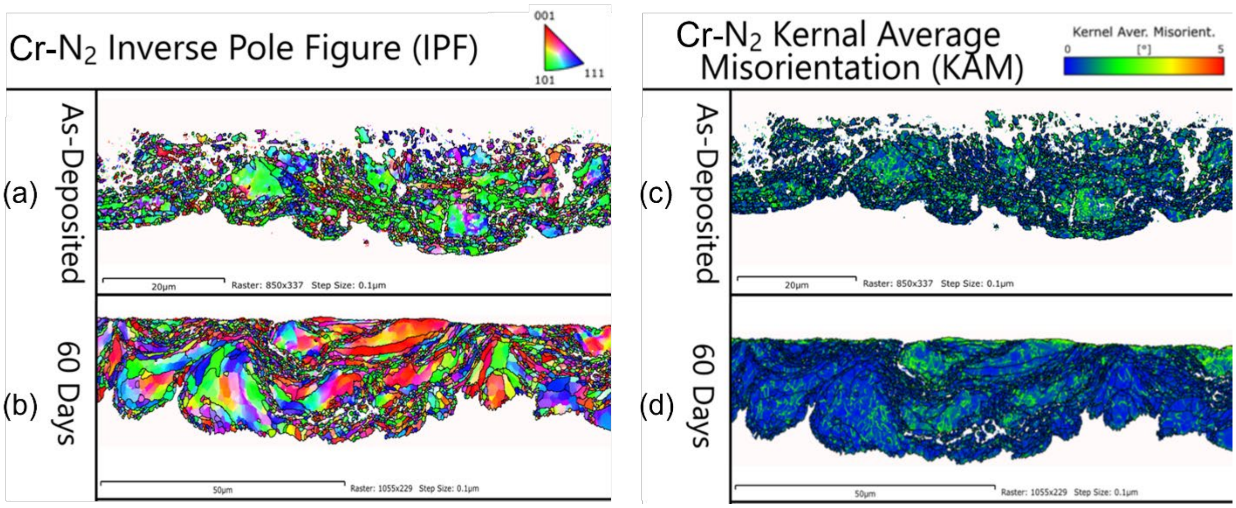

Fig. 8.2. EBSD results for Cr-N2 coatings annealed at 350 °C: (a-b) IPF maps before and after annealing for 60 days, respectively; (c-d) KAM maps before and after annealing 60 days, respectively.

Fig. 8.3 shows EBSD results for the as-deposited Cr-He coating before and after annealing for 60 days. The IPF map in Fig. 8.3 (a) shows larger grains that are slightly more deformed than in the Cr-N2 coating, due to higher particle impact velocities inducing greater plastic deformation. This is also revealed in the KAM map shown in Fig. 8.3 (c), where the large grains have a more uniform distribution of plastic strain (KAM > 2.5°) indicating higher dislocation density from plastic deformation. Indications of stress relief are observed as the mean KAM value dropped below 1° (Fig. 8.3 d). The average grain size for the Cr-N2 and Cr-He coatings calculated in the as-deposited and annealed conditions showed no difference. This suggests that annealing of the coating was in the recovery stage and higher temperatures and longer times are needed to induce recrystallization and grain growth.

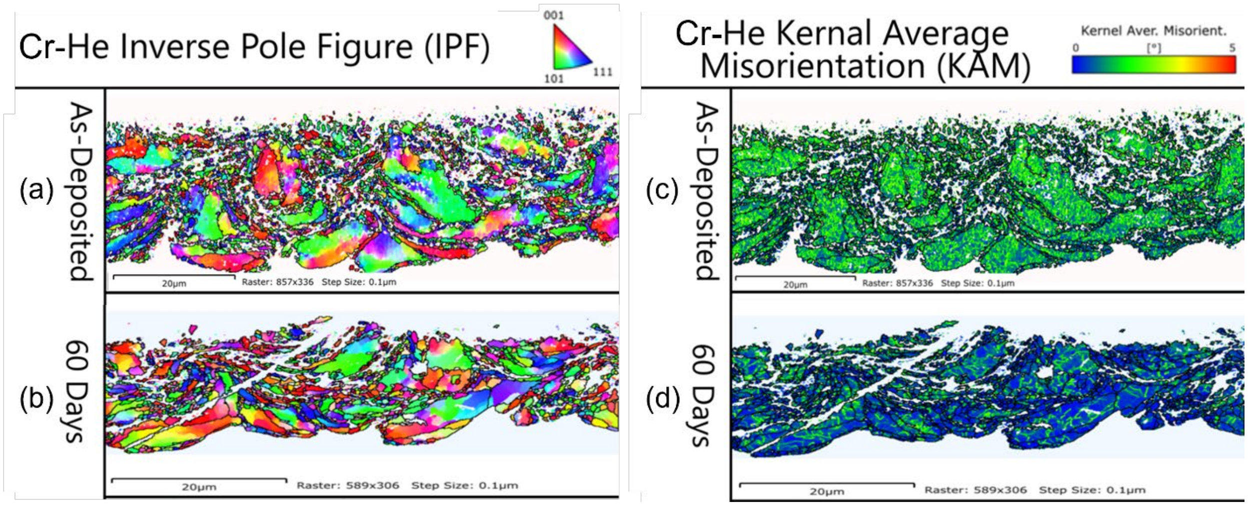

Fig. 8.3. EBSD results for Cr-He coatings annealed at 350 °C: (a-b) IPF maps before and after annealing for 60 days, respectively; (c-d) KAM maps before and after annealing 60 days, respectively.

The KAM results from Fig. 8.2 (c-d) and Fig. 8.3 (c-d) were compiled to get a quantitative sense of the amount of recovery during annealing of the cold spray coatings. Fig. 8.4 shows the evolution of KAM in the Cr-N2 and Cr-He coatings up to 60 days annealing at 350 °C. The y-axis represents the percentage of grains having KAM >2.5°, which represents plastically deformed grains in the coating and excludes dynamically recrystallized grains which typically have KAM <1°. Fig. 8.4 indicates that the as-deposited Cr-He coating contains a larger percentage of plastically deformed grains than the Cr-N2 coating (5.5% and 1.5%, respectively), which is expected due to higher impact velocities leading to more severe plastic deformation. After 60 days annealing, both coatings showed a decrease in the number of grains with higher kernel average misorientation, with the Cr-He coatings showing a more significant drop. The EBSD results suggest that the Cr coatings will undergo low-temperature stress relief during extended exposure to normal operating temperature in a PWR [37].

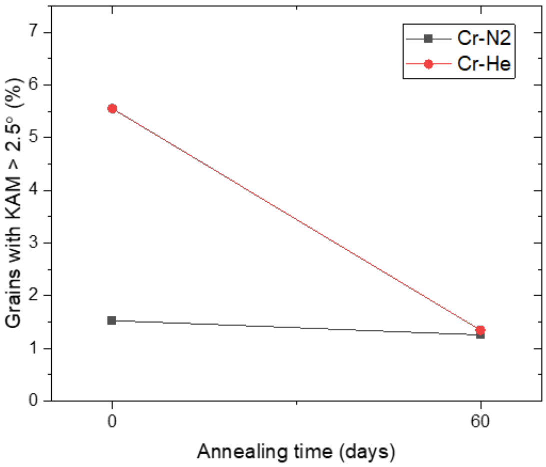

Fig. 8.4. Plot of kernel average misorientation vs. annealing time (in days) for Cr-N2 and Cr-He coatings annealed at 350 °C. The plot shows the percentage of grains with KAM > 2.5° decreases with annealing time.

Fig. 8.1 also shows results of annealing experiments performed at higher temperatures. Annealing at 650 °C (T/T_m ~0.42) for 24 h and 750 °C (T/T_m ~0.47) for 1 h (i.e., short times) resulted in modest hardness decreases of about 60 $HV_{.05}$, indicating the cold spray Cr coating underwent some degree of recrystallization. The microstructure of the Cr-He coating annealed at 750 °C for 1 hour was previously shown in Section 7, Fig. 7.2 (b). Annealing for longer times showed hardness decreases to 316 ± 17 $HV_{.05}$ (500 °C), 298 ± 21 $HV_{.05}$ (600 °C), and 215 ± 10 $HV_{.05}$ (700 °C) after 72 hours. Residual stresses in the coatings annealed at 500 °C were measured to be 53 ± 47 and 10 ± 84 MPa in the Cr-N2 and Cr-He coatings, respectively, using the XRD $\sin^2\psi$ method. These stresses have shifted slightly into the tensile regime. This represents a notable annealing away of compressive residual stresses present in the as-deposited cold sprayed Cr-N2 and Cr-He coatings, which were -329 ± 21 and -400 ± 21 MPa, respectively.

The results reveal that annealing temperature and time must be carefully selected to achieve the desired mechanical properties of the cold spray Cr coating. High temperatures and low annealing times could be an economical approach to intentionally to induce stress relief in the Cr coatings, but the temperatures should remain below the $\alpha \leftrightarrow \beta$ transformation temperature for the Zr-alloy (~860 °C from the Cr-Zr phase diagram shown in Fig. 8.5 [227]). The hardness of the Zry-4 substrates remained the same after all annealing treatments, though it is important to note that only a small fraction of the substrate thickness was affected by cold spray deposition (<50 μm). This is a positive result as cold spray was chosen to limit the thermal impact to the original Zr-alloy cladding during coating deposition.

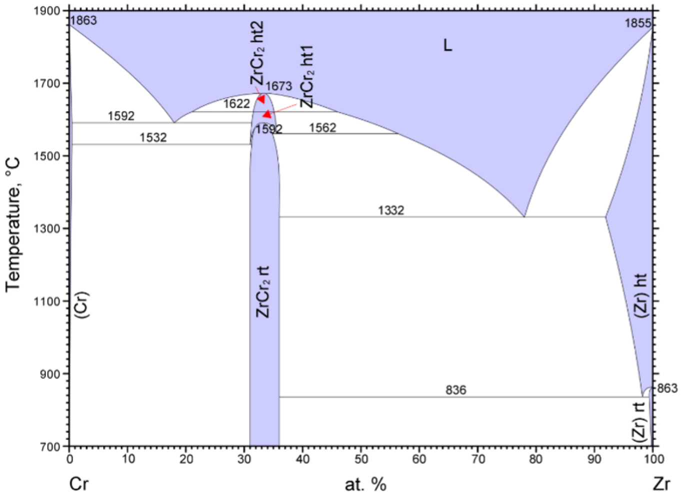

Fig. 8.5. Binary Cr-Zr phase diagram, reproduced from Okamoto [227].

8.2. Annealing treatments to simulate effect of reactor environment

Cr-coated Zr-alloy cladding is expected to operate in PWR systems for a minimum of 36 months at temperatures between 300-350 °C. In the case of a DBA or BDBA, however, power transients in the core can cause rapid heating of the Zr-alloy cladding. Fig. 8.6 shows a schematic of the accident progression inside a PWR core, reproduced from Zinkle et al. [7]. Thus, it is important to understand the mechanical properties and performance of Cr-coated Zr-alloy at normal operating conditions and potential accident scenarios. Carefully considered annealing treatments were designed to simulate different microstructures that the cold spray Cr coatings may experience during the simulated reactor environments shown in Fig. 8.6. These effects include:

a) As-deposited (*“Cr-AD”*) – represents reactor insertion and possibly normal operation

b) 600 °C, 24 h (*“Cr-600C”*) – represents power transient or long-term annealing

c) 1000 °C, 1 h (*“Cr-1000C”*) – represents extended LOCA

d) Ion irradiation up to 30 dpa (*“Cr-IRR”*) – represents end-of-life irradiation effects

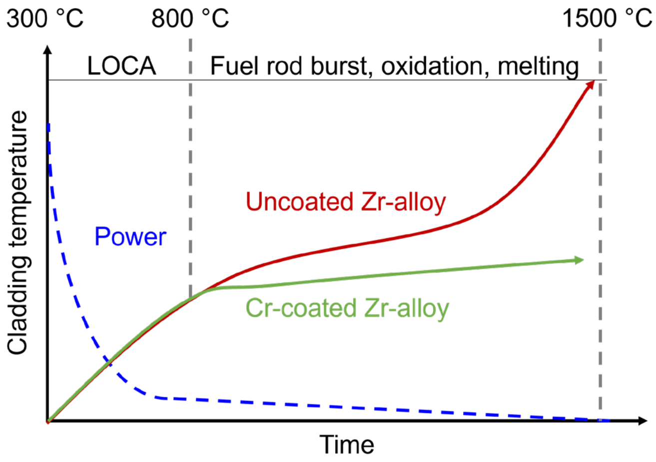

Fig. 8.6. Schematic overview of LOCA progression inside a PWR core, without ballooning/burst events (for simplicity). Reproduced from the work by Zinkle et al. [7].

The process for preparing samples for annealing treatments is shown in Fig. 8.7. Cold spray Cr coatings deposited on Zry-4 cladding tubes using both Cr-N2 and Cr-He conditions were polished down to 20-25 μm total thickness using the procedure outlined in Section 2.3.7. After sectioning, the samples designated for annealing (conditions (b) and (c) listed above) were encapsulated in high-purity quartz ampules backfilled with argon gas, as explained in Section 2.11, to prevent oxidation of the coatings or underlying substrates. After annealing, both sides of thin specimens were polished to a mirror-like finish to remove any residual surface effects from the cutting and/or annealing processes. The final cross-sectional specimen thickness was approximately 1.28 ± 0.02 mm.

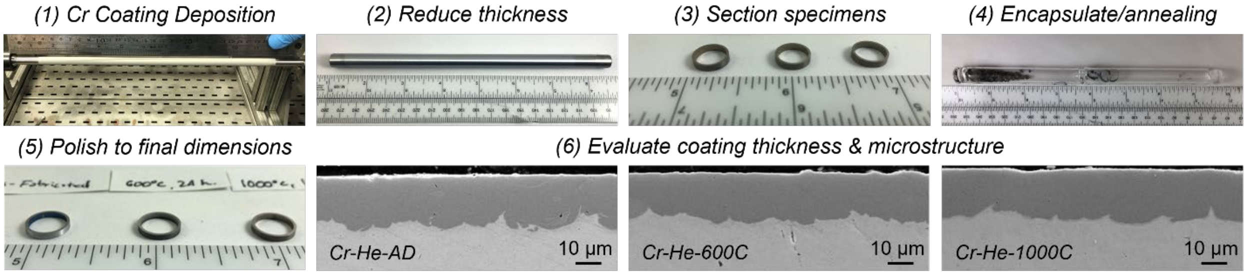

Fig. 8.7. Photographs of the sample preparation process for creating small specimens for annealing treatments and micro-cantilever beam bending tests.

Three representative specimens were mounted in cross-section and imaged using SEM to check coating thickness and microstructure after annealing treatment, as shown in Fig. 8.7. Following this, EBSD mapping was performed near the interfaces of the Cr-He-AD, Cr-He-600C, and Cr-He-1000C specimens, and the results are shown in Fig. 8.8. The legend at the top of the figure provides additional information about pixel intensity, phases, and grain orientations for the band contrast (a-c), phase (d-f), and IPF (g-i) maps. The BC map for the Cr-He-AD condition (Fig. 8.8 a) shows clearly defined deformed particles and particle boundaries within the cold spray coating. Nearly all grains in the coating are resolved besides the regions with the smallest dynamically recrystallized grains. The BC map for the Cr-He-600C condition (Fig. 8.8 b) shows similar resolution and slightly more smearing within the coating, which could be a result of recrystallization. The BC map for the Cr-He-1000C condition shows a very high-quality map due to the extent of recrystallization and grain growth in the coating.

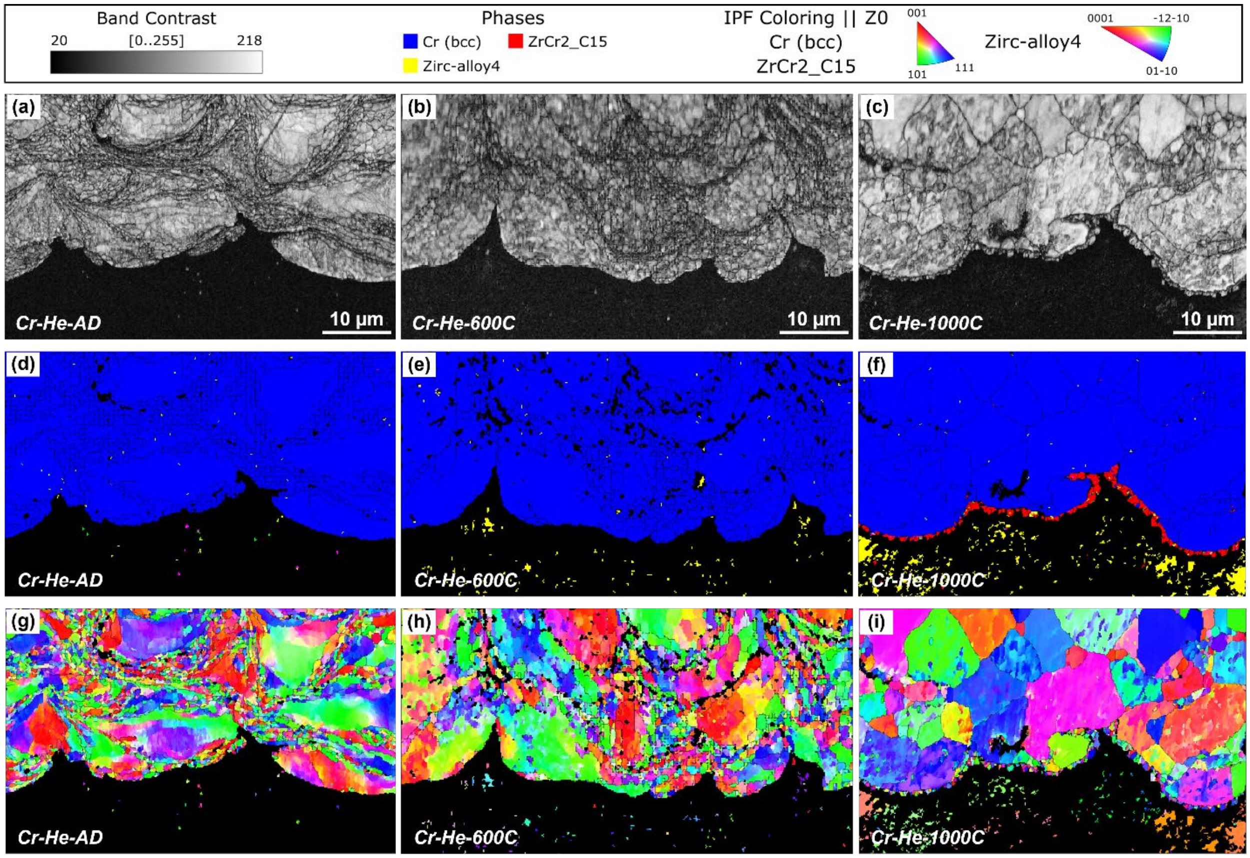

Fig. 8.8. EBSD results for the Cr-He coatings on Zry-4 in the following conditions: as-deposited (left column), 600 °C (center column), 1000 °C (right column). The maps show: (a-c) BC, (d-f) phases, (g-i) IPFs. The legend at the top provides additional information for the various maps.

The phase maps shown in Fig. 8.8 (d-f) reveal bcc Cr phase present in the coating with some misidentified Zry-4 pixels. Fig. 8.8 (f) also reveals a thin (~1 µm) $ZrCr_2$ intermetallic phase that formed during the 1 hour anneal at 1000 °C, which is possible due to high temperature inter-diffusion (Fig. 8.5). Indexing of the phases in the Zry-4 near the interfacial regions (5 to 10 μm) was limited for two reasons. First, this region contained very fine dynamically recrystallized grains as was shown through STEM imaging in Sections 3 and 4. While the extremely small grain size made it difficult to index using EBSD, the band contrast maps show it was possible within the Cr coating. This leads to the second reason, that is that Cr and Zr exhibit different polishing rates during metallographic preparation. Fig. 8.8 (d-f) reveals that the number of indexed grains in the Zry-4 substrate increases with annealing temperature due to the softening of the Cr coating.

The IPF maps in Fig. 8.8 (g & h) reveal a similar grain structure before and after 600 °C annealing for 24 hours. The Cr-He-600C IPF shows some unindexed pixels around particle boundaries, which could be due to porosity or inadequate polishing. However, the Cr-He-1000C IPF (Fig. 8.8 i) reveals a remarkably different grain structure, showing very large grains and hardly any nanoscale grains or particle boundaries. The large grains also show mixed coloring, indicative of multiple orientations present within one grain. The grain size statistics for the three conditions are shown in Fig. 8.9. Notably, the combined plot shown in Fig. 8.9 (d) reveals that the Cr-He-AD sample has the highest number density of grains lower than 2 μm in diameter, which decreases with annealing temperature. The individual plots show that the grain size shifts from a skewed-left to bi-modal to skewed-right as annealing temperature increases. Therefore, these plots appropriately demonstrate that the Cr coating is predominately fine-grained after deposition, undergoes recrystallization at 600 °C, and undergoes grain growth at 1000 °C.

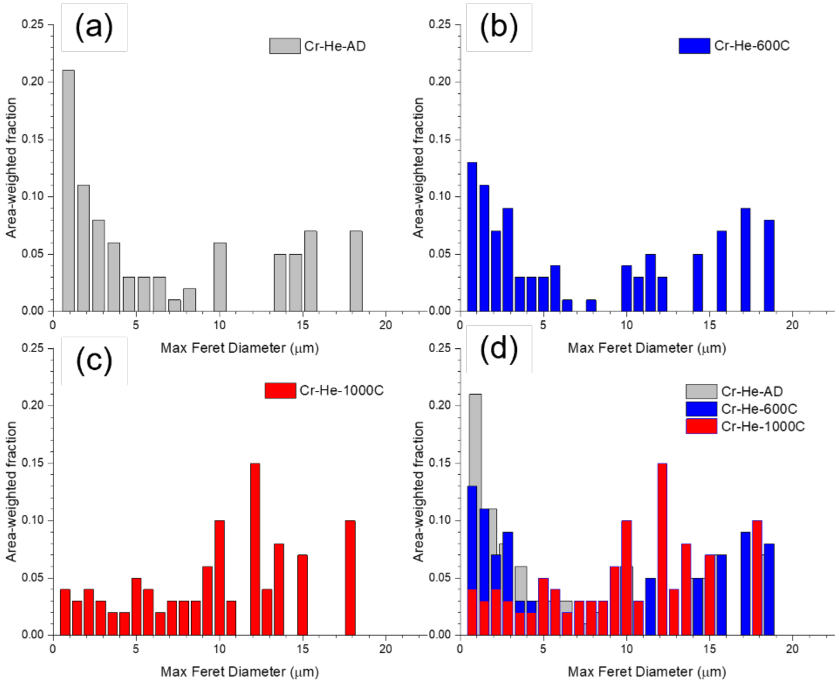

Fig. 8.9. Grain statistics for (a) Cr-He-AD, (b) Cr-He-600C, (c) Cr-He-1000C, and (d) combined. Plots show area-weighted fraction of grains according to max Feret diameter (in μm).

The extent of annealing in the Cr coating microstructure can also be characterized by internal misorientations. EBSD results in Fig. 8.10 show grain orientation spread (GOS), grain reference orientation deviation (GROD), and kernel average misorientation (KAM), which were defined in Section 2.5. The GOS maps shown in Fig. 8.10 (a-c) reveal the mean misorientation within each grain decreases with increasing annealing temperature. Several grains near the interface in the Cr-He-AD sample show high levels of internal misorientation (25-30°), while this number drops below 20° after 600 °C anneal and below 10° at 1000 °C. The GROD maps shown in Fig. 8.10 (d-f) are good illustrations of degree of recrystallization that has occurred in the Cr coatings. The Cr-He-AD sample shows dynamic recrystallization along inter-particle boundaries (denoted by nanoscale grains in blue color). Annealing at 600 °C reveals that recrystallization has taken place within the larger deformed particles. Annealing at 1000 °C results in an almost completely recrystallized microstructure. The KAM maps shown in Fig. 8.10 (g-i) revealed that high levels of plastic strain remain after 600 °C annealing, and a reasonably high density of dislocations is maintained within the particles near the Cr-Zr interface after the 1000 °C annealing. This suggests that the heavily deformed Cr coating may still provide enhanced strength at higher temperatures while simultaneously improving ductility. The next section will describe micro-mechanical testing experiments performed to assess the effects of these microstructural changes on the mechanical performance of Cr-coated Zr-alloy cladding.

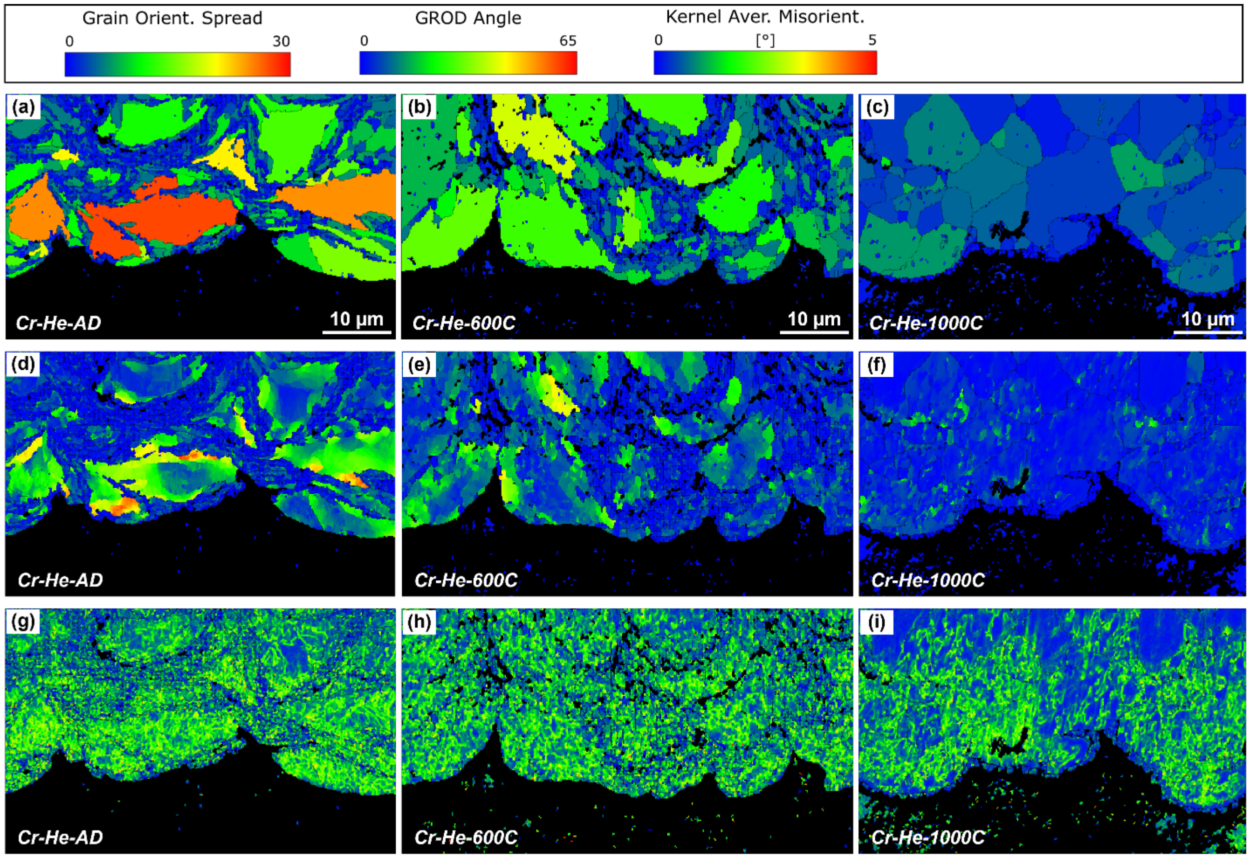

Fig. 8.10. EBSD results for the Cr-He coatings on Zry-4 in the following conditions: as-deposited (left column), 600 °C (center column), 1000 °C (right column). The maps show: (a-c) GOS, (d-f) GROD, (g-i) KAM. The legend at the top provides additional information for the various maps.

8.3. In situ micro-cantilever beam bending tests of cold spray Cr-coated Zr-alloy

8.3.1. Experimental description

The deformation and cracking behavior of Cr-coated Zr-alloy cladding were investigated by bending micro-cantilever beams (in various microstructural conditions) *in situ* in a SEM. The samples investigated in this study with associated details are summarized in Table 8.1. Thin ring samples of Cr-coated Zr-alloy cladding (shown in Fig. 8.7) in the conditions listed were fabricated according to the procedure described in Section 8.2. After final polishing, one third of the ring sample was sectioned using a low-speed saw equipped with a high concentration diamond blade and mounted to a standard aluminum SEM pin stub using high strength super glue and allowed to dry. A thin layer of conductive carbon paste was applied to the stub around the sample to increase conductivity in the SEM.

Table 8.1. Cold spray and post-processing conditions for Cr coated Zr-alloy cladding samples subjected to micro-cantilever beam bending studies.

Cold spray deposition parameters			**Velocity effect**	**Annealing effect**	**Intermetallic and grain growth effects**	**Irradiation effect**
Gas Composition	Gas Temperature	Particle velocity	Cr-AD	Cr- 600C	Cr-1000C	Cr-IRR
100%-N_2	750 °C	680 m/s	As-Deposited	600 °C, 24h	1000 °C, 1h	30 dpa
95%-He	500 °C	880 m/s	As-Deposited	600 °C, 24h	1000 °C, 1h	30 dpa

Micro-cantilever beams were fabricated using a PFIB available in the NIAC facilities at the University of Wisconsin-Madison. Five cantilever beams were fabricated for each sample. First, the Cr coating was milled into a rough rectangular shape using a Xe^+ ion beam (different from ion irradiation) at 30 kV and 0.2 μA current. Second, the beams were tilted to -8° with respect to the electron beam and milled at 30 kV using a 60 nA milling current. This was done to remove excess material and to create a pentagonal cross-section, resulting in a cantilever that is symmetrical on its vertical axis. Third, the sample (on the stub) was mounted to a pre-tilted 45° stage and milled using 1 nA beam current to remove re-redeposited material and to achieve a smooth, flat surface. This process was repeated using successively lower milling currents (15 nA, 4 nA, and 1 nA) until final dimensions were reached.

A schematic of the cantilever beam geometry alongside an SEM image of a finished beam is shown in Fig. 8.11. The beam dimensions for the as-deposited and annealed Cr coatings were 8 × 8 × 15 μm, while the beam dimensions for the ion-irradiated Cr coatings were 3 × 3 × 5 μm. The ion-irradiated cantilever beams were made smaller due to the limitation in size of the damage region imposed by the ion beam. For each sample condition, three cantilever beams remained un-notched while two samples received a thin trench (i.e., notch) less than 300 nm deep along the Cr-Zr interface to promote failure at the interface.

Finally, a shallow (2 μm × 2 μm × 300 nm) pit was milled approximately 10 μm from the Cr-Zr interface to prevent slipping of the indenter tip on the beam surface as it presses down to create a bending stress on the on the micro-cantilever beam. Once final milling was completed, SEM was used to image multiple sides of the cantilever beams to measure every dimension of the pentagonal cross section, as shown in Fig. 8.12.

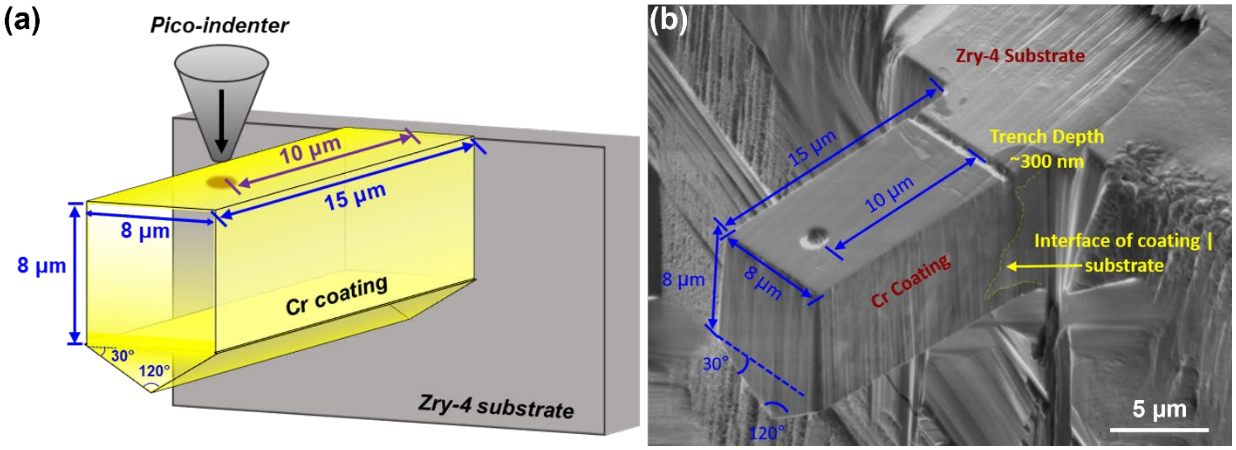

Fig. 8.11. (a) Schematic illustration of the micro-cantilever beam geometry with dimensions; (b) SEM image of a Cr cantilever beam on Zr-alloy cladding, fabricated using a PFIB, showing the Cr-Zr interface with a thin trench that serves as a notch (not all samples were notched).

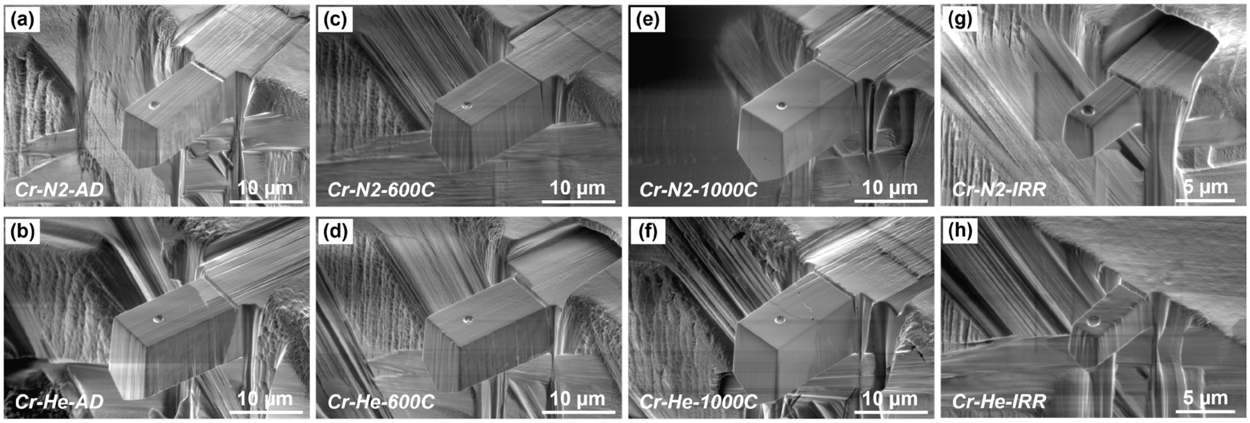

Fig. 8.12. SEM images of the PFIB-milled notched cantilever beams of Cr-coated Zr-alloy, showing Cr-N2 beams (top row) and Cr-He beams (bottom row) in the following conditions: (a, b) as-deposited; (c, d) 600 °C, 24 h anneal; (e, f) 1000 °C, 1 h anneal; (g, h) ion irradiated up to 30 dpa at the Cr-Zr interface.

The fabricated micro-cantilever beams were then transported to Los Alamos National Laboratory by the author for testing. Micro-cantilever beam bending tests were performed using a PI-85 picoindenter system (Bruker/Hysitron Inc., Madison, USA) located inside of an Apreo-2 FE/SEM (Thermo Scientific, Madison, USA) equipped with *in situ* video recording software. The beams were loaded using a spherical indenter tip (2 μm diameter) aligned with the pit and displaced downward and normal to the top face of the cantilever beam, shown schematically in Fig. 8.11 (a). The displacement rate was set to 10 nm/s to ensure a nominal strain rate of 10^{-3} s^{-1}. Each test was initially set to stop after 3 μm of total displacement; however, some tests were stopped immediately after fracture, and some tests continued beyond 3 μm displacement depending on the cracking and facture behavior observed during the *in situ* bending tests.

Ex situ imaging using SEM was used to examine all deformed surfaces of the cantilever beams. Crack lengths were measured using the *in situ* SEM video and compared to the final crack lengths measured using SEM imaging. PFIB was used to extract a thin lamella from the center of one representative cantilever beam from each microstructural condition (excluding irradiated beams which were characterized extensively in Section 6). The lamellae were welded to a conductive copper grid where FIB milling was used to reduce ion beam damage induced by the PFIB. EBSD was used to characterize the deformed surfaces according to the procedure described in Section 2.5. The Aztec Crystal software was used to generate phase, IPF, and KAM maps around the fractured region to ascertain information regarding cracking, deformation, and strain behavior during bending tests.

8.3.2. Micro-cantilever beam bending of as-deposited Cr coatings (particle velocity effect)

A typical load-displacement profile for an unnotched Cr-He-AD cantilever beam bent to failure is shown in Fig. 8.13 (a). At about 1130 nm of displacement (19.9 mN of applied load), cracking initiates and propagates at the interface of the Cr coating/Zry-4 substrate resulting in a load drop. The crack propagation event was abrupt, representing brittle failure, which is preferred in bending tests to gain an accurate representation of the fracture toughness and adhesion strength [274,275]. The load drop phenomenon was captured by the load-displacement profile and correlated with the crack extension captured by the *in situ* SEM video. Fig. 8.13 (b-f) shows the evolution of crack propagation during beam bending and the indicated displacements are labeled in Fig. 8.13 (a). The crack propagated a short distance and was arrested within the near-interface regions of the Zry-4 substrate. The final crack length was 2.8 and 4.2 μm, measured *ex situ* on both sides of the beam using SEM.

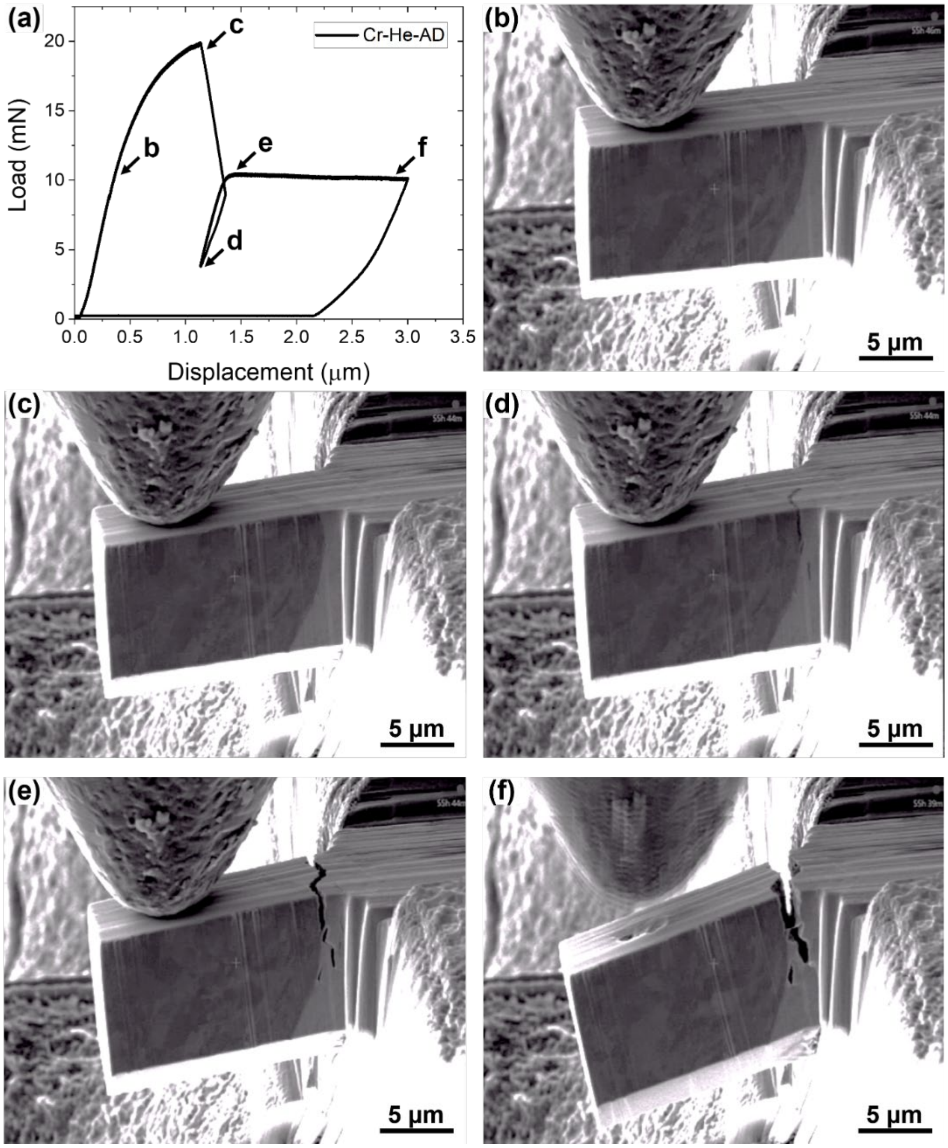

Fig. 8.13. (a) Load-displacement profile of a typical micro-cantilever beam bending test of Cr-He-AD on Zry-4; (b-f) In situ SEM images showing beam bending and crack propagation within the cantilever beam at various displacement magnitudes.

Fig. 8.14 shows *in situ* SEM images of selected cantilever beams bent to failure. Cracking in the Cr-N2 coating containing a milled trench (Fig. 8.14 a) began at a point near the trench, propagated along the interface and into the Zry-4 substrate and arrested just upon entry due to the ductility of Zry-4. Cracking in the Cr-N2 coating without a trench (Fig. 8.14 b) also initiated at the interface and propagated along the interface before entering the near-interface regions of Zry-4 substrate to be arrested there. Similarly, cracking in the Cr-He coating with and without a trench (Fig. 8.14 c & d, respectively) initiated at a small region of the Cr-Zr interface and then propagated slightly into the substrate. Interestingly, the presence of a trench was less important for the initiation of fracture compared to the location of the interface relative to the bending moment of the beam.

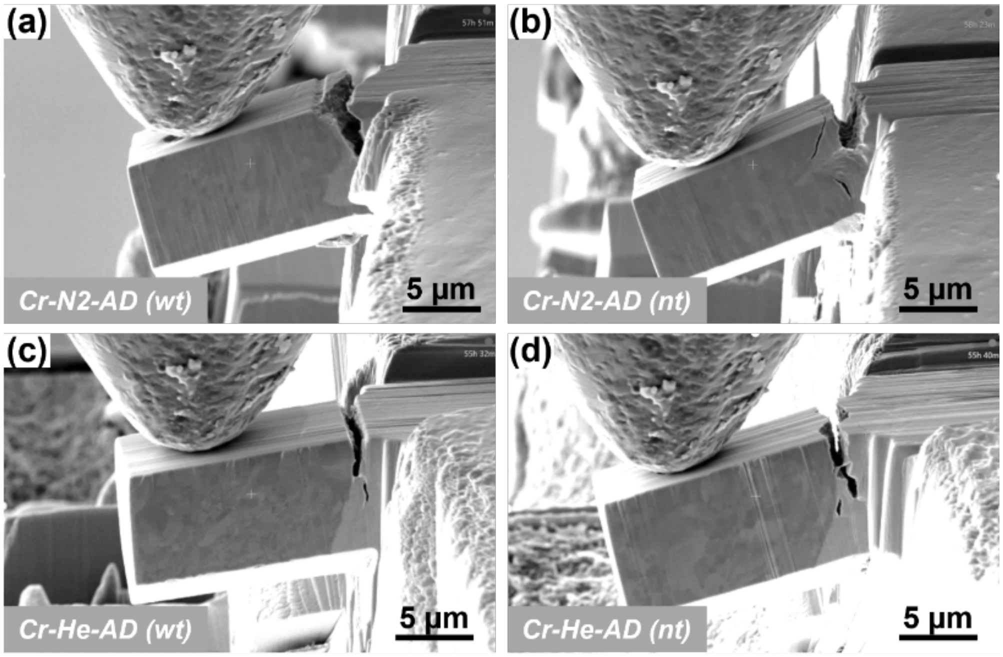

Fig. 8.14. SEM images of micro-cantilever beams with trench (wt) or no trench (nt) tested to failure, showing: Cr-N2-AD cantilever beams with trench (a) and no trench (b); Cr-He-AD cantilever beams with trench (c) and no trench (d).

8.3.3. Micro-cantilever beam bending of 600 °C annealed Cr coatings (annealing effect)

A typical load-displacement profile for a notched Cr-He-600C cantilever beam is shown in Fig. 8.15 (a), with the evolution of beam bending behavior captured by *in situ* SEM video stills shown in Fig. 8.15 (b-f). The beam exhibited ductile behavior and displayed no distinct crack initiation or failure up to 5 μm of displacement. Rather, a peeling of the coating from the substrate and peeling along some Cr-Cr interparticle boundaries was observed, which correlated with small drops and recovery in load (rather than larger drops in load observed for as-deposited samples). This behavior is suggestive of the ability of the materials system to resist crack propagation during plastic deformation.

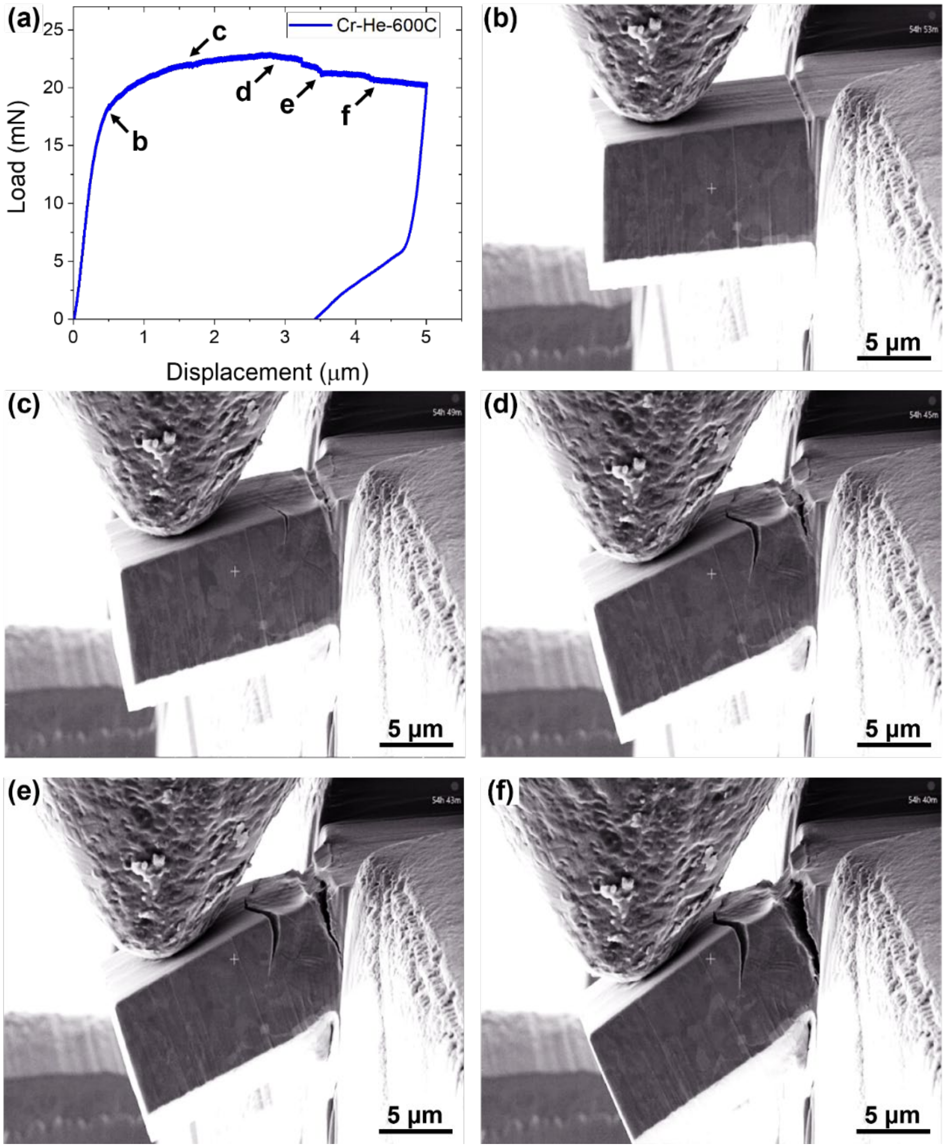

Fig. 8.15. (a) Load-displacement profile of a typical micro-cantilever beam bending test of Cr-He-600C on Zry-4; (b-f) In situ SEM images showing beam bending and ductile failure near the Cr-Zr interface and within Cr particle boundaries, corresponding to small decreases in applied load.

Fig. 8.16 shows *in situ* SEM images of selected micro-cantilever beams, which show ductile plastic deformation near the interface. The beams containing a trench (Fig. 8.16 a & c) were more likely to exhibit peeling near the interface. Beams without a trench showed mixed behavior, with some beams (Fig. 8.16 b) remaining intact up to 5 μm of displacement while other beams (Fig. 8.16 d) exhibited peeling and slow tearing behavior. Overall, the 600 °C annealed beams withstood higher loads than the other sample conditions and six of the ten beams were displaced up to 5 µm without showing any failure via crack propagation before the bending test was terminated.

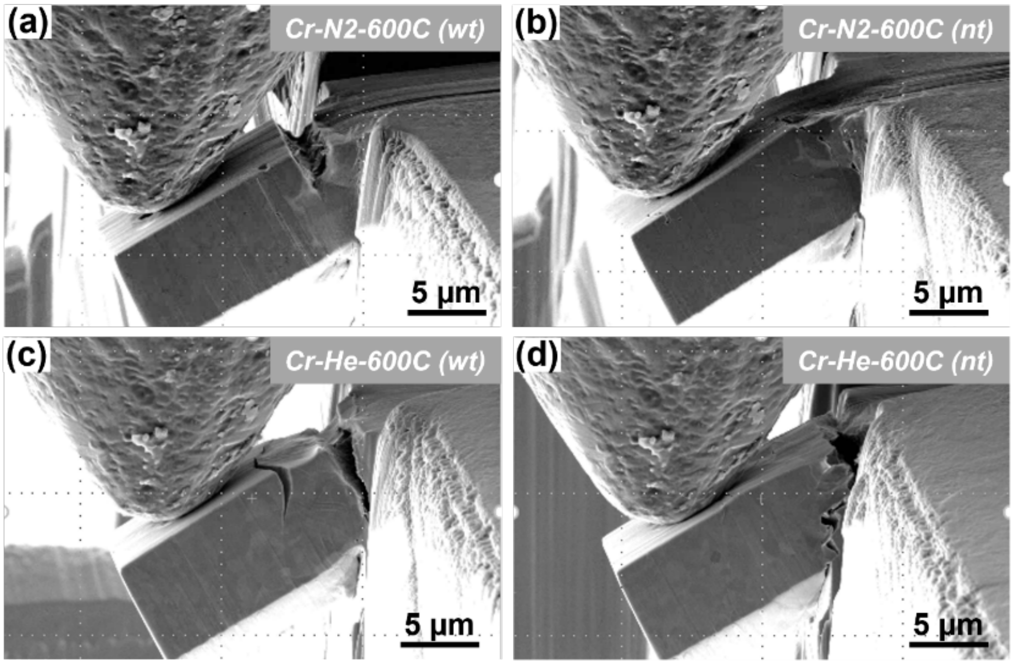

Fig. 8.16. SEM images of micro-cantilever beams with trench (wt) or no trench (nt) tested to failure, showing: Cr-N2-600C cantilever beams with trench (a) and no trench (b); Cr-He-600C cantilever beams with trench (c) and no trench (d).

8.3.4. Micro-cantilever beam bending of 1000 °C annealed Cr coatings (interdiffusion and intermetallic phase effect)

A typical load-displacement profile for a Cr-He-1000C cantilever beam bent to failure is shown in Fig. 8.17 (a). After about 510 nm of displacement (11.3 mN of applied load), the beam experienced its first minor cracking event as shown in Fig. 8.17 (b). The load continued to increase until 1.25 µm of displacement (13.8 mN of applied load), where the crack began to propagate along the interface (Fig. 8.17 c). The crack did not divert to the Zry-4 substrate but rather continued along interface, presumably due to the $ZrCr_2$ phase that formed due to high temperature interdiffusion between Cr and Zr. The minimal load drops captured by the load displacement profile that correlated with the short crack extensions captured by the *in* situ SEM video are indicative of improved ductility and the ability of the materials system to recover from crack damage. The first cracking event measured 1.2 µm along the side of the beam, and the final crack length was about 6.4 µm. Thus, while the formation of brittle $ZrCr_2$ phase at the interface high temperatures can influence crack initiation, the overall enhanced ductility of the coating and the substrate confines crack propagation to the interfacial regions and mitigates its propagation.

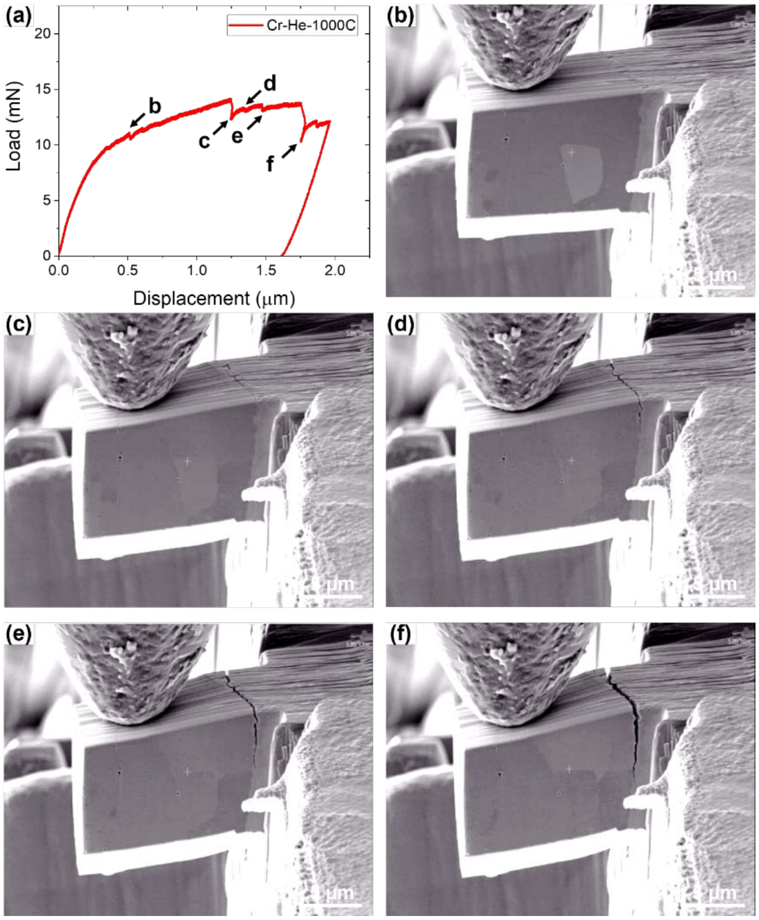

Fig. 8.17. (a) Load-displacement curve of a typical micro-cantilever beam bending test of Cr-He-1000C on Zry-4; (b-f) In situ SEM images showing beam bending and interrupted crack propagation within the cantilever beam at various displacement magnitudes.

Fig. 8.18 shows *in situ* SEM images of selected micro-cantilever beams bent to failure. Again, regardless of trench, all beams cracked near the interface and propagated into the near-surface regions of the Zr-alloy and propagated approximately parallel to the interface. The major difference between the fracture behavior of Cr-1000C beams (as compared to the Cr-AD beams) was in the length of crack propagation, in which the 1000 °C annealing promoted ductility by way of interrupted cracking behavior. The average crack length was about 4 μm and 2 μm for the Cr-AD and Cr-1000C cantilever beams, respectively.

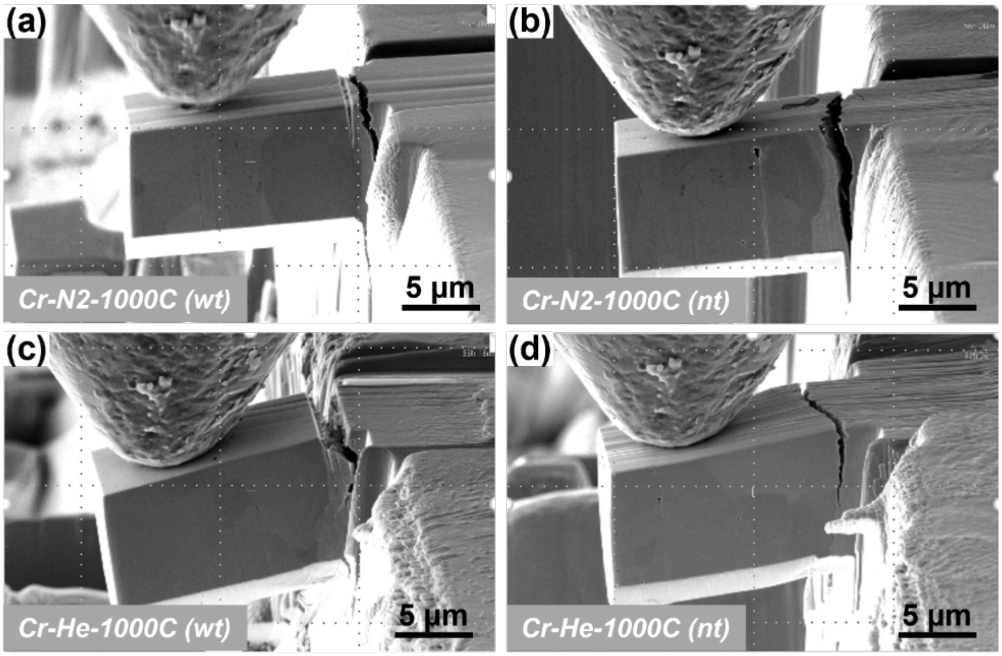

Fig. 8.18. SEM images of micro-cantilever beams with trench (wt) or no trench (nt) tested to failure, showing: Cr-N2-1000C cantilever beams with trench (a) and no trench (b); Cr-He-1000C micro-cantilever beams with trench (c) and no trench (d).

8.3.5. Micro-cantilever beam of ion irradiated Cr coatings (irradiation effect)

A typical load-displacement profile for a Cr-He-IRR micro-cantilever beam is shown in Fig. 8.19 (a). The beam exhibited ductile behavior and displayed no crack initiation or failure, which could be a result of irradiation-induced mixing at the interface enhancing the Cr-Zr interfacial bond. Fig. 8.19 (b-f) shows the evolution of bending behavior within the beam and the indicated displacements are labeled in Fig. 8.19 (a). At 455 nm of displacement (5.9 mN of applied load), the first peeling event occurred at the Cr-Zr interface as shown in Fig. 8.19 (c) and continued to widen with further bending as shown in Fig. 8.19 (d-f). The top surface of the beam near the interface exhibited failure by way of plastic collapse. The noticeable absence of drops in load compared to what was observed in previous samples clearly indicates the superior mechanical performance on the irradiated coating-substrate system.

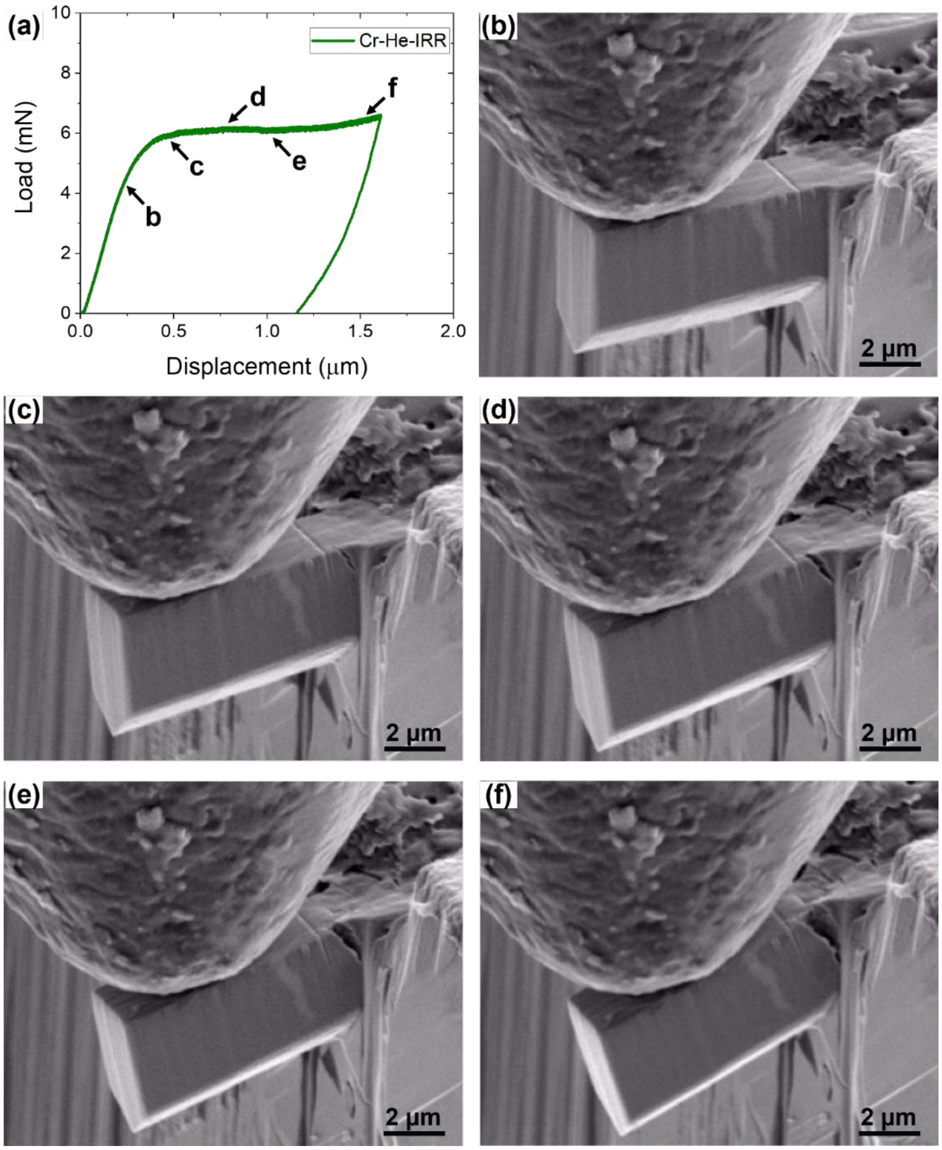

Fig. 8.19. (a) Load-displacement curve of a typical micro-cantilever beam bending test of Cr-He-IRR on Zry-4; (b-f) In situ SEM images showing beam bending and beam bending and ductile failure within the cantilever beam at various displacement magnitudes.

Fig. 8.20 shows additional *in situ* SEM images of selected micro-cantilever beams, which displayed mixed brittle-ductile behavior during bending tests. Both Cr-N2-IRR samples experienced peeling at the Cr-Zr interface with increasing load, as shown in Fig. 8.20 (a-b), which closely resembled the behavior of the Cr-600C coatings. The Cr-He-IRR coating with a trench (Fig. 8.20 c) saw sudden crack initiation away from the trench and crack propagation into the Zry-4 substrate, while the Cr-He-IRR coating without a trench (Fig. 8.20 d) exhibited ductile plastic deformation within the Zry-4 substrate and some peeling near the interface.

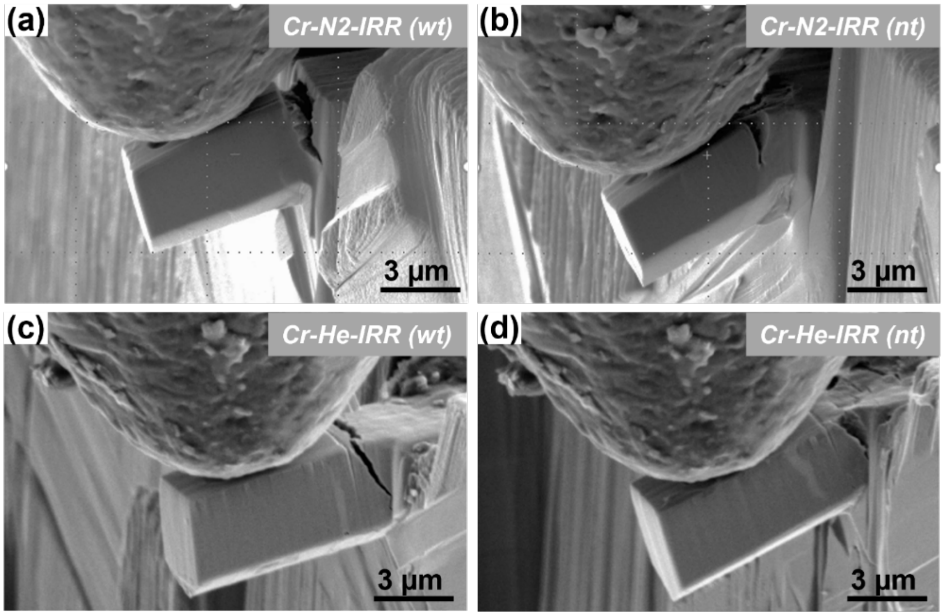

Fig. 8.20. SEM images of micro-cantilever beams with trench (wt) or no trench (nt) tested to failure, showing: Cr-N2-1000C cantilever beams with trench (a) and no trench (b); Cr-He-1000C cantilever beams with trench (c) and no trench (d).

8.3.6. Microstructure effect on beam bending behavior of Cr-coated Zr-alloy

To further understand the role of microstructure on the deformation behavior near the interface, FIB lift-outs were performed for select Cr-N2 micro-cantilever beams in the Cr-AD, Cr-600 °C , and Cr-1000 °C conditions as shown in Fig. 8.21 (a-c), respectively. SEM images of the cleaned lamellae are shown in Fig. 8.21 (d-f), which reveal the microstructure of the Cr coatings and Zry-4 substrates on either side of the interface, separated by a crack or peeling event. EBSD of the thinned lamellae was performed according to the procedure described in Section 2.5. The phase maps shown in Fig. 8.21 (g-i) give a sense of the Kukuchi band indexing fraction within the Cr and Zry-4. Indexing in the Cr-N2-AD could be accomplished but the band contrast remained low in the near-interfacial regions of Zry-4 substrate due to fine recrystallized microstructure. The Cr-N2-600C coating and substrate were fully indexable. Finally, the Cr-N2-1000C coating showed unindexed bands along the interface and near the surface of the Zry-4.

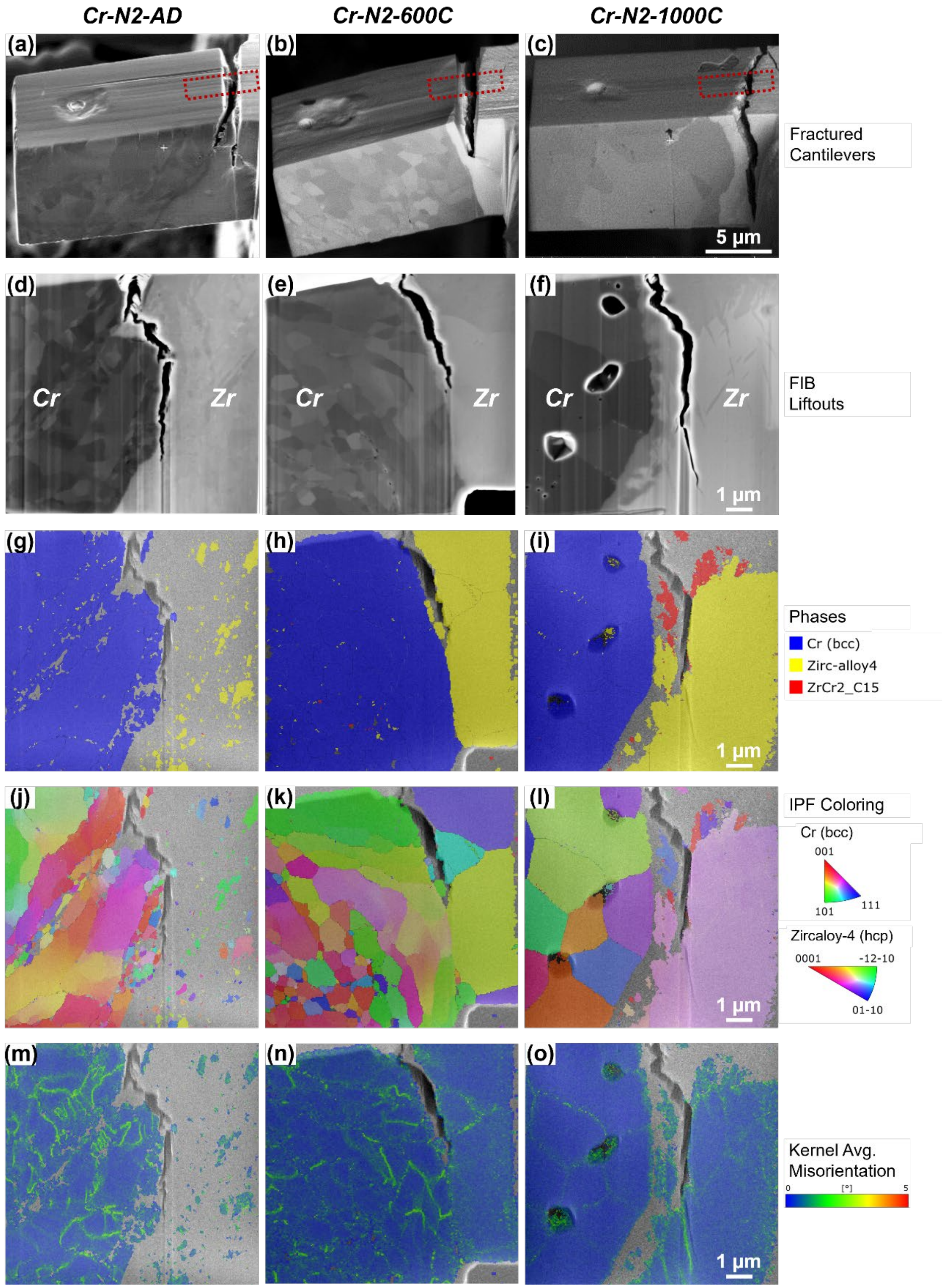

Fig. 8.21. Characterization of Cr-N2 micro-cantilevers after beam bending tests, showing Cr-AD (left column), Cr-600C (center column), and Cr-1000C (right column): (a-c) SEM images of Cr-N2 cantilevers after beam bending tests, with locations of FIB lift-outs marked in red; (d-f) SEM images of thin lamellae lifted out and cleaned using FIB, which were used for EBSD analysis; (g-i) Phase maps; (j-l) IPF maps; (m-o) KAM maps.

The phase map for the Cr-N2-AD coating (Fig. 8.21 g) reveals that cracking occurred within the Cr coating (shown in the top of the image), and then propagated along the Cr-Zr interface. The IPF map (Fig. 8.21 j) shows very fine grains within the Cr coating next to the crack, which could be a reason for the crack propagating in this region. Nanoindentation measurements taken in fine-grained regions of the Cr coating were typically indicative of higher hardness than measurements taken within the larger-grained particle interiors due to the Hall-Petch relationship. The KAM map in Fig. 8.21 (m) did not indicate a large stress concentration at the crack tip, which is indicative of brittleness. The SEM image in Fig. 8.21 (a) shows the crack terminated in a more ductile region of the Zry-4 about 2 μm away from the interface. The SEM image in Fig. 8.21 (d) shows a dark contrast microstructure within the Zry-4 at the surface of the cantilever beam, likely due to high tensile strains during bending, another reason for the poor indexability during EBSD characterization.

The phase map for the Cr-N2-600C coating (Fig. 8.21 h) shows ductile peeling along the Cr-Zr interface. The IPF shown in Fig. 8.21 (k) reveals large grains in the Cr coating and a fully recrystallized Zry-4 microstructure on the other side of the interface, which would provide more resistance to crack or peel propagation. The KAM map in Fig. 8.21 (n) displays a microstructure consisting of mostly low strain except along subgrain boundaries. There is a small stress concentration at the tip of crack or peeled region, which slows its propagation along the Cr-Zr interface. The EBSD images reveal that the 600 °C annealing treatment both strengthened the interface and enhanced ductility through recrystallization.

The phase map for the Cr-N2-1000C coating (Fig. 8.21 i) shows that crack propagation remained highly restricted to the interface, likely due to the formation of $ZrCr_2$ intermetallic layer at the interface. The IPF in Fig. 8.21 (l) shows a fine-grain structure of the $ZrCr_2$ surrounded by a single grain of Zry-4, which was recrystallized and experienced grain growth during high temperature annealing. The KAM map in Fig. 8.21 (o) shows a mostly strain-free microstructure within the Cr and Zry-4 with more strain contained within the $ZrCr_2$ grains. The large stress concentration present at the edge of the propagating crack tip explains why the load-displacement curves display recovery in load in-between crack propagation events. It is likely that the recrystallized Zry-4 microstructure, containing a low density of dislocations after annealing, provided considerable ductility to arrest the cracks soon after propagation. Additionally, the SEM image shown in Fig. 8.21 (f) reveals the same strain contrast near the top of the cantilever beam as seen in the as-deposited condition (Fig. 8.21 d). Overall, the results indicate good ductility of Cr-coated Zr-alloy under accident conditions. It is worth noting that micro-cantilever tests were performed at room temperature, so the Zry-4 substrate transformed back to the α-Zr phase. It is unknown if this same mechanical behavior would be present in the β-phase in Zry-4.

EBSD was not performed for the ion irradiated Cr coatings, though some insights may be gained from characterization of the annealed and irradiated samples described in Section 6. Most of the micro-cantilever beams experienced ductile behavior similar to the Cr-600 °C beams. This is likely due to a combination of effects, including amorphization and ion-beam mixing near the interface and softening of the Cr coating due to irradiation-induced recovery and recrystallization.

Compiled load-displacement profiles for all the tested micro-cantilever beams are shown in Fig. 8.22, plotted on the same scale. The differences in load-displacement behavior can be attributed to the microstructural conditions described above. It is important to note that the plots shown in Fig. 8.22 were not normalized with respect to the size of the micro-cantilever beams, so the magnitude of load and displacement for the Cr-IRR beams was lower due to having smaller beam size. Future work will involve removing beams that fractured at pre-existing defects (due to ion beam milling) and normalizing the load-displacement curves for a quantitative analysis of stress-strain behavior.

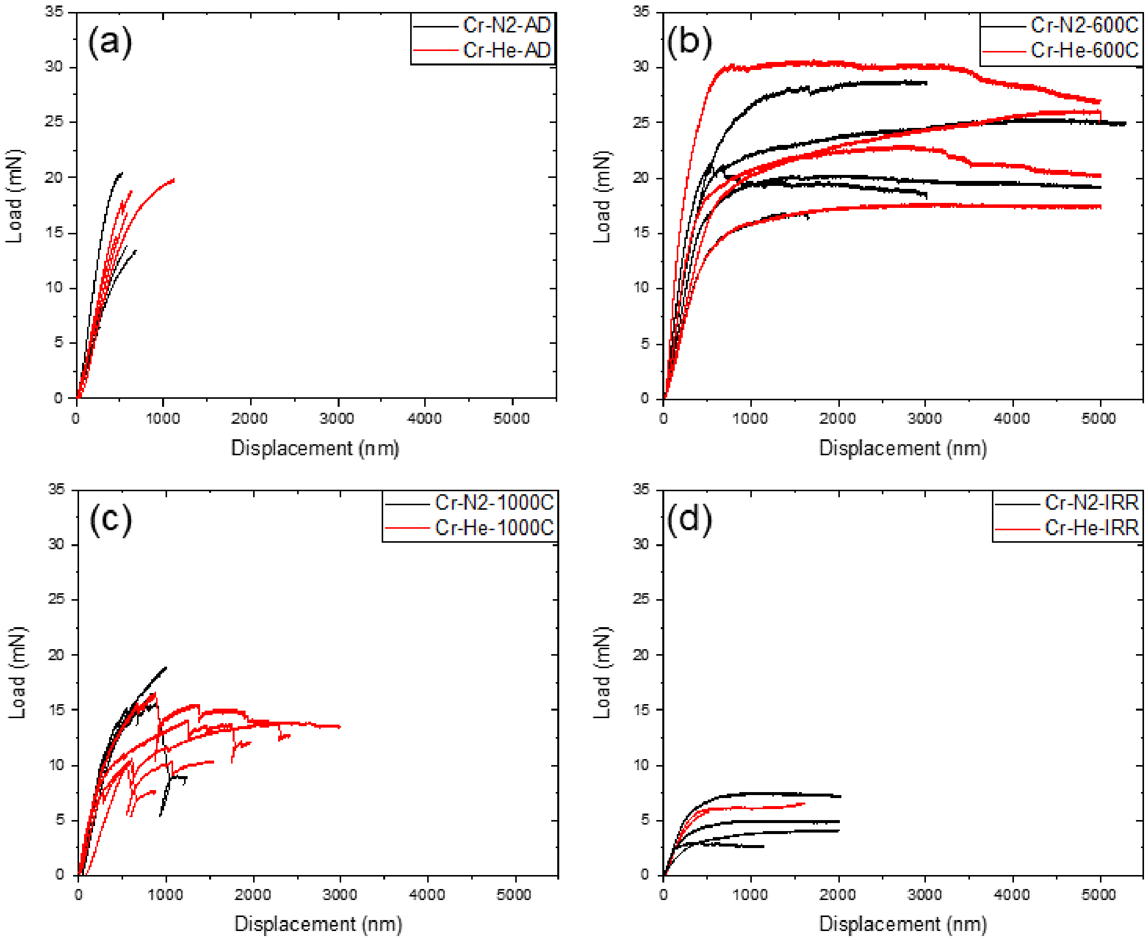

Fig. 8.22. Load-displacement profiles (up to failure) for the tested Cr-N2 (black) and Cr-He (red) micro-cantilever beams: (a) Cr-AD; (b) Cr-600C; (c) Cr-1000C; (d) Cr-IRR. Note the Cr-IRR beams experienced lower load due to the smaller beam size. Results are plotted on the same scale for comparison.

9. High temperature oxidation and hydrothermal corrosion of cold spray Cr coated Zr-alloy

9.1. High temperature air and steam oxidation testing of cold spray Cr coated Zr-alloy

The ability of chromium to provide high temperature oxidation resistance is well-known. Even as an alloying element, as for example in stainless steels, Cr provides outstanding oxidation resistance due to the formation of a tenacious and impervious Cr_2O_3 layer on the surface that resists further oxidation. This effect is likely to be even more accentuated in the case of pure Cr on account of its highly favorable Pilling-Bedworth ratio (approximately 2 for dense chromia [276]). This section evaluates the performance of cold spray Cr coatings for high temperature oxidation resistance, one of the most significant criteria for selecting Cr for the ATF application. For this limited study, samples of cold spray Cr coated Zry-4 were subjected to high temperature (> 1000 °C) air and steam environments, as per the procedure discussed in Section 2.11. The as-deposited samples were polished to a coating thickness of ~60 μm, as shown in Fig. 9.1 (a). Photographs of the coating surface after exposure to ambient air and flowing steam for 30 minutes are provided in Fig. 9.1 (b & c). While the surface morphology indicates slight differences in oxidation behavior between the samples tested in air and steam, the evolution of greenish coloration of the surface is indicative of chromium oxide formation.

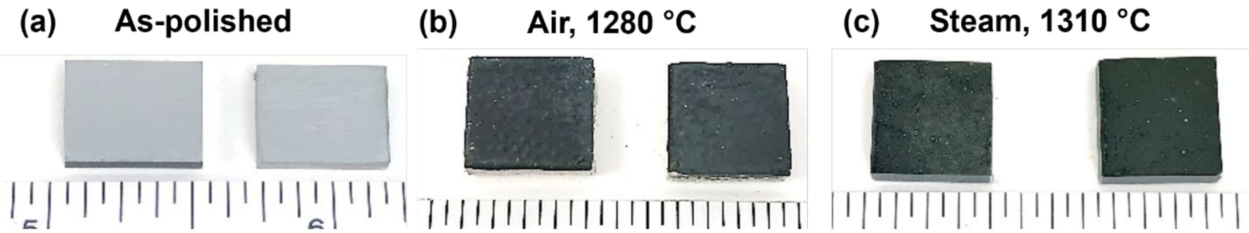

Fig. 9.1. Photographs of cold spray Cr coating on Zry-4: (a) polished to 60 um thickness, and tested at elevated temperatures (simulating accidents) for 30 minutes in the following environments: (b) ambient air at 1280 °C, (c) flowing steam at 1310 °C.

XRD patterns of the cold spray Cr coatings before and after oxidation are shown in Fig. 9.2. The typical bcc Cr peaks all but disappear as the thickness of the chromium oxide scale (identified as chromia, Cr_2O_3)

exceeded the X-ray penetration depth. The oxide peaks for all high temperature tested samples were consistent with chromia peaks (Cr_2O_3), though differences in peak intensities of this oxide phase could indicate slight changes in oxide thickness or texture. For example, Fig. 9.2 shows the Cr coating tested in 1310 °C flowing steam displayed preference for the (110) Cr_2O_3 orientation.

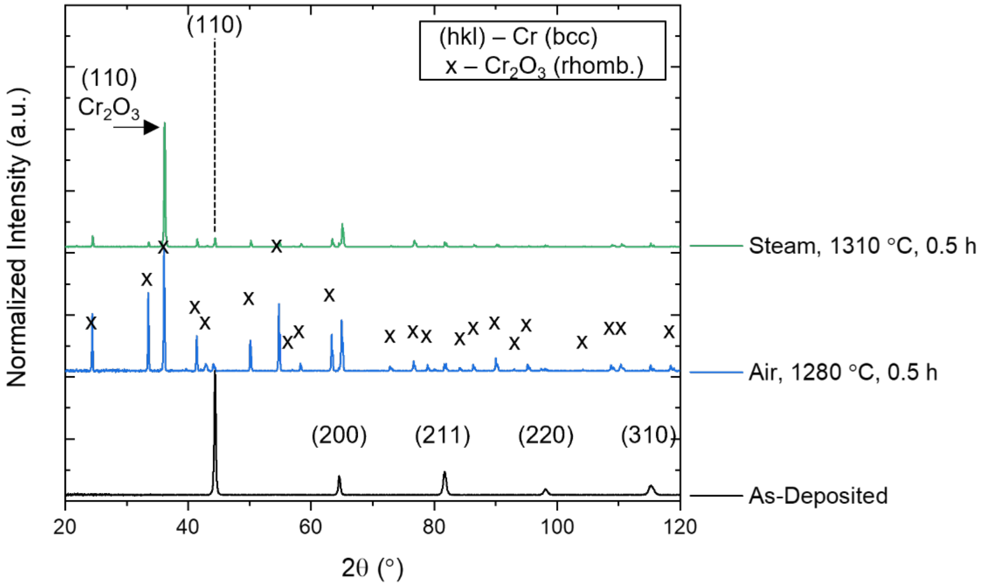

Fig. 9.2. XRD scans of as-deposited and high temperature tested cold spray Cr coatings. The bcc Cr peaks decrease in intensity as the thickness of the chromium oxide scale increases on the coating surface.

9.1.1. High temperature air oxidation

The Cr-coated Zry-4 sample tested in 1280 °C ambient air for 30 minutes produced a dark green oxide scale on the coating surface (Fig. 9.1 b). The cross-sectional SEM image shown in Fig. 9.3 (a) reveals the microstructure of the expected high temperature oxidation reaction of Cr-coated Zry-4 with the relevant phases labeled. A chromia oxide layer (10-12 µm) formed on the surface, followed by unreacted Cr coating (30-40 µm) and $ZrCr_2$ intermetallic compound (5-10 µm) at the interface. These phases were confirmed by the EDS line-scan shown in Fig. 9.3 (b). Below the $ZrCr_2$ phase an oxygen-stabilized alpha zirconium (referred to as α-Zr(O)) layer develops, which is typical during high temperature oxidation of Zr-alloys [277–279]. However, there was no oxygen profile in the interior of the Cr coating suggesting perhaps that the oxygen may have entered from the sides of the sample at these high temperatures. Otherwise, the EDS spectral maps in Fig. 9.3 (c) confirm oxygen was restricted to the Cr coating and outer surface oxide. Fig. 9.3 (c) also highlights many small (<1 µm) Cr-rich precipitates within the substrate, which emerge as the Zry-4 transitions from β-Zr to α-Zr upon cooling, resulting in reduced solubility of Cr in the Zry-4 matrix from 8% to less than 1% as seen from the Cr-Zr phase diagram in Fig. 8.5.

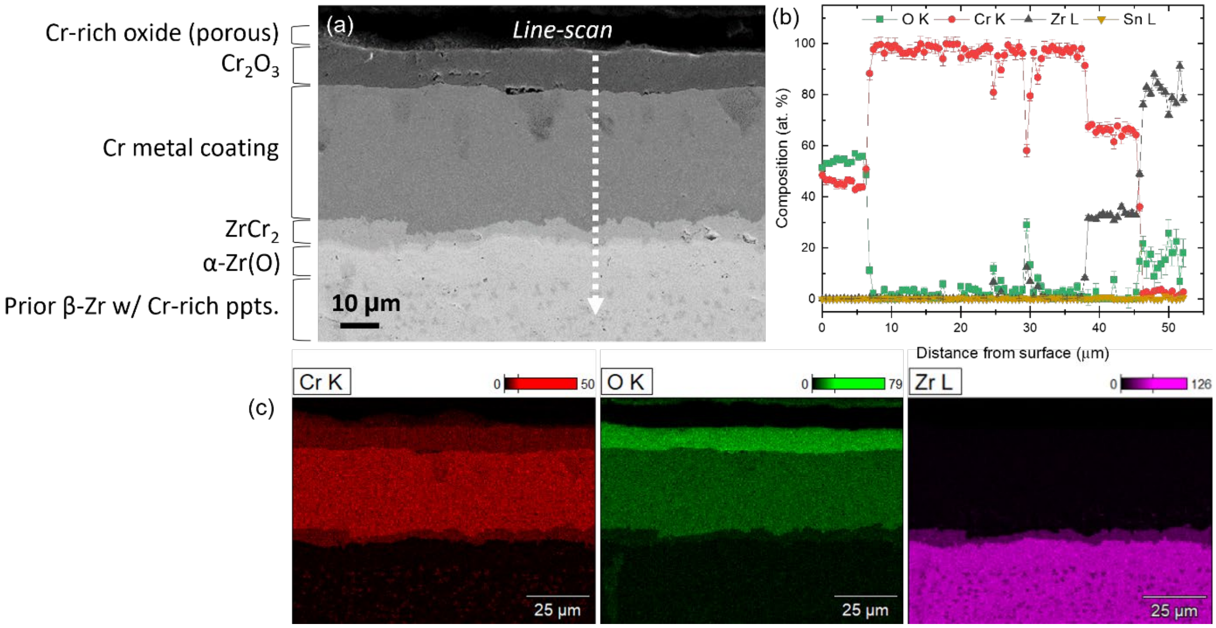

Fig. 9.3. (a) Cross-sectional SEM image showing Cr coating oxidized in 1280 °C air for 30 minutes; (b) EDS elemental line-scan showing the change in composition from surface oxide layer towards the substrate; (c) EDS spectral imaging maps of the same region.

Fig. 9.4 (a) shows that some porosity developed along the Cr_2O_3/Cr interface. Growth of the chromia oxide layer requires diffusion of chromium ions from the bulk metal through the existing oxide film to react with oxygen at the oxide/gaseous interface [280,281]. It's been suggested that solute elements (such as nitrogen) can accumulate at the oxide/metal interface due to the low solubility of chromium oxide, which can increase risk of spallation [280]. Alternatively, delamination of the oxide scale could be due to the thermal expansion coefficient mismatch between chromium and its oxide [282], outward diffusion of chromium and inward diffusion of oxygen along grain boundaries resulting in void growth and stresses [283], or simply an artifact of sample preparation. Fig. 9.4 (b) shows a higher magnification image of the chromia microstructure, revealing a fine (<2 µm) grain size with some nanoscale porosity along grain boundaries. Nonetheless, the chromium coating offered a factor of improvement of over 50 times in terms of high temperature oxidation resistance compared to uncoated Zr-alloy, which showed ~500 µm of unprotective zirconium-oxide (ZrO_2) growth under the same test conditions (Fig. 9.4 c).

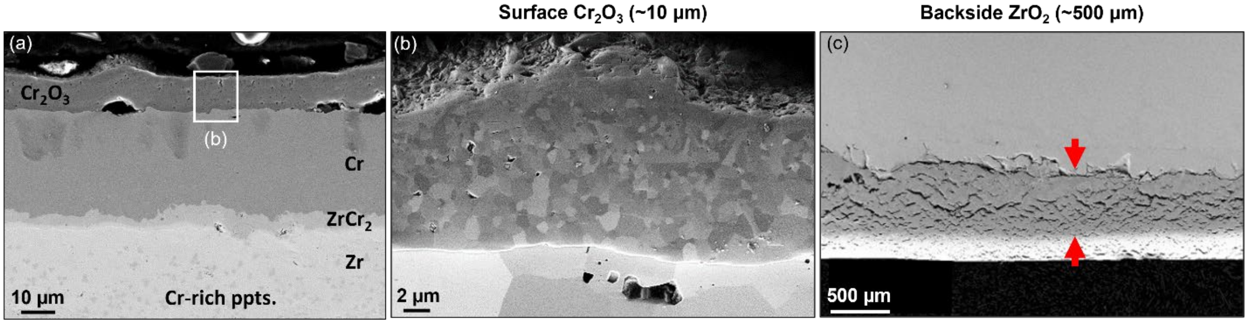

Fig. 9.4. Cross-sectional SEM images of (a) Cr coating oxidized in 1280 °C ambient air for 30 minutes; (b) Higher magnification image showing the microstructure of the chromium oxide film on the surface; (c) Backside of the sample (uncoated Zry-4) showing thick ZrO_2.

Interestingly, small protrusions were observed on the surface of the 1280 °C air oxidized sample Fig. 9.1 (c). Plan-view SEM images of the sample surface (Fig. 9.5 a) reveal the morphology of these protrusions. These lift-offs are shown in cross-section in Fig. 9.5 (b), and higher magnification SEM imaging shows that separation occurred beneath the $ZrCr_2$ intermetallic layer, below the Cr-Zr interface. This cracking initiated in the α-Zr(O) layer discussed earlier. It is important to emphasize that the coating remained adhered to the substrate in the peaks and valleys of the lifted-off regions. A similar observation was made by Hu et al. [284] for Cr coatings on Zircaloy-4, which was attributed to high temperature segregation of Sn and Cr within the Zr below the interface. It is important to note that this phenomenon has not been observed during any other high temperature experiments and is unlikely to occur with Cr-coated ZIRLO^{TM} (standard cladding for LWR operation) due the lower Sn content of the alloy.

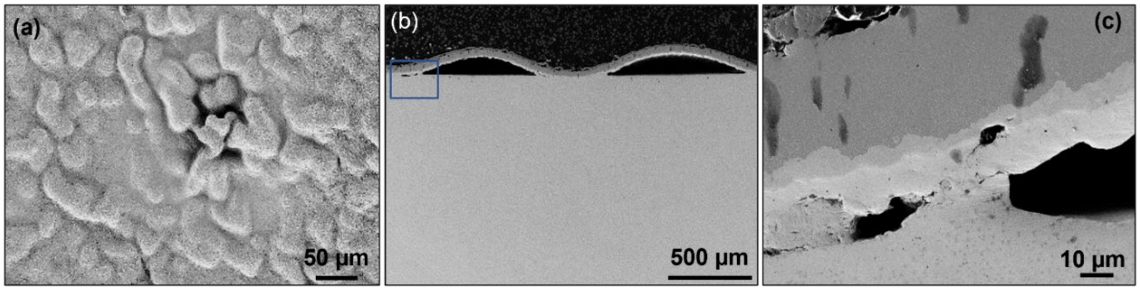

Fig. 9.5. SEM images of the Cr coating oxidized in 1280 °C air for 30 minutes: (a) Plan-view SEM image of protrusions on the Cr coating surface; (b) Low magnification cross-section shows areas of coating lift-off from the substrate; (c) High magnification image showing separation happens within the Zry-4, just below the coating.

9.1.2. High temperature steam oxidation

Visual examination of the Cr coating exposed to 1310 °C flowing steam environment showed a typical dark green oxide formed on the coating surface (Fig. 9.1 d). A continuous oxide layer was observed in the cross-sectional SEM images in Fig. 9.6, noting that the detached oxide layer was an artifact of metallographic sample preparation. High magnification imaging of the oxide layer (Fig. 9.6 b) shows it is about 5 μm thick, contains some porosity, and displays a heterogeneous grain size distribution. The coating also shows a thin (<2 μm) intermetallic $ZrCr_2$ layer formed at the Cr/Zr interface, with the existence of an α-Zr(O) layer followed by Cr-rich precipitates in the Zry-4 matrix. This experiment demonstrated the improved oxidation resistance of the cold spray Cr coating in high temperature steam environment. The thicknesses of both the surface Cr_2O_3 (Fig. 9.6 b) and the uncoated ZrO_2 (Fig. 9.6 c) were thinner after high temperature steam exposure compared with high temperature air exposure.

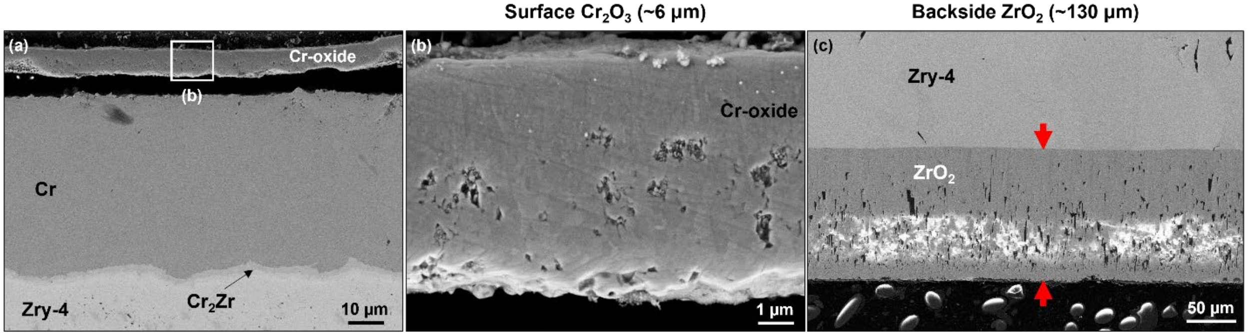

Fig. 9.6. Cross-sectional SEM images of (a) Cr coating oxidized in 1310 °C flowing steam for 30 minutes; (b) High-magnification image of Cr oxide layer; (c) Backside of the sample (uncoated Zry-4) showing thick ZrO_2. Note the detachment of the oxide layer was an artifact of sample preparation.

An extensive study of high temperature steam oxidation and microstructural evolution of cold spray Cr coatings on Zry-4 was performed by the author in collaboration with Yeom, et al. [35]. For this study, Cr coatings were deposited using spherical atomized Cr powder using the Cr-He condition [34]. It was hypothesized that the coatings used in this research, i.e., electrolytic soft Cr, with comparable deposition parameters (Cr-He), coating thickness, and surface finish, would exhibit similar behavior and performance as atomized Cr coating [137]. Fig. 9.7 shows XRD patterns of the as-deposited atomized Cr coating and steam-tested coatings subjected to increasing temperatures (1130, 1230, and 1310 °C) and increasing exposure times (10, 30, and 90 min). A clear evolution of decreasing bcc Cr peak intensity and increasing Cr_2O_3 peak intensity with temperature and time was observed, corresponding to thickening of the surface oxide scale. Narrowing (decrease in FWHM, full width half maximum) of the bcc Cr peaks was also observed, indicating high temperature exposure had relieved the residual stresses in the coating.

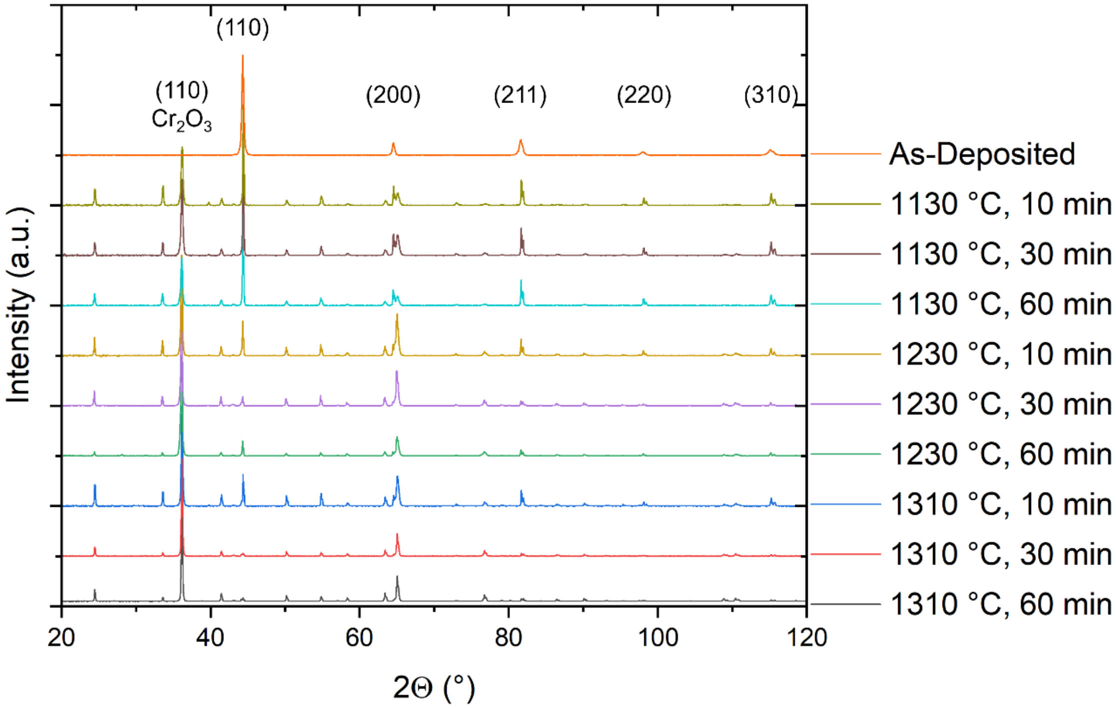

Fig. 9.7. XRD patterns of the as-deposited atomized Cr coating (top) and atomized Cr coatings oxidized at increasing temperatures (1130-1310 °C) for increasing exposure times (10-90 min) in steam [35].

Cross-sectional SEM images were used for measuring the thickness of the oxide layers for all tested conditions [35]. The oxidation kinetics at 1130 °C were fit to a parabolic growth function (n~0.5), while oxidation kinetics at 1230 °C and above were fit to power law growth (n~0.25-0.3). Deviation from typical parabolic oxidation kinetics was attributed to volatility of the oxide layer during initial stages of the tests and at higher temperatures. Nonetheless, it represented the first instance of estimating oxidation rate kinetics of cold spray Cr coatings. Thickness of the oxide layer for electrolytic Cr (6.1 ± 0.8 µm, this study) and atomized Cr (6.3 ± 0.6 µm, [35]) after 1310 °C steam exposure for 30 minutes were comparable. This is an important result as it shows that the high temperature steam oxidation resistance is similar for powders manufactured by distinctly different routes.

Detailed surface morphologies of the Cr coatings oxidized at 1310 °C for 30 minutes are shown in Fig. 9.8. High temperature steam oxidized atomized Cr coatings (Fig. 9.8 a) displayed needle-shaped and faceted blade morphologies on top of the dense, continuous oxide scales [35]. The size of these flakes tended to increase with increasing exposure time to steam, while the number density of flakes tended to decrease with temperature, indicating nucleation of flakes was affected by temperature. Oxide growth through whiskers and platelets in chromia-forming alloys has been reported in literature and typically occurs in water vapor environments with low oxygen potentials [285–287]. Fig. 9.8 (b) shows the surface morphology of the coatings produced from electrolytic soft Cr coatings after oxidation in steam (same coating shown in Fig. 9.6). The surface morphologies of both Cr coatings were identical, indicating cold spray Cr coatings that are dense and polished to similar conditions should behave similarly in high temperature steam environments. Fig. 9.8 (c) shows the surface morphology of air oxidized electrolytic soft Cr coating (same coating shown in Fig. 9.4), revealing large, plate-like oxide crystals on the coating surface surrounded by blocky, gravel-type crystals of smaller size. It is possible that there was some moisture present during air oxidation that resulted in the formation of oxide plates.

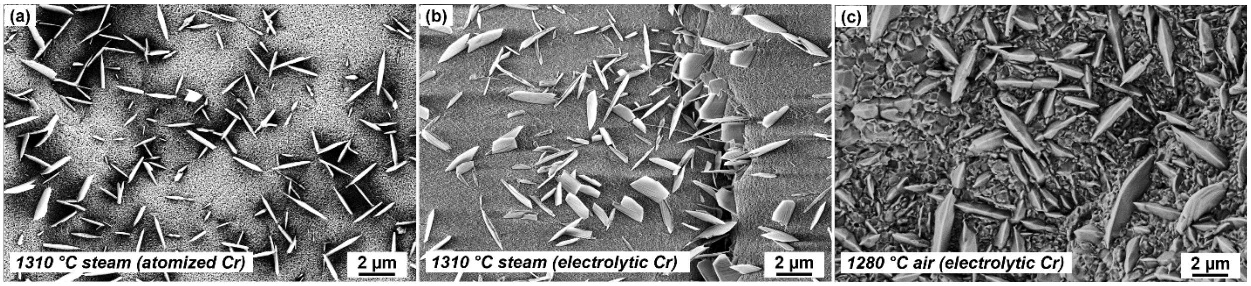

Fig. 9.8. Plan-view SEM image showing Cr coatings surfaces after 30 minutes of high temperature oxidation: (a) the surface of atomized Cr coating after 1310 °C steam (reproduced from Yeom and Dabney et al. [35]; (b) the surface of electrolytic soft Cr coating after 1310 °C steam; (c) the surface of electrolytic soft Cr after 1280 °C air.

9.2. Hydrothermal corrosion testing of cold spray Cr coated Zr-alloy

One key criterion for the selection of materials for accident tolerant fuels is that they maintain or improve hydrothermal corrosion performance during long-term normal operation in LWRs. This refers to the reactor operating under normal power generating conditions. Typical reactor coolant parameters and water chemistry in PWRs are provided in Table 9.1. To simulate hydrothermal corrosion behavior in PWR environment, cold spray Cr coated Zry-4 cladding were subjected to normal operation temperature, pressurized water corrosion experiments (360 °C, 18.6 MPa) for 30 days in accordance with the ASTM G2 standard [164]. These corrosion tests are slightly more aggressive than typical PWR conditions with the intent of accelerating corrosion and evaluate performance in shorter exposure times.

Table 9.1.Typical PWR coolant parameters and water chemistry specification [288].

Parameter	Specification
Coolant	H_2O with additives
Inlet temperature (°C)	280-295
Outlet temperature (°C)	310-330
Pressure (MPa)	~15
E(V) vs. SHE	-0.5
$[O_2]$ (ppb)	<5
$[H_2]$ (ppm)	2-5
pH	6.9-7.4
B (as H_3BO_3) (ppm)	0-2200
Li (as LiOH) (ppm)	0.5-5.0

Section 9.2.1 describes results of static water autoclave testing of Cr-coated Zr-alloy performed at the University of Wisconsin-Madison (UW), while Section 9.2.2 describes results of static water autoclave

testing of Cr-coated Zr-alloy performed in more prototypical PWR conditions at Westinghouse (WEC). The UW corrosion test used pure water coolant (<3 ppm [O_2]) in an Inconel 625 autoclave, while the water coolant for the WEC corrosion test contained 70 ppm lithium (<3 ppb [O_2]) and was performed in a 316 stainless steel autoclave. All other testing conditions were identical as described in Section 2.10.

9.2.1. Static, pure water autoclave corrosion testing

Weight change results after corrosion tests are shown in Fig 9.9 for uncoated Zry-4 and OPZ substrates and Cr-N2 and Cr-He coatings on Zry-4 substrates. The exposure time for uncoated Zry-4 was longer as these sample coupons are used as standards in every autoclave corrosion test. The results reveal significant improvement in hydrothermal corrosion resistance imparted by the cold spray Cr coatings, showing considerably lower (factor of 17) weight gain compared to uncoated Zry-4 and lower weight gain (factor of 7) compared to OPZ. The weight change data agrees well with previously published data on uniform corrosion of Zr-alloys and Cr-coated Zr-alloys (summarized by Motta [289] and Yang [26], respectively). Additionally, no significant difference in weight change was observed between Cr-N2 and Cr-He coatings, which is worthy of attention. Helium imparts higher particle velocities and hence results in denser coatings, which would be more beneficial for corrosion resistance given that corrosion is expected to occur preferentially at the interparticle boundaries. However, helium is also significantly more expensive than nitrogen. The observation that corrosion resistance is not compromised by using nitrogen carrier gas for cold spray is therefore significant.

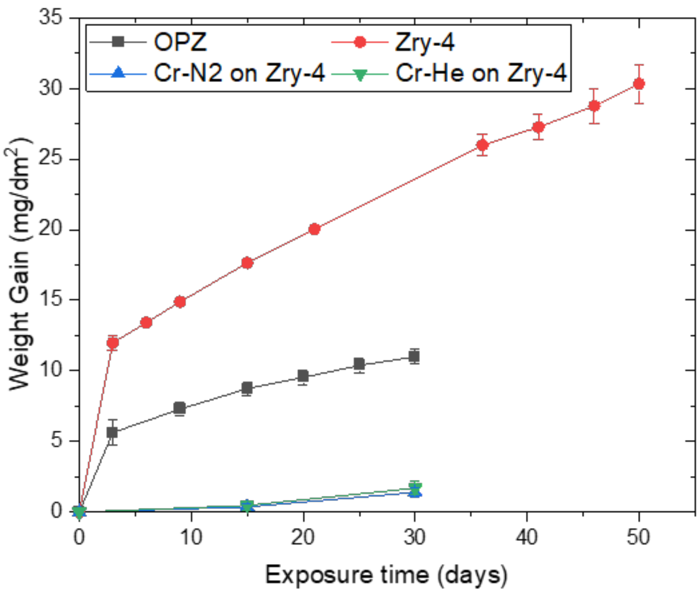

Fig 9.9. Weight change data after static, pure water autoclave corrosion testing of OPZ tubes, Zry-4 flat substrates, and cold spray Cr-N2 and Cr-He coatings on Zry-4 flat substrates. Note that the two types of Cr coatings show nearly identical corrosion resistance.

Photographs taken after 30 days of autoclave testing are shown in Fig. 9.10 (a-d). Both Zry-4 and OPZ show a dark gray oxide film on the surface, while the Cr coatings display a golden colored oxide film on the surface suggesting that the oxide film is hundreds of nanometers thick and of Cr_2O_3 stoichiometry [26,290]. Plan-view SEM images of the uncoated and Cr coated samples shown in Fig. 9.10 (e-g) reveal very fine (<100 nm) oxide particles on the surface. The visibility of scratches from polishing is also suggestive of formation of a thin oxide scale, though the oxide particles are much more numerous for the uncoated Zry-4 (Fig. 9.10 e) compared to the Cr coatings (Fig. 9.10 f,g). Cross-sectional SEM images shown in Fig. 9.10 (h-i) reveal a 1.0-1.5 µm ZrO_2 oxide scale on Zry-4, while the Cr_2O_3 oxide film on the Cr coatings are much thinner (<200 nm). The thickness of Cr_2O_3 film is somewhat speculative given the resolution limits of SEM, but the fact that they are largely not visible is a testament to the hydrothermal corrosion resistance imparted by Cr cold spray coatings. Fig. 1.4 of this document showed that under PWR conditions, Cr_2O_3 is the most thermodynamically stable corrosion product phase over a wide range of pH values and electrode potentials.

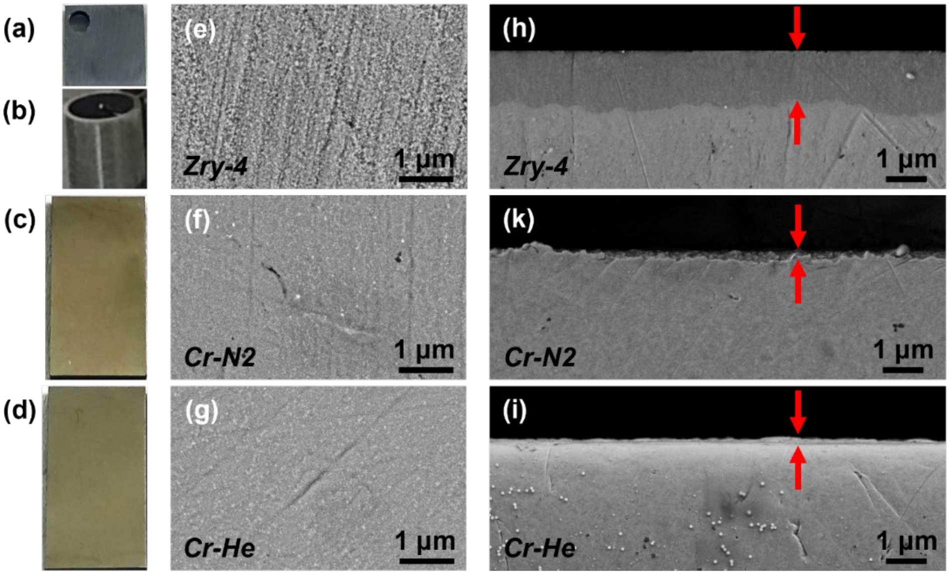

Fig. 9.10. (a-d) Photographs of samples exposed to 30 days of corrosion in pure water autoclave: (a) Zry-4; (b) OPZ; (c) Cr-N2 coating on Zry-4; (d) Cr-He coating on Zry-4. (e-g) Plan-view SEM images of sample surfaces after 30-day corrosion: (e) Zry-4; (f) Cr-N2 coating on Zry-4; (g) Cr-He coating on Zry-4. (j-i). Cross-sectional SEM images of samples after 30-day corrosion: (j) Zry-4; (k) Cr-N2 coating on Zry-4; (i) Cr-He coating on Zry-4.

X-ray diffraction patterns of the samples after corrosion tests are shown in Fig. 9.11. The uncoated Zry-4 showed a mixture of α-Zr and ZrO_2 peaks. The chromium coatings showed mainly bcc Cr peaks, again indicative of a thin surface oxide scale. Two low-intensity peaks were matched to CrO and CrO_2 phases, but it is highly likely that chromia film was too thin to be detected by XRD.

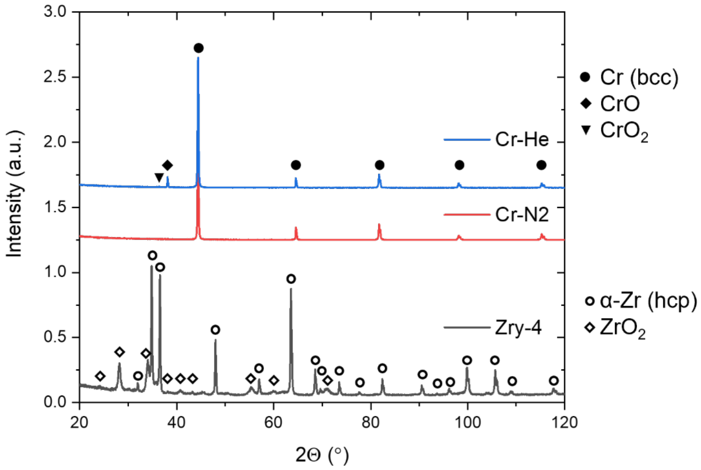

Fig. 9.11. XRD profiles of Zry-4, Cr-N2 and Cr-He coatings after 30 days autoclave corrosion in pure water, with phases labeled.

9.2.2. *Static, lithium-enhanced hydrothermal corrosion testing*

Photographs of uncoated Zry-4 and Cr-N2 and Cr-He coated Zry-4 after 30 days autoclave corrosion in 70 ppm Li-enhanced water chemistry are shown in Fig. 9.12. All samples appeared slightly dusty due to the presence of a corrosion product. The Zry-4 showed the typical gray oxide appearance, but the Cr coatings did not appear golden as they did after pure water autoclave exposure (Fig. 9.10 c,d), instead appearing slightly darker in color. This could indicate thinner oxide or a more discontinuous oxide layer than the one formed in pure water environment.

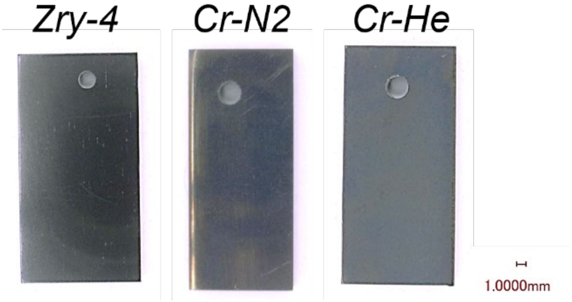

Fig. 9.12. Photographs of uncoated Zry-4 and Cr-N2 and Cr-He coated Zry-4 after exposure to 70 ppm Li-enhanced water chemistry during autoclave corrosion for 30 days.

Plan-view SEM images of the Cr coatings after Li-enhanced water corrosion are shown in Fig. 9.13. The surface of the uncoated Zry-4 after exposure is not shown as it closely resembled the surface of the uncoated Zry-4 exposed to pure water shown in Fig. 9.10 (e). At low magnification, the Cr-N2 coating shows some pits on the surface while the Cr-He coating appears dense (Fig. 9.13 a & c, respectively). These pits represent areas of rough Cr coating that were not fully polished before corrosion testing and do not represent spallation or loss of coating. At higher magnification nanoscale oxide crystals were resolved, measuring less than 500 nm in diameter. The Cr-N2 coating (Fig. 9.13 b) contained a higher number density of oxide particles of similar size, while the Cr-He coating (Fig. 9.13 d) contained a lower number density of oxide particles of mixed size distribution. Image analysis was used to calculate the number density of particles (>200 nm diameter) per square micrometer, revealing 11 and 6 particles$^{+200\text{ nm}}$/µm for the Cr-N2 and Cr-He coatings, respectively. It is possible that the unpolished sites on the surface of the Cr-N2 coating left a greater number of nucleation sites for the oxide particles to form due to preferential attack by Li-containing water.

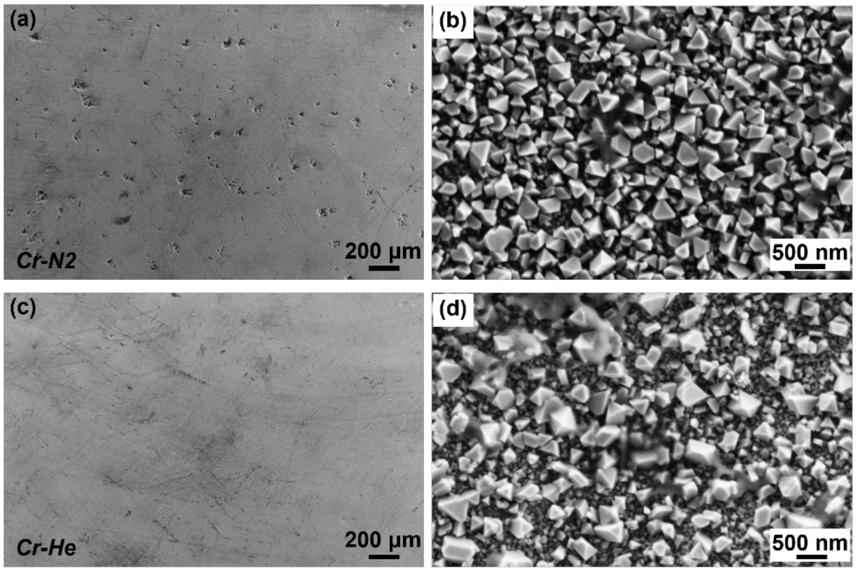

Fig. 9.13. Plan-view SEM images of Cr coatings on Zry-4 after 30 days autoclave corrosion in Li-enhanced water: (a,b) Cr-N2 coating; (c,d) Cr-He coating.

X-ray diffraction of the samples tested in Li-enhanced water for 30 days are shown in Fig. 9.14. For the uncoated Zry-4 sample the same phase mixture of α-Zr and ZrO_2 as the sample exposed to pure water was observed (Fig. 9.11). Previous autoclave corrosion of Zry-4 in 70 ppm Li water chemistry showed similar corrosion kinetics to pure water exposure during the first 100 days [24,291,292], so it's likely both Zry-4 samples experienced similar corrosion behavior over 30 days. XRD profiles of the Cr coatings showed bcc Cr peaks in addition to two low-intensity peaks matching iron chromite spinel ($FeCr_2O_4$). These peaks were not observed in the Cr coatings exposed to pure water corrosion. It is likely that this chromite phase was a result of deposition of corrosion product from the stainless-steel autoclave wall itself, and hence an artifact of this experiment. No chromia peak was observed on either Cr coating, suggesting that the oxide layer was quite thin.

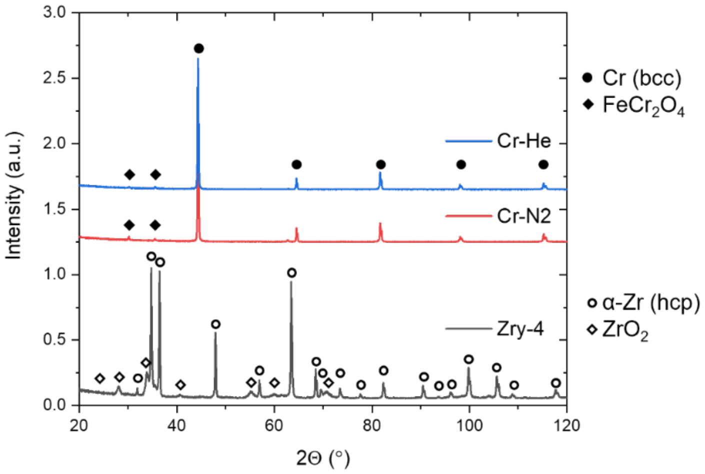

Fig. 9.14. XRD profiles of Zry-4, Cr-N2 and Cr-He coatings after 30 days autoclave corrosion in Li-enhanced water, with phases labeled.

FIB lift-outs were taken from the surfaces of the Cr coatings exposed to Li-enhanced water corrosion to characterize the microstructure of the oxide layers that developed in the near-surface regions of the sample due to corrosion. HAADF-STEM images in Fig. 9.15 (a,b) show the oxide films of the Cr-N2 and Cr-He coatings, respectively. Both coatings contained crystallites 100-400 nm in length resting on a uniform oxide layer 20-50 nm thick at the Cr metal surface. EDS spectral maps shown in Fig. 9.15 (c,d) revealed the crystallite particles to be comprised of mostly Fe and O with small amounts of Cr. Most of the Fe signal was contained within these crystallites. However, EDS signal at the Cr metal interface showed higher signal of Cr and O contained within the uniform oxide layer.

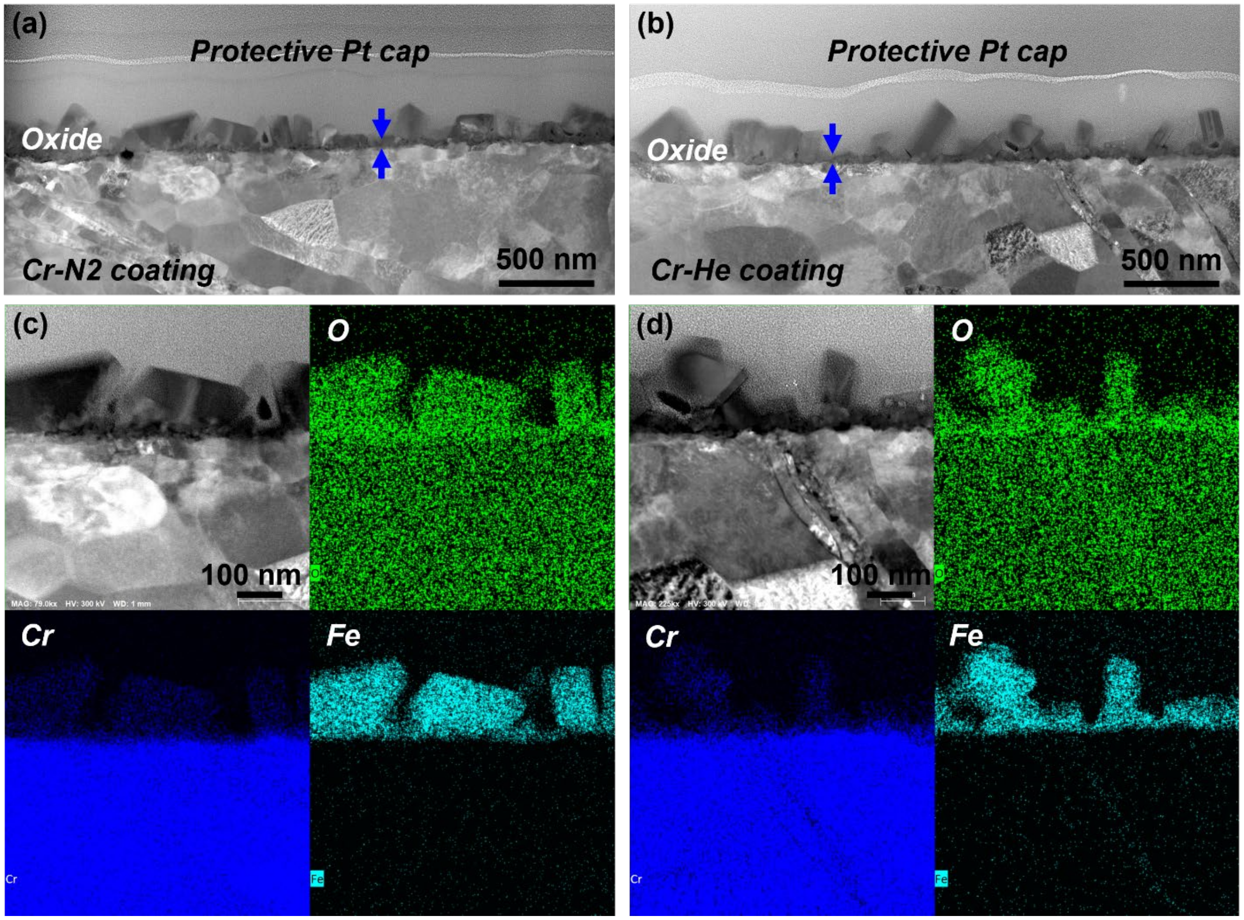

Fig. 9.15. HAADF-STEM images of (a) Cr-N2 and (b) Cr-He coating surfaces after 30 days autoclave corrosion in Li-enhanced water. The surface is comprised of a continuous (20-50 nm) oxide film (indicated by blue arrows) and larger (100-400 nm) oxide crystallites. The thin line above the oxide layer simply delineates two deposited layers of protective platinum film. (c,d) Higher magnification HAADF-STEM images with EDS spectral maps of the oxide films for (c) Cr-N2 and (d) Cr-He coatings.

From the nominal concentration of Fe in the Zry-4 cladding (~0.18-0.24 wt.%) and impurity levels in the Cr coating (~0.17-0.20 wt.%), it is unlikely that diffusion of Fe from the coating towards the surface promoted growth of these relatively large oxide crystallites. Therefore, as mentioned earlier, it is likely that these crystallites represent corrosion products of the 316 stainless steel autoclave in which the tests were conducted. The crystallites enter the coolant from the walls of the autoclave and deposit on the surface of the samples. This is very similar to what are commonly termed as CRUD (Chalk River Unidentified Deposits), which are oxides containing metallic impurities (Fe, Ni, Cu, etc.) that arise from corrosion of pressure vessel structural materials and deposit on the cladding surface [292]. CRUD contaminants in PWR vessels are typically iron-rich oxides (Fe_2O_3 and Fe_3O_4) and iron-rich spinels ($(Ni,Zn,Cr)_xFe_{3-x}O_4$) [292–

296]. Fig. 9.16 (a-b) shows high magnification HAADF-STEM images of the large oxide crystallite deposits observed on the Cr-He surface. These crystallites show blocky, faceted morphologies that closely resemble the morphology of oxide spinels with AB_2O_4 stoichiometry, with chromium cations in the coolant entering the spinel lattice structure via substitution [293,295]. Elevated lithium concentration in the coolant is used to accelerate corrosion in Zr-alloys, so it would also simultaneously accelerate the corrosion of the autoclave pressure vessel components [292].

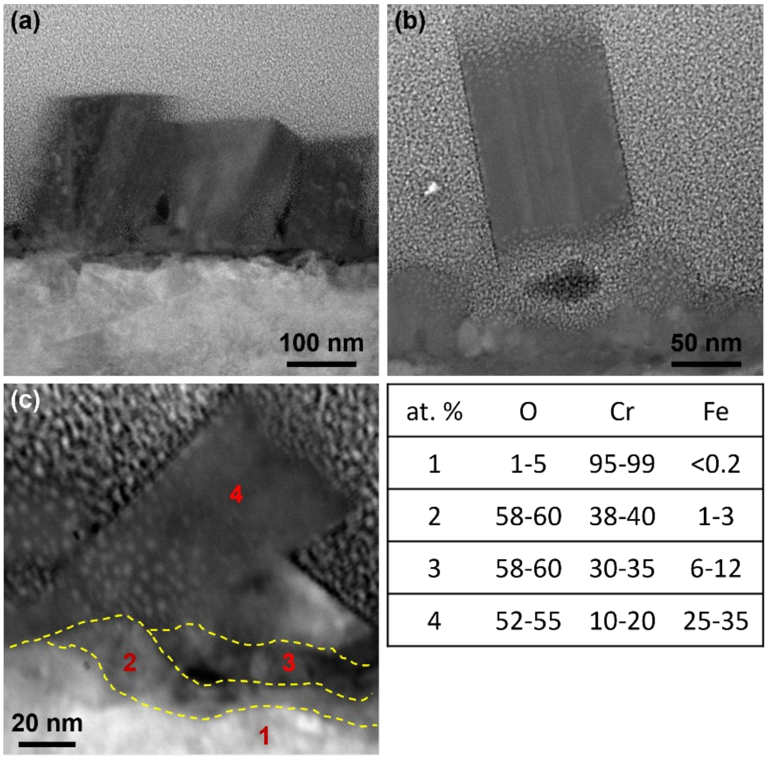

at. %	O	Cr	Fe
1	1-5	95-99	<0.2
2	58-60	38-40	1-3
3	58-60	30-35	6-12
4	52-55	10-20	25-35

Fig. 9.16. HAADF-STEM images of the Cr-He oxide layer after 30 days autoclave corrosion in Li-elevated water: (a,b) Images showing blocky and faceted morphologies of the oxide crystallites; (c) High-magnification image showing various layers in the oxide scale, with EDS point scan measurements (at. %): 1 – Cr metal, 2 – Cr_2O_3 continuous oxide, 3 – short, compact crystallites, 4 – large, blocky crystallites.

EDS point measurements of the surface oxide are shown in Fig. 9.16 (c), which distinguish three distinct layers of the oxide scale. EDS confirmed the stoichiometry of the rhombohedral Cr_2O_3 phase at the Cr metal interface, which is based on the corundum prototype crystal structure [297]. The protective Cr_2O_3 oxide scale was thinner than previously expected (<20 nm), which confirms its absence in the XRD scans. Above this layer rests a compact oxide scale consisting of 30-35 at.% Cr and 6-12 at.% Fe, which most closely matches the stoichiometry of $FeCr_2O_4$ spinel. The final layer containing the loose oxide crystallites measured 10-20 at.% Cr and 25-35 at.% Fe, which most closely matches the stoichiometry of $CrFe_2O_4$ spinel.

The HAADF-STEM image shown in Fig. 9.15 (d) indicate a particle boundary near the surface of the Cr-He coating. The EDS spectral maps highlight a slight enrichment of Fe and depletion of Cr at the particle boundary, though the oxygen signal at this boundary cannot be discerned from the background. It is well known that Cr depletion at grain boundaries is due to Cr cation transport to the surface to facilitate oxide formation. However, unsealed particle boundaries present pathways to oxygen diffusion from the coolant to the substrate. This phenomenon may be mitigated by modifying the cold spray parameters (such as increasing particle velocity) to create more well-bonded inter-particle boundaries.

For a greater understating of corrosion attack under hydrothermal corrosion conditions, electron probe micro-analysis (EPMA) in conjunction with wavelength dispersive X-ray spectroscopy (WDS) was performed on the as-deposited Cr-N2 coating, as shown in Fig. 9.17. The WDS line-scan was captured starting in the Zry-4 substrate and continuing across the interface and the Cr coating up to its surface. Fig. 9.17 (b) shows low concentrations of oxygen (2-2.5 wt.%), tin (~1.3 wt.%), and iron (0.15-0.25 wt.%) in the Zry-4 substrate. The Cr coating shows a slight increase in oxygen (~0.5 wt.%), particularly at regions where the line scan intercepts the interparticle boundaries. The maximum detectable nitrogen was about 0.18 wt.%, indicating the coating and substrate did not entrap nitrogen during N_2 gas cold spray deposition. Finally, no stoichiometric oxide or nitride phases were found in the coating and substrate.

Fig. 9.17 (c) shows maps of O, N, Fe, and Sn elemental distributions in the coating and substrate, presented as total counts. Nitrogen concentration was negligible, and Sn, being an alloying element in Zry-4, is concentrated within the substrate. Fe counts were also low, with some spikes found within inter-particle boundaries. There is some oxygen concentration along the Cr-Zr interface, though it was not uniform. This represents the innate oxide that was jetted from the Cr particle/Zry-4 surface during high velocity impact and shear during bonding. There is a noticeable concentration of oxygen along inter-particle boundaries within the cold spray Cr coating. This is the native oxide film that was present on the surface of the feedstock powder particles that could not be fully jetted away high velocity impact an associated high strain rate deformation. Furthermore, it has been shown in other sections of the thesis that adiabatic shear does not necessarily occur in the case of less deformable metal powders such as Cr. If instead, a sliding friction mechanism is responsible for interparticle bonding, which could lead to continued presence of the native oxide layer at the interparticle boundaries.

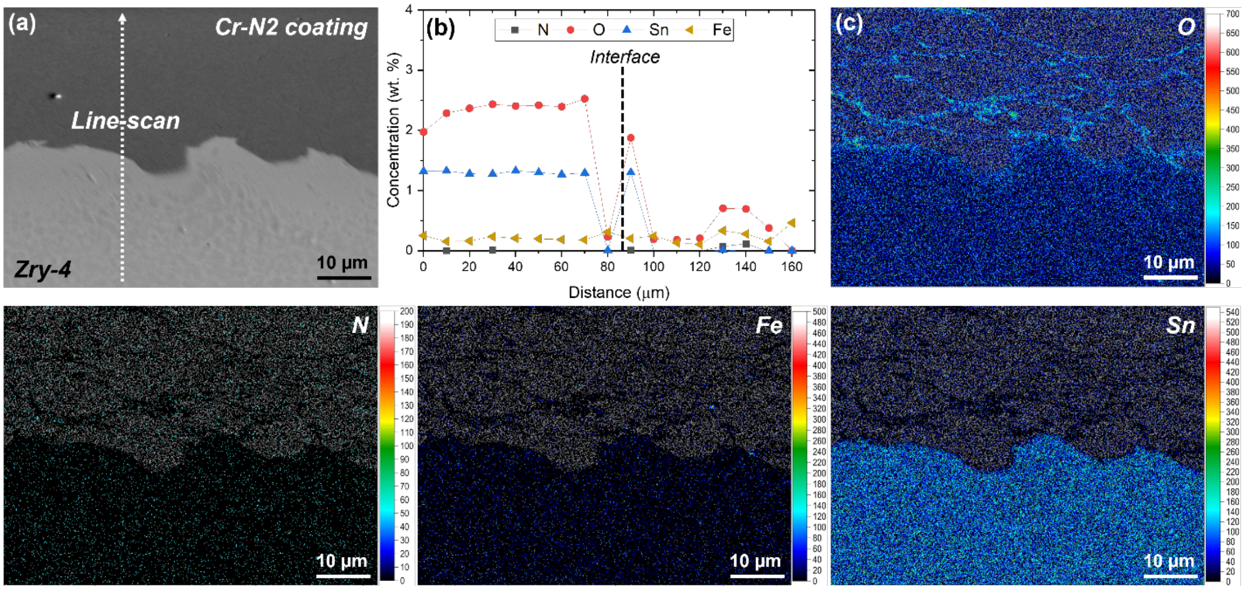

Fig. 9.17. EPMA near the interface of as-deposited Cr-N2 coating on Zry-4: (a) Cross-sectional SEM image of coating/substrate; (b) WDS line-scan (low magnification) of impurities, starting in Zry-4 moving across the interface into the Cr coating; (c) WDS elemental maps show counts of O, N, Fe, and Sn.

Fig. 9.18 shows maps of O, Fe, and Zr element distributions for the Cr-N2 and Cr-He coatings on Zry-4 after 30 days autoclave corrosion in Li-enhanced water. The oxygen signal present at the inter-particle boundaries after corrosion testing is comparable to the signal present in the as-deposited coatings shown in Fig. 9.17 (c). This suggests that the coatings were quite impervious to oxygen permeation. Diffusion of oxygen from the coolant through the inter-particle boundaries would likely have manifested as stoichiometric Cr_2O_3 along the particle boundaries or as ZrO_2 along the Zry-4 interface, neither of which were detected by WDS, a technique highly sensitive to stoichiometric oxide phases. Additionally, the Fe-rich oxides are present on the surface of the Cr-N2 coating (Fig. 9.18 a) but not on the Cr-He coating, which was likely removed during sample preparation. To summarize, the WDS maps confirm that oxygen did not permeate or diffuse through either Cr-N2 or Cr-He coatings during exposure to simulated PWR water environment, demonstrating the protective nature of the cold spray Cr coating.

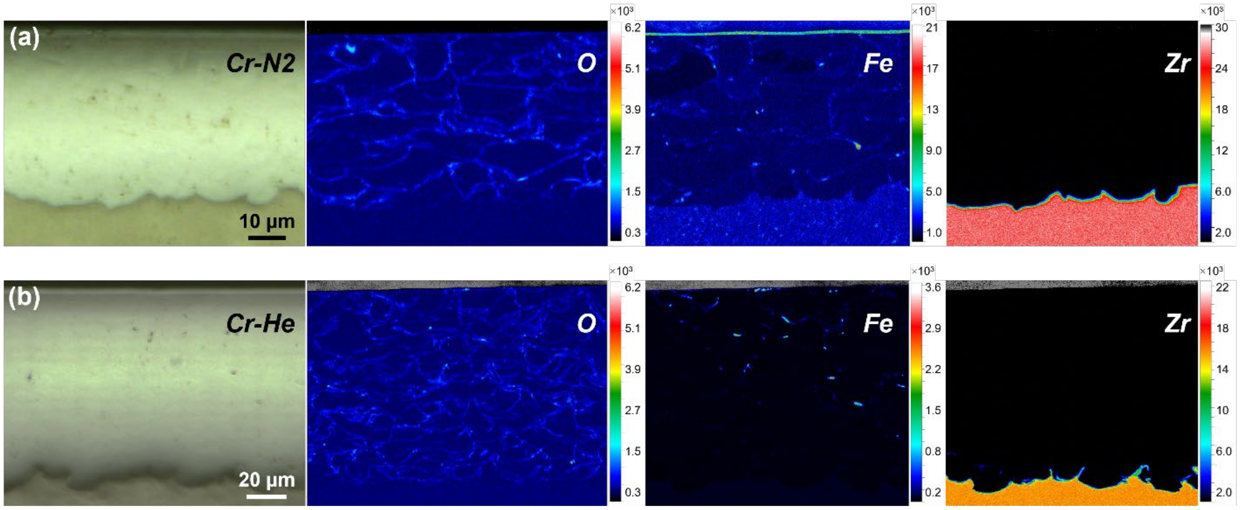

Fig. 9.18. EPMA results for (a) Cr-N2 and (b) Cr-He coatings on Zry-4 after 30 days autoclave corrosion in Li-enhanced water. WDS elemental maps show counts of O, Fe, and Zr.

10. Concluding Remarks

This research focused on the development of cold spray deposited chromium coatings on zirconium-alloy cladding for advanced nuclear fuel cladding. This technology has the potential to improve resistance to high temperature oxidation, ballooning, and burst during accident scenarios, thereby increasing the accident tolerance of light water reactor systems. What's more, Cr coatings impart improved hydrothermal corrosion resistance to Zr-alloy cladding, which opens the door to the use of higher burnup fuels for increased economic benefit in light water reactors. Cold spray Cr coatings deposited on full-length Zr-alloy fuel cladding and tested in a commercial reactor over a period of 36 months have shown good performance, exhibiting mechanical integrity, limited corrosion, and reduced hydrogen pickup compared to uncoated Zr-alloys.

The research focused on answering key scientific and engineering questions pertaining to four strategically selected areas of materials research, namely: (i) coating deposition and formation mechanisms, (ii) irradiation effects in coatings and at the coating-substrate interface, (iii) mechanical behavior of the coating and the coating-substrate system, and (iv) hydrothermal corrosion and oxidation in high temperature accident conditions. Testing of coatings in prototypical reactor environments and simulated accident conditions has realized the benefits of cold spray Cr coatings for advanced nuclear fuel.

Electrolytic soft Cr powders produced by a combination of electrolytic extraction, high temperature degassing, and gentle ball milling were used as the feedstock material in this research. Cold spray was used for deposition of pure Cr coatings on Zr-alloys specifically used as PWR cladding material, including Zircaloy-4, ZIRLO™, and Optimized ZIRLO™ in both flat and tubular cladding geometries. The Cr coatings exhibited a heterogeneous microstructure over multiple length scales, consisting of large, micron-sized grains containing high dislocation density and strained structures as well as inter-particle boundaries containing elongated, nanocrystalline, and dynamically recrystallized ultrafine grains. High resolution imaging techniques were utilized to characterize the microstructural evolution and characteristics of coatings as a function of independent deposition process variables in cold spray – including gas preheat temperature, carrier gas composition, spray gun traverse speed.

Because of the higher imparted particle velocity, the Cr-He coatings exhibited a denser microstructure with higher strain, more cohesive interparticle boundaries, and more dynamically recrystallized grain structure compared to the Cr-N2 coatings. Nitrogen cold spray is a more economically feasible option, and this study demonstrated that it can yield coating microstructures and interface bonding sufficiently similar to Cr-He coatings to yield sufficient performance for advanced nuclear fuel cladding. Given the importance of particle velocity, CFD models were developed and used to predict powder particle velocity as a function of process variables such as carrier gas mixture and particle size. The estimated particle velocities were fed into FEM simulations to gain insights into the high strain rate deformation mechanisms involved during high velocity particle impact on the substrate.

Single-particle impact experiments were performed separately on Zr-alloy and bulk Cr flat substrates to study interfacial bonding and inter-particle bonding during initial stages of coating formation and coating buildup, respectively. Critical velocity was experimentally determined based on the ratio of the number of particles adhered to the total number of particles impacted, and the results were verified using empirical equations based on materials properties of Cr. For the Cr-on-Zr system, the critical velocity was determined to be 540 m/s and the deposition efficiency reached 100% at 680 m/s, while for Cr-on-Cr system, the critical velocity was determined to be 640 m/s with deposition efficiency reaching a maximum of 35% at 880 m/s. EBSD characterization of the bonded particles revealed a penetration-dominant mechanism at the Cr-Zr interface, causing high strain rate deformation, jetting, and dynamic recrystallization in near-interface regions (<5 μm) of the Zr-alloy substrate while the Cr particles experienced deformation only in their outer regions. HRTEM of the interface provided a graphic demonstration of crystallographic coherency between the Cr and Zr-alloy which, in combination with mechanical interlocking, resulted in strong particle-substrate adhesion.

For the Cr-on-Cr system, EBSD revealed that deformation and high dislocation densities extended to the particle interior, and regions of dynamically recrystallized grains were observed at the interparticle boundaries. It was determined that interparticle bonding could be achieved even at particle velocities where clear jetting was not observed. In this case, the critical factor governing Cr interparticle bonding is dictated by the localized plastic strain necessary to trigger dynamic recrystallization across interparticle boundaries. This is further supported by the observation that Cr-to-Cr bonding occurs much more readily (i.e., at lower particle velocities) in multiple particle impact than indicated by single particle impact studies. It is proposed that interparticle intrusions provide the necessary local plastic deformation for dynamic recrystallization and bonding. This suggests that cold spray is not limited to the widely held notion that bulk plastic deformation of the particle and associated adiabatic shear mechanisms are necessary to induce interparticle bonding, but rather that such bonding is also possible for relatively difficult-to-deform material particles. TKD characterization of the microstructural developments in as-deposited Cr coatings correlated well with the insights gained from single particle impacts.

As a part of the campaign to understand coating formation mechanisms, experiments were conducted using low particle velocity deposition ($v_{crit}^{Cr-Zr} < v_p < v_{crit}^{Cr-Cr}$) to first form a seed layer (to induce low interface roughness) followed by spraying at high particle velocities ($v_p > v_{crit}^{Cr-Cr}$) to build up a coating. This study provided additional insights into the deformation behavior of the Cr-on-Zr system during cold spray but was not successful in lowering interface roughness. To lower the coating's outer surface roughness, a cold spray shot peening (CSSP) process was developed in which larger particle sizes of Cr (<44 μm) propelled under low velocity conditions were effectively used to peen the surface to notably lower the surface roughness of the coatings. This process has the potential to bypass expensive post-deposition mechanical grinding processes and the use of Cr particles for this process eliminates the possibility of material cross-contamination.

STEM characterization of the coating-substrate interface of the as-deposited Cr-He cold spray coatings revealed cold spray induced co-segregation of Cr and Fe at the interface. Irradiation studies of these samples were performed at 350 °C using 80 MeV Xe^{26+} ions, with damage profiles reaching 30 dpa at the Cr-Zr interface. Irradiation led to homogenization of Fe in the Zr-alloy matrix and the formation of a 20 nm thick amorphous layer at the Cr-Zr interface. Thermodynamic calculations revealed that both Fe dissolution and amorphization are favored due to the increased enthalpy provided by the high energy irradiation. STEM characterization of the irradiated Cr coating revealed obliteration of elongated grains and recrystallization across interparticle boundaries, in essence densifying the coating. Nanoindentation testing revealed softening of the coating, which was attributed to irradiation-induced recrystallization and deformation recovery. Overall, the heterogeneous, dislocation-heavy microstructure of cold spray Cr coatings exhibit good radiation damage resistance.

In situ high energy synchrotron X-ray diffraction coupled with tensile deformation capabilities was used to investigate the mechanical behavior of the Cr coating-Zr-alloy substrate bimetal composite system in as-deposited and 750 °C annealed conditions. X-ray line profile analysis of the as-deposited Cr coating revealed a high dislocation density with a unique distribution of edge and screw fractions and non-zero lattice strain caused by high strain-rate deformation during cold spray deposition. The annealing treatment reduced both residual lattice strain and dislocation density in the Cr coating, with preferentially higher reduction in edge dislocations. This led to a heterogeneous distribution of dislocation density and character among different grains that is believed to enhance resistance to crack propagation in the annealed Cr coating. The mechanical properties of the Zr-alloy in both types of samples were not significantly altered by the presence of the Cr coating.

The adhesion, ductility, and cracking behavior of the Cr-coated Zr-alloy was evaluated via micro-cantilever beam bending tests in conjunction with *in situ* SEM imaging and acquisition of load-displacement profiles. Four microstructural conditions of micro-cantilevers were studied to simulate different environmentally-induced changes in the reactor, including coating insertion (as-deposited Cr-N2 and Cr-He), high temperature transients (600 °C anneal), extended LOCA event (1000 °C anneal), and extended irradiation damage (30 dpa at the Cr-Zr interface). EBSD revealed that recovery and partial recrystallization occurred after annealing at 600 °C, while recrystallization, grain growth, and high temperature interdiffusion leading to a 1 µm thick $ZrCr_2$ intermetallic occurred after annealing at 1000 °C. Full recrystallization of the Zr-alloy substrate occurred during both annealing treatments. In all cases the cracks initiated at the coating-substrate interface and the trends in the load-displacement plots (supported by post-test *ex situ* EBSD) provided profound insights into crack propagation. For the as-deposited coating, cracking initiated at high load (indicative of high adhesion strength) in a brittle manner as observed by an associated sharp drop in load. For the 1000 °C annealed condition, failure initiated at the Cr-Zr interface at a lower load (due to the presence of a $ZrCr_2$ intermetallic phase) and then propagated slightly into the near-interface region of the Zr-alloy but still parallel to the interface. However, the high ductility of both the substrate and the coating led to shorter crack propagation. The 600 °C annealed and ion irradiated Cr coatings resulted in ductile failure behavior involving peeling of the Cr/Zr interface and interparticle boundaries within the Cr coating, which was attributed to the effects of interdiffusion (with no intermetallic phase formation) and ion-beam mixing, respectively, at the Cr-Zr interface. The load-displacement plots in these cases showed small drops in load and recovery suggesting ductile behavior.

Hydrothermal corrosion testing of Cr-He and Cr-N2 coatings in prototypical PWR conditions (of temperature and pressure) performed in pure water and Li-enhanced water chemistries showed that the coatings imparted significant enhancement in corrosion resistance. Testing for 30 days in pure water showed a factor of 10 improvement in corrosion rate compared to uncoated Zr-alloy cladding. Cross-sectional SEM imaging of the coatings tested in Li-enhanced water revealed the uncoated Zr-alloy developed a 1.5 µm thick ZrO_2 oxide layer, while STEM imaging revealed less than 50 nm of Cr_2O_3 formed on the surfaces of both Cr-N2 and Cr-He coatings over the same exposure time. There was no significant difference in performance between Cr-N2 and Cr-He coatings, suggesting that the lower particle velocity Cr-N2 coating provided sufficient interparticle bonding to resist corrosion attack. WDS scans acquired using EPMA revealed no oxygen permeation into the bulk of either type of cold spray Cr coating. High temperature air and steam oxidation tests at 1300 °C demonstrated that Cr coatings provide a high degree of protection due to the formation of a thin, tenacious Cr_2O_3 layer on their surface.

References

[1] S. Chu, A. Majumdar, Opportunities and challenges for a sustainable energy future, Nature 488 (2012) 294–303. https://doi.org/10.1038/nature11475.

[2] S.J. Zinkle, G.S. Was, Materials challenges in nuclear energy, Acta Mater. 61 (2013) 735–758. https://doi.org/10.1016/j.actamat.2012.11.004.

[3] National Research Council, ed., Background on Japanese and U.S. Nuclear Plants, in: Lessons Learn. Fukushima Nucl. Accid. Improv. Saf. US Nucl. Power Plants, The National Academies Press, Washington, DC, n.d.

[4] S.J. Zinkle, G.S. Was, Materials challenges in nuclear energy, Acta Mater. 61 (2013) 735–758. https://doi.org/10.1016/j.actamat.2012.11.004.

[5] F. Onimus, S. Doriot, Radiation Effects in Zirconium Alloys, (n.d.).

[6] R.J.M. Konings, ed., Radiation Effects in Structural and Functional Materials for Fission and Fusion Reactors, in: Compr. Nucl. Mater., Elsevier, n.d.

[7] S.J. Zinkle, K.A. Terrani, J.C. Gehin, L.J. Ott, L.L. Snead, Accident tolerant fuels for LWRs: A perspective, J. Nucl. Mater. 448 (2014) 374–379. https://doi.org/10.1016/j.jnucmat.2013.12.005.

[8] B.A. Pint, K.A. Terrani, M.P. Brady, T. Cheng, J.R. Keiser, High temperature oxidation of fuel cladding candidate materials in steam–hydrogen environments, J. Nucl. Mater. 440 (2013) 420–427. https://doi.org/10.1016/j.jnucmat.2013.05.047.

[9] K.A. Terrani, Accident tolerant fuel cladding development: Promise, status, and challenges, J. Nucl. Mater. 501 (2018) 13–30. https://doi.org/10.1016/j.jnucmat.2017.12.043.

[10] Supplemental Guidance Regarding the Chromium-Coated Zirconium Alloy Fuel Cladding Accident Tolerant Fuel Concept, Nuclear Regulatory Commission, 2020. https://www.nrc.gov/docs/ML1934/ML19343A121.pdf.

[11] C. Tang, M. Klimenkov, U. Jaentsch, H. Leiste, M. Rinke, S. Ulrich, M. Steinbrück, H.J. Seifert, M. Stueber, Synthesis and characterization of Ti 2 AlC coatings by magnetron sputtering from three elemental targets and ex-situ annealing, Surf. Coat. Technol. 309 (2017) 445–455. https://doi.org/10.1016/j.surfcoat.2016.11.090.

[12] J.G. Gigax, M. Kennas, H. Kim, T. Wang, B.R. Maier, H. Yeom, G.O. Johnson, K. Sridharan, L. Shao, Radiation response of Ti2AlC MAX phase coated Zircaloy-4 for accident tolerant fuel cladding, J. Nucl. Mater. 523 (2019) 26–32. https://doi.org/10.1016/j.jnucmat.2019.05.021.

[13] C. Tang, M. Große, S. Ulrich, M. Klimenkov, U. Jäntsch, H.J. Seifert, M. Stüber, M. Steinbrück, High-temperature oxidation and hydrothermal corrosion of textured Cr2AlC-based coatings on zirconium alloy fuel cladding, Surf. Coat. Technol. 419 (2021) 127263. https://doi.org/10.1016/j.surfcoat.2021.127263.

[14] E. Alat, A.T. Motta, R.J. Comstock, J.M. Partezana, D.E. Wolfe, Multilayer (TiN, TiAlN) ceramic coatings for nuclear fuel cladding, J. Nucl. Mater. 478 (2016) 236–244. https://doi.org/10.1016/j.jnucmat.2016.05.021.

[15] C. Meng, L. Yang, Y. Wu, J. Tan, W. Dang, X. He, X. Ma, Study of the oxidation behavior of CrN coating on Zr alloy in air, J. Nucl. Mater. 515 (2019) 354–369. https://doi.org/10.1016/j.jnucmat.2019.01.006.

[16] O.V. Maksakova, R.F. Webster, R.D. Tilley, V.I. Ivashchenko, B.O. Postolnyi, O.V. Bondar, Y. Takeda, V.M. Rogoz, R.E. Sakenova, P.V. Zukowski, M. Opielak, V.M. Beresnev, A.D. Pogrebnjak, Nanoscale architecture of (CrN/ZrN)/(Cr/Zr) nanocomposite coatings: Microstructure, composition, mechanical properties and first-principles calculations, J. Alloys Compd. 831 (2020) 154808. https://doi.org/10.1016/j.jallcom.2020.154808.

[17] J. Liu, Z. Hao, Z. Cui, D. Ma, J. Lu, Y. Cui, C. Li, W. Liu, S. Xie, P. Huang, G. Bai, D. Yun, Investigation of the oxidation mechanisms of superlattice Cr-CrN/TiSiN-Cr multilayer coatings on Zircaloy substrates under high-temperature steam atmospheres, Corros. Sci. 192 (2021) 109782. https://doi.org/10.1016/j.corsci.2021.109782.

[18] H. Yeom, B. Maier, G. Johnson, T. Dabney, J. Walters, K. Sridharan, Development of cold spray process for oxidation-resistant FeCrAl and Mo diffusion barrier coatings on optimized ZIRLO^{TM}, J. Nucl. Mater. 507 (2018) 306–315. https://doi.org/10.1016/j.jnucmat.2018.05.014.

[19] T. Dabney, G. Johnson, H. Yeom, B. Maier, J. Walters, K. Sridharan, Experimental evaluation of cold spray FeCrAl alloys coated zirconium-alloy for potential accident tolerant fuel cladding, Nucl. Mater. Energy 21 (2019) 100715. https://doi.org/10.1016/j.nme.2019.100715.

[20] M. Kennas, H. Kim, J.G. Gigax, T. Wang, B.R. Maier, H. Yeom, G.O. Johnson, T. Dabney, K. Sridharan, K.L. Peddicord, L. Shao, Radiation response of FeCrAl-coated Zircaloy-4, J. Nucl. Mater. 536 (2020) 152175. https://doi.org/10.1016/j.jnucmat.2020.152175.

[21] X. Li, C. Meng, X. Xu, X. He, C. Wang, Effect of Al content on high-temperature oxidation behavior and failure mechanism of CrAl-coated Zircaloy, Corros. Sci. 192 (2021) 109856. https://doi.org/10.1016/j.corsci.2021.109856.

[22] S. Zeng, P. Li, J. Tian, C. Chen, Y. Meng, C. Zhu, H. Shen, X. Han, H. Zhang, Influence of Al content on the oxidation behavior of CrAl coating on Zry-4 alloys in 1200 °C steam, Corros. Sci. 198 (2022) 110115. https://doi.org/10.1016/j.corsci.2022.110115.

[23] J. Yang, X. Wu, L. Wu, Y. Zhong, H. Xin, Q. Chen, W. Zhang, J. Yang, C. Zhu, Z. Ning, N. Liu, J. Yang, Microstructure, mechanical properties and corrosion behavior of AlxCrMoNbZr multiprincipal element alloy coatings for accident-tolerant fuel claddings: Effect of Al content, Surf. Coat. Technol. 444 (2022) 128656. https://doi.org/10.1016/j.surfcoat.2022.128656.

[24] J. Bischoff, C. Delafoy, C. Vauglin, P. Barberis, C. Roubeyrie, D. Perche, D. Duthoo, F. Schuster, J.-C. Brachet, E.W. Schweitzer, K. Nimishakavi, AREVA NP's enhanced accident-tolerant fuel developments: Focus on Cr-coated M5 cladding, Nucl. Eng. Technol. 50 (2018) 223–228. https://doi.org/10.1016/j.net.2017.12.004.

[25] J.-C. Brachet, I. Idarraga-Trujillo, M.L. Flem, M.L. Saux, V. Vandenberghe, S. Urvoy, E. Rouesne, T. Guilbert, C. Toffolon-Masclet, M. Tupin, C. Phalippou, F. Lomello, F. Schuster, A. Billard, G. Velisa, C. Ducros, F. Sanchette, Early studies on Cr-Coated Zircaloy-4 as enhanced accident tolerant nuclear fuel claddings for light water reactors, J. Nucl. Mater. 517 (2019) 268–285. https://doi.org/10.1016/j.jnucmat.2019.02.018.

[26] J. Yang, M. Steinbrück, C. Tang, M. Große, J. Liu, J. Zhang, D. Yun, S. Wang, Review on chromium coated zirconium alloy accident tolerant fuel cladding, J. Alloys Compd. 895 (2022) 162450. https://doi.org/10.1016/j.jallcom.2021.162450.

[27] H. Yeom, K. Sridharan, Cold spray technology in nuclear energy applications: A review of recent advances, Ann. Nucl. Energy 150 (2021) 107835. https://doi.org/10.1016/j.anucene.2020.107835.

[28] K.A. Terrani, B.A. Pint, Y.-J. Kim, K.A. Unocic, Y. Yang, C.M. Silva, H.M. Meyer, R.B. Rebak, Uniform corrosion of FeCrAl alloys in LWR coolant environments, J. Nucl. Mater. 479 (2016) 36–47. https://doi.org/10.1016/j.jnucmat.2016.06.047.

[29] H. Okamoto, Fe-Zr (iron-zirconium), J. Phase Equilibria 14 (1993) 652–653. https://doi.org/10.1007/BF02669163.

[30] F. Stein, G. Sauthoff, M. Palm, Experimental determination of intermetallic phases, phase equilibria, and invariant reaction temperatures in the Fe-Zr system, J. Phase Equilibria 23 (2002) 480–494. https://doi.org/10.1361/105497102770331172.

[31] H. Yeom, B. Maier, G. Johnson, T. Dabney, J. Walters, K. Sridharan, Development of cold spray process for oxidation-resistant FeCrAl and Mo diffusion barrier coatings on optimized ZIRLO^{TM}, J. Nucl. Mater. 507 (2018) 306–315. https://doi.org/10.1016/j.jnucmat.2018.05.014.

[32] H. Okamoto, Supplemental Literature Review of Binary Phase Diagrams: B-Fe, Cr-Zr, Fe-Np, Fe-W, Fe-Zn, Ge-Ni, La-Sn, La-Ti, La-Zr, Li-Sn, Mn-S, and Nb-Re, J. Phase Equilibria Diffus. 37 (2016) 621–634. https://doi.org/10.1007/s11669-016-0465-z.

[33] Clifford A. Hampel, The Encyclopedia of the Chemical Elements, Reinhold Book Corp., New York, 1968.

[34] B. Maier, H. Yeom, G. Johnson, T. Dabney, J. Walters, P. Xu, J. Romero, H. Shah, K. Sridharan, Development of cold spray chromium coatings for improved accident tolerant zirconium-alloy cladding, J. Nucl. Mater. 519 (2019) 247–254. https://doi.org/10.1016/j.jnucmat.2019.03.039.

[35] H. Yeom, B. Maier, G. Johnson, T. Dabney, M. Lenling, K. Sridharan, High temperature oxidation and microstructural evolution of cold spray chromium coatings on Zircaloy-4 in steam environments, J. Nucl. Mater. 526 (2019) 151737. https://doi.org/10.1016/j.jnucmat.2019.151737.

[36] B.R. Maier, H. Yeom, G. Johnson, T. Dabney, J. Hu, P. Baldo, M. Li, K. Sridharan, In situ TEM investigation of irradiation-induced defect formation in cold spray Cr coatings for accident tolerant fuel applications, J. Nucl. Mater. 512 (2018) 320–323. https://doi.org/10.1016/j.jnucmat.2018.10.023.

[37] A. Fazi, K. Stiller, H.-O. Andrén, M. Thuvander, Cold sprayed Cr-coating on Optimized ZIRLO^{TM} claddings: the Cr/Zr interface and its microstructural and chemical evolution after autoclave corrosion testing, J. Nucl. Mater. 560 (2022) 153505. https://doi.org/10.1016/j.jnucmat.2022.153505.

[38] Y. Wang, W. Zhou, Q. Wen, X. Ruan, F. Luo, G. Bai, Y. Qing, D. Zhu, Z. Huang, Y. Zhang, T. Liu, R. Li, Behavior of plasma sprayed Cr coatings and FeCrAl coatings on Zr fuel cladding under loss-of-coolant accident conditions, Surf. Coat. Technol. 344 (2018) 141–148. https://doi.org/10.1016/j.surfcoat.2018.03.016.

[39] Z. Yang, Y. Niu, J. Xue, T. Liu, C. Chang, X. Zheng, Steam oxidation resistance of plasma sprayed chromium-containing coatings at 1200 C, Mater. Corros. 70 (2018) 37–47. https://doi.org/10.1002/maco.201810156.

[40] J. Jiang, M. Du, Z. Pan, M. Yuan, X. Ma, B. Wang, Effects of oxidation and inter-diffusion on the fracture mechanisms of Cr-coated Zry-4 alloys: An in situ three-point bending study, Mater. Des. 212 (2021) 110168. https://doi.org/10.1016/j.matdes.2021.110168.

[41] J. Liu, M. Steinbrück, M. Große, U. Stegmaier, C. Tang, D. Yun, J. Yang, Y. Cui, H.J. Seifert, Systematic investigations on the coating degradation mechanism during the steam oxidation of Cr-coated Zry-4 at 1200 °C, Corros. Sci. 202 (2022) 110310. https://doi.org/10.1016/j.corsci.2022.110310.

[42] Y. Wang, L. Wang, L. Shang, G. Bai, J. Li, F. Xue, W. Gong, Fiber texture-dependent oxidation behaviour of Cr-coated zirconium alloy in high temperature steam, Corros. Sci. 205 (2022) 110449. https://doi.org/10.1016/j.corsci.2022.110449.

[43] J.-H. Park, H.-G. Kim, J. Park, Y.-I. Jung, D.-J. Park, Y.-H. Koo, High temperature steam-oxidation behavior of arc ion plated Cr coatings for accident tolerant fuel claddings, Surf. Coat. Technol. 280 (2015) 256–259. https://doi.org/10.1016/j.surfcoat.2015.09.022.

[44] T. Wei, R. Zhang, H. Yang, H. Liu, S. Qiu, Y. Wang, P. Du, K. He, X. Hu, C. Dong, Microstructure, corrosion resistance and oxidation behavior of Cr-coatings on Zircaloy-4 prepared by vacuum arc plasma deposition, Corros. Sci. 158 (2019) 108077. https://doi.org/10.1016/j.corsci.2019.06.029.

[45] J. Huang, S. Zou, W. Xiao, C. Yang, D. Tang, H. Yu, L. Zhang, K. Zhang, Influences of arc current on microstructure of Cr coating for Zr-4 alloy prepared by multi-arc ion plating via EBSD, Mater. Charact. 178 (2021) 111211. https://doi.org/10.1016/j.matchar.2021.111211.

[46] W.G. Cook, R.P. Olive, Pourbaix diagrams for chromium, aluminum and titanium extended to high-subcritical and low-supercritical conditions, Corros. Sci. 58 (2012) 291–298. https://doi.org/10.1016/j.corsci.2012.02.002.

[47] E.J. Opila, N.S. Jacobson, D.L. Myers, E.H. Copland, Predicting oxide stability in high-temperature water vapor, JOM 58 (2006) 22–28. https://doi.org/10.1007/s11837-006-0063-3.

[48] M. Michalik, M. Hänsel, J. Zurek, L. Singheiser, W.J. Quadakkers, Effect of water vapour on growth and adherence of chromia scales formed on Cr in high and low pO2-environments at 1000 and 1050°C, Mater. High Temp. 22 (2005) 213–221. https://doi.org/10.1179/mht.2005.025.

[49] K.G. Geelhood, W.G. Luscher, Degradation and Failure Phenomena of Accident Tolerant Fuel Concepts -- Chromium Coated Zirconium Alloy Cladding, Pacific Northwest National Laboratory, 2019.

[50] A. Hellouin De Menibus, J. Sercombe, Q. Auzoux, C. Poussard, Thermomechanical loading applied on the cladding tube during the pellet cladding mechanical interaction phase of a rapid reactivity initiated accident, J. Nucl. Mater. 453 (2014) 210–213. https://doi.org/10.1016/j.jnucmat.2014.06.046.

[51] F. Qi, Z. Liu, Q. Li, H. Yu, P. Chen, Y. Li, Y. Zhou, C. Ma, C. Tang, Y. Huang, B. Zhao, H. Lu, Pellet-cladding mechanical interaction analysis of Cr-coated Zircaloy cladding, Nucl. Eng. Des. 367 (2020) 110792. https://doi.org/10.1016/j.nucengdes.2020.110792.

[52] I. Alakiozidis, C. Hunt, R. Thomas, D. Lunt, A.D. Smith, M. Maric, Z. Shah, A. Ambard, P. Frankel, Quantifying cracking and strain localisation in a cold spray chromium coating on a zirconium alloy substrate under tensile loading at room temperature, J. Nucl. Mater. 591 (2024) 154899. https://doi.org/10.1016/j.jnucmat.2024.154899.

[53] G. Yuan, J. Paul Forna-Kreutzer, J. Ell, H. Barnard, B.R. Maier, E. Lahoda, J. Walters, R.O. Ritchie, D. Liu, In situ X-ray computed micro-tomography imaging of failure processes in Cr-coated Zircaloy nuclear fuel cladding materials, Mater. Des. 234 (2023) 112373. https://doi.org/10.1016/j.matdes.2023.112373.

[54] J. Kim, S. Joung, Y. Lee, Effect of Cr coating on the mechanical integrity of Accident Tolerant Fuel cladding under ring compression test, J. Nucl. Mater. 585 (2023) 154603. https://doi.org/10.1016/j.jnucmat.2023.154603.

[55] D.C. Roache, C.H. Bumgardner, T.M. Harrell, M.C. Price, A. Jarama, F.M. Heim, J. Walters, B. Maier, X. Li, Unveiling damage mechanisms of chromium-coated zirconium-based fuel claddings at LWR operating temperature by in-situ digital image correlation, Surf. Coat. Technol. 429 (2022) 127909. https://doi.org/10.1016/j.surfcoat.2021.127909.

[56] T. Zhou, H. Chen, Y. Yue, X. Fang, R. Zhang, X. Gao, Z. Cai, Effect of coating thickness on interfacial adhesion and mechanical properties of Cr-coated zircaloy, Trans. Nonferrous Met. Soc. China 33 (2023) 2672–2686. https://doi.org/10.1016/S1003-6326(23)66289-2.

[57] J. Jiang, H. Zhai, M. Du, D. Wang, X. Pei, X. Ma, B. Wang, Temperature-dependent deformation and cracking behavior in Cr coating for accident tolerant fuel cladding: An in situ SEM study, Surf. Coat. Technol. 427 (2021) 127815. https://doi.org/10.1016/j.surfcoat.2021.127815.

[58] D.V. Nguyen, M. Le Saux, L. Gélébart, J.-C. Brachet, J.-P. Bonthonneau, A. Courcelle, R. Guillou, E. Rouesne, S. Urvoy, Mechanical behavior of a chromium coating on a zirconium alloy substrate at room temperature, J. Nucl. Mater. 558 (2022) 153332. https://doi.org/10.1016/j.jnucmat.2021.153332.

[59] R. Fritz, V. Maier-Kiener, D. Lutz, D. Kiener, Interplay between sample size and grain size: Single crystalline vs. ultrafine-grained chromium micropillars, Mater. Sci. Eng. A 674 (2016) 626–633. https://doi.org/10.1016/j.msea.2016.08.015.

[60] R. Fritz, D. Wimler, A. Leitner, V. Maier-Kiener, D. Kiener, Dominating deformation mechanisms in ultrafine-grained chromium across length scales and temperatures, Acta Mater. 140 (2017) 176–187. https://doi.org/10.1016/j.actamat.2017.08.043.

[61] I. Issa, A. Hohenwarter, R. Fritz, D. Kiener, Fracture properties of ultrafine grain chromium correlated to single dislocation processes at room temperature, J. Mater. Res. 34 (2019) 2370–2383. https://doi.org/10.1557/jmr.2019.140.

[62] D. Kiener, R. Fritz, M. Alfreider, A. Leitner, R. Pippan, V. Maier-Kiener, Rate limiting deformation mechanisms of bcc metals in confined volumes, Acta Mater. 166 (2019) 687–701. https://doi.org/10.1016/j.actamat.2019.01.020.

[63] Y. Gan, K. Mo, D. Yun, D.T. Hoelzer, Y. Miao, X. Liu, K.-C. Lan, J.-S. Park, J. Almer, T. Chen, H. Zhao, Temperature effect of elastic anisotropy and internal strain development in advanced nanostructured alloys: An in-situ synchrotron X-ray investigation, Mater. Sci. Eng. A 692 (2017) 53–61. https://doi.org/10.1016/j.msea.2017.03.068.

[64] Y. Miao, K. Mo, Z. Zhou, X. Liu, K.-C. Lan, G. Zhang, M.K. Miller, K.A. Powers, Z.-G. Mei, J.-S. Park, J. Almer, J.F. Stubbins, On the microstructure and strengthening mechanism in oxide dispersion-strengthened 316 steel: A coordinated electron microscopy, atom probe tomography and in situ synchrotron tensile investigation, Mater. Sci. Eng. A 639 (2015) 585–596. https://doi.org/10.1016/j.msea.2015.05.064.

[65] Y. Miao, K. Mo, Z. Zhou, X. Liu, K.-C. Lan, G. Zhang, J.-S. Park, J. Almer, J.F. Stubbins, Load-partitioning in an oxide dispersion-strengthened 310 steel at elevated temperatures, Mater. Des. 111 (2016) 622–630. https://doi.org/10.1016/j.matdes.2016.09.015.

[66] Y. Miao, K. Mo, J.-S. Park, J. Almer, C. Massey, C. Havrilak, A.T. Nelson, H. Connaway, A.M. Yacout, In situ synchrotron tensile investigations on ultrasonic additive manufactured (UAM) zirconium, J. Nucl. Mater. 568 (2022) 153843. https://doi.org/10.1016/j.jnucmat.2022.153843.

[67] P. Hosemann, Small-scale mechanical testing on nuclear materials: bridging the experimental length-scale gap, Scr. Mater. 143 (2018) 161–168. https://doi.org/10.1016/j.scriptamat.2017.04.026.

[68] A. Jokisaari, W. Chen, Y. Chen, R. Song, S. Taller, Promoting the Regulatory Acceptance of Combined Ion and Neutron Irradiation for Material Degradation in Nuclear Reactors, 2023. https://doi.org/10.2172/2251504.

[69] S.J. Zinkle, Microstructures and Mechanical Properties of Irradiated Metals and Alloys, in: V. Ghetta, D. Gorse, D. Mazière, V. Pontikis (Eds.), Mater. Issues Gener. IV Syst., Springer Netherlands, Dordrecht, 2008: pp. 227–244. https://doi.org/10.1007/978-1-4020-8422-5_11.

[70] F.A. Garner, M.B. Toloczko, B.H. Sencer, Comparison of swelling and irradiation creep behavior of fcc-austenitic and bcc-ferritic/martensitic alloys at high neutron exposure, J. Nucl. Mater. 276 (2000) 123–142. https://doi.org/10.1016/S0022-3115(99)00225-1.

[71] Z. Yu, Y.-R. Lin, M.J. Zachman, S.J. Zinkle, H. Xu, The role of stacking fault tetrahedra on void swelling in irradiated copper, Commun. Mater. 5 (2024) 53. https://doi.org/10.1038/s43246-024-00491-7.

[72] A.S. Kuprin, V.A. Belous, V.N. Voyevodin, R.L. Vasilenko, V.D. Ovcharenko, G.D. Tolstolutskaya, I.E. Kopanets, I.V. Kolodiy, Irradiation resistance of vacuum arc chromium coatings for zirconium alloy fuel claddings, J. Nucl. Mater. 510 (2018) 163–167. https://doi.org/10.1016/j.jnucmat.2018.07.063.

[73] A.S. Kuprin, R.L. Vasilenko, G.D. Tolstolutskaya, V.N. Voyevodin, V.A. Belous, V.D. Ovcharenko, I.E. Kopanets, Irradiation resistance of chromium coatings for ATFC in the temperature range 300–550°C, J. Nucl. Mater. 549 (2021) 152908. https://doi.org/10.1016/j.jnucmat.2021.152908.

[74] E. Ryabikovskaya, A. French, A. Gabriel, H. Kim, T. Wang, K. Shirvan, F.A. Garner, L. Shao, Irradiation-induced swelling of pure chromium with 5 MeV Fe ions in the temperature range 450–650 °C, J. Nucl. Mater. 543 (2021) 152585. https://doi.org/10.1016/j.jnucmat.2020.152585.

[75] V.V. Bryk, V.N. Voyevodin, I.M. Neklyudov, A.N. Rakitskij, Microstructure investigation of Cr and Cr alloys irradiated with heavy ions, J. Nucl. Mater. 225 (1995) 146–153. https://doi.org/10.1016/0022-3115(95)00066-6.

[76] J. Zhang, H. He, W. Liu, L. Kang, D. Yun, P. Chen, Effects of grain boundaries on the radiation-induced defects evolution in BCC Fe–Cr alloy: A molecular dynamics study, Nucl. Mater. Energy 22 (2020) 100726. https://doi.org/10.1016/j.nme.2020.100726.

[77] Z. Yu, H. Xu, Dislocation loop bias and void swelling in irradiated α-iron from mesoscale and atomistic simulations, Commun. Mater. 4 (2023) 29. https://doi.org/10.1038/s43246-023-00356-5.

[78] L. Song, B. Huang, J. Li, X. Ma, M. Liu, J. Jiang, Y. Hu, Effects of ion irradiation on Cr, CrN, and TiAlCrN coated Zircaloy-4 for accident tolerant fuel claddings, Ann. Nucl. Energy 156 (2021) 108206. https://doi.org/10.1016/j.anucene.2021.108206.

[79] Z. Sun, Y. Li, X. Qiu, D. Sun, P. Du, R. Zhang, Y. Xin, G. Ran, An in-situ TEM investigation of microstructure evolution in Cr-coated zirconium alloy under heavy ion irradiation: Simultaneous

evolution of both Cr coating and Zr-4 matrix, Nucl. Instrum. Methods Phys. Res. Sect. B Beam Interact. Mater. At. 536 (2023) 97–103. https://doi.org/10.1016/j.nimb.2023.01.002.

[80] L. Wei, Y. Li, G. Zhao, Q. Zheng, J. Li, Z. Zeng, Key factors in radiation tolerance of BCC metals under steady state, Nucl. Instrum. Methods Phys. Res. Sect. B Beam Interact. Mater. At. 455 (2019) 134–139. https://doi.org/10.1016/j.nimb.2019.06.032.

[81] W.V. Vaidya, K. Ehrlich, Radiation-induced recrystallization, its cause and consequences in heavy-ion irradiated 20% cold-drawn steels of type 1.4970, J. Nucl. Mater. 113 (1983) 149–162. https://doi.org/10.1016/0022-3115(83)90137-X.

[82] A. Jain, S. Loganathan, J.D. Kanjilal, G. Mehta, High energy heavy ion irradiation of chromium films, Vacuum 46 (1995) 369–371. https://doi.org/10.1016/0042-207X(94)00081-6.

[83] R. Wang, B. Li, P. Li, X. Bai, L. Hu, Q. Huang, J. Xu, F. Huang, F. Ge, Effect of low-dose Xe20+ ion irradiation on the deformation behavior of the magnetron sputtered Cr coatings under nanoindentation, Surf. Coat. Technol. 428 (2021) 127907. https://doi.org/10.1016/j.surfcoat.2021.127907.

[84] C.W. Weaver, Irradiation and the ductility of chromium, Scr. Metall. 2 (1968) 463–466. https://doi.org/10.1016/0036-9748(68)90195-6.

[85] H. Chen, C. Zhan, W. Gong, P. Du, R. Zhang, J. Yang, Y. Wang, T. Wei, H. Yang, Y. Zou, B. Fu, Surface growth, inner defects and interface mixing of Cr coating on Zr alloy irradiated by 5 MeV protons at 400°C, J. Nucl. Mater. 586 (2023) 154696. https://doi.org/10.1016/j.jnucmat.2023.154696.

[86] W. Gong, H. Chen, C. Zhan, P. Du, R. Zhang, Y. Wang, T. Wei, H. Yang, Y. Zou, J. Yang, Formation of voids in the Cr coatings with (110)-preferred orientation prepared by arc ion plating under an Au+ irradiation of 20 dpa, Surf. Coat. Technol. 425 (2021) 127750. https://doi.org/10.1016/j.surfcoat.2021.127750.

[87] J. Ribis, A. Wu, J.-C. Brachet, F. Barcelo, B. Arnal, Atomic-scale interface structure of a Cr-coated Zircaloy-4 material, J. Mater. Sci. 53 (2018) 9879–9895. https://doi.org/10.1007/s10853-018-2333-1.

[88] A. Wu, J. Ribis, J.-C. Brachet, E. Clouet, F. Leprêtre, E. Bordas, B. Arnal, HRTEM and chemical study of an ion-irradiated chromium/zircaloy-4 interface, J. Nucl. Mater. 504 (2018) 289–299. https://doi.org/10.1016/j.jnucmat.2018.01.029.

[89] A. Fazi, H. Aboulfadl, A.H.S. Iyer, M. Sattari, K.M. Stiller, P. Lokhande, M. Thuvander, H.-O. Andren, Characterization of as-deposited cold sprayed Cr-coating on Optimized ZIRLO^{TM} claddings, J. Nucl. Mater. 549 (2021) 152892. https://doi.org/10.1016/j.jnucmat.2021.152892.

[90] D. Helfritch, V.K. Champagne, A. Papyrin, The development of the cold spray process, in: Adv. Cold Spray, Elsevier, 2023: pp. 9–41. https://doi.org/10.1016/B978-0-08-103015-8.00013-X.

[91] K.A. Kowalsky, V.K. Champagne, M.F. Smith, Comparing cold spray with thermal spray coating technologies, in: Adv. Cold Spray, Elsevier, 2023: pp. 43–63. https://doi.org/10.1016/B978-0-08-103015-8.00012-8.

[92] K. Sakaki, The influence of nozzle design in the cold spray process, in: Cold Spray Mater. Depos. Process, Elsevier, 2007: pp. 117–126. https://doi.org/10.1533/9781845693787.2.117.

[93] R.C. Dykhuizen, M.F. Smith, Gas Dynamic Principles of Cold Spray, J. Therm. Spray Technol. 7 (1998) 205–212. https://doi.org/10.1361/105996398770350945.

[94] V.F. Kosarev, S.V. Klinkov, A.N. Papyrin, Supersonic jet/substrate interaction in the cold spray process, in: Cold Spray Mater. Depos. Process, Elsevier, 2007: pp. 178–216. https://doi.org/10.1533/9781845693787.2.178.

[95] V.K. Champagne, Introduction, in: Adv. Cold Spray, Elsevier, 2023: pp. 1–7. https://doi.org/10.1016/B978-0-08-103015-8.00003-7.

[96] O.Ç. Özdemir, Process parameters and control, in: Adv. Cold Spray, Elsevier, 2023: pp. 89–134. https://doi.org/10.1016/B978-0-08-103015-8.00005-0.

[97] H. Assadi, T. Schmidt, H. Richter, J.-O. Kliemann, K. Binder, F. Gärtner, T. Klassen, H. Kreye, On Parameter Selection in Cold Spraying, J. Therm. Spray Technol. 20 (2011) 1161–1176. https://doi.org/10.1007/s11666-011-9662-9.

[98] T. Schmidt, F. Gärtner, H. Assadi, H. Kreye, Development of a generalized parameter window for cold spray deposition, Acta Mater. 54 (2006) 729–742. https://doi.org/10.1016/j.actamat.2005.10.005.

[99] H. Assadi, F. Gärtner, T. Stoltenhoff, H. Kreye, Bonding mechanism in cold gas spraying, Acta Mater. 51 (2003) 4379–4394. https://doi.org/10.1016/S1359-6454(03)00274-X.

[100] H. Assadi, H. Kreye, F. Gärtner, T. Klassen, Cold spraying – A materials perspective, Acta Mater. 116 (2016) 382–407. https://doi.org/10.1016/j.actamat.2016.06.034.

[101] M. Hassani, D. Veysset, Y. Sun, K.A. Nelson, C.A. Schuh, Microparticle impact-bonding modes for mismatched metals: From co-deformation to splatting and penetration, Acta Mater. 199 (2020) 480–494. https://doi.org/10.1016/j.actamat.2020.08.038.

[102] M.V. Vidaller, A. List, F. Gaertner, T. Klassen, S. Dosta, J.M. Guilemany, Single Impact Bonding of Cold Sprayed Ti-6Al-4V Powders on Different Substrates, J. Therm. Spray Technol. 24 (2015) 644–658. https://doi.org/10.1007/s11666-014-0200-4.

[103] W. Xie, A. Alizadeh-Dehkharghani, Q. Chen, V.K. Champagne, X. Wang, A.T. Nardi, S. Kooi, S. Müftü, J.-H. Lee, Dynamics and extreme plasticity of metallic microparticles in supersonic collisions, Sci. Rep. 7 (2017) 5073. https://doi.org/10.1038/s41598-017-05104-7.

[104] M. Hassani-Gangaraj, D. Veysset, K.A. Nelson, C.A. Schuh, In-situ observations of single micro-particle impact bonding, Scr. Mater. 145 (2018) 9–13. https://doi.org/10.1016/j.scriptamat.2017.09.042.

[105] A.A. Tiamiyu, C.A. Schuh, Particle flattening during cold spray: Mechanistic regimes revealed by single particle impact tests, Surf. Coat. Technol. 403 (2020) 126386. https://doi.org/10.1016/j.surfcoat.2020.126386.

[106] A.A. Tiamiyu, Y. Sun, K.A. Nelson, C.A. Schuh, Site-specific study of jetting, bonding, and local deformation during high-velocity metallic microparticle impact, Acta Mater. 202 (2021) 159–169. https://doi.org/10.1016/j.actamat.2020.10.057.

[107] T. Liu, J.D. Leazer, L.N. Brewer, Particle deformation and microstructure evolution during cold spray of individual Al-Cu alloy powder particles, Acta Mater. 168 (2019) 13–23. https://doi.org/10.1016/j.actamat.2019.01.054.

[108] J.-H. Lee, M. Hassani, Studies of single-particle impact, in: Adv. Cold Spray, Elsevier, 2023: pp. 135–148. https://doi.org/10.1016/B978-0-08-103015-8.00011-6.

[109] J.-H. Lee, D. Veysset, J.P. Singer, M. Retsch, G. Saini, T. Pezeril, K.A. Nelson, E.L. Thomas, High strain rate deformation of layered nanocomposites, Nat. Commun. 3 (2012) 1164. https://doi.org/10.1038/ncomms2166.

[110] J.-H. Lee, P.E. Loya, J. Lou, E.L. Thomas, Dynamic mechanical behavior of multilayer graphene via supersonic projectile penetration, Science 346 (2014) 1092–1096. https://doi.org/10.1126/science.1258544.

[111] M. Hassani, V.K. Champagne, D. Helfritch, Bonding mechanisms in cold spray, in: Adv. Cold Spray, Elsevier, 2023: pp. 149–163. https://doi.org/10.1016/B978-0-08-103015-8.00004-9.

[112] M. Grujicic, Particle/substrate interaction in the cold-spray bonding process, in: Cold Spray Mater. Depos. Process, Elsevier, 2007: pp. 148–177. https://doi.org/10.1533/9781845693787.2.148.

[113] C. Chen, Y. Xie, R. Huang, S. Deng, Z. Ren, H. Liao, On the role of oxide film's cleaning effect into the metallurgical bonding during cold spray, Mater. Lett. 210 (2018) 199–202. https://doi.org/10.1016/j.matlet.2017.09.024.

[114] C.D. Reddy, Z.-Q. Zhang, S. Msolli, J. Guo, N. Sridhar, Impact induced metallurgical and mechanical interlocking in metals, Comput. Mater. Sci. 192 (2021) 110363. https://doi.org/10.1016/j.commatsci.2021.110363.

[115] Z. Liu, H. Wang, M. Haché, E. Irissou, Y. Zou, Formation of refined grains below 10 nm in size and nanoscale interlocking in the particle–particle interfacial regions of cold sprayed pure aluminum, Scr. Mater. 177 (2020) 96–100. https://doi.org/10.1016/j.scriptamat.2019.09.018.

[116] M. Hassani-Gangaraj, D. Veysset, V.K. Champagne, K.A. Nelson, C.A. Schuh, Adiabatic shear instability is not necessary for adhesion in cold spray, Acta Mater. 158 (2018) 430–439. https://doi.org/10.1016/j.actamat.2018.07.065.

[117] M. Hassani-Gangaraj, D. Veysset, V.K. Champagne, K.A. Nelson, C.A. Schuh, Response to Comment on "Adiabatic shear instability is not necessary for adhesion in cold spray," Scr. Mater. 162 (2019) 515–519. https://doi.org/10.1016/j.scriptamat.2018.12.015.

[118] Y. Sun, D. Veysset, K.A. Nelson, C.A. Schuh, The Transition From Rebound to Bonding in High-Velocity Metallic Microparticle Impacts: Jetting-Associated Power-Law Divergence, J. Appl. Mech. 87 (2020) 091002. https://doi.org/10.1115/1.4047206.

[119] S. Rahmati, B. Jodoin, Physically Based Finite Element Modeling Method to Predict Metallic Bonding in Cold Spray, J. Therm. Spray Technol. 29 (2020) 611–629. https://doi.org/10.1007/s11666-020-01000-1.

[120] T. Van Steenkiste, The role of particle temperature and velocity in cold spray coating formation, in: Cold Spray Mater. Depos. Process, Elsevier, 2007: pp. 127–147. https://doi.org/10.1533/9781845693787.2.127.

[121] T.H. Van Steenkiste, J.R. Smith, R.E. Teets, Aluminum coatings via kinetic spray with relatively large powder particles, Surf. Coat. Technol. 154 (2002) 237–252. https://doi.org/10.1016/S0257-8972(02)00018-X.

[122] A.A. Tiamiyu, T. Lucas, E.L. Pang, X. Chen, J.M. LeBeau, C.A. Schuh, Heterogeneous microstructural evolution during hydrodynamic penetration of a high-velocity copper microparticle impacting copper, Mater. Today 72 (2024) 71–86. https://doi.org/10.1016/j.mattod.2023.11.015.

[123] K. Kim, M. Watanabe, J. Kawakita, S. Kuroda, Grain refinement in a single titanium powder particle impacted at high velocity, Scr. Mater. 59 (2008) 768–771. https://doi.org/10.1016/j.scriptamat.2008.06.020.

[124] J.Y. Lek, A. Bhowmik, A.W.-Y. Tan, W. Sun, X. Song, W. Zhai, P.J. Buenconsejo, F. Li, E. Liu, Y.M. Lam, C.B. Boothroyd, Understanding the microstructural evolution of cold sprayed Ti-6Al-4V coatings on Ti-6Al-4V substrates, Appl. Surf. Sci. 459 (2018) 492–504. https://doi.org/10.1016/j.apsusc.2018.07.175.

[125] Z. Liu, H. Wang, M.J.R. Haché, X. Chu, E. Irissou, Y. Zou, Prediction of heterogeneous microstructural evolution in cold sprayed copper coatings using local Zener-Hollomon parameter and strain, Acta Mater. 193 (2020) 191–201. https://doi.org/10.1016/j.actamat.2020.04.041.

[126] H. Zhou, Z. Li, S. Jiang, Effect of gas temperature on the interfacial bonding of cold-spray additive-manufactured Ti6Al4V, Surf. Interfaces 44 (2024) 103676. https://doi.org/10.1016/j.surfin.2023.103676.

[127] B. Maier, H. Yeom, G. Johnson, T. Dabney, J. Walters, P. Xu, J. Romero, H. Shah, K. Sridharan, Development of cold spray chromium coatings for improved accident tolerant zirconium-alloy cladding, J. Nucl. Mater. 519 (2019) 247–254. https://doi.org/10.1016/j.jnucmat.2019.03.039.

[128] H. Yeom, T. Dabney, G. Johnson, B. Maier, M. Lenling, K. Sridharan, Improving deposition efficiency in cold spraying chromium coatings by powder annealing, Int. J. Adv. Manuf. Technol. 100 (2019) 1373–1382. https://doi.org/10.1007/s00170-018-2784-1.

[129] H. Yeom, B. Maier, G. Johnson, T. Dabney, M. Lenling, K. Sridharan, High temperature oxidation and microstructural evolution of cold spray chromium coatings on Zircaloy-4 in steam environments, J. Nucl. Mater. 526 (2019) 151737. https://doi.org/10.1016/j.jnucmat.2019.151737.

[130] H. Yeom, G. Johnson, B. Maier, T. Dabney, K. Sridharan, High temperature oxidation of cold spray Cr-coated accident tolerant zirconium-alloy cladding with Nb diffusion barrier layer, J. Nucl. Mater. 588 (2024) 154822. https://doi.org/10.1016/j.jnucmat.2023.154822.

[131] B.R. Maier, H. Yeom, G. Johnson, T. Dabney, J. Hu, P. Baldo, M. Li, K. Sridharan, In situ TEM investigation of irradiation-induced defect formation in cold spray Cr coatings for accident tolerant

fuel applications, J. Nucl. Mater. 512 (2018) 320–323. https://doi.org/10.1016/j.jnucmat.2018.10.023.

[132] High-Purity Chromium Metal: Supply Issues for Gas-Turbine Superalloys, National Academies Press, Washington, D.C., 1995. https://doi.org/10.17226/9248.

[133] G. Mucsi, A review on mechanical activation and mechanical alloying in stirred media mill, Chem. Eng. Res. Des. 148 (2019) 460–474. https://doi.org/10.1016/j.cherd.2019.06.029.

[134] C. Cai, K. Zhou, Metal additive manufacturing, in: Digit. Manuf., Elsevier, 2022: pp. 247–298. https://doi.org/10.1016/B978-0-323-95062-6.00005-X.

[135] R. Dolbec, M. Boulos, E. Bouchard, N. Kuppuswamy, Nanopowders synthesis at industrial-scale production using the inductively-coupled plasma technology, in: Int. Conf. Adv. Nanomater. Emerg. Eng. Technol., IEEE, Chennai, India, 2013: pp. 21–24. https://doi.org/10.1109/ICANMEET.2013.6609224.

[136] M.H. Sehhat, A.T. Sutton, C.-H. Hung, B. Brown, R.J. O'Malley, J. Park, M.C. Leu, Plasma spheroidization of gas-atomized 304L stainless steel powder for laser powder bed fusion process, Mater. Sci. Addit. Manuf. 1 (2022) 1. https://doi.org/10.18063/msam.v1i1.1.

[137] H. Yeom, T. Dabney, G. Johnson, B. Maier, M. Lenling, K. Sridharan, Improving deposition efficiency in cold spraying chromium coatings by powder annealing, Int. J. Adv. Manuf. Technol. 100 (2019) 1373–1382. https://doi.org/10.1007/s00170-018-2784-1.

[138] M. Pfeifer, Chapter 6 - Degradation and Reliability of Materials, in: M. Pfeifer (Ed.), Mater. Enabled Des., Butterworth-Heinemann, Boston, 2009: pp. 161–187. https://doi.org/10.1016/B978-0-7506-8287-9.00006-9.

[139] M.A. Meyers, K.K. Chawla, Mechanical Behavior of Materials, 2nd ed., Cambridge University Press, New York, NY, 2009.

[140] Y. Lu, Y.-H. Zhang, E. Ma, W.-Z. Han, Relative mobility of screw versus edge dislocations controls the ductile-to-brittle transition in metals, Proc. Natl. Acad. Sci. 118 (2021) e2110596118. https://doi.org/10.1073/pnas.2110596118.

[141] J. Heieck, Mechanical Properties of High-Purity Chromium, European Joint Centre, Institute for Advanced Materials, Ispra (VA), Italy, 1977.

[142] L.L. Snead, D.T. Hoelzer, M. Rieth, A.A.N. Nemith, Refractory Alloys: Vanadium, Niobium, Molybdenum, Tungsten, in: Struct. Alloys Nucl. Energy Appl., Elsevier, 2019: pp. 585–640. https://doi.org/10.1016/B978-0-12-397046-6.00013-7.

[143] B10 Committee, Specification for Zirconium and Zirconium Alloy Sheet, Strip, and Plate for Nuclear Application, ASTM International, n.d. https://doi.org/10.1520/B0352_B0352M-17R21.

[144] A. Hulton, Investigation of the effects of particle temperature and spacing on multi-particle impacts in cold spray, Northeastern University, 2013. https://doi.org/10.17760/d20003333.

[145] A.H. Osman, Investigation into Gas Pressure Variation at Inlet of a Converging-Diverging Nozzle, Int. J. Res. Appl. Sci. Eng. Technol. 7 (2019) 1656–1664. https://doi.org/10.22214/ijraset.2019.5280.

[146] ANSYS FLUENT, (2009). https://www.afs.enea.it/project/neptunius/docs/fluent/html/ug/node984.htm.

[147] A. Haider, O. Levenspiel, Drag coefficient and terminal velocity of spherical and nonspherical particles, Powder Technol. 58 (1989) 63–70. https://doi.org/10.1016/0032-5910(89)80008-7.

[148] J. Pattison, S. Celotto, A. Khan, W. O'Neill, Standoff distance and bow shock phenomena in the Cold Spray process, Surf. Coat. Technol. 202 (2008) 1443–1454. https://doi.org/10.1016/j.surfcoat.2007.06.065.

[149] W.-Y. Li, C.-J. Li, Optimal Design of a Novel Cold Spray Gun Nozzle at a Limited Space, J. Therm. Spray Technol. 14 (2005) 391–396. https://doi.org/10.1361/105996305X59404.

[150] A. Fardan, C.C. Berndt, R. Ahmed, Numerical modelling of particle impact and residual stresses in cold sprayed coatings: A review, Surf. Coat. Technol. 409 (2021) 126835. https://doi.org/10.1016/j.surfcoat.2021.126835.

[151] G.R. Johnson, W.H. Cook, A Constitutive Model And Data For Metals, (n.d.).

[152] V. Kumar Reddy Sirigiri, V. Yadav Gudiga, U. Shankar Gattu, G. Suneesh, K. Mohan Buddaraju, A review on Johnson Cook material model, Mater. Today Proc. 62 (2022) 3450–3456. https://doi.org/10.1016/j.matpr.2022.04.279.

[153] M. Murugesan, D. Jung, Johnson Cook Material and Failure Model Parameters Estimation of AISI-1045 Medium Carbon Steel for Metal Forming Applications, Materials 12 (2019) 609. https://doi.org/10.3390/ma12040609.

[154] L. Brewer, M. Othon, L. Young, T. Angeliu, Misorientation Mapping for Visualization of Plastic Deformation via Electron Back-Scattered Diffraction, Microsc. Microanal. 12 (2006) 85–91. https://doi.org/10.1017/S1431927606060120.

[155] S. Wright, M. Nowell, D. Field, A Review of Strain Analysis Using Electron Backscatter Diffraction, Microsc. Microanal. 17 (2011) 316–329. https://doi.org/10.1017/S1431927611000055.

[156] M.E. Fitzpatrick, A.T. Fry, P. Holdway, F.A. Kandil, J. Shackleton, L. Suominen, Determination of residual stresses by X-ray diffraction., Teddington, 2005. http://eprintspublications.npl.co.uk/2391/.

[157] E28 Committee, Standard Test Method for Verifying the Alignment of X-Ray Diffraction Instrumentation for Residual Stress Measurement, ASTM International, n.d. https://doi.org/10.1520/E0915-21.

[158] E28 Committee, Standard Test Method for Determining the X-Ray Elastic Constants for Use in the Measurement of Residual Stress Using X-Ray Diffraction Techniques, ASTM International, n.d. https://doi.org/10.1520/E1426-14R19E01.

[159] E28 Committee, Standard Test Method for Residual Stress Measurement by X-Ray Diffraction for Bearing Steels, ASTM International, n.d. https://doi.org/10.1520/E2860–20.

[160] E28 Committee, Standard Test Methods for Vickers Hardness and Knoop Hardness of Metallic Materials, ASTM International, n.d. https://doi.org/10.1520/E0092-17.

[161] E04 Committee, Standard Test Method for Microindentation Hardness of Materials, ASTM International, n.d. https://doi.org/10.1520/E0384-22.

[162] A. Slagter, J. Everaerts, A. Mortensen, Nanoindentation of embedded particles, J. Mater. Res. 38 (2023) 1694–1705. https://doi.org/10.1557/s43578-023-00920-2.

[163] K. Quillin, H. Yeom, T. Dabney, E. Willing, K. Sridharan, Microstructural and nanomechanical studies of PVD Cr coatings on SiC for LWR fuel cladding applications, Surf. Coat. Technol. 441 (2022) 128577. https://doi.org/10.1016/j.surfcoat.2022.128577.

[164] B10 Committee, Standard Test Method for Corrosion Testing of Products of Zirconium, Hafnium, and Their Alloys in Water at 680°F (360°C) or in Steam at 750°F (400°C), ASTM International, n.d. https://doi.org/10.1520/G0002_G0002M-19.

[165] D19 Committee, Standard Test Methods for Dissolved Oxygen in Water, ASTM International, n.d. https://doi.org/10.1520/D0888-18.

[166] Hach Company, Luminescence Measurement of Dissolved Oxygen in Water and Wastewater and for Use in the Determination of BOD5 and cBOD5, Hach Company, n.d. https://www.regulations.gov/document/EPA-HQ-OW-2010-0192-0355.

[167] C.B. Carter, D.B. Williams, eds., Transmission Electron Microscopy, Springer International Publishing, Cham, 2016. https://doi.org/10.1007/978-3-319-26651-0.

[168] T. Ungár, Microstructural parameters from X-ray diffraction peak broadening, Scr. Mater. 51 (2004) 777–781. https://doi.org/10.1016/j.scriptamat.2004.05.007.

[169] B. Maier, Investigation of Mechanisms of Metallic Cold Spray Coating Formation and Relevant Corrosion and Irradiation Behaviors, Ph.D. Thesis, University of Wisconsin-Madison, 2019. https://digital.library.wisc.edu/1711.dl/BJRV34JR4ACWR8J.

[170] D. Boruah, B. Ahmad, T.L. Lee, S. Kabra, A.K. Syed, P. McNutt, M. Doré, X. Zhang, Evaluation of residual stresses induced by cold spraying of Ti-6Al-4V on Ti-6Al-4V substrates, Surf. Coat. Technol. 374 (2019) 591–602. https://doi.org/10.1016/j.surfcoat.2019.06.028.

[171] W.G. Burgers, On the process of transition of the cubic-body-centered modification into the hexagonal-close-packed modification of zirconium, Physica 1 (1934) 561–586. https://doi.org/10.1016/S0031-8914(34)80244-3.

[172] H.-R. Wenk, I. Lonardelli, D. Williams, Texture changes in the hcp→bcc→hcp transformation of zirconium studied in situ by neutron diffraction, Acta Mater. 52 (2004) 1899–1907. https://doi.org/10.1016/j.actamat.2003.12.029.

[173] G. Bradfield, Elastic properties, damping capacity and shape memory alloys, (n.d.).

[174] P.F. Weck, E. Kim, V. Tikare, J.A. Mitchell, Mechanical properties of zirconium alloys and zirconium hydrides predicted from density functional perturbation theory, Dalton Trans. 44 (2015) 18769–18779. https://doi.org/10.1039/C5DT03403E.

[175] R. Wadsack, R. Pippan, B. Schedler, FRACTURE IN CHROMIUM: AN ATTEMPT TO IMPROVE DUCTILITY, (n.d.).

[176] K.J. Geelhood, C.E. Beyer, W.G. Luscher, PNNL Stress/Strain Correlation for Zircaloy, 2008. https://doi.org/10.2172/969740.

[177] J.E. Talia, F. Povolo, Tensile properties of Zircaloy-4, J. Nucl. Mater. 67 (1977) 198–206. https://doi.org/10.1016/0022-3115(77)90174-X.

[178] K.L. Johnson, Contact Mechanics, Cambridge University Press, 1985. https://doi.org/10.1017/CBO9781139171731.

[179] S.P. Marsh, LASL Shock Hugoniot Data, University of California Press, Berkeley, CA, 1980.

[180] J.G. Callanan, D.T. Martinez, S. Ricci, B.K. Derby, K.J. Hollis, S.J. Fensin, D.R. Jones, Spall strength of additively repaired 304L stainless steel, J. Appl. Phys. 134 (2023) 245102. https://doi.org/10.1063/5.0177097.

[181] D.R. Jones, S.J. Fensin, C.P. Trujillo, D.T. Martinez, G.T. Gray, Stress and Strain Rate Effects on Incipient Spall in Tantalum, EPJ Web Conf. 183 (2018) 03021. https://doi.org/10.1051/epjconf/201818303021.

[182] G.J. Appleby-Thomas, A. Hameed, R. Vignjevic, P.J. Hazell, J. Painter, S. Cademartori, On the dynamic tensile strength of Zirconium, J. Phys. Conf. Ser. 500 (2014) 112004. https://doi.org/10.1088/1742-6596/500/11/112004.

[183] P.A. Rigg, R.A. Saavedra, R.J. Scharff, Sound speed measurements in zirconium using the front surface impact technique, J. Phys. Conf. Ser. 500 (2014) 032014. https://doi.org/10.1088/1742-6596/500/3/032014.

[184] E.B. Zaretsky, G.I. Kanel, The high temperature impact response of tungsten and chromium, J. Appl. Phys. 122 (2017) 115901. https://doi.org/10.1063/1.4997674.

[185] P.A. Zinkovich, A.P. Rudoi, P.G. Yakovenko, Impact strength of chromium and chromium-base alloys, Met. Sci. Heat Treat. 36 (1994) 426–428. https://doi.org/10.1007/BF01395227.

[186] P.S. Komarov, E.V. Struleva, S.I. Ashitkov, Generation of giant elastic ultrashort shock waves in chromium films by femtosecond laser pulses, J. Phys. Conf. Ser. 1147 (2019) 012023. https://doi.org/10.1088/1742-6596/1147/1/012023.

[187] M. Yaghoobi, G.Z. Voyiadjis, The effects of temperature and strain rate in fcc and bcc metals during extreme deformation rates, Acta Mater. 151 (2018) 1–10. https://doi.org/10.1016/j.actamat.2018.03.029.

[188] R.V. Umretiya, B. Elward, D. Lee, M. Anderson, R.B. Rebak, J.V. Rojas, Mechanical and chemical properties of PVD and cold spray Cr-coatings on Zircaloy-4, J. Nucl. Mater. 541 (2020) 152420. https://doi.org/10.1016/j.jnucmat.2020.152420.

[189] D. Kamerman, F. Cappia, K. Wheeler, P. Petersen, E. Rosvall, T. Dabney, H. Yeom, K. Sridharan, M. Ševeček, J. Schulthess, Development of axial and ring hoop tension testing methods for nuclear fuel cladding tubes, Nucl. Mater. Energy 31 (2022) 101175. https://doi.org/10.1016/j.nme.2022.101175.

[190] M. Ševeček, J. Krejčí, M.H. Shahin, J. Petrik, R.G. Ballinger, K. Shirvan, FATIGUE BEHAVIOR OF COLD SPRAY-COATED ACCIDENT TOLERANT CLADDING, (n.d.).

[191] M. Ševeček, A. Gurgen, A. Seshadri, Y. Che, M. Wagih, B. Phillips, V. Champagne, K. Shirvan, Development of Cr cold spray–coated fuel cladding with enhanced accident tolerance, Nucl. Eng. Technol. 50 (2018) 229–236. https://doi.org/10.1016/j.net.2017.12.011.

[192] J.L. Walters, J.E. Romero, A.J. Mueller, B.R. Maier, J.M. Partezana, J.L. Lyons, W.A. Byers, G. Wang, A. Parsi, R.S. Stiteler, M. Limbäck, Effects of Cold Spray Chromium Coatings on the Properties of Zirconium Alloys, in: Zircon. Nucl. Ind. 19th Int. Symp., ASTM International100 Barr Harbor Drive, PO Box C700, West Conshohocken, PA 19428-2959, 2021: pp. 211–231. https://doi.org/10.1520/STP162220190065.

[193] M. Grujicic, C.L. Zhao, W.S. DeRosset, D. Helfritch, Adiabatic shear instability based mechanism for particles/substrate bonding in the cold-gas dynamic-spray process, Mater. Des. 25 (2004) 681–688. https://doi.org/10.1016/j.matdes.2004.03.008.

[194] H. Assadi, F. Gärtner, T. Klassen, H. Kreye, Comment on 'Adiabatic shear instability is not necessary for adhesion in cold spray,' Scr. Mater. 162 (2019) 512–514. https://doi.org/10.1016/j.scriptamat.2018.10.036.

[195] M.R. Rokni, S.R. Nutt, C.A. Widener, V.K. Champagne, R.H. Hrabe, Review of Relationship Between Particle Deformation, Coating Microstructure, and Properties in High-Pressure Cold Spray, J. Therm. Spray Technol. 26 (2017) 1308–1355. https://doi.org/10.1007/s11666-017-0575-0.

[196] K. Kim, M. Watanabe, S. Kuroda, Bonding mechanisms of thermally softened metallic powder particles and substrates impacted at high velocity, Surf. Coat. Technol. 204 (2010) 2175–2180. https://doi.org/10.1016/j.surfcoat.2009.12.001.

[197] W. Li, C. Cao, S. Yin, Solid-state cold spraying of Ti and its alloys: A literature review, Prog. Mater. Sci. 110 (2020) 100633. https://doi.org/10.1016/j.pmatsci.2019.100633.

[198] X.-T. Luo, C.-X. Li, F.-L. Shang, G.-J. Yang, Y.-Y. Wang, C.-J. Li, High velocity impact induced microstructure evolution during deposition of cold spray coatings: A review, Surf. Coat. Technol. 254 (2014) 11–20. https://doi.org/10.1016/j.surfcoat.2014.06.006.

[199] R.J. Mccabe, D.F. Teter, Analysis of recrystallized volume fractions in uranium using electron backscatter diffraction, J. Microsc. 223 (2006) 33–39. https://doi.org/10.1111/j.1365-2818.2006.01595.x.

[200] J.I. Omale, E.G. Ohaeri, A.A. Tiamiyu, M. Eskandari, K.M. Mostafijur, J.A. Szpunar, Microstructure, texture evolution and mechanical properties of X70 pipeline steel after different thermomechanical treatments, Mater. Sci. Eng. A 703 (2017) 477–485. https://doi.org/10.1016/j.msea.2017.07.086.

[201] T. Yeo, N. Shigematsu, T. Katori, Dynamically recrystallized grains identified via the application of Gaussian mixture model to EBSD data, J. Struct. Geol. 167 (2023) 104800. https://doi.org/10.1016/j.jsg.2023.104800.

[202] A. Ayad, M. Ramoul, A.D. Rollett, F. Wagner, Quantifying primary recrystallization from EBSD maps of partially recrystallized states of an IF steel, Mater. Charact. 171 (2021) 110773. https://doi.org/10.1016/j.matchar.2020.110773.

[203] T. Schmidt, F. Gaertner, H. Kreye, New Developments in Cold Spray Based on Higher Gas and Particle Temperatures, J. Therm. Spray Technol. 15 (2006) 488–494. https://doi.org/10.1361/105996306X147144.

[204] L.L. Shaw, Surface Nanocrystallization and Hardening (SNH), in: Q.J. Wang, Y.-W. Chung (Eds.), Encycl. Tribol., Springer US, Boston, MA, 2013: pp. 3455–3464. https://doi.org/10.1007/978-0-387-92897-5_1163.

[205] S. Bagherifard, R. Ghelichi, M. Guagliano, Numerical and experimental analysis of surface roughness generated by shot peening, Appl. Surf. Sci. 258 (2012) 6831–6840. https://doi.org/10.1016/j.apsusc.2012.03.111.

[206] R.K. Kumar, P. SampathKumaran, S. Seetharamu, S.A. Kumar, T. Pramod, G.J. Naveen, Investigation of Shot Peening Effect on Titanium Alloy Affecting Surface Residual Stress and

Roughness for Aerospace Applications, Procedia Struct. Integr. 14 (2019) 134–141. https://doi.org/10.1016/j.prostr.2019.05.018.

[207] Y.G. Liu, M.Q. Li, H.J. Liu, Nanostructure and surface roughness in the processed surface layer of Ti-6Al-4V via shot peening, Mater. Charact. 123 (2017) 83–90. https://doi.org/10.1016/j.matchar.2016.11.020.

[208] M. Taro, T. Chaise, D. Nélias, A methodology to predict the roughness of shot peened surfaces, J. Mater. Process. Technol. 217 (2015) 65–76. https://doi.org/10.1016/j.jmatprotec.2014.10.016.

[209] O. Unal, Optimization of shot peening parameters by response surface methodology, Surf. Coat. Technol. 305 (2016) 99–109. https://doi.org/10.1016/j.surfcoat.2016.08.004.

[210] S. Yang, W. Zeng, J. Yang, Characterization of shot peening properties and modelling on the fatigue performance of 304 austenitic stainless steel, Int. J. Fatigue 137 (2020) 105621. https://doi.org/10.1016/j.ijfatigue.2020.105621.

[211] L. Zhu, Y. Guan, Y. Wang, Z. Xie, J. Lin, J. Zhai, Influence of process parameters of ultrasonic shot peening on surface roughness and hydrophilicity of pure titanium, Surf. Coat. Technol. 317 (2017) 38–53. https://doi.org/10.1016/j.surfcoat.2017.03.044.

[212] H. Chen, S. Wang, S. Lu, Y. Qiao, X. Wang, N. Fan, P. Guo, J. Niu, Simulation and experimental validation of residual stress and surface roughness of high manganese steel after shot peening, Procedia CIRP 71 (2018) 227–231. https://doi.org/10.1016/j.procir.2018.05.066.

[213] A.C. Karaoglanli, K.M. Doleker, B. Demirel, A. Turk, R. Varol, Effect of shot peening on the oxidation behavior of thermal barrier coatings, Appl. Surf. Sci. 354 (2015) 314–322. https://doi.org/10.1016/j.apsusc.2015.06.113.

[214] J.-J. Tian, Y.-K. Wei, C.-X. Li, G.-J. Yang, C.-J. Li, Effect of Post-spray Shot Peening Treatment on the Corrosion Behavior of NiCr-Mo Coating by Plasma Spraying of the Shell–Core–Structured Powders, J. Therm. Spray Technol. 27 (2018) 232–242. https://doi.org/10.1007/s11666-017-0659-x.

[215] K.M. Doleker, A.C. Karaoglanli, Comparison of Oxidation Behavior of Shot-Peened Plasma Spray Coatings with Cold Gas Dynamic Spray Coatings, Oxid. Met. 88 (2017) 121–132. https://doi.org/10.1007/s11085-016-9691-3.

[216] S.V. Klinkov, V.F. Kosarev, Measurements of Cold Spray Deposition Efficiency, J. Therm. Spray Technol. 15 (2006) 364–371. https://doi.org/10.1361/105996306X124365.

[217] S. Yin, J. Cizek, J. Cupera, M. Hassani, X. Luo, R. Jenkins, Y. Xie, W. Li, R. Lupoi, Formation conditions of vortex-like intermixing interfaces in cold spray, Mater. Des. 200 (2021) 109444. https://doi.org/10.1016/j.matdes.2020.109444.

[218] R.E. Stoller, M.B. Toloczko, G.S. Was, A.G. Certain, S. Dwaraknath, F.A. Garner, On the use of SRIM for computing radiation damage exposure, Nucl. Instrum. Methods Phys. Res. Sect. B Beam Interact. Mater. At. 310 (2013) 75–80. https://doi.org/10.1016/j.nimb.2013.05.008.

[219] B.C. Sousa, M. Aindow, S.-W. Lee, D. Lados, A.G. Spangenberger, C.M. Sample, D.L. Cote, Characterization of cold-sprayed material consolidations, in: Adv. Cold Spray, Elsevier, 2023: pp. 205–298. https://doi.org/10.1016/B978-0-08-103015-8.00002-5.

[220] J. Schemel, ASTM Manual on Zirconium and Hafnium, ASTM International100 Barr Harbor Drive, PO Box C700, West Conshohocken, PA 19428-2959, 1977. https://doi.org/10.1520/STP639-EB.

[221] G.M. Pharr, E.G. Herbert, Y. Gao, The Indentation Size Effect: A Critical Examination of Experimental Observations and Mechanistic Interpretations, Annu. Rev. Mater. Res. 40 (2010) 271–292. https://doi.org/10.1146/annurev-matsci-070909-104456.

[222] P. Lafaye, C. Toffolon-Masclet, J.-C. Crivello, J.-M. Joubert, Experimental study, first-principles calculation and thermodynamic modelling of the Cr–Fe–Nb–Sn–Zr quinary system for application as cladding materials in nuclear reactors., J. Nucl. Mater. 544 (2021) 152692. https://doi.org/10.1016/j.jnucmat.2020.152692.

[223] B. Sundman, B. Jansson, J.-O. Andersson, The Thermo-Calc Databank System, CALPHAD 9 (1985) 153–190. https://doi.org/10.1016/0364-5916(85)90021-5.

[224] G.S. Was, Fundamentals of Radiation Materials Science, Springer New York, New York, NY, 2017. https://doi.org/10.1007/978-1-4939-3438-6.
[225] G.M. Hood, Point Defect Properties of a-Zr and their Influence on Irradiation Behaviour of Zr Alloys, Atomic Energy of Canada Limited, Chalk River Nuclear Laboratories, 1977.
[226] M. Griffiths, R.W. Gilbert, G.J.C. Carpenter, Phase instability, decomposition and redistribution of intermetallic precipitates in Zircaloy-2 and -4 during neutron irradiation, J. Nucl. Mater. 150 (1987) 53–66. https://doi.org/10.1016/0022-3115(87)90093-6.
[227] H. Okamoto, Supplemental Literature Review of Binary Phase Diagrams: B-Fe, Cr-Zr, Fe-Np, Fe-W, Fe-Zn, Ge-Ni, La-Sn, La-Ti, La-Zr, Li-Sn, Mn-S, and Nb-Re, J. Phase Equilibria Diffus. 37 (2016) 621–634. https://doi.org/10.1007/s11669-016-0465-z.
[228] D. Goldbaum, R.R. Chromik, N. Brodusch, R. Gauvin, Microstructure and Mechanical Properties of Ti Cold-Spray Splats Determined by Electron Channeling Contrast Imaging and Nanoindentation Mapping, Microsc. Microanal. 21 (2015) 570–581. https://doi.org/10.1017/S1431927615000240.
[229] S. Julie, K. Mariappan, C. David, N.P. Wasekar, V. Shankar, A study on the competition and synergy between irradiation and temperature on the texture and recrystallization of nanocrystalline nickel, Appl. Surf. Sci. 638 (2023) 158085. https://doi.org/10.1016/j.apsusc.2023.158085.
[230] D. Kaoumi, A.T. Motta, R.C. Birtcher, Grain Growth in Nanocrystalline Metal Thin Films under In Situ Ion-Beam Irradiation, J. ASTM Int. 4 (2007) 206–218. https://doi.org/10.1520/JAI100743.
[231] J. Zhou, M.I. Islam, S. Guo, Y. Zhang, F. Lu, Radiation-Induced Grain Growth of Nanocrystalline Al $_x$ CoCrFeNi High-Entropy Alloys, J. Phys. Chem. C 125 (2021) 3509–3516. https://doi.org/10.1021/acs.jpcc.0c09061.
[232] Annealing, in: Phys. Metall. Princ., 4th ed, SI, Cengage Learning, Stamford, 2010: pp. 216–260.
[233] T. Dabney, K.N. Sasidhar, H. Yeom, Y. Miao, K. Mo, L. Jamison, K. Sridharan, In situ synchrotron investigation of tensile deformation and failure mechanisms in cold spray Cr-coated Zr-alloy system, Mater. Des. 239 (2024) 112755. https://doi.org/10.1016/j.matdes.2024.112755.
[234] H. Yeom, T. Dabney, N. Pocquette, K. Ross, F.E. Pfefferkorn, K. Sridharan, Cold spray deposition of 304L stainless steel to mitigate chloride-induced stress corrosion cracking in canisters for used nuclear fuel storage, J. Nucl. Mater. 538 (2020) 152254. https://doi.org/10.1016/j.jnucmat.2020.152254.
[235] D. Arias, J.P. Abriata, The Cr−Zr (Chromium-Zirconium) system, Bull. Alloy Phase Diagr. 7 (1986) 237–244. https://doi.org/10.1007/BF02868997.
[236] H. Liu, Y. Shen, S. Yang, P. Zheng, L. Zhang, A comprehensive solution to miniaturized tensile testing: Specimen geometry optimization and extraction of constitutive behaviors using inverse FEM procedure, Fusion Eng. Des. 121 (2017) 188–197. https://doi.org/10.1016/j.fusengdes.2017.07.016.
[237] M.R. Daymond, The determination of a continuum mechanics equivalent elastic strain from the analysis of multiple diffraction peaks, J. Appl. Phys. 96 (2004) 4263–4272. https://doi.org/10.1063/1.1794896.
[238] V. Valvoda, M. Järvinen, On The Harris Texture Index, Powder Diffr. 5 (1990) 200–203. https://doi.org/10.1017/S0885715600015797.
[239] T. Ungár, A. Borbély, The effect of dislocation contrast on x-ray line broadening: A new approach to line profile analysis, Appl. Phys. Lett. 69 (1996) 3173–3175. https://doi.org/10.1063/1.117951.
[240] T. Ungár, Á.;. Révész, A. Borbély, Dislocations and Grain Size in Electrodeposited Nanocrystalline Ni Determined by the Modified Williamson–Hall and Warren–Averbach Procedures, J. Appl. Crystallogr. 31 (1998) 554–558. https://doi.org/10.1107/S0021889897019559.
[241] I.C. Dragomir, A. Borbély, T. Ungár, Contrast Factors and Character of Dislocations in Cubic and Hexagonal Crystals, Mater. Sci. Forum 443–444 (2004) 95–98.

[242] T. Ungár, I. Dragomir, Á. Révész, A. Borbély, The contrast factors of dislocations in cubic crystals: the dislocation model of strain anisotropy in practice, J. Appl. Crystallogr. 32 (1999) 992–1002. https://doi.org/10.1107/S0021889899009334.

[243] W.F. Gale, T.C. Totemeier, Elastic properties, damping capacity and shape memory alloys, in: Smithells Met. Ref. Book, Eighth, Elsevier, 2004: pp. 15–2.

[244] E28 Committee, Test Methods for Tension Testing of Metallic Materials, ASTM International, n.d. https://doi.org/10.1520/E0008_E0008M-22.

[245] O.N. Pierron, D.A. Koss, A.T. Motta, Tensile specimen geometry and the constitutive behavior of Zircaloy-4, J. Nucl. Mater. 312 (2003) 257–261. https://doi.org/10.1016/S0022-3115(02)01554-4.

[246] M.N. Gussev, J.T. Busby, K.G. Field, M.A. Sokolov, S.E. Gray, Role of Scale Factor During Tensile Testing of Small Specimens, in: M.A. Sokolov, E. Lucon (Eds.), Small Specim. Test Tech. 6th Vol., ASTM International, 100 Barr Harbor Drive, PO Box C700, West Conshohocken, PA 19428-2959, 2014: pp. 1–19. https://doi.org/10.1520/STP157620140013.

[247] C.P. Massey, N. Bibhanshu, M.N. Gussev, C.J. Havrilak, A.T. Nelson, Deformation and fracture characteristics of zirconium plate produced via ultrasonic additive manufacturing, J. Mater. Res. 37 (2022) 236–246. https://doi.org/10.1557/s43578-021-00380-6.

[248] C.P. Massey, C.J. Havrilak, M.N. Gussev, K.A. Terrani, A.T. Nelson, Ultrasonic additive manufacturing of zirconium: Pilot results, Mater. Lett. 302 (2021) 130330. https://doi.org/10.1016/j.matlet.2021.130330.

[249] N. Mozzani, Q. Auzoux, D. Le Boulch, E. Andrieu, C. Blanc, C.P. Scott, N. Barnel, Mechanical behavior of recrystallized Zircaloy-4 under monotonic loading at room temperature: Tests and simplified anisotropic modeling, J. Nucl. Mater. 447 (2014) 94–106. https://doi.org/10.1016/j.jnucmat.2014.01.003.

[250] H. Li, G. Sun, W. Woo, J. Gong, B. Chen, Y. Wang, Y.Q. Fu, C. Huang, L. Xie, S. Peng, Tensile deformation behaviors of Zircaloy-4 alloy at ambient and elevated temperatures: In situ neutron diffraction and simulation study, J. Nucl. Mater. 446 (2014) 134–141. https://doi.org/10.1016/j.jnucmat.2013.12.006.

[251] H. Lee, K. Kim, J.-S. Kim, Y.-S. Kim, Effects of hydride precipitation on the mechanical property of cold worked zirconium alloys in fully recrystallized condition, Nucl. Eng. Technol. 52 (2020) 352–359. https://doi.org/10.1016/j.net.2019.07.032.

[252] M. Kim, F. Rickhey, H. Lee, N. Kim, Analytical determination of forming limit curve for zirlo and its experimental validation, J. Manuf. Process. 23 (2016) 122–129. https://doi.org/10.1016/j.jmapro.2016.06.006.

[253] F. Xu, R.A. Holt, M.R. Daymond, Modeling lattice strain evolution during uniaxial deformation of textured Zircaloy-2, Acta Mater. 56 (2008) 3672–3687. https://doi.org/10.1016/j.actamat.2008.04.019.

[254] F. Xu, R.A. Holt, M.R. Daymond, Evidence for basal 〈a〉-slip in Zircaloy-2 at room temperature from polycrystalline modeling, J. Nucl. Mater. 373 (2008) 217–225. https://doi.org/10.1016/j.jnucmat.2007.05.052.

[255] É. Maras, E. Clouet, Secondary slip of screw dislocations in zirconium, Acta Mater. 223 (2022) 117398. https://doi.org/10.1016/j.actamat.2021.117398.

[256] Y. Li, G. Po, Y. Cui, N. Ghoniem, Prismatic-to-basal plastic slip transition in zirconium, Acta Mater. 242 (2023) 118451. https://doi.org/10.1016/j.actamat.2022.118451.

[257] N. Chaari, E. Clouet, D. Rodney, First-Principles Study of Secondary Slip in Zirconium, Phys. Rev. Lett. 112 (2014) 075504. https://doi.org/10.1103/PhysRevLett.112.075504.

[258] O.T. Woo, G.J.C. Carpenter, S.R. MacEWEN, (c)-COMPONENT DISLOCATIONS IN ZIRCONIUM ALLOYS, (n.d.).

[259] E. Tenckhoff, P.L. Rittenhouse, Annealing textures in zircaloy tubing, J. Nucl. Mater. 35 (1970) 14–23. https://doi.org/10.1016/0022-3115(70)90022-X.

[260] R.G. Ballinger, G.E. Lucas, R.M. Pelloux, The effect of plastic strain on the evolution of crystallographic texture in Zircaloy-2, J. Nucl. Mater. 126 (1984) 53–69. https://doi.org/10.1016/0022-3115(84)90532-4.

[261] W. Guo, G. Li, F. Yuan, F. Han, Y. Zhang, M. Ali, J. Ren, G. Yuan, Texture development and mechanical behavior of Zircaloy-4 alloy plates fabricated by cold rolling and annealing, Mater. Sci. Eng. A 807 (2021) 140846. https://doi.org/10.1016/j.msea.2021.140846.

[262] U. Essmann, H. Mughrabi, Annihilation of dislocations during tensile and cyclic deformation and limits of dislocation densities, Philos. Mag. A 40 (1979) 731–756. https://doi.org/10.1080/01418617908234871.

[263] Z. Arabgol, M. Villa Vidaller, H. Assadi, F. Gärtner, T. Klassen, Influence of thermal properties and temperature of substrate on the quality of cold-sprayed deposits, Acta Mater. 127 (2017) 287–301. https://doi.org/10.1016/j.actamat.2017.01.040.

[264] G.N. Devi, A.V. Gopal, S. Kumar, Investigations on inter-splat boundaries of cold sprayed Ni Cr coatings upon high temperature oxidation, Surf. Coat. Technol. 467 (2023) 129691. https://doi.org/10.1016/j.surfcoat.2023.129691.

[265] S. Kumar, B.R. Bodapati, G. Vinay, K. Vamshi Kumar, N.M. Chavan, P. Suresh Babu, A. Jyothirmayi, Estimation of inter-splat bonding and its effect on functional properties of cold sprayed coatings, Surf. Coat. Technol. 420 (2021) 127318. https://doi.org/10.1016/j.surfcoat.2021.127318.

[266] Y. Harada, M. Ohmori, Ductile–brittle transition behavior of rolled chromium, J. Mater. Process. Technol. 153–154 (2004) 93–99. https://doi.org/10.1016/j.jmatprotec.2004.04.011.

[267] R.W. Armstrong, S.M. Walley, High strain rate properties of metals and alloys, Int. Mater. Rev. 53 (2008) 105–128. https://doi.org/10.1179/174328008X277795.

[268] Y. Lu, W.-Z. Han, Pre-stored edge dislocations-enabled pseudo-toughness in chromium, Acta Mater. 248 (2023) 118788. https://doi.org/10.1016/j.actamat.2023.118788.

[269] C. Ren, Z.Z. Fang, M. Koopman, B. Butler, J. Paramore, S. Middlemas, Methods for improving ductility of tungsten - A review, Int. J. Refract. Met. Hard Mater. 75 (2018) 170–183. https://doi.org/10.1016/j.ijrmhm.2018.04.012.

[270] F.C. Campbell, Recovery, Recrystallization, and Grain Growth, in: Elem. Metall. Eng. Alloys, A S M International, Materials Park, UNITED STATES, 2008. http://ebookcentral.proquest.com/lib/wisc/detail.action?docID=3002354.

[271] C.R. Brinkman, C.H. Pitt, The recrystallization of 99.997% chromium, J. Common Met. 11 (1966) 323–341. https://doi.org/10.1016/0022-5088(66)90065-8.

[272] E.T. Hayes, Malleable Chromium and Its Alloys, (n.d.).

[273] S.T.M. Johnstone, F. Henderson, H.L. Wain, Recrystallization and the Ductility of Chromium, Nature 180 (1957) 806–806. https://doi.org/10.1038/180806a0.

[274] J. Ast, M. Ghidelli, K. Durst, M. Göken, M. Sebastiani, A.M. Korsunsky, A review of experimental approaches to fracture toughness evaluation at the micro-scale, Mater. Des. 173 (2019) 107762. https://doi.org/10.1016/j.matdes.2019.107762.

[275] D. Rajpoot, P. Tandaiya, R.L. Narayan, U. Ramamurty, Size effects and failure regimes in notched micro-cantilever beam fracture, Acta Mater. 234 (2022) 118041. https://doi.org/10.1016/j.actamat.2022.118041.

[276] J.-C. Brachet, E. Rouesne, J. Ribis, T. Guilbert, S. Urvoy, G. Nony, C. Toffolon-Masclet, M. Le Saux, N. Chaabane, H. Palancher, A. David, J. Bischoff, J. Augereau, E. Pouillier, High temperature steam oxidation of chromium-coated zirconium-based alloys: Kinetics and process, Corros. Sci. 167 (2020) 108537. https://doi.org/10.1016/j.corsci.2020.108537.

[277] M. Moalem, D.R. Olander, Oxidation of Zircaloy by steam, J. Nucl. Mater. 182 (1991) 170–194. https://doi.org/10.1016/0022-3115(91)90428-A.

[278] R.E. Pawel, Oxygen diffusion in beta zircaloy during steam oxidation, J. Nucl. Mater. 50 (1974) 247–258. https://doi.org/10.1016/0022-3115(74)90095-6.

[279] M. Steinbrück, High-temperature reaction of oxygen-stabilized α-Zr(O) with nitrogen, J. Nucl. Mater. 447 (2014) 46–55. https://doi.org/10.1016/j.jnucmat.2013.12.024.

[280] C. Brunner, H. Hutter, K. Piplits, P. Wilhartitz, R. Stroosnijder, M. Grasserbauer, Investigation of the synthesis and internal structure of protective oxide layers on high-purity chromium with SIMS scanning techniques, Fresenius J. Anal. Chem. 358 (1997) 233–236. https://doi.org/10.1007/s002160050392.

[281] C. Brunner, H. Hutter, P. Wilhartitz, M. Grasserbauer, Investigation of the formation and properties of protective oxide layers on high purity chromium with SIMS imaging techniques, Mikrochim. Acta 125 (1997) 69–72. https://doi.org/10.1007/BF01246164.

[282] H.-G. Kim, I.-H. Kim, J.-Y. Park, Y.-H. Koo, Application of Coating Technology on Zirconium-Based Alloy to Decrease High-Temperature Oxidation, in: B. Comstock, P. Barberis (Eds.), Zircon. Nucl. Ind. 17th Vol., ASTM International, 100 Barr Harbor Drive, PO Box C700, West Conshohocken, PA 19428-2959, 2015: pp. 346–369. https://doi.org/10.1520/STP154320120161.

[283] E.W.A. Young, J.H. Gerretsen, The Oxygen Partial PressureDependenceof the Defect Structure of Chromium(Ill)Oxide, (1987).

[284] X. Hu, C. Dong, Q. Wang, B. Chen, H. Yang, T. Wei, R. Zhang, W. Gu, D. Chen, High-temperature oxidation of thick Cr coating prepared by arc deposition for accident tolerant fuel claddings, J. Nucl. Mater. 519 (2019) 145–156. https://doi.org/10.1016/j.jnucmat.2019.01.039.

[285] N.K. Othman, N. Othman, J. Zhang, D.J. Young, Effects of water vapour on isothermal oxidation of chromia-forming alloys in Ar/O2 and Ar/H2 atmospheres, Corros. Sci. 51 (2009) 3039–3049. https://doi.org/10.1016/j.corsci.2009.08.032.

[286] M. Hansel, W.J. Quadakkers, D.J. Young, Role of Water Vapor in Chromia-Scale Growth at Low Oxygen Partial Pressure, (n.d.).

[287] L. Mikkelsen, S. Linderoth, High temperature oxidation of Fe–Cr alloy in O2–H2–H2O atmospheres; microstructure and kinetics, Mater. Sci. Eng. A 361 (2003) 198–212. https://doi.org/10.1016/S0921-5093(03)00527-6.

[288] V.A. Zuyok, Yu.I. Kovalenko, V.V. Shtefan, R.O. Rud, M.V. Tretiakov, Ya.O. Kushtym, Corrosion Resistance of Traditional and Advanced Fuel Rod Cladding Materials for Water-Cooled Reactors, Prog. Phys. Met. 25 (2024) 243–275. https://doi.org/10.15407/ufm.25.02.243.

[289] A.T. Motta, A. Couet, R.J. Comstock, Corrosion of Zirconium Alloys Used for Nuclear Fuel Cladding, Annu. Rev. Mater. Res. 45 (2015) 311–343. https://doi.org/10.1146/annurev-matsci-070214-020951.

[290] J. Bischoff, C. Vauglin, C. Delafoy, P. Barberis, D. Perche, B. Guerin, Development of Cr-coated Zirconium Alloy Cladding for Enhanced Accident Tolerance, in: Topfuel 2016, Boise, ID, 2016.

[291] E. Hillner, J.N. Chirigos, THE EFFECT OF LITHIUM HYDROXIDE AND RELATED SOLUTIONS ON THE CORROSION RATE OF ZIRCALOY IN 680 F WATER, Westinghouse Electric Corporation, Pittsburgh, PA, 1962. https://www.osti.gov/biblio/4747690.

[292] T.R. Allen, R.J.M. Konings, A.T. Motta, Corrosion of Zirconium Alloys, in: Compr. Nucl. Mater., Elsevier, 2012: pp. 49–68. https://doi.org/10.1016/B978-0-08-056033-5.00063-X.

[293] D.E. Janney, D.L. Porter, Characterization of phases in ‘crud’ from boiling-water reactors by transmission electron microscopy, J. Nucl. Mater. 362 (2007) 104–115. https://doi.org/10.1016/j.jnucmat.2006.11.009.

[294] M. Le Calvar, Corrosion issues in pressurized water reactor (PWR) systems, in: Nucl. Corros. Sci. Eng., Elsevier Science & Technology, San Diego, UNITED KINGDOM, 2012. http://ebookcentral.proquest.com/lib/wisc/detail.action?docID=1584634.

[295] Y.L. Sandler, Structure of PWR Primary Corrosion Products, Corrosion 35 (1979) 205–208. https://doi.org/10.5006/0010-9312-35.5.205.

[296] J.-F. Parisot, France, eds., Corrosion and alteration of nuclear materials, Editions le Moniteur, for the Commissariat à l’énergie atomique et aux énergies alternatives, Paris, 2010.

[297] M. Catti, G. Sandrone, G. Valerio, R. Dovesi, Electronic, magnetic and crystal structure of Cr 2 O 3 by theoretical methods, J. Phys. Chem. Solids 57 (1996) 1735–1741. https://doi.org/10.1016/0022-3697(96)00034-0.

[298] I.C. Dragomir, T. Ungár, Contrast factors of dislocations in the hexagonal crystal system, J. Appl. Crystallogr. 35 (2002) 556–564. https://doi.org/10.1107/S0021889802009536.

[299] G. Sundararajan, N.M. Chavan, S. Kumar, The Elastic Modulus of Cold Spray Coatings: Influence of Inter-splat Boundary Cracking, J. Therm. Spray Technol. 22 (2013) 1348–1357. https://doi.org/10.1007/s11666-013-0034-5.

[300] D. Faurie, Determination of elastic constants of a fiber-textured gold film by combining synchrotron x-ray diffraction and in situ tensile testing, J Appl Phys (2023).

[301] W. He, P. Goudeau, E.L. Bourhis, P.-O. Renault, J.C. Dupré, P. Doumalin, S. Wang, Study on Young’s modulus of thin films on Kapton by microtensile testing combined with dual DIC system, Coat. Technol. (2016).

Appendices

Appendix A: Supplementary information for single particle impact tests

For the spraying of Cr particles on the Zry-4 substrate (i.e., the Cr-Zr system), EDS was used to distinguish the bonded Cr particles from impact craters on the Zr-alloy substrate surface. For the spraying of Cr particles on the Cr substrate (i.e., the Cr-Cr system), individually bonded particles and craters were counted for each image using ImageJ software. The deposition efficiency was calculated as the ratio of the total number of bonded particles to the total number of bonded particles plus impact craters. Representative SEM/EDS images used for image analysis are shown in Fig. A.1.

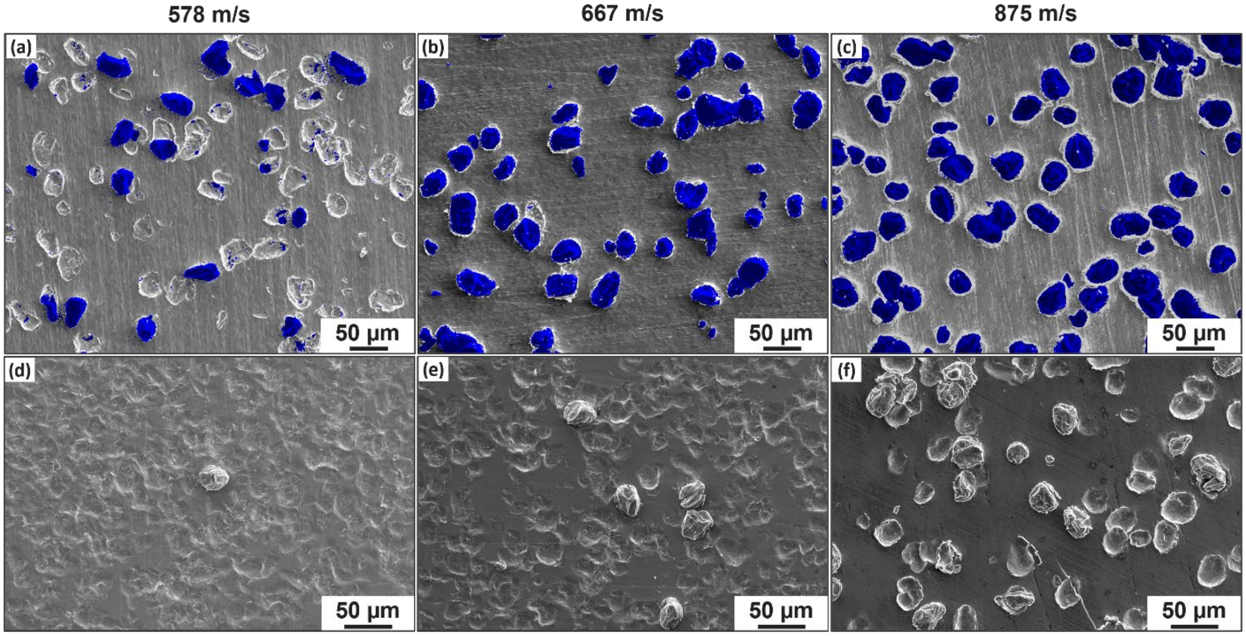

Fig. A.1. SEM images of deposition at 580, 680, and 880 m/s: (a-c) single Cr particle impacts on Zry-4 substrates, with EDS overlay of Cr (blue); (d-f) single Cr particle impacts on pure Cr substrates.

At lower particle velocities ($v_p \sim 580\ m/s$), a number of impact craters on the Zry-4 substrate showed remnants of impacted Cr particles, highlighted in white using EDS mapping (Fig. A.2. a). The higher magnification SEM image of the selected region, shown in Fig. A.2. (b), reveals the morphologies of these unique impact features. Excluding bonded Cr particles and bare impact craters, two notable phenomena were observed: (i) some of the craters contained bonded flakes that detached from the bulk Cr particles, and (ii) some of the craters contained portions of bonded particles that fragmented from the bulk Cr particles. The occurrence of these detached flakes and fragmented particles within craters decreased with increasing impact velocity. It is also worth noting that the number of craters decreased as well due to increase in deposition efficiency.

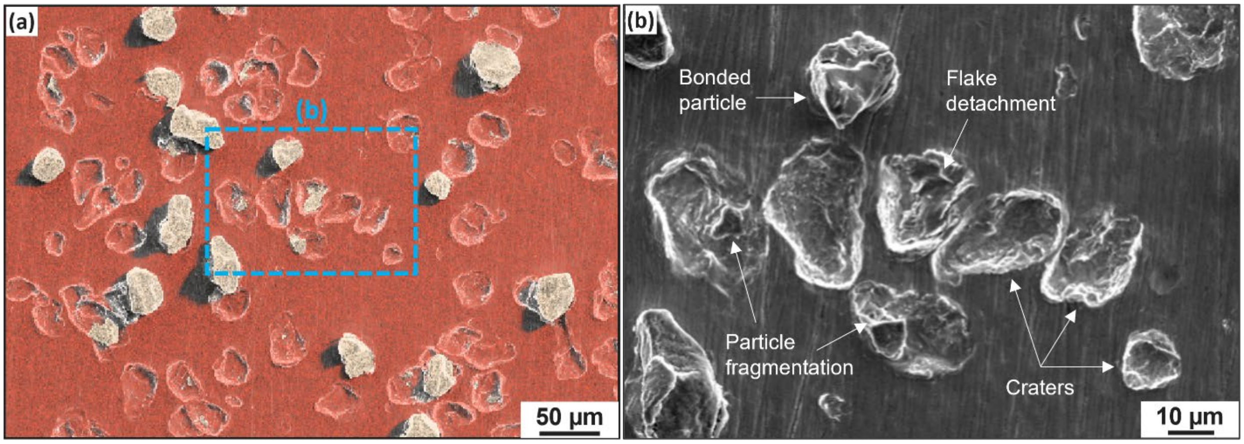

Fig. A.2. Single Cr particle impacts on Zry-4, deposited at 580 m/s: (a) EDS overlay of single Cr particles (white) on Zry-4 (red) substrate, with some Cr particle remnants within craters; (b) Higher magnification SEM image (from 'b' region) with notable impact phenomena labeled.

Cross-sectional SEM imaging and EBSD mapping showed conclusively that the Zry-4 substrate deformed to a higher degree than the Cr particles. Thus, during impact, a higher fraction of kinetic energy was expended in deforming the substrate compared to the particles themselves. Rahmati and Jordoin [119] divided the cold spray process into two parts: first, impact and plastic deformation occur at high strain rates; second, particle rebounding from the substrate occurs at low strain rates due to releasing of elastic energy. In this framework, the Cr particle initially deforms the Zry-4 plastically, causing substrate jetting at high strain rates. However, at lower particle velocities, only incipient/localized jetting around the particle/substrate interface was observed, meaning a larger fraction of the total energy was expended in elastically rebounding the particles [118]. This localized bonding likely occurred more frequently within particles containing more flakes or surface defects – if the propagating pressure wave reaches a flake/defect, that portion of the particle may experience bonding while the rest of the particle may fragment across this interface and rebound. At higher impact velocities, more kinetic energy is spent on jetting across the particle/substrate interface, leading to a higher fraction of metallic contact and metallurgical bonding. This promotes more thorough adhesion of the particle to the substrate and diminishes the effects of elastic rebound forces during high velocity impact.

FEM simulations were performed for a 30 µm Ni particle impacting a SS304 substrate at 500 m/s. The spherical morphology was altered by adding several flakes to the surface of the particle, as shown in the top row of Fig. A.3 (a-c). The maximum elastic and plastic strains were similar between the particles at the end of the impact simulations. One difference observed was the deformation behavior at the interface – the particle without a flake showed deeper penetration into the substrate. It appears the flake acts like a cushion that limits penetration into the substrate. Another difference observed was deformation within the particle, in which the presence of flakes led to increased material being ejected from the particle bulk, which supports the theory of flakes acting as initiation sites for fracture.

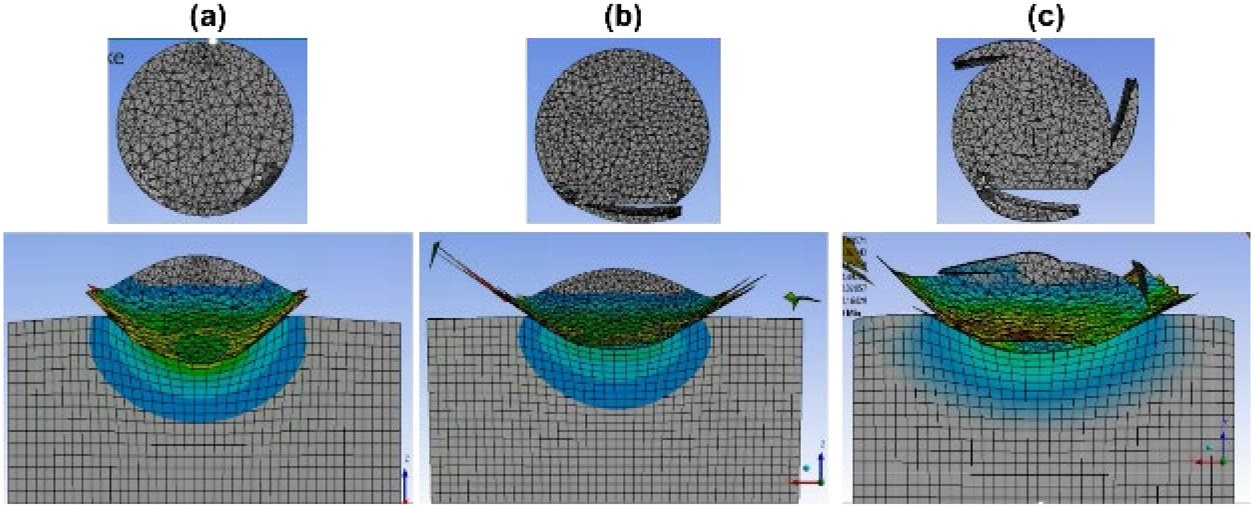

Fig. A.3. FEM simulations of a 30 µm Ni particle impacting a SS304 substrate at 500 m/s impact velocity. The particle morphology before impact (top row) consisted of (a) defect-free, (b) containing one flake, and (c) containing three flakes. The main difference observed during impact was an increase in material ejected from the particle.

The phenomena of flake detachment and particle fragmentation were not observed in the Cr-on-Cr system because the Cr particles deformed more than the bulk Cr substrates. In other words, if the Cr particle did not reach the critical velocity for bonding, the entire particle rebounded from the substrate. Fig. A.4. shows plan-view SEM images of bonded particles deposited at the three particle velocities discussed in

Section 4. One interesting finding was that jetting was not obvious for the particles impacting at lower velocities. Some of the particles (Fig. A.4. b & d) show what appear to be small ejecta in localized areas around the periphery, but others (Fig. A.4. a & c) do not show this feature. Meanwhile, many particles that impacted at the highest velocity (like the one shown in Fig. A.4. e) contained this ejecta, while a select few particles (Fig. A.4. f) showed complete peripheral jetting. In this case, the substrate clearly participates in jetting as indicated by wrinkling/raising of the substrate (blue arrows). This feature was not observed in the lower velocity conditions, indicating the substrate did not participate in jetting to any significant extent (also observed in cross-section in Section 4.1.4, Fig. A.4. a).

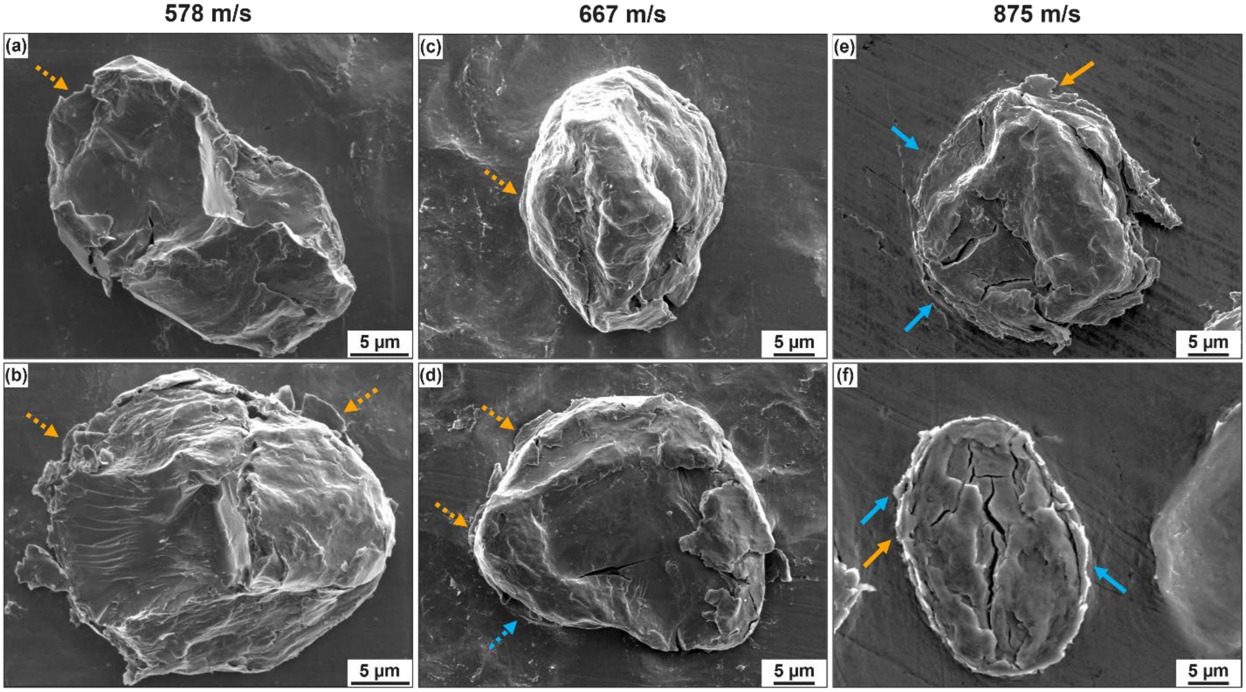

Fig. A.4. SEM images of single Cr particle impact on bulk Cr substrates: (a-b) deposition at 580 m/s; (c-d) deposition at 680 m/s; (e-f) deposition at 880 m/s. The arrows refer to particle jetting (orange) and substrate jetting (blue), with dotted arrows possibly jetting.

Appendix B: Supplementary information for synchrotron diffraction experiment

This section contains supplementary information pertinent to Section 7. Table B.1., B.2., and B.3. contain materials parameters used for calculating contrast factors for the cold spray Cr coatings and ZIRLO^{TM} substrates, taken from the references included in the table captions.

Table B.1. Parameters used in the calculation of contrast factors for Cr coating [242,243].

Parameter	Cr
a (Å)	2.884
c11 (GPa)	346
c44 (GPa)	100
c12 (GPa)	66.0
A_i = 2*c44/(c11-c12)	0.714
c12/c44	0.660
$\bar{C}_{h00,s}$	0.140
$\bar{C}_{h00,e}$	0.138
q_s	1.409
q_e	-1.533

Table B.2. Materials constants obtained for ZIRLO^{TM} substrates [174].

Parameter	Zr
a (Å)	3.239
c (Å)	5.156
c11 (GPa)	145.5
c33 (GPa)	168
c44 (GPa)	26.6
c12 (GPa)	71.3
c13 (GPa)	71.8

Table B.3. Parameters used in the calculation of contrast Burgers factors for ZIRLO^{TM} substrate [298].

Slip System	Burgers Vector Notation	$C_{hk.0}$	q_1	q_2
BE	a	0.813	0.428	-0.416
PrE	a	0.344	-1.184	0.351
PrE2	c	0.045	5.851	-0.270
PrE3	a+c	0.089	3.224	-1.317
PyE	a	0.301	-0.855	0.163
Py2E	a+c	0.084	2.506	-0.359
PyE3	a+c	0.086	3.130	-1.089
PyE4	a+c	0.084	2.759	-0.605
S1	a	0.119	1.436	-1.199
S2	a+c	0.105	0.640	-0.138
S3	c	4.7e-6	2440	-1440

Fig. B.1. shows synchrotron diffraction line profiles of the as-deposited specimen from the beginning (bottom) to the end (top) of tensile straining up to failure. Fig. B.1. (a) shows integrated diffraction profiles from the GE1 detector (direction of tensile straining), and Fig. B.1. (b) shows profiles from the GE2 detector (transverse direction). Five fitted Cr peaks are labeled, and noticeable peak shift and broadening can be observed for {200}, {211}, and {220} peaks. Noticeable peak shift and broadening can be seen in the unlabeled α-Zr peaks as well, indicative of uniform and non-uniform plastic strain, respectively.

Fig. B.2. shows similar synchrotron diffraction line profiles for the annealed specimen in the (a) axial, and (b) transverse, directions. The larger annealed specimen size allowed for more scanning points along the gauge section, and the adjusted beam parameters allowed for higher quality scans. This resulted in a clearer evolution of diffraction peaks in Fig. B.2. (a & b). For example, the (010) α-Zr peak (d~1.89 Å) shows lower intensity peaks shifting to the right with increasing strain (Fig. B.2. a), indicative of tensile strain. Meanwhile, the same lattice plane shows higher intensity peaks shifting to the left with increasing strain (Fig. B.2. b), indicative of compressive strain. Texture evolution was also observed in the annealed ZIRLO substrate. In Fig. B.2. (a), the {200} bcc-Cr peak was observed near the low-intensity (103) α-Zr peak (d~1.46 Å) at the beginning of tensile strain, but this peak quickly subsided into the background due to broadening. Meanwhile, Fig. B.2. (b) showed the same (103) α-Zr peak at higher intensities that remain throughout tensile straining. Peak shifting and broadening caused the {200} bcc-Cr peak and the (103) α-Zr peak to move towards each other as tensile straining increased.

To summarize, Fig. B.1. and Fig. B.2. provide visual examples of the challenges with peak fitting the synchrotron diffraction line profiles at different stages of tensile straining. Care was taken to utilize sophisticated peak separation and fitting techniques to obtain accurate peak information (d-spacing, FWHM, etc.) at all selected peaks at all stages of tensile straining.

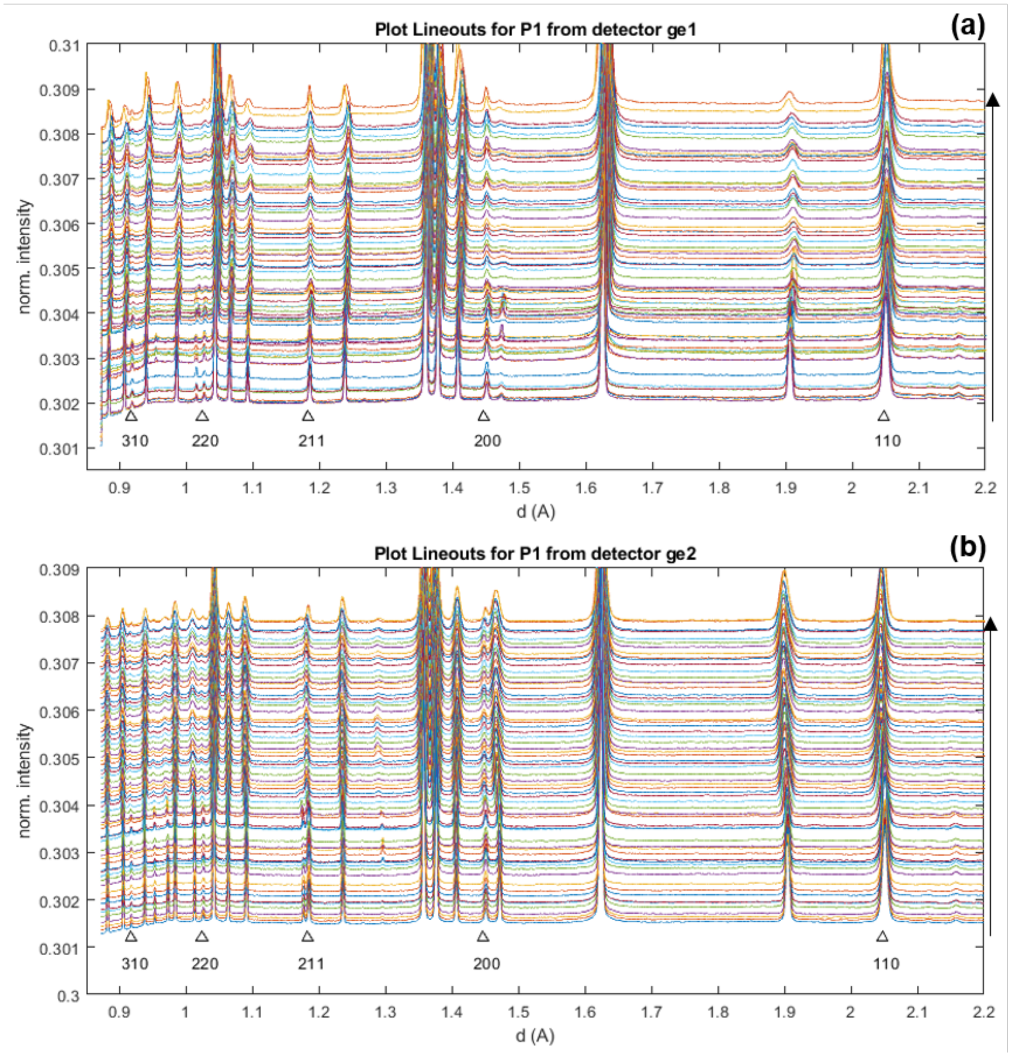

Fig. B.1. Evolution of peak position and peak width for as-deposited sample from beginning of tensile test (bottom of plots) until failure (top of plots), as indicated by the arrow, for (a) GE-1 detector (tensile direction) and (b) GE-2 detector (transverse direction), respectively. The five fitted Cr peaks are labeled. Notice the shift and broadening of the {200}, {220}, and {310} Cr peaks towards the higher-intensity Zr peaks as the applied strain increases.

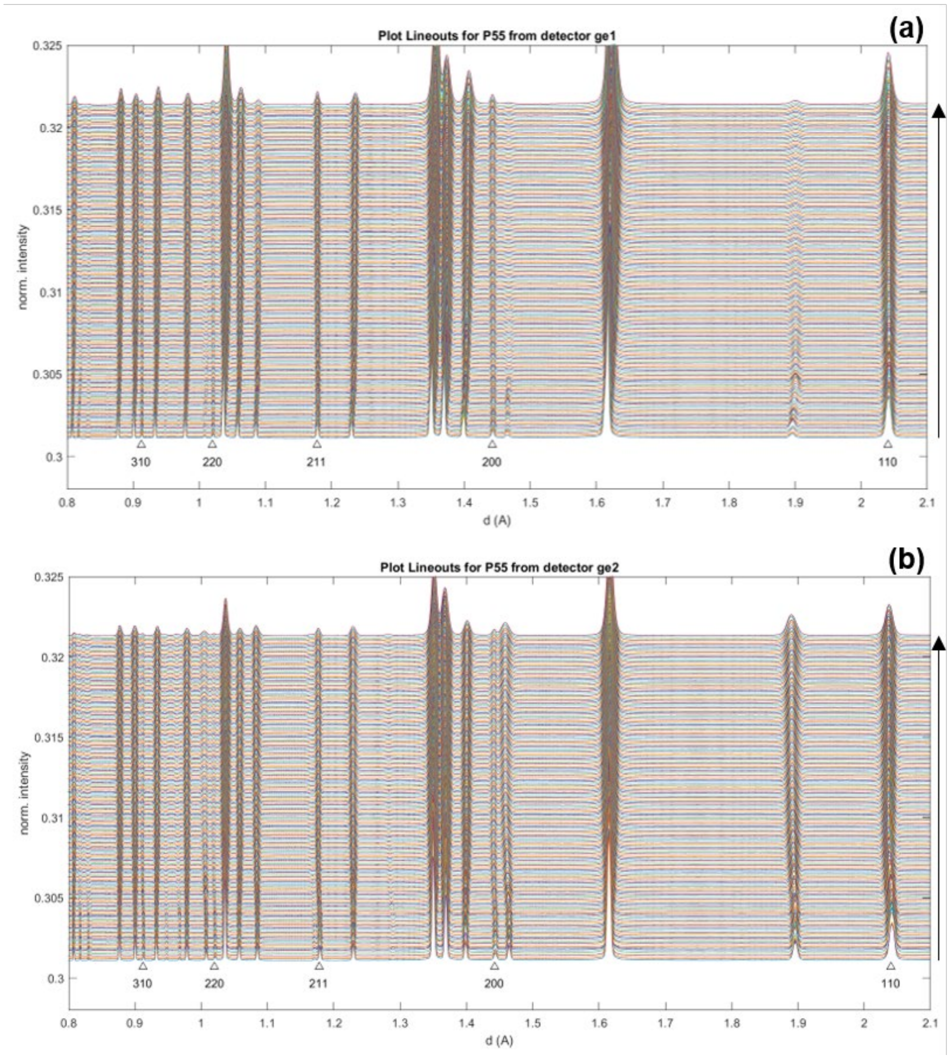

Fig. B.2. Evolution of peak position and peak width for annealed sample from beginning of tensile test (bottom of plots) until failure (top of plots), as indicated by the arrow, for (a) GE-1 detector (axial/tensile direction) and (b) GE-2 detector (transverse direction), respectively. The five fitted Cr peaks are labeled. Notice the shift and broadening of the {200}, {220}, and {310} Cr peaks towards the higher-intensity Zr peaks as the applied strain increases.

Table B.4. and Table B.5. show calculated elastic moduli for certain reflections of Cr and Zr for the as-deposited specimens. The bulk elastic constants for Cr and ZIRLO^{TM} are known to be ~270 GPa [243] and ~95.7 ± 5.4 GPa [174], respectively. In the loading direction, the modulus of the Zr-alloy substrate is within the range of bulk values while the modulus of the cold spray Cr coating is lower. However, the trend in Cr modulus variation across reflections is consistent with values calculated from bulk elastic stiffness constants [243]. While it has been repeatedly shown that the elastic moduli of cold spray coatings are lower as compared to their bulk material counterparts [299], most experiments completely exclude the substrate effects and assess the elastic properties of the free-standing cold spray deposit. Although it is possible to use the lattice strains measured by synchrotron in combination with texture analysis [300,301], this was not performed as was not the focus of this study.

Table B.4. Elastic moduli for certain reflections of Cr and Zr for the as-deposited specimens (units: GPa).

Reflection	{110}	{200}	{211}	{220}	{310}
Cr, As-Dep. (ε_{yy})	103	144	104	107	126
Cr, Anneal (ε_{yy})	125	143	130	134	139
Cr, Calculated	268	298	268	268	287
Reflection	{010}	{110}	{210}	{211}	{320}
Zr, As-Dep. (ε_{yy})	114	99.6	91.1	99.6	115
Zr, Anneal (ε_{yy})	92.6	93.3	89.6	95.7	96.1

Table B.5. List of Harris Texture Index, T_{hkl}, calculated using Eqn. 7.6 for certain reflections of the Zr-alloy substrate. These values were calculated from diffraction measurements made at the start of the tensile test (i.e., just before straining); thus, they represent the texture of the material in its as-fabricated or as-annealed state. Values closer to 1 indicate a random orientation of crystallites.

Reflection	{010}	{110}	{210}	{011}	{020}	{211}	{120}
As-Deposited	0.96	0.34	0.06	1.14	0.97	0.48	4.08
Annealed	0.86	0.42	0.12	1.64	1.11	0.62	2.79
Reflection	{220}	{320}	{021}	{121}	{221}	{030}	{321}
As-Deposited	0.14	0.82	0.23	0.88	1.51	0.37	2.01
Annealed	0.13	0.90	0.33	0.97	0.90	0.44	2.77

Table B.6. shows calculated Harris texture index, T_{hkl}, calculated using Eqn. 7.6 for certain reflections of the cold spray Cr coatings taken from diffraction peaks measured at the start of the tensile tests. Thus, they represent the texture of the material in its as-fabricated or as-annealed state. Values closer to 1 indicate a random orientation of crystallites. Slight differences are observed between the two coated specimens, but the differences are not very significant. However, a full texture analysis (i.e., rotation of the sample during synchrotron diffraction) would be better appropriate to determine the effect of annealing on texture within the Cr coatings.

Table B.6. List of Harris Texture Index, T_{hkl}, calculated using Eq. (7.6) for certain reflections of the cold spray Cr coating. These values were calculated from diffraction measurements made at the start of the tensile test (i.e., just before straining).

Reflection	{110}	{200}	{211}	{220}	{310}
As-Deposited	1.07	1.13	0.98	0.94	0.87
Annealed	0.92	1.08	0.95	1.03	1.01